University of Cape Town

Submitted in partial fulfilment of the requirements of the degree of Doctor of Philosophy

SPECIALITY : HIGH ENERGY PARTICLE PHYSICS

Heavy-flavour production at forward rapidity as a function of charged-particle multiplicity with ALICE at the LHC

Candidate:
Sibaliso MHLANGA

Supervisor:
Prof. Jean Cleymans
University of Cape Town

Co supervisor:
Prof. Zinhle Buthelezi
iThemba LABS, Cape Town

May 20, 2020

Declaration

I know the meaning of plagiarism and do herby declare that this written submission represents my own work and effort and that it has not been submitted anywhere for any award. Where other sources of information have been used, they have been acknowledged.

(Sibaliso Mhlanga)

Student Number: MHLSIB027

Date: May 20, 2020

Place: University of Cape Town

Abstract

Heavy-flavour hadrons are hadrons made up of at least a charm or beauty heavy quark. They are produced in the early stages of ultra-relativistic collisions via hard scatterings and are important tools for studying different aspects of Quantum Chromodynamics (QCD) in hadronic collisions. Charged-particle multiplicity gives information on the global characteristics of the event and could be used to characterize particle production mechanisms. In hadronic collisions at Large Hadron Collider (LHC) energies, there is a significant contribution of Multiple Parton Interactions (MPI), i.e. several hard partonic interactions occurring in a single collision between nucleons. Therefore, the measurement of heavy-flavour hadrons as a function of charged-particle multiplicity gives insight into the mechanisms influencing their production in hadronic collisions at these energies and is a tool to test the influence of MPIs. Furthermore, charged-particle multiplicity dependence of heavy-flavour hadron production is used to test the ability of QCD theoretical models to reproduce data.

In this thesis we investigate the production of heavy flavours via the single muon decay channel at forward rapidity as a function of the charged-particle multiplicity measured at central rapidity in proton-lead (p–Pb) collisions at $\sqrt{s_{\rm NN}}$ = 8.16 TeV using ALICE (A Large Ion Collider Experiment) at the LHC. ALICE is a dedicated detector optimized to study ultra-relativistic heavy-ion collisions in which the Quark-Gluon Plasma (QGP - the state of matter which prevailed in the Early Universe shortly after the Big Bang) is created. ALICE also studies proton-proton (pp) and p–Pb collisions. In pp collisions, production cross sections obtained from data provide information used to test pQCD theories while in p–Pb collisions, where the energy density is believed to be too low to produce the QGP, the presence of additional nuclear matter can alter the wavefunction of the nucleus leading to modified observables - the so-called cold nuclear matter (CNM) effects.

The study of the multiplicity dependence of heavy-flavour production in p-Pb collisions may give important information regarding initial-state effects in CNM. Both pp and p–Pb collisions provide reference for comparison with heavy-ion (Pb–Pb) collisions. ALICE measures hadrons, leptons, and photons up to very high transverse momentum ($p_{\rm T}$) ≈100 GeV/c. The detector consists of a central barrel, which covers a rapidity of $|y| < 1$ and a Muon Spectrometer which covers the forward rapidity, $-4 < y < -2.5$. In this thesis, the production of heavy flavours via the contribution of their muonic decays to the inclusive $p_{\rm T}$-differential muon yield at forward ($2.03 < y_{cms} < 3.53$) and backward (-4.46

$< y_{cms} <$ -2.96) rapidity reconstructed with the Muon Spectrometer and charged-particle multiplicity using the Silicon Pixel Detector located in the central barrel ($|y| <1$) in p-Pb collisions at $\sqrt{s_{\mathrm{NN}}} = 8.16$ TeV in the forward and backward rapidity are studied.
The aim of the study is to probe the role of MPIs in the production of heavy flavours focusing on the contribution of hard and soft processes as well as to investigate effects of the presence of multiple binary nucleon-nucleon interactions and the initial state effects modified by CNM in particle production.

Acronyms

ALICE	A Large Ion Collider Experiment
ATLAS	A Toroidal Lhc ApparatuS
A x ϵ	Acceptance x Efficiency
ADC	Analogue to Digital Converter
AOD	Analysis Object Data
$\langle N_{ch} \rangle$	Average charged-particle multiplicity
$\langle p_{\mathrm{T}} \rangle$	Average or mean transverse momentum
μB.	Baryon chemical potential
B.R	Branching ratio
CPC	Cathode Pad Chambers
CTP	Central Trigger Processor
SPS	CERN Super Proton Synchrotron
CNM	Cold nuclear matter
CMS	Compact Muon Solenoid
CROCUS	Concentrator Read-Out Cluster Unit System
DAQ	Data Acquisition system
DCAHI	Detector Control Agent Human Interface
DCS	Detector Control System
EMCal	ElectroMagnetic Calorimeters
dE/dx	Energy loss
CERN	European Organisation for Nuclear Research
ESD	Event Summary Data
ECS	Experimental Control System
FONLL	First Order Next to Leading Log
HMPID	High Momentum Particle Identification Detector

HLT	High-Level Trigger
ITS	Inner Tracking System
IP	Interaction point
λ_{int}	Interaction length
LHC-	Large Hadron Collider
LHCb	Large Hadron Collider beauty
LO	Leading order
Pb-Pb	Lead-lead collisions
Pb-p	Lead-proton collisions
LTU	Local Trigger Units
LUT	Look-Up-Tables
MANU	MAnas NUmerique
MB	Minimum bias trigger
MonALISA	Monitoring Agents using a Large Integrated Services Architecture
MC	Monte Carlo
MPI	Multiple parton interactions
MANAS	Multiplexed ANAlogic Signal processor chips
N_{ch}	Multiplicity
MARC	Muon Arm Readout Chip
MSH	Muon single high p_{T}
MSL	Muon single low p_{T}
R_{AA}	Nuclear modification factor
AA	Nucleus Nucleus collisions
N_{coll}	Number of binary nucleon-nucleon collisions
N_{part}	Number of participating nucleons
N_{cl}	Number of SPD clusters
N_{trkl}	Number of tracklets
OCDB	Offine Calibration Database

PID	Particle identification
PDFs	Parton distribution functions
PCA	Partition Contol Agent
PCAHI	Partition Contol Agent Human Interface
nPDF	PDFs of nucleons bound in nuclei
pQCD	Pertubative Qunatum Chromodynamics
PHOS	Photon Spectrometer
Z_v^{SPD}	Primary vertex and inside the SPD
p–Pb	Proton-lead collisions
pp	Proton-proton collisions
η	Pseudorapidity
QCD	Quantum Chromodynamics
QGP	Quark-Gluon Plasma
RAMSES	RAdiation Monitoring System for the Environment and Safety
y	Rapidity
RHIC	Relativistic Heavy Ion Collider
RPC	Resistive Plate Chamber
SDD	Silicon Drift Detectors
SPD	Silicon Pixel Detectors
SSD	Silicon Strip Detectors
TOF	Time of Flight Detector
TPA	Trigger Partition Agent
TPC	Time Projection Chamber
TRD	Transition Radiation Detector
p_{T}	Transverse momentum
T0	TZERO
V0	VZERO
WLCG	Worldwide LHC Computing Grid
ZDC	Zero Degree Calorimeter

Contents

CHAPTER 1

Introduction

Matter as we know it today is made up of atoms made up of protons and neutrons bound into a nucleus and electrons orbiting the nucleus. Protons and neutrons are also composite particles made up of quarks and gluons. Quarks and gluons are fundamental particles called partons. Fundamental particles and the forces governing their interactions are described in the Standard Model of particles [1].

Quarks and gluons cannot be observed in isolation under normal temperature but are always confined in composite particles called hadrons. Hadrons are particles containing three quarks (baryons, e.g. protons, neutrons, etc) or two quarks one of which is an antiquark (mesons, e.g. pions, kaons, etc). However, at extreme temperatures ($\approxeq 2$ x 10^{12} ^{o}K), nuclear matter is expected to transition into a strongly interacting medium, a state where quarks and gluons are no longer confined and can be considered as basic degrees of freedom. This state is known as the Quark-Gluon Plasma. The strong interaction is governed by the fundamental theory called Quantum Chromdynamics (QCD) [2, 3], within which the state of nuclear matter is described. The QCD phase diagram describes the different phases of nuclear matter at a given temperature (T) as a function of the baryon chemical potential[1] (μ_b). At these extreme temperatures, the masses of quarks diminish and chiral symmetry determines the characteristics of the QCD phase diagram [4]. Therefore, one of the main purposes of the experiments of ultra-relativistic heavy-ion

[1] Baryon chemical potential measures the imbalance between matter and antimatter, and zero indicates perfect balance

collisions at Large Hadron Collider (LHC) [5] and other lower energy collider experiments e.g. at the Relativistic Heavy Ion Collider (RHIC) [6] is to observe the restoration of chiral symmetry at finite temperature and energy density [7, 8]. Hence the interest in the study of strongly interacting matter at extreme temperature and energy densities [9].

The study of strongly interacting matter using heavy-ion collisions has tremendeously evolved since the advent of the 2000s with important milestones. The evolution started with the CERN Super Proton Synchrotron (SPS) Pb beam results which showed that "compelling evidence has been found for a new state of matter featuring characteristics of the QGP" [10]. This was followed by the result from Au–Au collisions at 130 GeV per nucleon at RHIC which characterised the state of matter produced in these collisions as an extremely strongly interacting and almost perfect fluid [11]. At the Large Hadron Collider (LHC) [5], the available energies at the centre-of-mass system are increased by four orders of magnitude making it possible for the LHC to fulfill its main goal of measuring with an increased precision and new and unique probes the parameters that characterise the QGP. The increase of the collision energy is of paramount importance as it results in increased production rates for hard probes (high p_{T} particles), such as jets, electroweak particles and heavy-flavour quarks (charm (c) and beauty (b)). Heavy quarks include two historical pillars: open heavy flavour (B, D mesons) hadrons and the full family of quarkonia or bound chamonium and bottomium states (J/ψ, $\psi^{'}$, Υ). The high production rates of these probes make precision studies of the QGP possible. The interactions of these probes with the medium constituents are studied in order to infer its properties. The main interest of the study is open heavy-flavour hadrons, which will be referred to as "heavy flavours" from here onwards.

1.1 Heavy-ion physics at the LHC

ALICE (A Large Ion Collider Experiment) [12], is one of the LHC experiments which is dedicated to studying heavy-ion collisions such as Pb ions, where the QGP is expected to be formed. The production rates of the different probes mentioned above, are studied in different collision systems. The deviations of the production cross sections due to interactions with the medium produced, with respect to the heavy-ion cross sections, give information on the properties of the medium produced. In heavy-ion collisions it is important to distinguish deviations resulting from the presence of the medium, the so-called final state effects, from those resulting from other effects. The modifications resulting from effects other than the presence of the strongly interacting medium are studied in p–Pb collisions - the so called "control experiments", where the presence of a nucleus in the asymetric collision provides the initial state environment. These effects are

referred to as Cold Nuclear Matter (CNM) effects or initial state effects. Furthermore, it is also crucial to compare the heavy-ion (Pb–Pb) collision results systematically with reference pp (and p–Pb) collisions at the same centre-of-mass energy and appropriate kinematic regime. Therefore, ALICE also studies proton-proton (pp) and p–Pb collisions as a comparison to heavy-ion collisions in order to provide a reference point as well as disentangle final state from initial state effects.

Amongst the many probes used to study the properties of the QGP and CNM, this thesis is mainly focused on heavy-flavour production. In the current study the correlation of heavy-flavour production with the charged-particle multiplicity of the collision is done. Therefore, from henceforth we streamline the following discussion to focus on the aspects.

1.2 Heavy-flavour production at the LHC

Heavy quarks and subsequently heavy-flavour hadrons are produced via hard scattering in the early stages of the collisions (See Figure 2.4). As a consequence of the large center-of-mass energies and the high luminosities[2] delivered, the LHC is a heavy-quark factory, producing $b\bar{b}$ [13] and $c\bar{c}$ [14] 10 and 100 times more than the cross sections obtained at RHIC [15], respectively, as shown in Figure 1.1. Figure 1.1 also shows that heavy-quark productions measurements are in good agreement with FONLL calculations within uncertainties.

The Leading order (LO) process for the production of a heavy quark m_Q in hadronic collisions is flavour creation i.e. quark-anti-quark annihilation and gluon-gluon fusion.

$$q\bar{q} \rightarrow Q\bar{Q} \tag{1.1}$$

and

$$gg \rightarrow Q\bar{Q} \tag{1.2}$$

The leading order diagrams are shown in Figure 1.2.

The large limit of the partonic cross section is given by Equation 1.3 [17],

$$\sigma(q\bar{q} \rightarrow Q\bar{Q}) \approx 1/s \tag{1.3}$$

[2]The ratio of the number of events detected (N) in a certain time (t) to the interaction cross section (σ) L = $\frac{1}{\sigma}\frac{dN}{dt}$

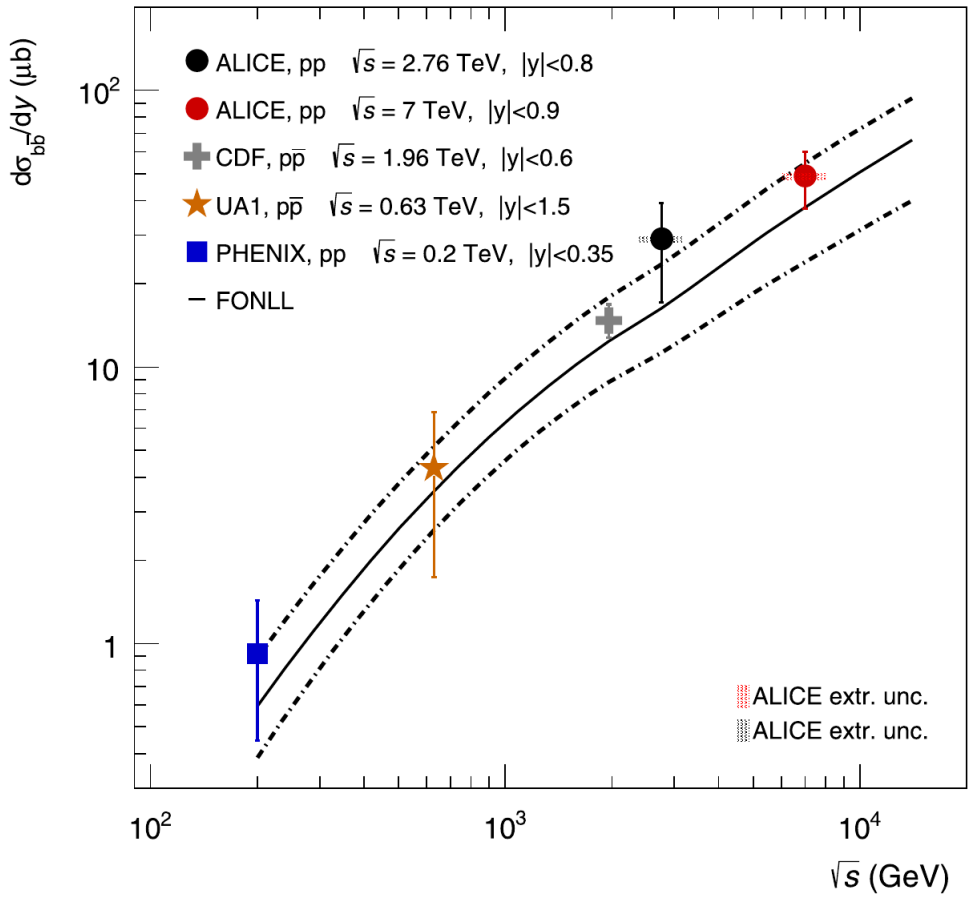

Fig. 1.1 Beauty-antibeauty cross sections as a function of the centre-of-mass energy for different experiments at low energies to RHIC and ultimately the LHC, for different collisions systems (pp collisions for the LHC points) [13].

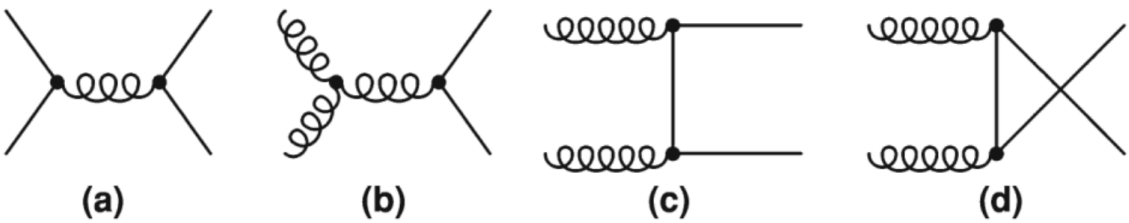

Fig. 1.2 Leading order diagrams for heavy quark pair production, quark-quark annihilation (a), gluon-gluon fusion(b) - (d) [16, 17].

where s is the centre-of-mass energy available in the system and $\sqrt{1-\frac{4m_Q^2}{s}}$ is the velocity of the heavy quark. The quark annihilation process vanishes at high s, therefore, gluon-gluon fusions is the dominant process for heavy-quark production at the LHC.

1.3 Charged-particle multiplicity

Since the LHC presents an unprecedented energy regime, one of the crucial and most anticipated measurement concerns the global properties of the collisions. Global event properties allow the characterization of collisions by describing the initial state and the following dynamical evolution. The global characteristics of the collision can be quantified in the produced charged-particle multiplicity, i.e. the number of charged particles produced per event.

The measured charged-particle production in p–Pb compared to pp collisions at $\sqrt{s_{\rm NN}}$= 5.02 TeV [18] at the LHC, showed significant differences, particulary at low $p_{\rm T}$. Consequently, a slightly smaller average multiplicity per number of participating nucleons in p–Pb compared to pp collisions [19] was observed. This difference could be attributed to the effects of the presence of a nucleus in p–Pb collisions, the so-called Cold Nuclear Matter effects (to be discussed in 2.5) that alter the interactions compared to pp collisions. Figure 1.3 shows that the multiplicities of charged particles produced in pp and p–Pb collisions at LHC energies are comparable or higher than the ones measured at lower energy experiments such as the RHIC and SPS [20].

The energy densities exceed those achieved in central collisions at SPS and RHIC [21]. For this reason, multiplicity measurements at LHC energies are of importance as they are used to test Monte Carlo (MC) generators such as PYTHIA[22] and EPOS [23] for their ability to reproduce data at these energies.

Charged-particle production at the LHC is better described by models that include MPIs. The number of charged particles produced is connected to the number of elementary collisions. ALICE measured the average mean transverse momentum ($\langle p_{\rm T}\rangle$) of charged particles as a function of charged-particle multiplicity in a quest to study the process occuring at partonic level in hadronic collisions [24]. The results obtained are shown in Figure 1.4 and were well reproduced by PYTHIA6.4. It was shown from this study that the $\langle p_{\rm T}\rangle$ of charged particles increases linearly with the multiplicity for pp and p–Pb collisions, however, in p–Pb collisions at higher charged-particle multiplicity the increase is slower while Pb–Pb collisions reach a saturation at high multiplicity. The result probed further investigations and the need for more differential measurements, in particular, heavy particle production as a function of charged-particle multiplicity, in

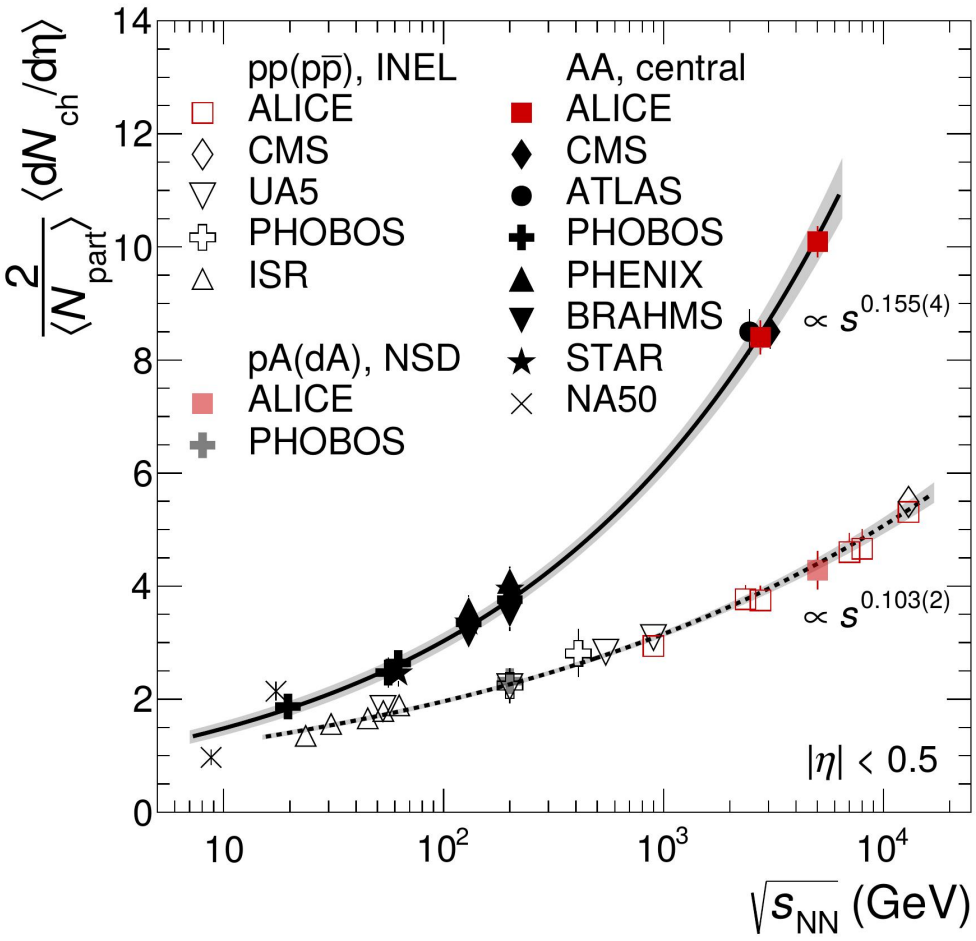

Fig. 1.3 Mean charged particle density $\langle dN_{ch}/d\eta \rangle$ normalised by the average number of participating nucleon pairs, $\langle N_{part} \rangle$ as a function of the centre-of-mass energy [21].

order to understand particle production mechanisms at the LHC, the interplay between hard and soft processes and the role of MPIs in particle production.

Furthermore, "measurements of particle correlations in azimuth and pseudorapidity [25] have raised the question whether collective effects in p–Pb collisions, as modeled for example in hydrodynamical approaches [26], are the origin of the observed correlations. It remains questionable if the small system size created in pp or p–Pb collisions could exhibit collective, fluid-like, features due to early thermalization, as observed in Pb–Pb collisions" [27]. One way to address these issues is to investigate production mechanisms, correlations, and event shapes as a function of the particle multiplicity. Moreover, the charged-particle multiplicity produced in p–Pb collisions is linked to the initial energy density hence can provide constraints on the particle production mechanisms, allowing the discrimination of the soft (low p_{T}) from the hard (high p_{T}) regime. Therefore, we can investigate correlations of produced high p_{T} particles with all charged hadrons produced

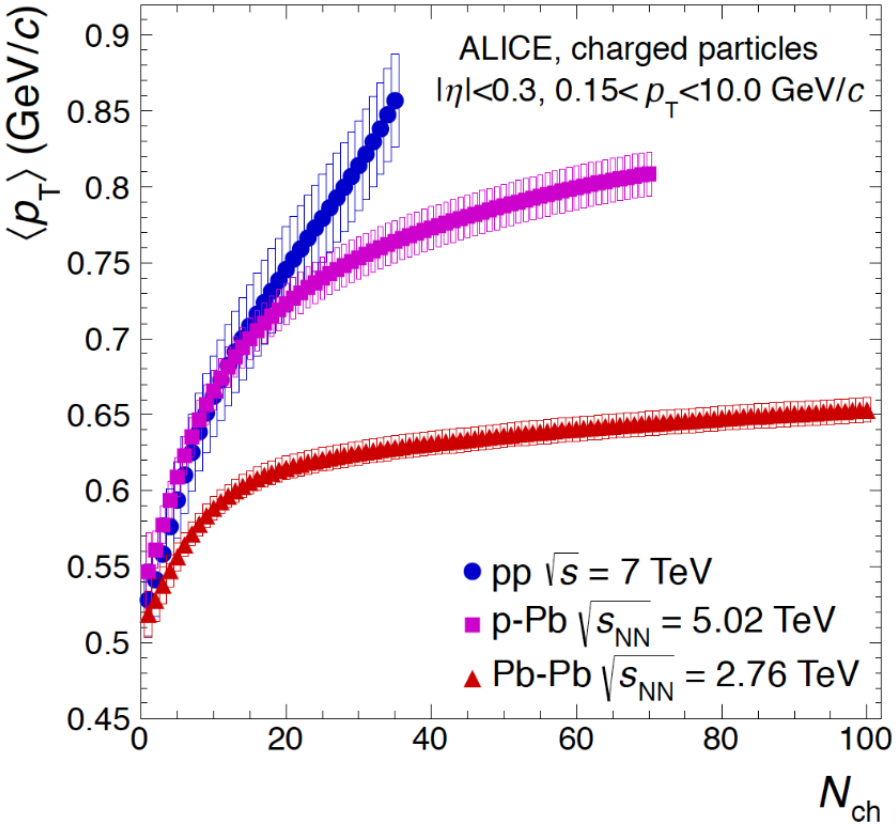

Fig. 1.4 Mean p_T of charged particles as a function of charged particle multiplicity [24].

per event.

In this regard, an interesting field of study is being explored by the ALICE Collaboration where the production of heavy-flavour hadrons is studied as a function of the charged-particle multiplicity. These studies have recently produced interesting questions pertaining to what could be the processes influencing heavy-flavour hadron production at LHC energies [28]. To provide answers to these questions, more studies are needed in all heavy flavour sectors, namely, hadronic, electronic and muonic channels in pp and p–Pb collisions. Therefore, the goal of this thesis is to study the production of heavy-flavour decay muons as a function of charged-particle multiplicity.

1.4 Heavy-flavour production as a function charged-particle multiplicity

Measurements of the heavy-flavour production as a function of the charged-particle multiplicity give insight on the processes occuring at partonic level. Since the charged-particle

multiplicity at the LHC is influenced by MPIs it is therefore sensitive to light particle production. Consequently, studying the multiplicity dependence of heavy-flavour production may shed more light on the interplay between hard and soft processes in particle production. In p–Pb collisions, the multiplicity dependence of heavy-flavour production is also affected by the presence of multiple binary nucleon-nucleon interactions and the initial conditions of the collision are modified due to CNM effects. Therefore multiplicity dependence of heavy-flavour production helps to disentangle CNM effects from the effects of the QGP. Furthermore, the measurements might help to constrain the dependence of heavy-flavour production on the collision geometry and the density of final state particles because enhancement of particle production due to multiple-parton scattering (p_{T} broadening see section 2.5.0.2) was observed to be stronger in central collisions than in peripheral collisions [29]. Moreover, final-state effects, energy loss, and collective behaviour are also sensitive to the particle multiplicity.

1.4.1 Thesis objectives and outline

As already mentioned, the aim is to study the yields of heavy-flavour production via the muonic channel to investigate CNM effects as well as the interplay between soft and hard processes in particle production. To do this, I analysed data collected by the ALICE detector at the LHC in 2016 during p–Pb and Pb–p collisions. The charged-particle multiplicity was measured at $|\eta| < 1$ while the yields of heavy flavour were measured at forward rapidity -4 $< \eta <$ -2.5, in the Muon Spectrometer [30].

The yields of heavy-flavour decay muons were obtained inclusively (c,b $\rightarrow \mu$ + X brancing ratio 10.33 %) because currently it is not possible to reconstruct muons from charm and beauty hadron decays seperately in the muon spectrometer due to the limitation in mass resolution in the muon tracking chambers as well as the lack of detectors close to the interaction vertex. However, with the upgrade [31], it would be possible in Run 3 foreseen to commence in the last half of 2021. The muonic channel is also advantageous for this study since it eliminates "auto-correlation" biases anticipated when the heavy-flavour signal is measured in the same region as the charged-particle multiplicity.

The thesis outline is as follows;

Chapter 2 An overview of the experimental and theoretical aspects to be considered in understanding this study are presented. Recent experimental results pertaining to the aspect under discussion will also be reviewed.

Chapter 3 gives the outline of the ALICE Detector with emphasis on the Muon Spectrometer. Details about the data taking conditions and the ALICE offline framework will

also be given.

Chapter 4 details the work done by the author. The methods used to extract the charged-particle multiplicity as well as the procedure followed for the muon analysis will be discussed. The procedure followed in order to obtain the heavy-flavour decay muon signal, namely, background subtraction, efficiency corrections as well as normalisation procedures will be detailed as well as the systematic uncertainties associated with the measurements.

Chapter 5 will be dedicated to presentation and discussion of the final results obtained from the study of heavy-flavour decay muons as a function of charged particle multiplicity by the author. A comparison of the results to other multiplicity measurements will also be presented.

Chapter 6 consists of the summary, conclusions and the outlook.

CHAPTER 2

Theoretical and experimental concepts

This chapter describes the theoretical and experimental concepts of heavy-ion collisions. Among the several different probes used to study the medium formed in heavy-ion collisions, the attention is given to heavy flavours (charm and beauty), the main focus of this thesis. A brief introduction to the QGP, which will set the ground for (final state) medium effects expected in Heavy Ion collisions is provided. A discussion will follow on Cold Nuclear Matter effects, an important phenomenon to study initial state nuclear modifications occuring in heavy-ion, in particular, proton-nucleus collisions due to the presence and structure of the nucleus. Also a discussion on charged-particle production at the LHC, in particular, as the topic of this thesis states, we will focus on the important aspects of the multiplicity dependence of heavy-flavour production. The chapter will conclude by discussing recent measurements of the correlation of heavy-flavour production as a function of the charged-particle multipicity.

2.1 The Standard Model

The Standard Model of particle physics is a theory that describes the interactions of elementary matter with the three of the four forces of nature, electromagnetic, weak and strong force. The elementary particles are characterised by their masses and quantum numbers, such as the spin (S), electric charge (Q), baryon number (B), lepton number

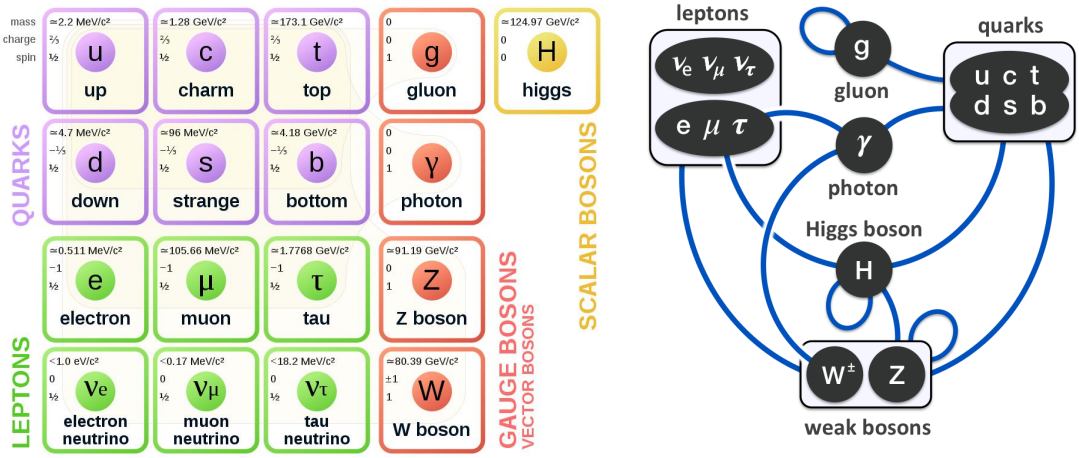

Fig. 2.1 Fundamental particles (Left) and fundamental interations (right) of the standard modela of particles [35].

(L), color charge, etc. The elementary particles are classified into two basic types, namely, fermions [1] and bosons[2] using their spin. Fermions, namely, quarks and leptons are the fundamental constituents of matter. There are six quarks, also called flavours, namely, up (u), down (d), strange (s), charm (c), top (t) and bottom (b) and there are six leptons: electron (e), electron neutrino (ν_e), muon (μ), muon neutrino (ν_μ), tau (τ) and tau neutrino (ν_τ). Quarks have fractional charges (-1/3 or +2/3) and have an additional intrinsic property called colour charge. The matter particles interact transferring energy between them via gauge bosons, the mediators of fundamental interactions. The mediator of the electromagnetic force is the photon (γ), it affects electrically charged particles while the mediator of the weak force are the electroweak bosons $W^{\pm}$ and Z^0. Electroweak bosons are also responsible for nuclear decays. The strong force is carried by the gluon (g) and it affects the interactions of quarks and gluons, the so-called color charged particles. Lastly, gravitation, which is not yet described by the standard model. The electromagnetic and weak interactions are unified in the electroweak theory [32]. The higgs mechanism breaks the electroweak symmetry, by the generation of the $W^{\pm}$ and Z^0 masses via their interaction with the Higgs bosons. The Higgs boson has no spin. it was recently confirmed by A Toroidal Lhc ApparatuS (ATLAS) [33] and Compact Muon Solenoid (CMS) [34] experiments at the CERN Large Hadron Collider (LHC) [5]. The Nobel Prize in Physics 2013 was awarded to F. Englert and P. W. Higgs for the prediction of the Higgs boson. Figure 2.1 shows a summary of the fundamental particles and their masses as well as the fundamental interactions.

The strong interaction between quarks and gluons is described by the theory of Quantum

[1] Half integer spin particles
[2] Integer spin particles

chromodynamics (QCD). The following sections will briefly describe aspects of this theory.

2.2 Quantum chromodynamics

Quarks and gluons have not been observed in isolation below the Hagerdon temperature[3] of approximately 2 trillion kelvin (corresponding to an energy of 130 MeV - 140 MeV per particle), but clump together to form hadrons as a consequence of the strong interaction. They can be combined to form mesons[4] or baryons[5]. However, when two (anti)quarks do not carry the same quantum numbers, other states beyond mesons and baryons are also allowed e.g. the Large Hadron Collider beauty (LHCb) recently reported observation of pentaquarks [36]. Quarks have fractional charges (-1/3 or +2/3) and have intrinsic property called "colour charge". The gluon is neutral but like the quark carries colour charge. Gluons are carriers of the strong force which clumps quarks and antiquarks together to form hadrons.

2.2.1 Asymptotic freedom and confinement

Analogous a polarised QED vacuum which forms many virtual electron-positron pairs are the QCD vacuum excitations. These excitation result in the formation of quark-antiquark pairs. Since quarks are fermions they behave in a similar manner as electron-positron pairs, screening other colour charges. However, gluons tend to have an anti-screening effect which outweighs the screening effect of quarks. Consequently, the intensity of the strong coupling (α_s) constant becomes weaker at short distances (high energy and large transverse momentum transfer (Q^2)) as can be seen in Figure 2.2.

Thus for small values of Q^2 (small energies), the strong coupling constant has large values $\alpha_s \gg 1$. This explains the magnitude of the strong force and the fact that quarks are confined in colour neutral states (baryons and mesons), this is the so-called "confinement". At high Q^2 (short distances), quarks behave as free particles due to the asymptotic decreases of the α_s. This is called "asymptotic freedom".

Another important phenomenon that accompanies asymptotic freedom is chiral symmetry restoration. When quarks are confined in hadrons, they acquire effective masses e.g in a proton it is about 300 MeV roughly one third of the hadron mass. However, in the

[3] The temperature where hadronic matter is no longer stable, and must either "evaporate" or convert into quark matter.

[4] Particles made up of one quark, one antiquark pair e.g pions

[5] Particles made up of 3 quarks and/or antiquarks e.g. protons

deconfinement state, quarks are expected to interact with their bare masses thus restoring the symmetry. Experimentally, this phenomenon can be investigated through spectral properties of the light vector mesons ρ, ω and ϕ. The chiral symmetry restoration is expected to affect their spectral feature namely, mass and/or width.

Pertubative QCD (pQCD) is a subfield of physics in which QCD is studied by using the fact that strong coupling constant α_s is small at high energy and short distance interactions, thus allowing the interactions to be dealt with as a perturbative series in powers of α_s. At low energies, α_s is too large. Most processess cannot be calculated directly with pQCD since quarks and gluons cannot be directly observed due to colour confinement and the hadron structure has a non-pertubative nature. Consequently, almost all applications of pQCD separate the cross sections in two parts,

1. process dependent pQCD calculable short-distance parton [6] cross section
2. universal long-distance functions which can be measured with global fits to experimental data in order to obtain a partly calculable prediction to particle reaction processes.

Long-distance functions include parton distribution functions (PDFs), see section 2.5.0.1, fragmentation functions, multi-parton correlation functions, etc.

QCD predicts a deconfined medium, the QGP above a critical temperature ($T_c \approxeq 155$ MeV).

2.3 The Quark Gluon Plasma (QGP)

The Universe is believed to have been composed of deconfined quarks and gluons a few microseconds after the Big Bang. This deconfined state is known as the QGP. The QGP expanded and cooled down thus transitioning to hadronic matter, the state the Universe is in presently. A sizeable amount of QGP can be created in the laboratory by colliding beams of heavy-ions where large amounts of energy densities and temperatures are produced in a small volume. This results in the hadrons overlapping and the strong interaction clumping them together becomes weak and matter transitions into the QGP. The QCD phase transition diagram is characterised by the temperature as a function of the baryon chemical potential (μ_B). The baryon chemical potential is a measure of the differences between the amount of matter and anti-matter observed. For example, it is believed that soon after the Big Bang the amount of matter and anti-matter were equal,

[6] A parton is a particle that is a constituent of a hadron, e.g. quarks and gluons

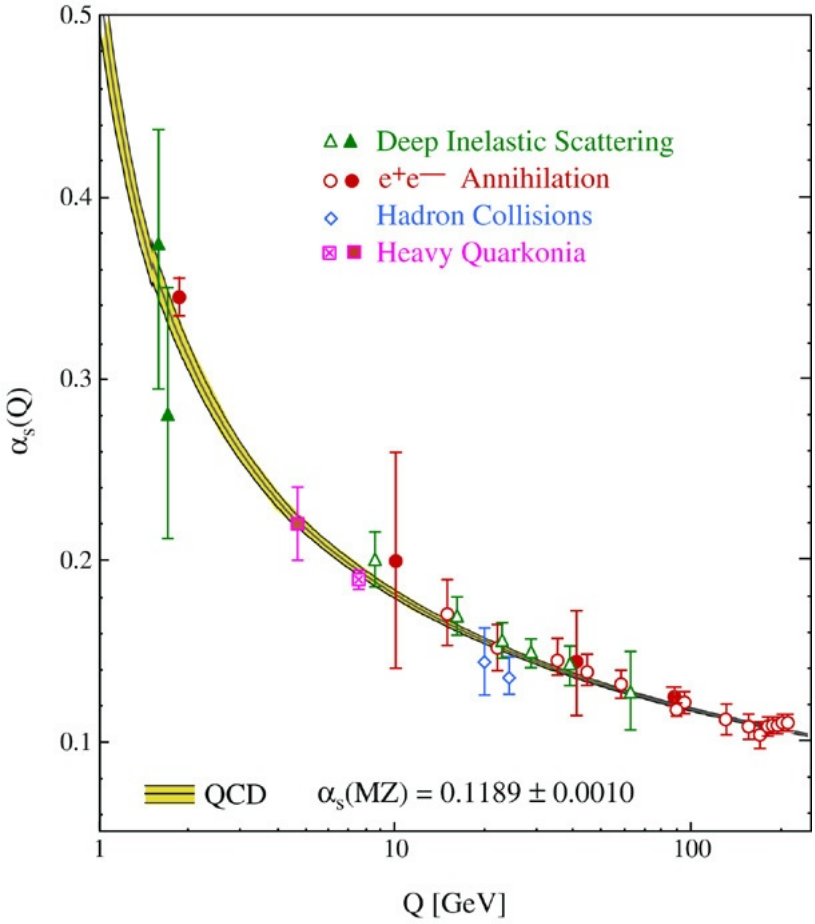

Fig. 2.2 The QCD coupling constant. α_s(MZ)is a reference scale in which α_s is given. Q is the transferred momentum. [37].

therefore, $\mu_B = 0$, and now we have more matter than anti-matter and $\mu_B > 0$. Figure 2.3 shows the QCD phase diagram.

The crossover temperature depends on the observed μ_B. The LHC observes matter at $\mu_B \approxeq 0$. Lattice QCD calculations, show that the cross over temperature at these condition is ≈ 170 MeV [39]. Studies at the LHC, particularly by ALICE have confirmed the value of T_c to be 150 - 160 MeV [40]. The transitional stages from QGP to hadronic matter are shown in Figure 2.4.

2.3.1 Evolution of the QGP

The collisions starts at t = 0 fm/c.

Pre-equilibrium ($t \lesssim 1$ fm/c): partons scatter among each other and give rise to an abundant production of deconfined quarks and gluons. High transverse momentum par-

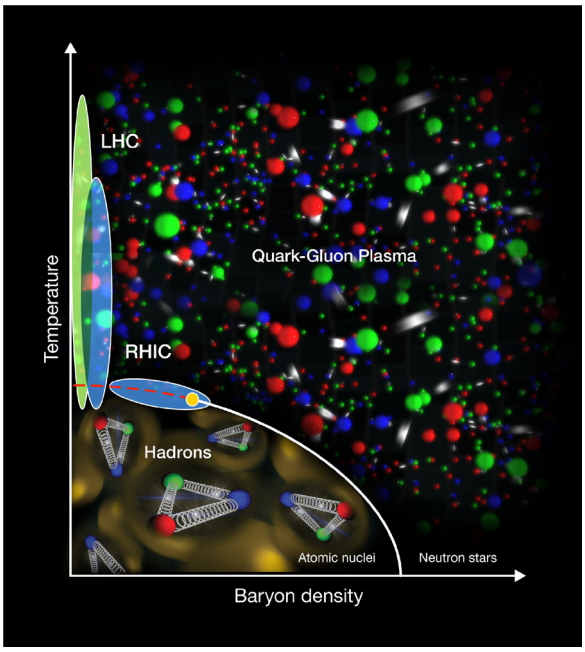

Fig. 2.3 The QCD phase diagram [38].

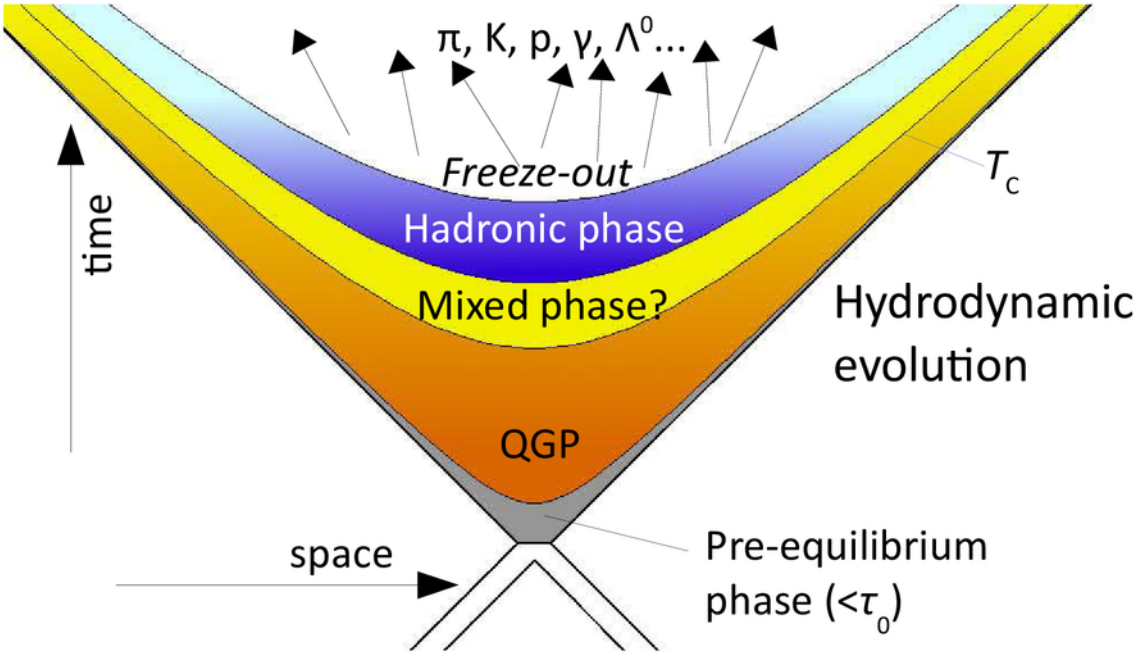

Fig. 2.4 Evolution of the QGP [38].

ticles ($p_T \gg 1$ GeV/c) are produced at this stage.

Thermalization (1 < t < 10 fm/c): elastic and inelastic interactions between partons in QGP lead to the thermalization phase. Inelastic interactions can modify the flavour composition of particles. Due to its internal pressure, the system at thermal equilibrium rapidly expands. The system expands until chemical freeze-out, a state where the number of particles formed is fixed and inelastic scatterings have ceased.

Hadronization (t > 20 fm/c): As the system continues to expand, its density decreases until it is too low and elastic scatterings among hadrons cease. This is called kinetic freeze out. At this point the hadrons are decoupled and their momenta are fixed.

2.3.2 Collision geometry

By the virtue of the constituents of colliding nuclei we expect that more than one nucleon may collide from each of the ions. Also, some nucleons may encounter more than one nucleon on their path. The number of collisions and the number of nucleons that collide depends on the impact parameter [7], b, of the collision. The impact parameter cannot be directly measured in experiment, therefore a model of nuclear collisions connecting the geometry to the observed particle multiplicity was developed by Roy Glauber [41]. The Glauber model connects the particle production to the number of colliding nucleons and the geometry of the collision i.e. the multiplicity (N_{ch}) [8] decreases as a function of the impact parameter of the collision.

Apart from connecting multiplicity to the impact parameter, Glauber modelling is used to calculate other characteristics of the collision geometry, such as the number of participating nucleons (N_{part}), and the number of binary nucleon-nucleon collisions (N_{coll}). These quantities are often used to present the data. Furthermore, the centrality of heavy-ion collisions is often expressed as a percentile of the total inelastic cross-section. Typically, a "peripheral" collision is considered to be 80-100% of the cross-section where the impact parameter approaches two times the radius of the nuclei. Collisions referred to as "central" are at typically 0-10% (or 0-5%) of the cross-section. Figure 2.5, shows the differences between central and peripheral collisions while Figure 2.6 shows an example of Glauber calculated quantities b and N_{part} correlated with an experimental observable N_{ch} in Pb–Pb collisions[41].

[7] A measure of the distance between the centres of the colliding nuclei.
[8] Number of charged particles produced per event

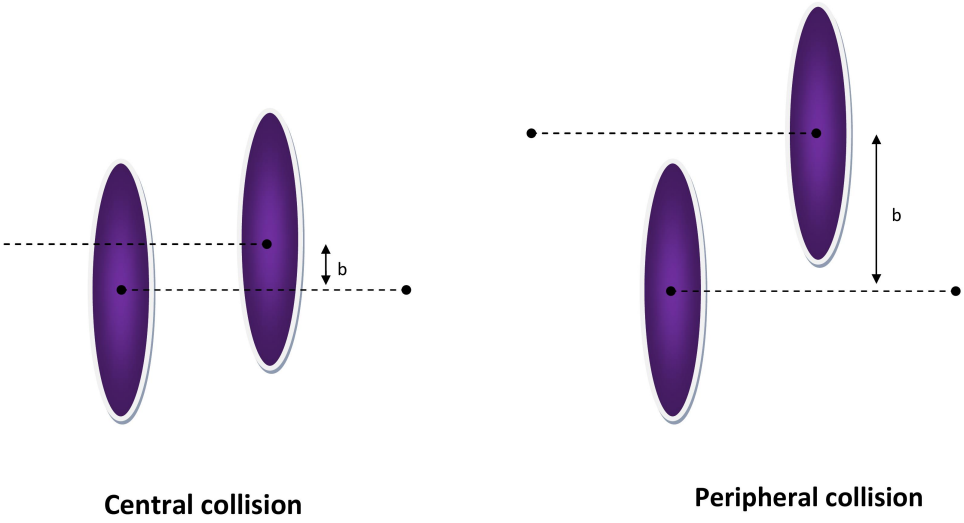

Fig. 2.5 A schematic representation of the collison geometry.

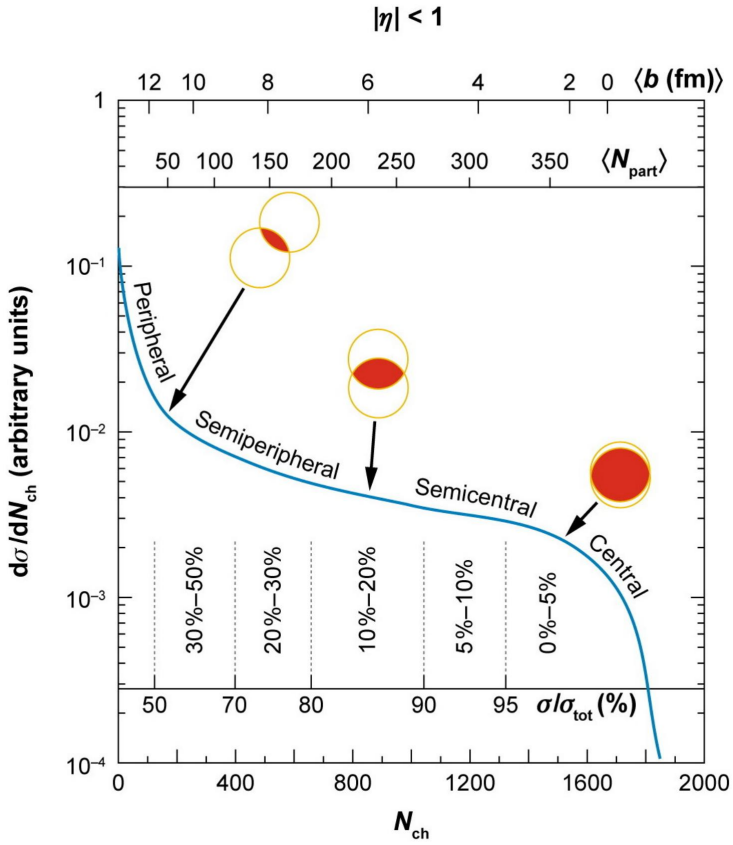

Fig. 2.6 An example of Glauber calculated quantities b and N_{part} correlated with an experimental observable N_{ch} in Pb–Pb collisions., [41].

2.3.3 Signatures of the QGP

The QGP has a very short lifetime ($\tau \approx 10^{-23}$s), therefore it is impossible to observe it directly from experiments. Final state observables are various signatures used to observe and study its properties. A good signature forms quickly with a long lifetime with respect to the QGP and lastly, its production rates are calculable with pQCD with experimental verification in pp collisions. Here a brief detail on the probes relevant for discussion in this thesis are given, but it should be noted that there are many other probes to study the QGP.

Two types of probes are used to study the QGP and its properties, namely, soft and hard probes.

- **Soft probes**
  Soft are those resulting from low p_{T} transfer. Particles classified as soft probes are produced at all stages of the QGP. Examples of soft probes include among others, photons, thermal dileptons, anisotropic flow of charged particles, etc.

- **Hard probes**
  On the other hand, hard probes are produced at the initial stages of the collision via hard scattering [42]. Hard probes include heavy particles since the p_{T} transfer at the initial stages of the collisions is very high hence influences creation of heavy particles. Examples of hard probes are the electro weak bosons, W and Z, heavy quarks (c and b) and their hadrons[9] as well as jets[10].

2.4 Nuclear modification

Final state effects are a result of in-medium energy loss in the QGP. The energy loss can be quantified in the so-called **nuclear modification** factor, R_{AA}, defined in Equation 2.4.

$$R_{AA} = \frac{1}{\langle N_{coll} \rangle} \frac{dN_{AA}/dp_T}{dN_{pp}/dp_T} \tag{2.1}$$

where $\mathrm{dN_{AA}}/\mathrm{d}p_{\mathrm{T}}$ and $\mathrm{dN_{pp}}/\mathrm{d}p_{\mathrm{T}}$, are the differential particle yields per event in nucleus-nucleus (AA) and proton-proton (pp) collisions, respectively, and $\langle\ \mathrm{N_{coll}}\ \rangle$ is the average number of binary nucleon–nucleon collisions. In the absence of the

[9] Hadrons of heavy quarks are particles consisting of at least one heavy quark or antiquark
[10] A narrow cone of hadrons and other particles

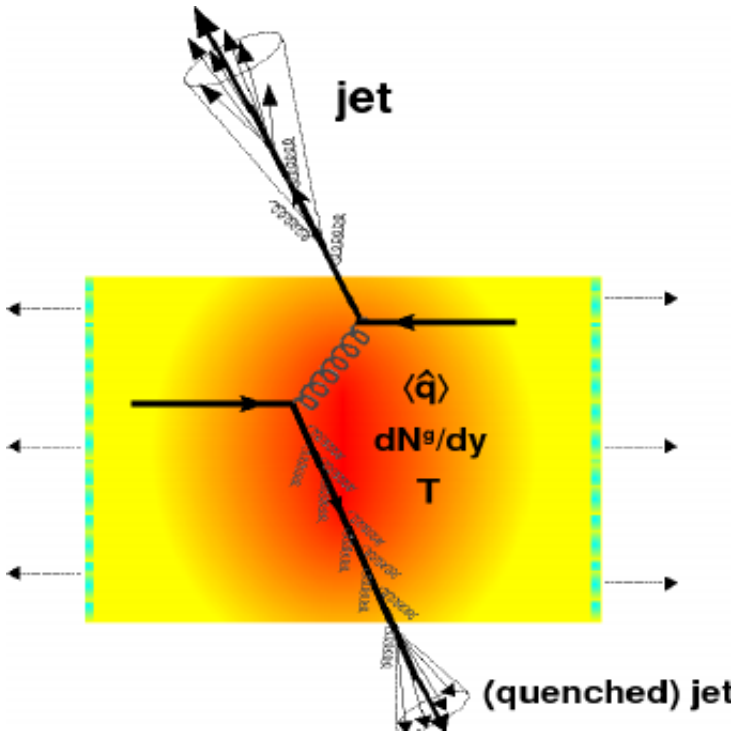

Fig. 2.7 Jet quenching in AA collisions [44].

initial state effects, so-called cold nuclear matter (CNM) effects, which are not effects originating from the presence of the QGP, $R_{AA} = 1$ indicates no effects from the hot nuclear matter. $R_{AA} < 1$ indicates suppression from hot nuclear matter. CNM will be discussed later in the chapter.

High p_T transfer may result in the formation of high energy quark anti-quark pairs. These pairs propagate in opposite directions while radiating gluons, if the energy is high enough the radiated gluons form more quark-antiquark pairs which result in a collimated structure of hadrons and other particles, called a "jet". In the presence of the QGP, one of these resultant jets will experience collisional and radiative losses as it interacts with the medium and may appear suppressed compared to the other [43]. This phenomenon is called "jet quenching" and has been used to ascertain the presence of the QGP and infer its properties. Figure 2.7, shows the two jets of which one of them crosses the QGP medium. Again here, R_{AA} is a useful quantity to study these effects.

2.4.1 Heavy quarks

As already mentioned, heavy quarks, charm ($\approx$ 1.5 GeV/c^2) and beauty ($\approx$ 5 GeV/c^2) and their hadrons are produced in the initial stages of the collisions via

hard scattering. At collider energies it is generally acceptable that the production mechanism of heavy quarks is either gluon-gluon fusion, (see Equation 1.1) or quark-antiquark annihilation (see Equation 1.2). At high energies it is mainly the gluons and not the quark that form these pre-resonance states in the initial hard scattering [45]. They are produced with a high Q^2 and short formation time $\tau \approx 0.1$ fm/c $\ll \tau_{QGP} \approx 5$ - 10 fm/c. The subsequent strong interaction with QGP constituents does not affect the masses of the heavy quarks as well as their flavour. This means that they experience the full evolution of the QGP (1/M, where M is the mass of the particle). Consequently, heavy quarks allow one to probe the mechanisms of multiple interactions with the QGP, as well as the strength of the collective expansion of the created system. Heavy quarks suffer energy loss as they traverse the hot and dense medium via radiative and collisional energy loss. Radiative energy loss is expected as the main mechanism at high p_{T} whereas at low p_{T} an interplay with collisional energy loss is expected. The radiative energy loss mechanism refers to where the partons interact by an exchange of color emitting gluons in the process. The medium induced radiative energy loss depends on;

1. **Medium properties and path length (L) in the medium**
   When partons encounter medium they interact with its constitiuents by exchanging color charges thus experiencing radiative loss by emitting gluons. The gluons (soft partons) thus emitted may couple with the medium constituents and the subsequent interactions depend on mean free path, a property of the medium and the heavy quarks may traverse a distance L inside the medium [46].

2. **Dead cone effect**
   This refers to the suppression of the probability of gluon radiation for heavy quarks at small angles. [47]

3. **Casimir effect**
   Model calculations for radiative energy losses show that the average energy loss of partons in the hot and dense medium shows a color charge and mass dependence, particularly in the forward rapidity region [48]. Equation 2.2, shows the ordering of the average energy loss of different particles.

$$\Delta E_g^{(M=0,C_R=3)} > \Delta E_q^{(M\approx 0,C_R=4/3)} > \Delta E_c^{(M\approx 1.5GeV,C_R=4/3)} > \Delta E_b^{(M\approx 5GeV,C_R=3)} \tag{2.2}$$

   where C_R is the casimir factor, M is the mass of the parton, g, q, c and b are the gluon, light quark, charm and beauty respectively.

Collisional energy loss refers to where partons lose energy through multiple scattering with the constituents of the medium.

The production yields of heavy quarks can be modified by the presence of the QGP [49]. Their production yields in AA collisions are studied in comparison with pp collision to quantify R_{AA}. Heavy quarks are studied by measuring the heavy-flavour hadrons (including charm and beauty quarks) such as D mesons (D^0, D^{*+} and D^+ originated from charm quark), B mesons (B^0, B^+ and B^s originated from beauty quark) and the bound states known as quarkonia (J/Ψ, Υ, etc). Heavy-flavour hadrons have a lifetime of 5×10^{-13} s $< \tau < 2 \times 10^{-12}$ s and decay length 100 μm $< c\tau <$ 500 μm, therefore can be studied via the recostruction of their decay products in the detector. In ALICE, heavy-flavour production is measured within three channels: hadronic decay channels and electronic decay channel at mid-rapidity, as well as muonic decay channel at forward rapidity. In this thesis heavy-flavour production is studied at forward rapidity via the semi-muonic decay channel.

2.4.2 Heavy-flavour production measurements in Nucleus–Nucleus (AA) collisions

The nuclear modification factor of heavy-flavour production obtained in AA collisions for different heavy-flavour species are compared to theoretical calculations that take into account the mass dependence of energy loss processes, transport dynamics, charm and beauty quark interactions with the QGP constituents, hadronisation mechanisms of heavy quarks in the hot and dense medium as well as heavy-quark production cross section in AA collisions. In the following discussion their measurements are reviewed.

ALICE measured the R_{AA} of electrons from inclusive heavy-flavour (c, b $\rightarrow$ e + X) decays in central (0–10%) Pb–Pb collisions at $\sqrt{s_{NN}} = 5.02$ TeV [50]. Figure 2.8 shows the results compared with models that also include nuclear modification of the parton distribution functions. The nuclear modification of parton distribution functions are necessary to predict the observed suppression of the R_{AA} at low p_{T}. The measured R_{AA} shows a strong suppression of heavy-flavour decay electron yields as a function of p_{T}, a clear signature of the medium induced energy loss on heavy quarks traversing the QGP produced in heavy-ion collisions. The data were compared with various theoretical predictions. Both radiative and collisional energy loss are included in the pQCD model. In BAMPS, POWLANG and TAMU interactions are only described by elastic processes (collisional energy loss); BAMPS+rad, LBT, MC@sHQ+EPOS2 and PHSD, include energy loss from medium-induced gluon radiation in addition to collisional process, while CUJET3.0 and

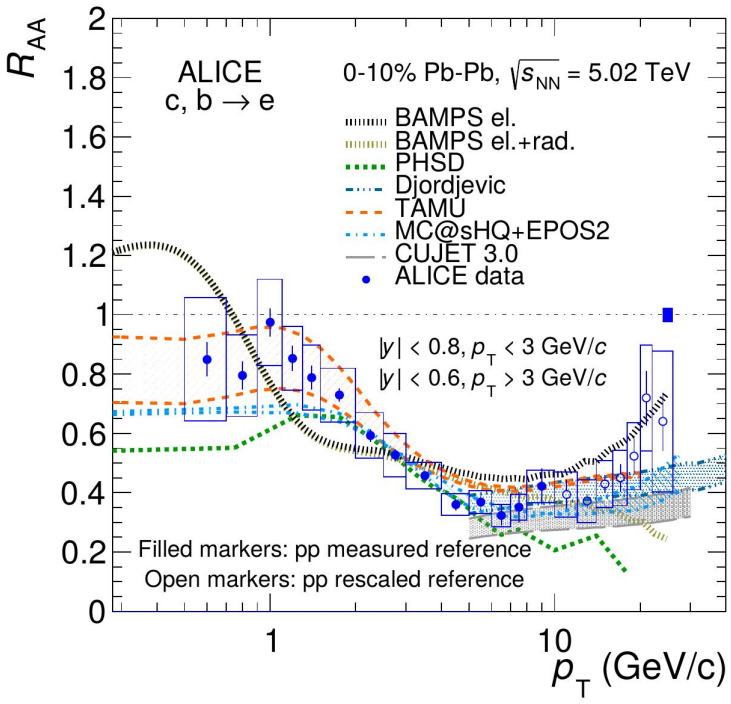

Fig. 2.8 Nuclear modification factor for heavy flavours measured in the electronic decay channel as a function of p_{T} in Pb–Pb collisions at $\sqrt{s_{NN}} = 5.02$ TeV [50].

Djordjevic models include both radiative and collisional energy loss processes and SCET model implements medium-induced gluon radiation via modified splitting functions with finite quark masses. All models, with the exception of BAMPS and CUJET3.0, include a nuclear modification of the parton distribution functions. The agreement with TAMU at low p_{T} confirms the dominance of elastic collisions at low momenta, together with the importance of the inclusion of shadowing effects in the model which reduce the total heavy-flavour production in Pb–Pb collisions with respect to an expectation from the binary scaling. TAMU tends to overestimate the R_{AA} for $p_{\mathrm{T}} > 3$ GeV/c, probably due to the missing implementation of the radiative energy loss in the model, which becomes the dominant energy loss mechanism at high p_{T}.

The R_{AA} of average D mesons as a function of p_{T} is shown in Figure 2.9. The R_{AA} is measured in the centrality class 30-50% at $\sqrt{s_{NN}} = 5.02$ TeV. The results show that the suppression of the average D mesons with $p_{\mathrm{T}}$is compatible within uncertainties with theoretical model calculations [51] that include substantial elastic interactions with an expanding medium.

ALICE also measured the R_{AA} of muons from the decay of inclusive heavy-flavour (c, b $\rightarrow$ μ + X) at $\sqrt{s_{NN}} = 5.02$ TeV at forward rapidity for central collisions [52]. The results of the measurements in different centrality bins are shown in Figure 2.10. A strong suppression of heavy flavour decay muons was observed. The measurement shows an agreement

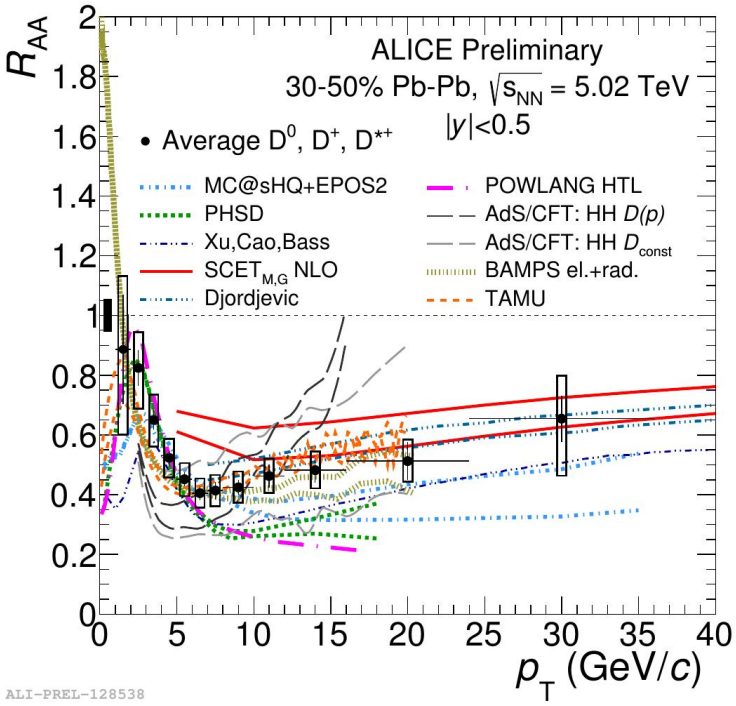

Fig. 2.9 Nuclear modification factor for average D mesons measured in the hadronic decay channels as a function of p_{T} in Pb–Pb collisions at $\sqrt{s_{NN}}$ = 2.76 TeV and $\sqrt{s_{NN}}$ = 5.02 TeV [51].

with theoretical models within uncertainties. The Vitev model [53] describes the $\mathrm{R_{AA}}$ of heavy-flavour hadron decay muons in central collisions. The TAMU model [54] tends to overestimate the $\mathrm{R_{AA}}$ of muons from heavy-flavour hadron decays in central collisions and reproduces the measurement in peripheral collisions. These $\mathrm{R_{AA}}$ measurements at $\sqrt{s_{NN}}$ = 5.02 TeV provide new constraints on energy loss models. In addition to final-state effects where in-medium energy loss would be dominant, initial-state effects could influence the $\mathrm{R_{AA}}$ measurement.

The measurements of the $\mathrm{R_{AA}}$ of heavy-flavour hadron decays in different centrality classes give information on the dependence of the energy loss on the path length and properties of the medium (particularly, the energy density). As discussed, from these studies it is observed that the comparison of $\mathrm{R_{AA}}$ in $p_{\mathrm{T}} < 10$ GeV/c with various models in central collisions is well described. However, most models fail to describe the centrality dependence of $\mathrm{R_{AA}}$. These measurements provide significant constraints for the understanding of the interaction of heavy-flavour hadrons with the high-density QCD medium (QGP), especially at low and intermediate p_{T}, where the $\mathrm{R_{AA}}$ is the result of a more complex interplay among several effects.

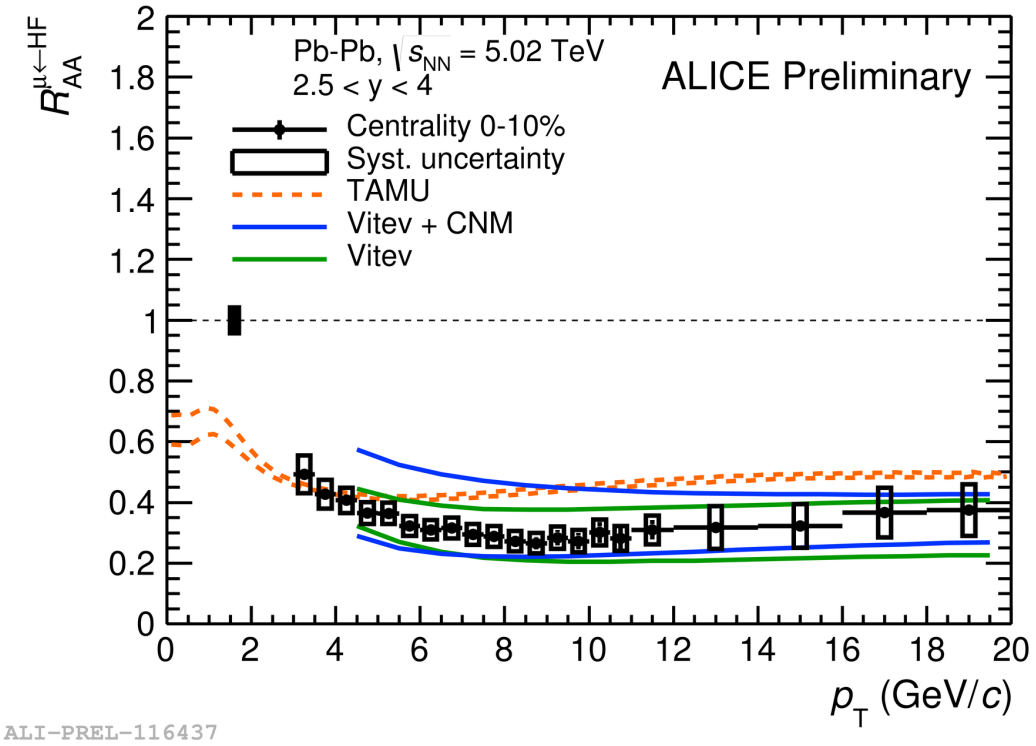

Fig. 2.10 Nuclear modification factor for heavy flavours measured in the muonic decay channels as a function of p_{T} in Pb–Pb collisions at $\sqrt{s_{NN}} = 5.02$ TeV [52].

2.5 Cold Nuclear Matter Effects

The effects of the QGP, i.e hot nuclear matter effects, on the production of heavy flavours are better explained via understanding the effects of the presence of nuclear matter in collisions. These effects are studied in proton–nucleus (p–A) collisions, where the QGP is not expected to be formed. The effects are therefore, referred to as Cold Nuclear Matter (CNM) effects.

2.5.0.1 Nuclear modification of the parton distribution functions(PDFs)

Parton Distribution Functions (PDFs), represent the structure of a nucleon. They are defined as the probability of finding a parton with momentum x in a nucleon, where x is the so-called Bjorken x[11]. Studies of deep-inelastic scattering on nuclei revealed that the PDFs of nucleons bound in nuclei (nPDF) differ from those of free nucleons (PDF). This

[11] Bjorken x is the fraction of the momentum of a proton carried by a parton

effect is the CNM effect $R_i^A(x,Q^2)$, defined as

$$R_i^A(x,Q^2) = \frac{f_i^A(x,Q^2)}{f_i(x,Q^2)} \tag{2.3}$$

where $f_i^A(x,Q^2$ and $f_i(x,Q^2)$ are nPDFs and PDF respectively.

In Figure 2.11, a typical form of modification of PDFs of a bound nucleus and the nuclear modifications of valence quarks, sea quarks and gluons for a Lead (Pb) nucleus are shown, respectively [55], where the bottom figure shows the distributions obtained using a bound nucleus taking into account nuclear shadowing. As shown in Figure 2.11 (top), CNM effects include the following;

1. **Shadowing effect** ($x < 0.1$ and $R_i^A < 1$)
   This effect refers to a suppression of parton densities relative to the free proton at low-x region. Penetration of the partons of the projectile into the face of the nucleus modifies the gluons available for fusion. It was shown in [56] that in a Pb nucleus, the shadowing effect is largest on the gluon distribution, and this is probably attributed to self-interaction of high-density gluons known as gluon saturation.

2. **Anti-shadowing effect** ($0.1 < x < 0.3$ and $R_i^A > 1$)
   The anti-shadowing effect is complementary to the shadowing effect. It refers to an enhancement of parton densities relative to the free proton at intermediate x region. The anti-shadowing effect is clearly seen at the gluon distribution and barely seen at the valence and seaquark, in Figure 2.11. In case of the gluon anti-shadowing, this is believed to be a counter effect of the gluon shadowing where two low-x gluons fuse and make a high-x gluon.

3. **EMC Effect** ($0.3 < 0 < x < 0.7$)
   The physical interpretation for this EMC effect where protons and neutrons in the nucleus do not behave as free nucleons is still ambiguous [57, 58].

4. **Fermi motion** ($x \approx 1$)
   This effect refers to a large increase of $R_i^A(x,Q^2)$ at highest-x region due to the Fermi (quantum) motion of nucleons inside a nucleus [59, 60].

The shadowing (or anti-shadowing) effects are important phenomena to consider in particle production in heavy-ion collisions. The consequence of shadowing and anti-shadowing is clearly the fact that at small x, R_{AA} can be suppressed due to the shadowing while at intermediate x they can be enhanced due to anti-shadowing.

As already mentioned, at LHC energies, the leading order process for the production of

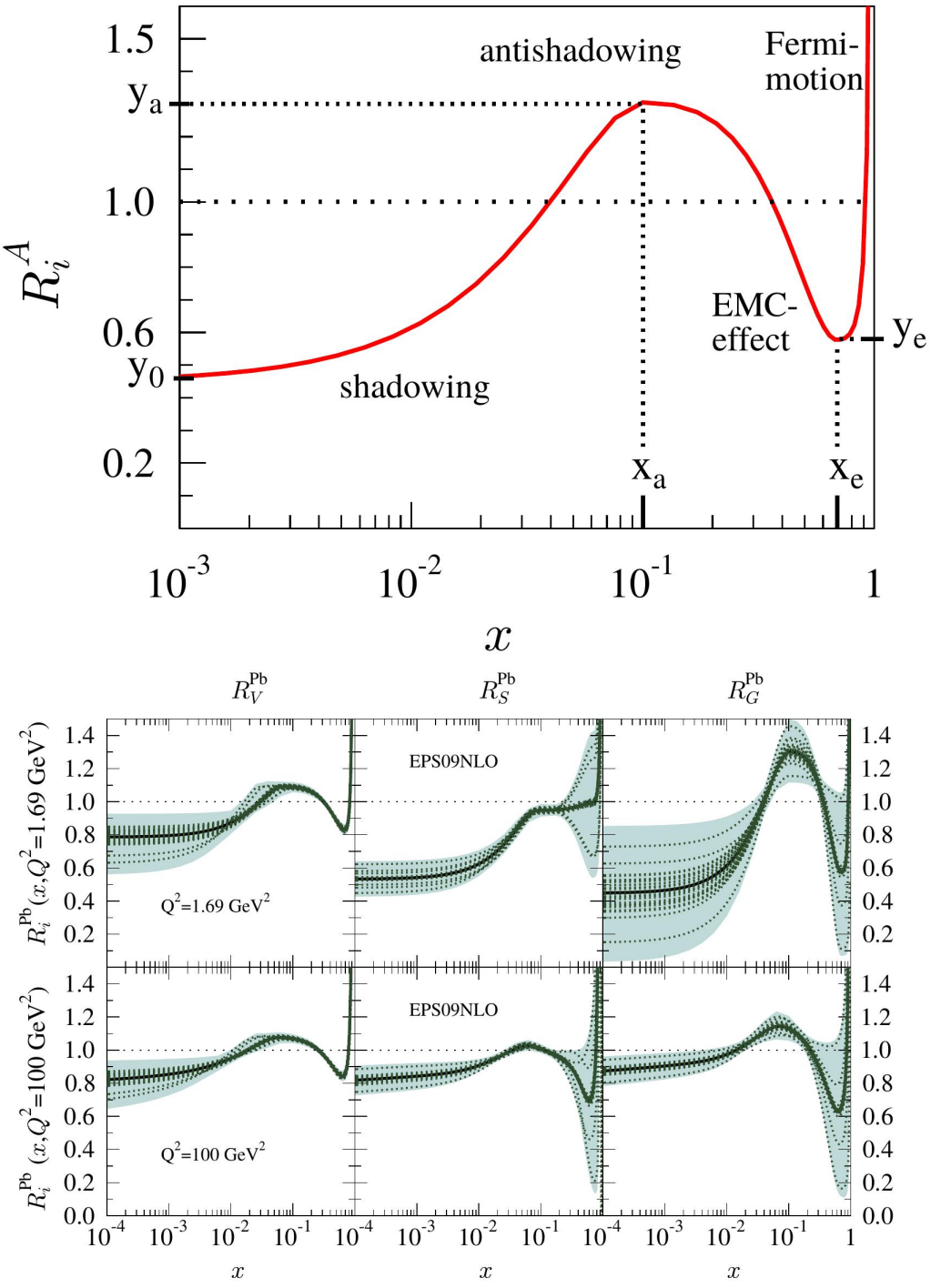

Fig. 2.11 Top and bottom figures show typical form of modification of Parton Distribution functions of a bound nucleus and the nuclear modifications valence quarks, sea quarks and gluons for a Lead nucleus, respectively [55].

heavy flavours is gluon fusion. This means that in p–Pb collisions, the production of heavy flavours is particularly sensitive to modification of gluon nPDFs at high Q^2 ($Q \approx M_{b/c}$) as shown in Figure 2.11. Similarly to AA collisions, CNM effects in p–A collisions are defined as:

$$R_{pA} = \frac{1}{\langle N_{coll} \rangle} \frac{dN_{pA}/dp_T}{dN_{pp}/dp_T} \tag{2.4}$$

where, dN_{pA}/dp_T and (dN_{pp}/dp_T) are the differential yields of the heavy-flavours per event in p–nucleus (pA) and pp collisions, respectively, and $\langle N_{coll} \rangle$ is the average number of binary collisions.

As already mentioned, heavy-flavour production in this thesis is measured via the semi muonic decay channel,

$$c, b \rightarrow \mu + X \tag{2.5}$$

(Branching ratio (B.R) 10.33 ± 0.28 %).
The muons are detected at forward rapidity in the Forward Muon Spectrometer (to be discussed in detail in Chapter 3). Therefore, the measurements are able to probe small Bjorken-x values, where x can be calculated as ;

$$x_{i,j} = \frac{M_{b/c}}{\sqrt{s_{NN}}} e^{\pm y} \tag{2.6}$$

where y is the rapidity, $x_{i,j}$ is the Bjorken-x of the annihilating partons i and j, $\sqrt{s_{NN}}$ is the centre-of-mass energy and $M_{b/c}$ is the mass of the particle formed by the annihilating partons.

2.5.0.2 p_T broadening

This refers to enhancement of particle production at intermediate p_T region, which results in a deficit of low p_T particle. This enhancement is thought to be attributed to multiple scattering of partons inside a nucleus before the hard scattering. During the elastic multiple scatterings, partons gain transverse momentum, and this leads to the enhancement of final state particles at moderate p_T region.

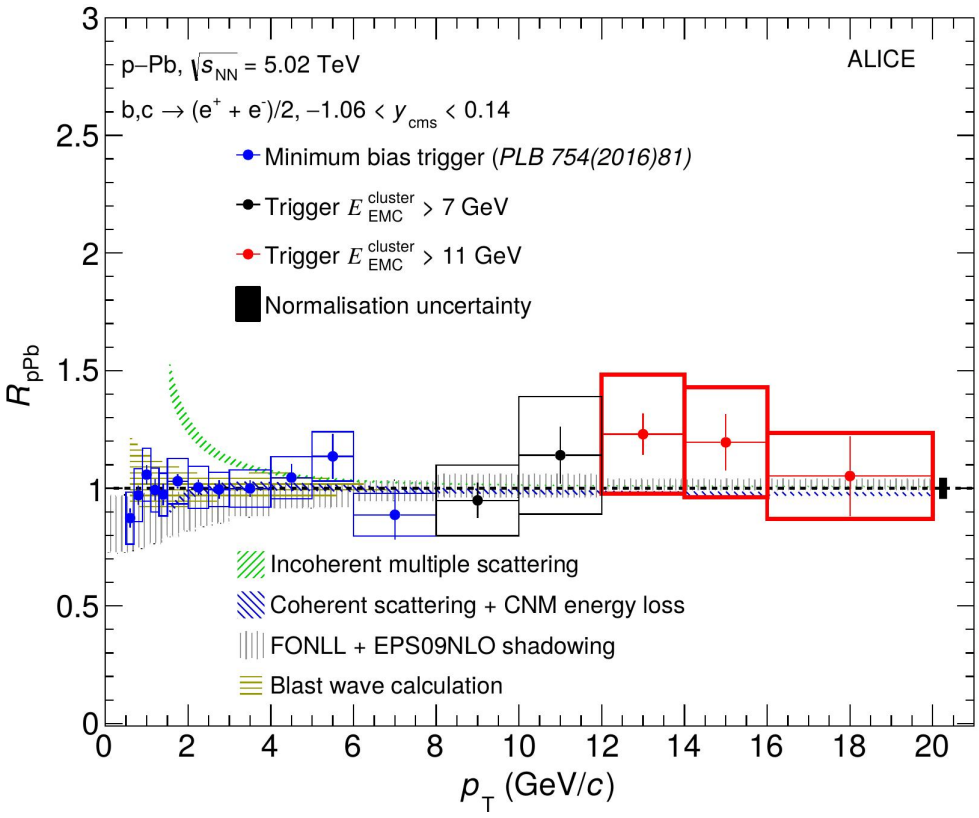

Fig. 2.12 Nuclear modification factor for heavy-flavour decay electrons as a function of p_{T} in p–Pb collisions at $\sqrt{s_{NN}} = 5.02$ TeV [61].

2.6 Heavy-flavour production in p–A collisions

This section reviews some of the measurements in ALICE performed in different heavy-flavour decay channels.

ALICE measured the $\mathrm{R_{pA}}$ of inclusive heavy-flavour at mid-rapidity in the electronic channel [61]. The results obtained from the measurements are shown in Figure 2.12. The results are compared to theoretical model calculations from First Order Next to Leading Log (FONLL)+EPS09 NLO which consider coherent multiple scatterings, including energy loss in the CNM nuclear shadowing and hydrodynamically expanding medium [61]. The results are well reproduced by theoretical calculations.

ALICE also measured the $\mathrm{R_{pA}}$ of hadrons, namely Λ_c [62] and D mesons [14]. The results, taken from [62], are shown in Figure 2.13. Both results are compatible with unity within large systematic and statistical uncertainties. The current model calculations predict a deviation from unity by 20-40%. These results cannot in existing models. These results were obtained using run 1 data, new results with better agreement with data are anticipated from Run2, Run 3 and 4 after detector upgrades.

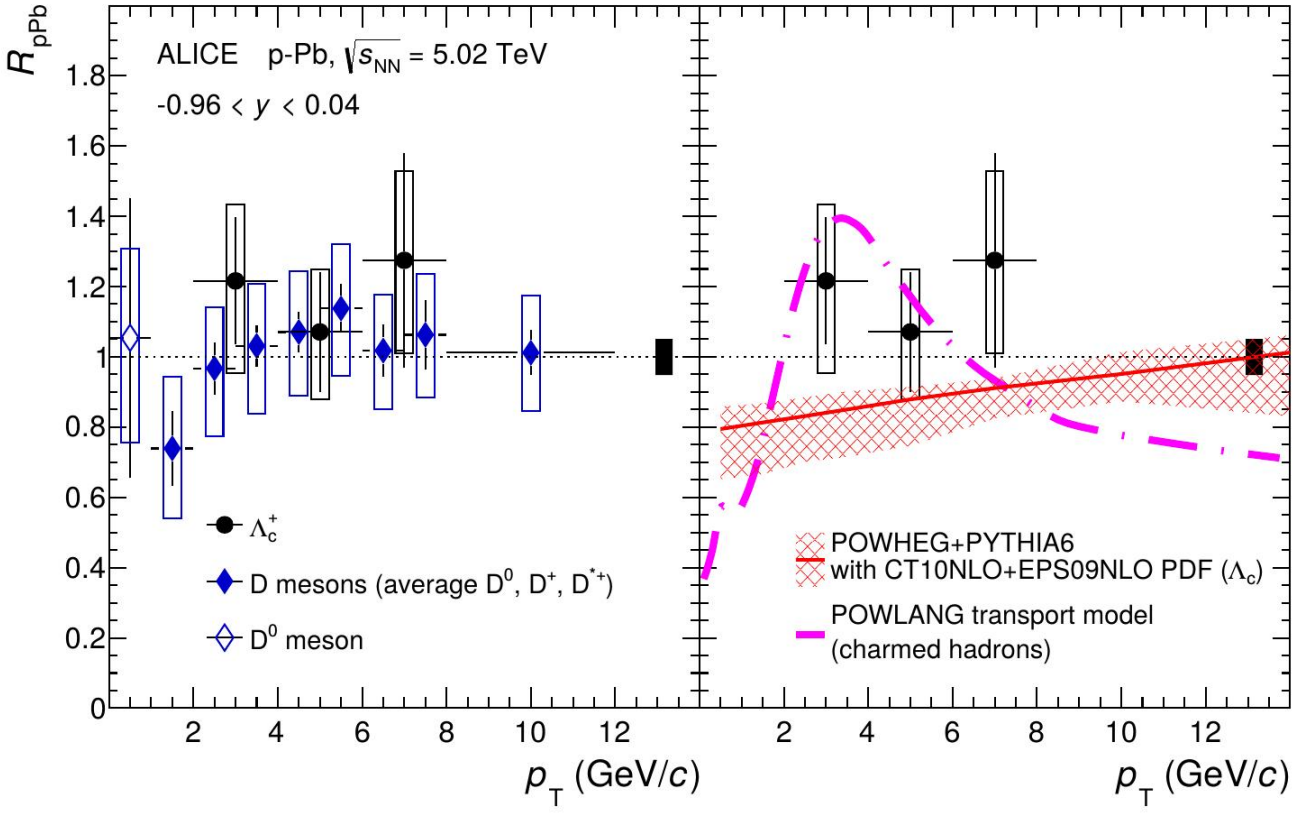

Fig. 2.13 Nuclear modification factor for Λ_c and average D mesons and D^0 as a function of p_T in p–Pb collisions at $\sqrt{s_{NN}} = 5.02$ TeV [62].

Heavy-flavour decay muon production was also studied in p–Pb collisions at $\sqrt{s_{NN}} = 5.02$ TeV at forward and backward rapidity [63]. Figure 2.14 shows the R_{pA} results obtained in the study. The results show that at forward rapidity, the R_{pA} is compatible with unity in the whole p_T range, however, at backward rapidity, there is a deviation in $2.5 < p_T < 3.5$ GeV/c which is suggested to be the result from binary scaling in the p_T interval. The R_{pA} at forward rapidity is in agreement with model calculations including CNM effects based on a nuclear shadowing, p_T broadening and energy loss in CNM while at backward rapidity the results are reproduced by a model including incoherent multiple scattering effects.

"These results indicate that the suppression of the production of high-p_T muons from heavy-flavour hadron decays in the 0–10% most central Pb–Pb collisions measured by ALICE is due to final state effects induced by the hot and dense medium formed in these collisions [63]."

ALICE has also studied heavy-flavour production in differential measurements in order to understand the mechanisms influencing their production at LHC energies. One of the burning topics is their production as a function of charged-particle multiplicity. This topic

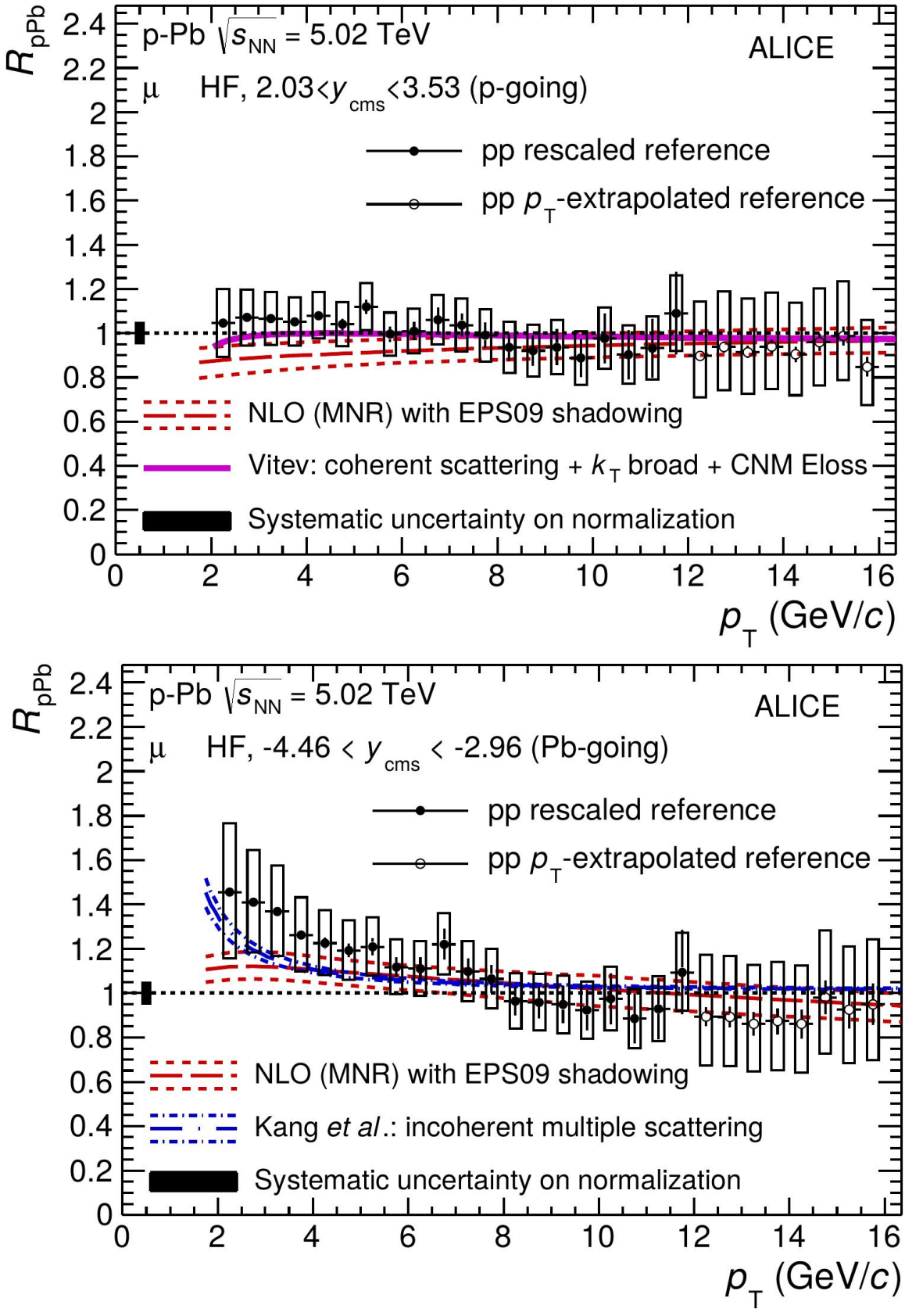

Fig. 2.14 Nuclear modification factor of heavy-flavour decay muons as a function of p_{T} in p–Pb collisions at $\sqrt{s_{NN}} = 5.02$ TeV [63].

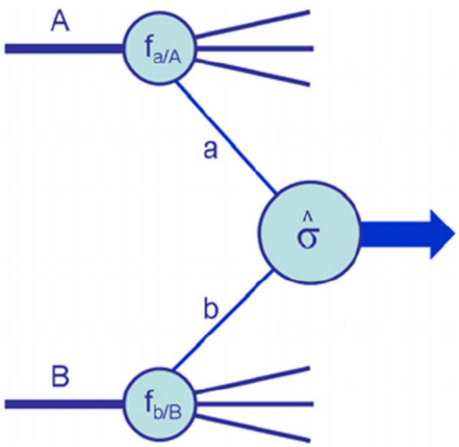

Fig. 2.15 Structure of hard process in a pp collision [64].

a source of information on the interplay between soft and hard processes as well as the role of multiple-parton interactions in particle production. The following section discusses the multiplicity dependence of heavy-flavour production in hadronic collisions.

2.7 Multiplicity dependence of heavy-flavour production in hadronic collisions

QCD is the underlying theory for soft and hard processes in high energy hadronic collisions, e.g. in pp collisions. A complete pp event contains an interplay of hard and soft processes. For soft processes, e.g. underlying event, etc., the rates and production processes are dominated by non-perturbative QCD effects, which are still not yet well understood. The hard processes, e.g. hard scattering can be described by pQCD as it involves large Q^2 transfer. Other examples of hard processes are production of hadrons containing heavy quarks or jets. The underlying event comprises production of all the final states associated with the hard scattering, such as the multiple parton interactions, soft hadron processes and fragmentation of beam remnants. Therefore, the effects of soft processes must be well understood to allow comparisons with the pertubative predictions. Moreover, soft processes are are important for understanding both the signal and the backgrounds for hard processes.

In a high energy pp collisions, Figure 2.15, the two partons of the incoming protons undergo a hard scattering process, characterized by the cross section, $\hat{\sigma}$.

The structure of the incoming protons (A and B) is described by their parton distribution functions (PDFs), $f_{\frac{a}{A}}(x_a,{\mu_F}^2)$ and $f_{\frac{b}{B}}(x_b,{\mu_F}^2)$, respectively. The PDFs give the probability

to find a parton a in proton A with a momentum fraction x_a at the energy scale ${\mu_F}^2$. The cross section of this process is determined by obtaining a summation over all possible parton-parton scattering processes and integrating over the momentum fractions as shown in equation 2.7:

$$\sigma_{AB} = \sum_{a,b} \int dx_a dx_b f_{\frac{a}{A}}(x_a, \mu_F^2) f_{\frac{b}{B}}(x_b, \mu_F^2) \hat{\sigma}(x_a, x_b, \alpha_s(\mu_R^2)) \tag{2.7}$$

The calculations of the hard-scattering process cross sections are performed in pQCD and the results depend on the strong coupling constant, α_s, and its renormalization scale ${\mu_F}^2$, which is also the scale that separates long and short distance physics [64]. Equation 2.7 can only be used to describe hard scattering events where the effective centre-of-mass energy of the interaction is far less than the centre-of-mass energy of the collider. Each interacting parton carries a certain fraction of the proton momentum which depends on its mass and rapidity[12] (y). An example of the parton momentum distributions in a proton is shown in Figure 2.16. As Up (u) and down (d) quarks contribute to the quantum numbers of the protons, they form the *valence quarks*. Therefore, they carry a large fraction of the proton momentum. As can be seen in Figure 2.16 a proton contains also gluons and other quarks that give rise to the so-called *sea* and they carry much smaller momenta. Parton momentum distributions depend on the momentum transfer in the interaction, Q^2. At large Q^2 the interacting particles see the short-distance structure of the proton and hence have access to the *sea* of quarks and gluons inside the proton, in addition to the valence quarks. Consequently, the PDFs are shifted towards small x values, where x is the fraction of the proton momentum carried by the interacting partons, also known as the Bjorken-x [65]. For small Q^2, only the valence quarks are visible and the PDFs peak at large x values.

At LHC energies where the Q^2 is very large, there is access to more particles in a single pp collision, mostly gluons as they dominate the small x region. Due to the high gluon density in each colliding proton, the short-distance hard scattering process occurs concurrently with multiple parton interactions (MPIs) [67] where two or more parton interactions occur simultaneously in a single collision.

2.7.1 Multi-parton interactions

As discussed above, MPIs, describe the phenomenon when a hard primary interaction is accompanied by a second scattering process. MPIs are often split into two groups, soft

[12] Rapidity is the representation of the speed of motion of the parton.

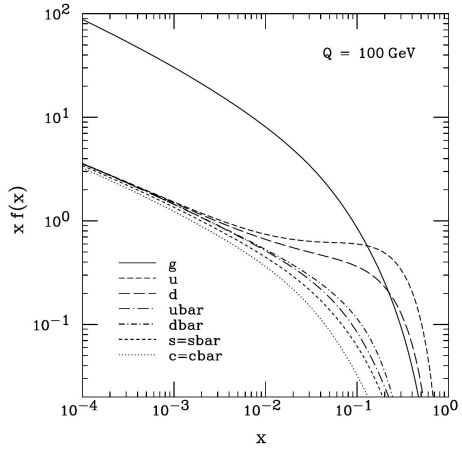

Fig. 2.16 Parton Distribution Functions of a proton as a function of Bjorken-x [66].

and hard MPIs i.e. if the resulting particles have a rather high transverse momentum it is called hard MPI, otherwise it is called soft MPI. While hard MPIs occur rather rarely, soft MPIs are a very frequent process. There can be even higher numbers of additional subprocesses which would lead to triple or even higher parton interactions.

As mentioned above, due to the gluon dominated PDFs, hadronic collisions at the LHC are dominated by MPIs. Most events are due to large distance collisions between the two incoming protons, a non-pertubative process. In this case the momentum transfer of the interaction is small (soft collisions) and therefore particle scattering at large angles is suppressed. The particles produced in the final state of such interactions have large longitudinal momentum, but small transverse momentum (p_T) relative to the beam line. Due to several interactions occuring at parton level in the collision, particle production becomes dependent on the total charged-particle multiplicity. Head-on collisions may occur occasionally between two partons of the incoming protons. These are interactions at small distances, and are characterised by large momentum transfers (hard MPI). In this case, particles in the final state can be produced at large angles with respect to the beam line (high p_T) and massive particles can be created. Consequently, in such events, the production of heavy quarks can be affected by MPIs. Therefore, studying the correlation of heavy quark as well as heavy flavour production with charged particles, be they heavy or light, one can unveil information on relative contributions of the individual processes to the total production. Hence, studying the correlation of massive particles with other particles in the event is vital to advance our understanding of the elementary processes taking place in hadronic collisions.

In the following sections a review of the recent measurements of the multiplicity dependence of heavy-flavour production by the ALICE Collaboration are discussed.

2.8 Studies of heavy-flavour production as a function of multiplicity in p–Pb collisions

Heavy-flavour production has been studied by the ALICE Collaboration as a function of multiplicity in p–Pb collisions. In the following the measurements and results from these studies are reviewed. Self normalised yields of heavy flavour are plotted as a function of the self normalised charged-particle multplicity.

The self normalised heavy flavour yields are calculated using Equation 2.8.

$$\frac{dN^{HF}/d\eta_i}{\langle dN^{HF}/d\eta \rangle} \tag{2.8}$$

where $\mathrm{dN}^{HF}/\mathrm{d}\eta_i$ and $\langle \mathrm{dN}^{HF}/\mathrm{d}\eta \rangle$ are the yields of heavy-flavour in multiplicity bins i and the yield averaged over all multiplicity bins, respectively.

The self normalised charged-particle multiplicity is given by Equation 2.9

$$\frac{\langle dN_{ch}/d\eta \rangle_i}{\langle dN_{ch}/d\eta \rangle} = \frac{\langle N_{ch} \rangle_i}{\Delta\eta \times \langle dN_{ch}/d\eta \rangle} \tag{2.9}$$

where $\langle N_{ch} \rangle_i$ is the average charged-particle multiplicity in bin i, $\Delta\eta$ is the pseudorapidity region where the measurement is done and $\langle dN_{ch}/d\eta \rangle$ is the charged-particle multiplicity averaged over all multiplicity bins.

2.8.0.1 D mesons

ALICE presented results on the self normalised yield of the D mesons (D^0, D^+ and D^{*+}) measured at mid-rapidity in the hadronic decay at $\sqrt{s}_{NN} = 5.02$ TeV [68]. The self normalised yields of D mesons increase with the charged-particle multiplicity. Figure 2.17 shows a comparison of EPOS 3 with and without hydrodynamical evolution with data for the self normalised yield of D mesons as a function of charged-particle multiplicity at $\sqrt{s}_{NN} = 5.02$ TeV.

In the EPOS 3 event generator, individual scatterings are identified as parton ladders associated to pomerons[13]. The number of pomeron exchanges is used to infer the geometry of the collision. Each parton ladder eventually breaks into individual strings and later jets and hadrons. The strings close to the surface of the bulk and/or with high p_{T} will escape

[13] A family of "effective particles" with increasing spin used to explain the slowly rising cross section of hadronic collisions at high energies

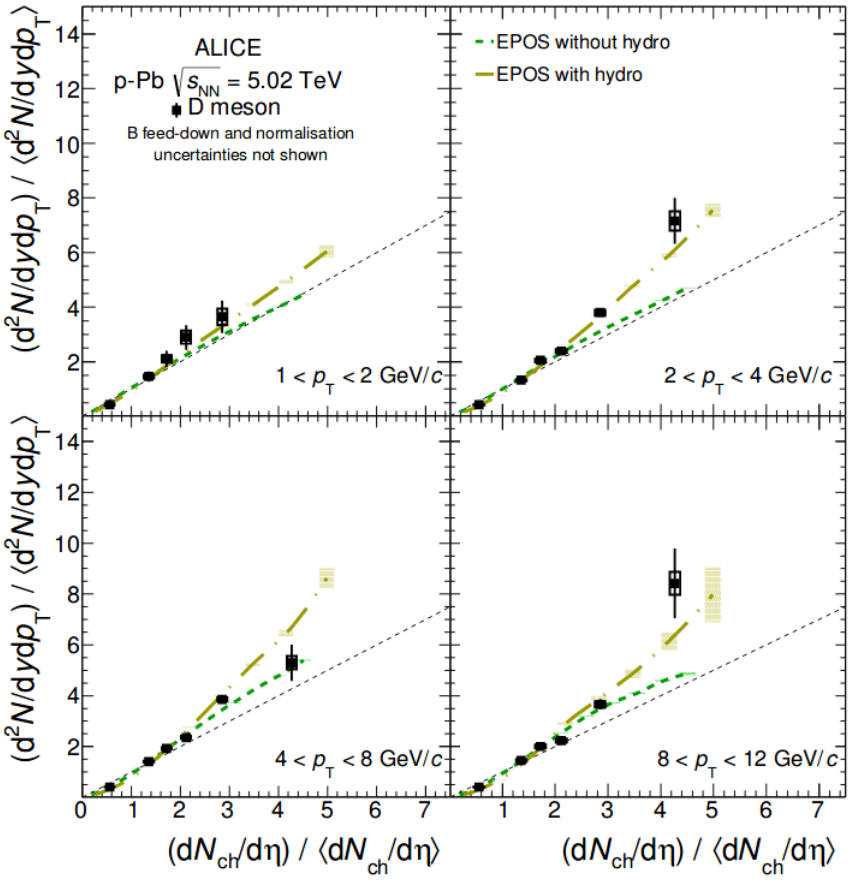

Fig. 2.17 Self normalised yields of D mesons as a function of charged-particle multiplicity at mid-rapidity in p–Pb collisions at $\sqrt{s_{NN}} = 5.02$ TeV compared to EPOS with and without hydrodynamical evolution [68].

the bulk and produce hadrons and jets. This separation provides the initial conditions for the subsequent hydrodynamical evolution.

In p–Pb collisions, we have already mentioned that the multiplicity dependence of heavy-flavour production is also affected by the presence of multiple binary nucleon-nucleon interactions, and the initial conditions of the collision are modified due to CNM effects. The increasing yield in pp collision is best described by theoretical model calculations taking into account the contribution of Multiple-Parton Interactions (MPI) [69, 70, 71], the influence of the interactions between colour sources as described in the percolation model [25, 72], or by the effect of the initial conditions of the collision followed by a hydrodynamic evolution computed with the EPOS 3 event generator [73, 74].

The measurements agree with the EPOS 3 model calculations within uncertainties. At high multiplicity the agreement is better reproduced by the calculation including hydrodynamical evolution of the collision, which predicts a faster than linear increase of the

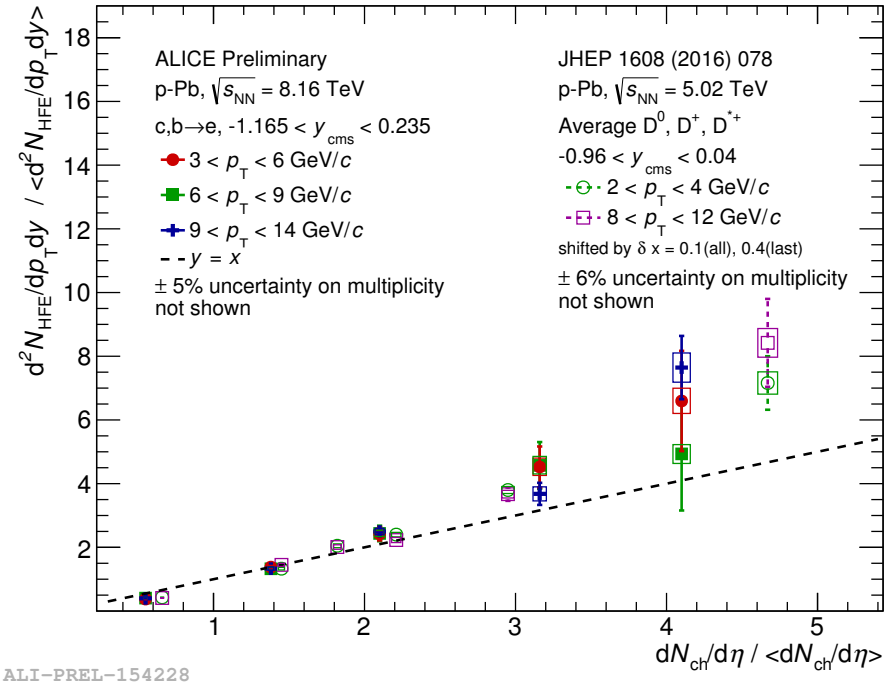

Fig. 2.18 Self normalised yields of heavy-flavour electrons at $\sqrt{s_{NN}} = 8.16$ TeV compared to the average self normalised yield of D^0, D^+ and D^{*+} at $\sqrt{s_{NN}} = 5.02$ TeV in p–Pb collisions as a function of charged-particle multiplicity at mid-rapidity [75].

D-meson yield with multiplicity at mid-rapidity.

2.8.0.2 Heavy flavour decay electron

ALICE also measured inclusive heavy-flavour decay electron yields as a function of charged-particle multiplicity at $\sqrt{s_{NN}} = 8.16$ TeV [75]. Figure 2.18, shows the results obtained from the measurements.

The inclusive heavy-flavour decay electron self normalised yields were measured in three different p_T bins, from low to high p_T. Their yields increases faster than linear towards higher multiplicity and the increase is compatible for the three p_T bins. The measurement was compared to the average of D^0, D^+ and D^{*+} self normalised yield at $\sqrt{s_{NN}} = 5.02$ TeV. The increase is similar for both D mesons and the heavy-flavour decay electron yields. As expected, the multiplicity reach is slightly higher for $\sqrt{s_{NN}} = 8.16$ TeV compared to $\sqrt{s_{NN}} = 5.02$ TeV.

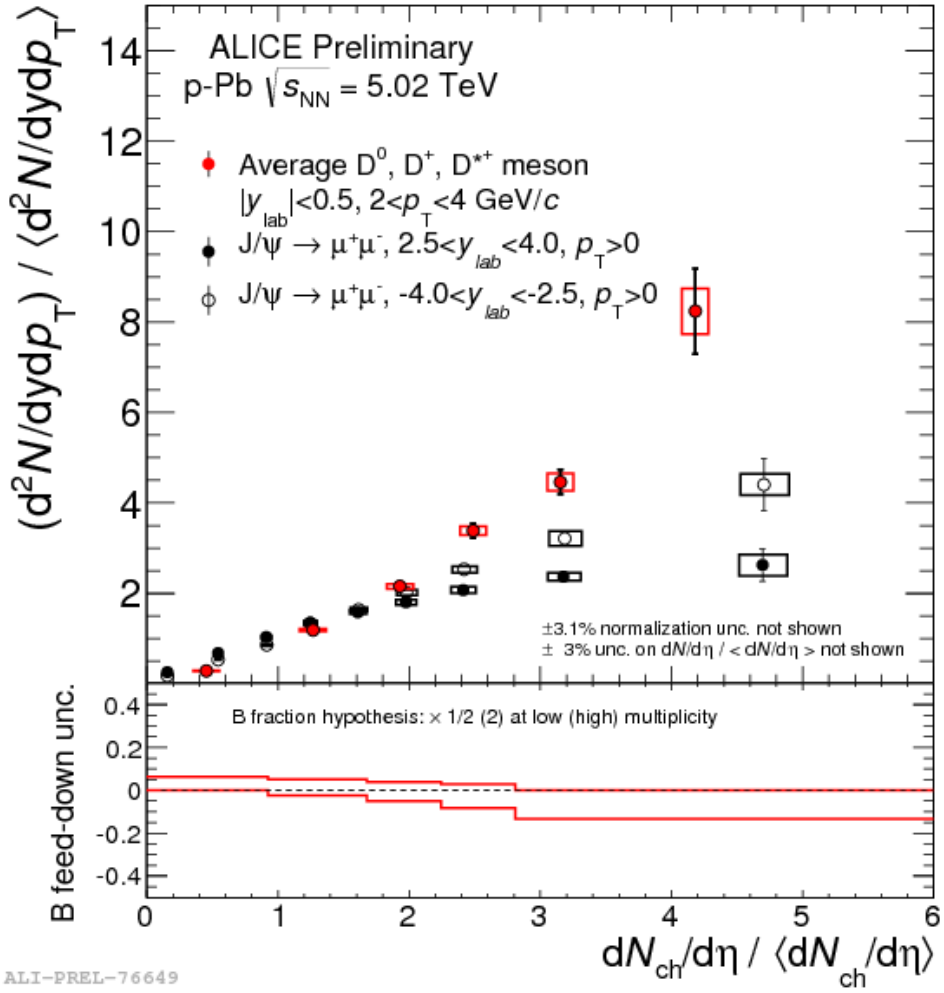

Fig. 2.19 Self normalised yields of J/ψ at forward and backward rapidity compared to the average of D^0, D^+ and D^{*+} self normalised yield in p–Pb collisions at $\sqrt{s_{NN}} = 5.02$ TeV as a function of charged-particle multiplicity at mid-rapidity [76].

2.8.0.3 J/ψ

The yields of J/ψ at forward and backward rapidity in the muonic channel as a function of charged-particle multiplicity in p–Pb collisions at 5.02 TeV [76] are shown in Figure 2.19. An increasing yield of J/ψ with multiplicity is observed for both rapidities, however, the forward rapidity yields seem to saturate at high multiplicity. The results are compared to the average of D^0, D^+ and D^{*+} self normalised yield at the same centre-of-mass energy. The increase of J/ψ yields is similar, particularly, at backward rapidity, to the one of D mesons, although, the D mesons yield shows a sharper increase at higher multiplicity. This could be an indication of collective effects in small systems where the formation of QGP is not expected.

The differences between the yields of J/ψ and those of the D mesons could be attributed

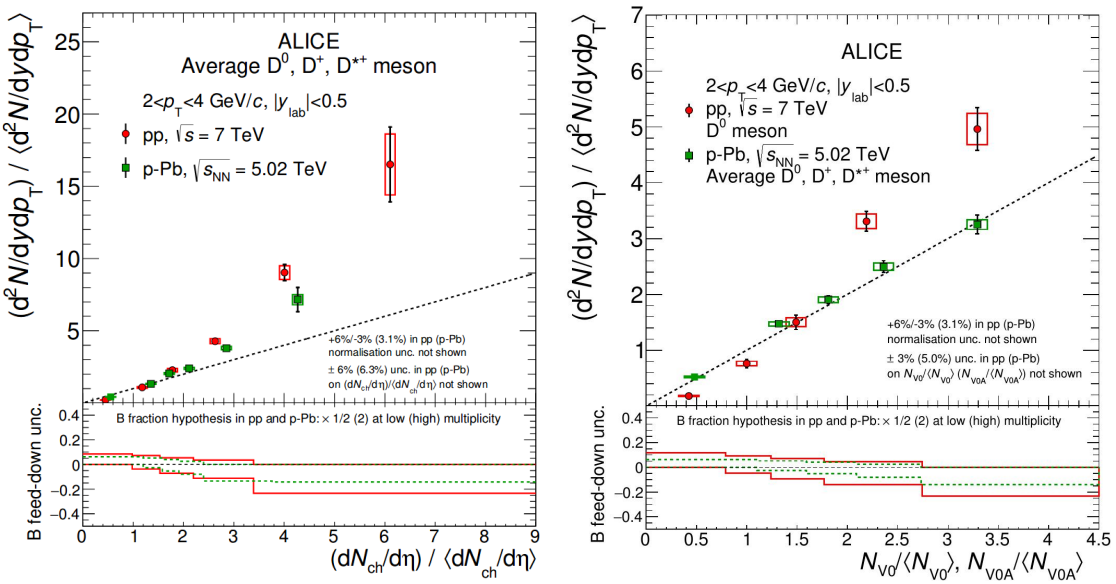

Fig. 2.20 Left: Average of D^0, D^+ and D^{*+} self normalised yields as a function of charged-particle multiplicity at mid (left) and forward (right) rapidity in p–Pb collisions at $\sqrt{s_{NN}} = 5.02$ TeV compared to measurement in pp collisions at $\sqrt{s} = 7$ TeV [68].

to initial state effects such as shadowing and/or anti-shadowing at forward and backward rapidity [76, 77].

2.8.0.4 pp vs p–Pb collisions

Average of D^0, D^+ and D^{*+} self normalised yields as a function of charged-particle multiplicy at mid-rapidity are compared to corresponding measurements in pp collisions at $\sqrt{s} = 7$ TeV for $2 < p_T < 4$ GeV/c [68]. The results are shown in Figure 2.20.

The multiplicity is measured in the same pseudorapidity range in the laboratory system, which corresponds to different ranges in the centre-of-mass frame for the two collision systems, due to the asymmetry of the beam energies in the p–Pb case. A similar increase of the average D meson yield with charged-particle multiplicity is observed in pp and p–Pb collisions.

Another comparison of the measurements in pp and p–Pb collisions was also studied. In these measurements, the charged particle multiplicity for p-Pb collisions was measured at backward rapidity while in pp collisions the charged-particle multiplicity was taken from the sum of the measurements at forward and backward rapidity. The results showed an increase in the yield of D mesons with the charged-particle multiplicity, however, the yields of the D mesons increase faster in pp collisions than in p–Pb collisions with the charged-particle multiplicity. This could be attributed to the different pseudorapidity intervals of

the measurement of charged-particle multiplicity. Furthermore, the non trivial differences between pp and p–Pb collisions, namely, the initial conditions introduced by the presence of a nucleus in p-Pb collisions, could be a contributing factor.

The increase in pp collisions could be attributed to the presence of MPIs while in p–Pb collisions the multiplicity dependence is also affected by the presence of multiple binary nucleon-nucleon interactions and the initial conditions of the collision are modified due to CNM effects.

In the next chapter the discussion of the experimental set-up, data taking conditions as well as the analysis tools used for this analysis are given.

CHAPTER 3

Experimental set up

This chapter introduces the ALICE detector at the Large Hadron Collider. A detailed description of the ALICE detector, in particular, the detectors used for measurements and particle identification in this thesis, will be given. Offline and online computing, data processing and reconstruction at various stages will be outlined. In addition a brief introduction to the AliROOT framework used in the data analysis is given. The candidate also participated in Run 2 data taking, particularly the p–Pb and Pb–p data concerned in this thesis. Therefore the last part of this chapter will be dedicated on the data taking procedure.

3.1 The Large Hadron Collider (LHC)

The LHC [5] is the world's largest particle accelerator developed by the European Organisation for Nuclear Research (CERN). It is a 27 km circular tunnel located 45 - 150 metres below the French-Swiss border.

The LHC is designed to deliver proton-proton (pp) collisions up to $\sqrt{s} = 14$ TeV, Pb–Pb collisions up to $\sqrt{s_{NN}} = 5.5$ TeV and p–Pb collisions up to $\sqrt{s_{NN}} = 8.8$ TeV. The beams are accelerated step by step utilising the CERN accelerator chain until they can be injected into the LHC. The schematic representation of the LHC together with other smaller accelerators is given in Figure 3.1, where the LHC is shown together with other

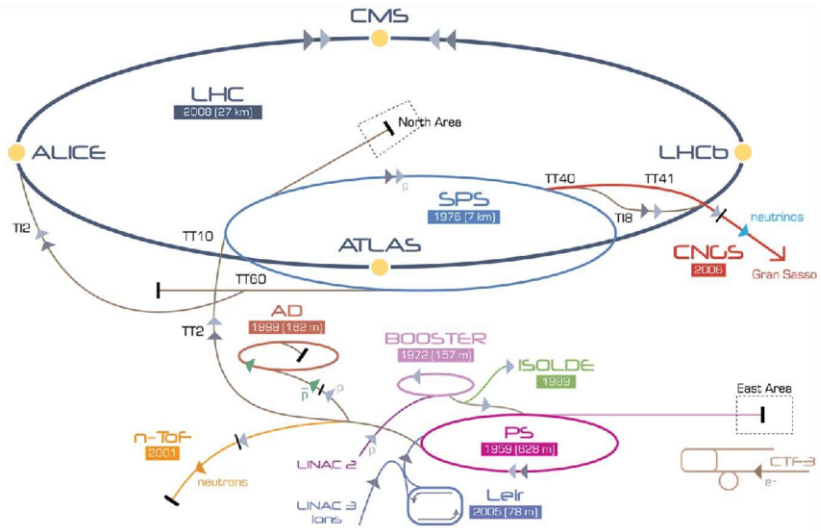

Fig. 3.1 The LHC at the CERN accelerator complex [78].

accelerators in a chain. For example, as depicted in Figure 3.1, when proton beams are to be delivered for collisions, they are first injected into a linear accelerator, LINAC2 which accelerates them to an energy of 50 MeV. The protons are then transfered into a Proton Synchrotron Booster (PSB) which accelerates them to an energy of 1.4 GeV. They are then injected into a Proton synchrotron (PS) where they are accelerated to 26 GeV. The next acceleration is done by the Super Proton Synchrotron (SPS) which accelerates them to 450 GeV. Two transfer lines inject the proton beams from the SPS to the LHC such that they circulate in opposite direction and can be steered by magnets to collide at the four main collision points where the LHC experiments are located. Likewise, lead (Pb) ions undergo a complex step by step acceleration. The ions are first injected into the Linear Accelerator 3 (LINAC3) and then they are injected into the Low Energy Ion Ring (LIER) where they are transformed from long pulses to short and dense bunches which are suitable for injection into the LHC. The acceleration sequence is summarised in Figure 3.2

Delivering the maximum integrated luminosity to the experiments is one of the most important challenges in the operation of the LHC. The integrated luminosity is a measurement of the collected data size i.e. the integral of the instantaneous luminosity over time. The instantaneous luminosity refers to the number of particles per unit cross-sectional area with the potential of colliding per second and for Gaussian beams it can be defined as;

$$\pounds = f\frac{N_1 N_2}{4\pi\sigma_x\sigma_y} \tag{3.1}$$

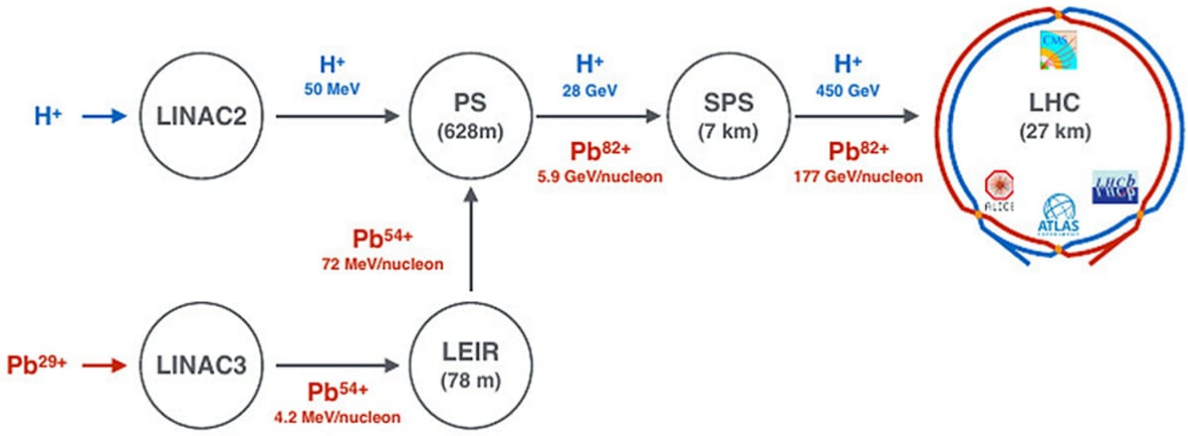

Fig. 3.2 Acceleration sequence of protons and Pb ions [79].

where N_1 and N_2 refer to the number of particles in each beam, f is the frequency of bunch crossings and σ_x and σ_y are the horizontal and vertical widths of the beam.

As can be seen from Equation 3.1, the luminosity is dependent on the beam parameters. The LHC is well equipped for its requirements. Superconducting dipole magnets are used to keep the proton beams on a circular trajectory. The magnets are cooled by superfluid helium to temperatures as low as 2 Kelvins, giving rise to a magnetic fields of 8 T which acts perpendicular to the direction of the beams. During acceleration the beams may diverge from the desired circulation path and this might have a negative effect on the luminosity. For this reason, the LHC ring has quadrupole magnets installed to refocus the beams' vertical and horizontal widths, while the sextupole magnets refocus the beam chromaticity caused by momentum changes in the bunches [80]. Closer to the collision points are the eight inner tripplet magnet systems, each containing three quadrupole magnets which are used to squeeze the beams making them 12.5 times narrower and focusing them to the collision point. The LHC also increases its luminosity by increasing the number of bunches colliding.

The LHC ring hosts four main experiments, namely, ATLAS , CMS, LHCb and ALICE . The experiments are located around the LHC ring as shown in Figure 3.3.

The four experiments focus on different physics programs outlined as follows: The two multi-purpose detectors ATLAS and CMS investigate a wide range of physics, from the search for the Higgs boson to extra dimensions and particles that could make up dark matter. The LHCb experiment is designed to study the differences between matter and anti-matter and other rare phenomena in the decay of B-mesons with very high precision. This should provide a profound understanding of quark flavour physics in the framework of the Standard Model, and may reveal a sign of the physics beyond. Lastly, the ALICE

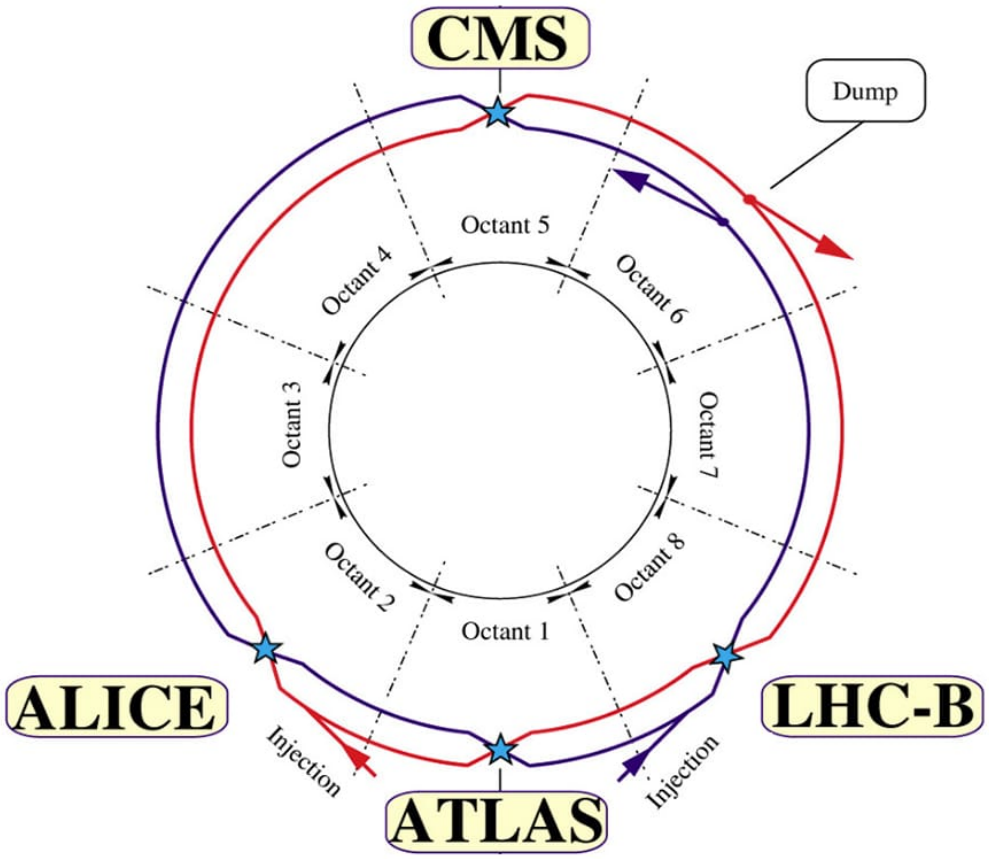

Fig. 3.3 The LHC experiments [78]

detector, whose research goals and detailed description are given in Section 3.5.

Although the LHC experiments focus on different physics programs, they cover different geometric acceptances hence they are complementary to each other as shown in Figure 3.4 e.g inopen-heavy-flavour and quarkonia measurements.

3.2 The ALICE detector

ALICE is a dedicated heavy-ion experiment designed to study the physics of strongly interacting matter and the quark-gluon plasma (QGP) in nucleus-nucleus collisions at the

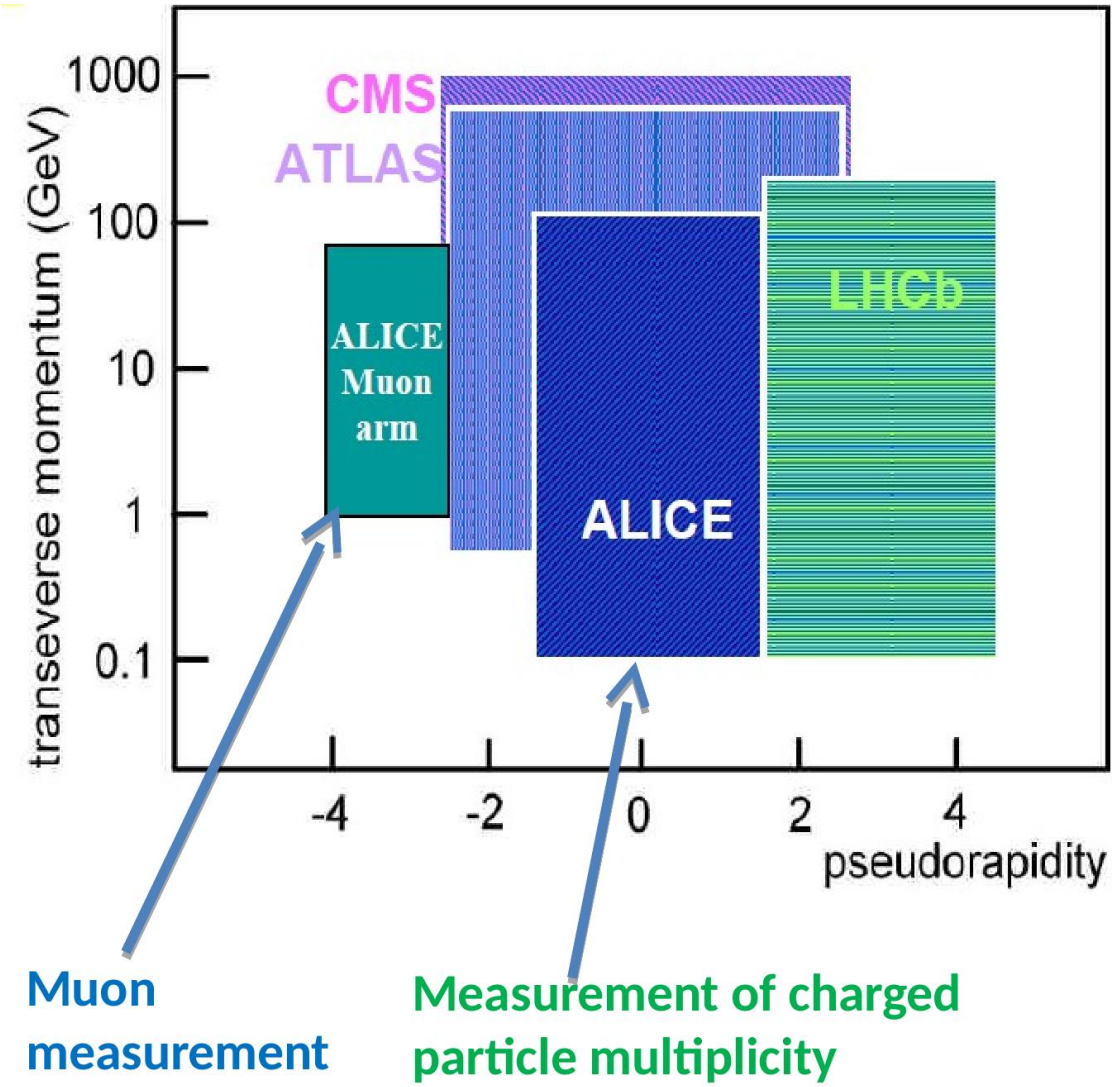

Fig. 3.4 The kinematic reaches of different LHC experiments. [81]

LHC. A schematic of the ALICE detector is shown in Figure 3.5. The ALICE detector consists of a central barrel at $|\eta| < 0.9$, which is contained in the L3 solenoid magnet. The solenoid magnet provides a magnetic field of 0.5 T. The detectors of the central barrel are optimized for the reconstruction of hadrons, electrons, photons and jets. It also has global detectors which are used for measuring global properties of the collisions such as centrality, particle multiplicity, and collision time. At forward rapidity, $-4 < \eta < -2.5$, is the Muon Spectrometer, which is responsible for the reconstruction of muon decay products of heavy-flavours, quarkonia and electroweak bosons. The following sections discuss ALICE sub-detectors in Run 1 and 2 in detail.

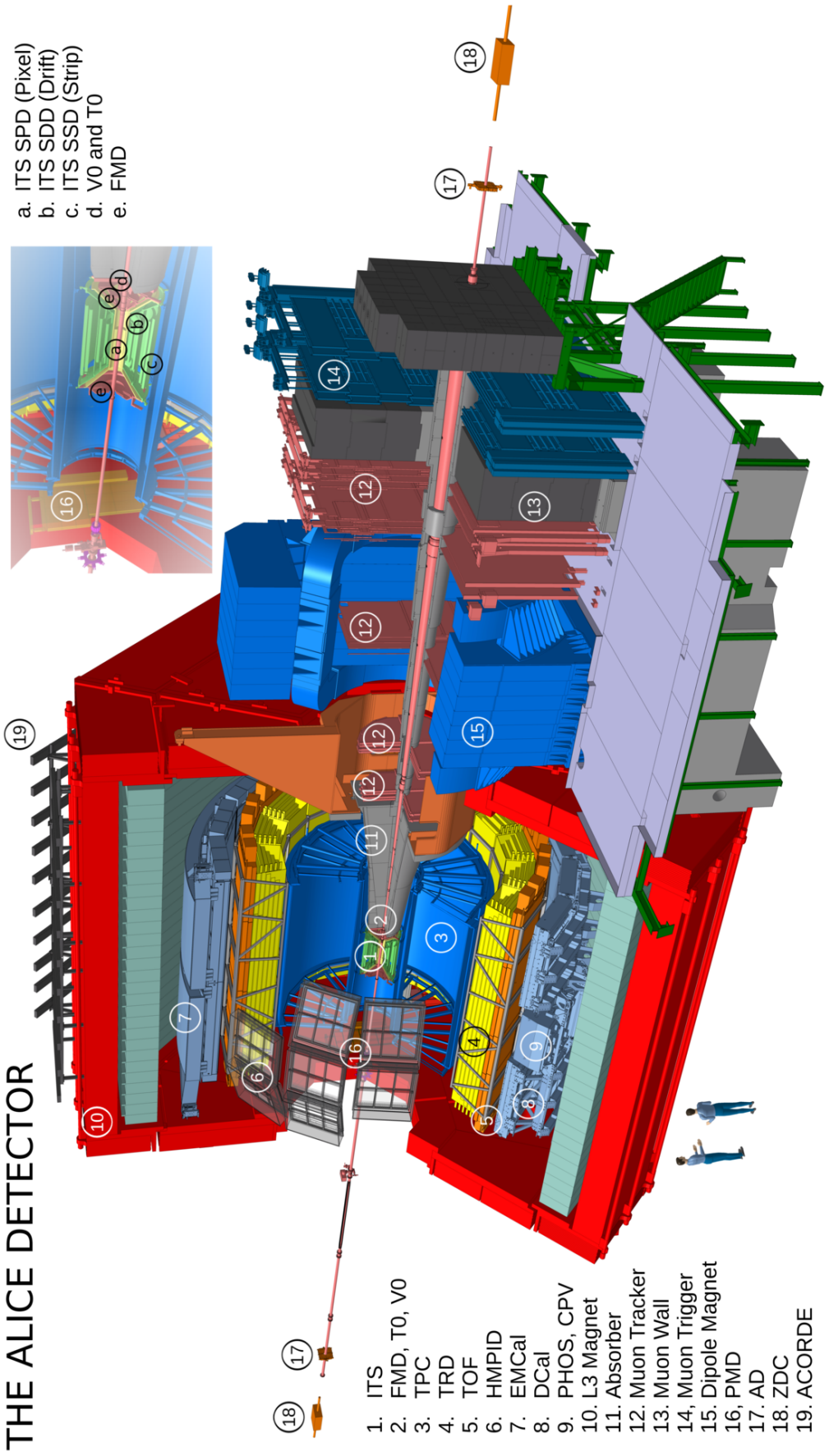

Fig. 3.5 The ALICE detector [12].

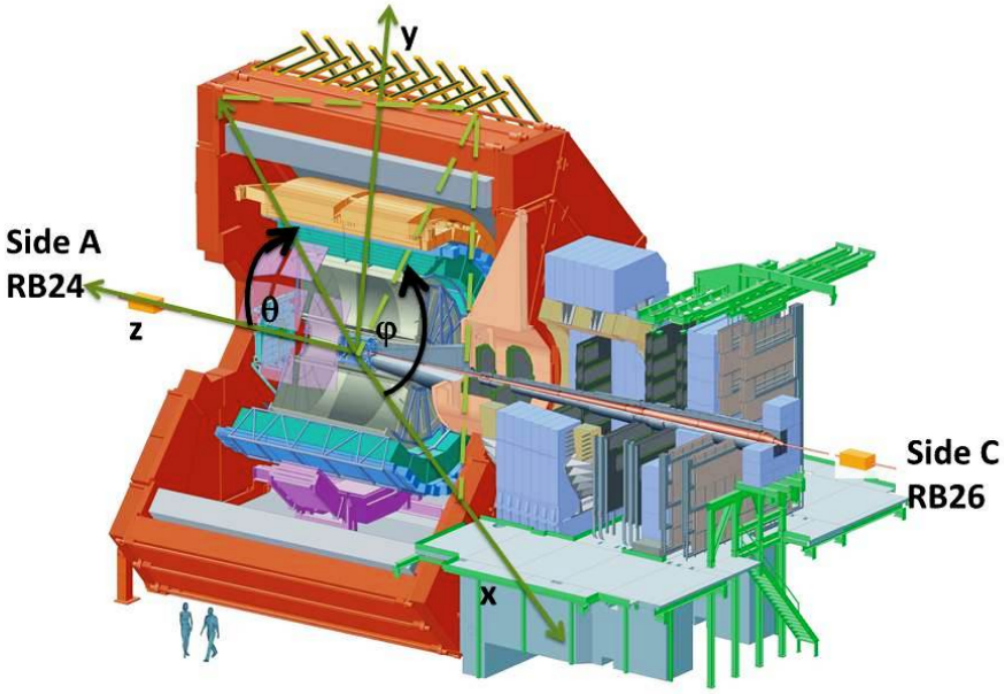

Fig. 3.6 The ALICE detector co-ordinate system [82].

3.2.1 Geometry and coordinate system

The ALICE detector has a right-handed co-ordinate system, shown in Figure 3.6, whose origin is defined as the nominal interaction point (IP). The z-axis runs along the beam line, with positive z called the A-Side, and negative z the C-Side. Perpendicular to the z-axis is the x-y plane with positive x pointing directly from the origin towards the centre of the LHC ring and positive y pointing directly up to the surface of the Earth.

In spherical co-ordinates system, the azimuthal angle φ is measured around the beam axis, and the polar angle θ is measured from the positive z-axis. The rapidity (y) is used instead of θ and φ.

The rapidity is defined as

$$y = \frac{1}{2} ln \left[\frac{E + P_z}{E - P_z} \right] \tag{3.2}$$

where E and P_z are the particles energy and momentum component in the z direction, respectively. The sum and difference in rapidities is invariant under beam line boosts. However, at LHC energies, collisions are assumed to be highly relativistic, consequently, the masses of the particles are assumed to be negligible. Therefore, for massless particles,

rapidity can be reduced to pseudorapidity (η) defined as

$$\eta = -\ln\left[\tan\left(\frac{\theta}{2}\right)\right] \tag{3.3}$$

Another important kinematic variable is the transverse momentum (p_{T}), measured in the x-y plane and defined as

$$p_{\mathrm{T}} = \sqrt{p_x^2 + p_y^2} \tag{3.4}$$

where p_x and p_y refer to the momentum components in the x and y direction.

3.2.2 Central barrel detectors

The L3 magnet houses the central barrel detectors that cover the pseudorapidity range -0.9 $< \eta <$ 0.9, a polar angle 45° $< \theta <$ 135°. From the inside out, the central barrel consists of the Inner Tracking System (ITS), made up of six planes of high resolution Silicon Pixel Detectors (SPD), Silicon Drift Detectors (SDD) and Silicon Strip Detectors (SSD), a cylindrical Time Projection Chamber (TPC), a Transition Radiation Detector (TRD), the Time of Flight Detector (TOF), the High Momentum Particle Identification Detector (HMPID) and two ElectroMagnetic Calorimeters (EMCal) and the Photon Spectrometer (PHOS). These detectors allow for primary vertex reconstruction, charged-particle tracking over a momentum range of 10 MeV to 100 GeV and particle identification for charged hadrons, electrons and photons.

The ALICE experiment is well documented and the details of the detector can be found in [12]. In this chapter we will focus only on the sub-detectors used in the analysis.

3.2.2.1 Inner Tracking System

The Inner Tracking System (ITS) [83], shown in Figure 3.7, surrounds the beam pipe. It is designed to reconstruct the primary vertex, with a precision better than 100 μm. It also reconstructs the secondary vertices of the decay of neutral strange particles as well as the D[1] and B mesons. The ITS also tracks and identifies particles with momentum below 200 MeV/c. It improves the momentum and angle resolution for particles reconstructed in the Time Projection Chamber (TPC, the main tracking device in ALICE) and reconstructs

[1]Mesons consisting of a charm quark or anti-quark and either an up, down or strange quark

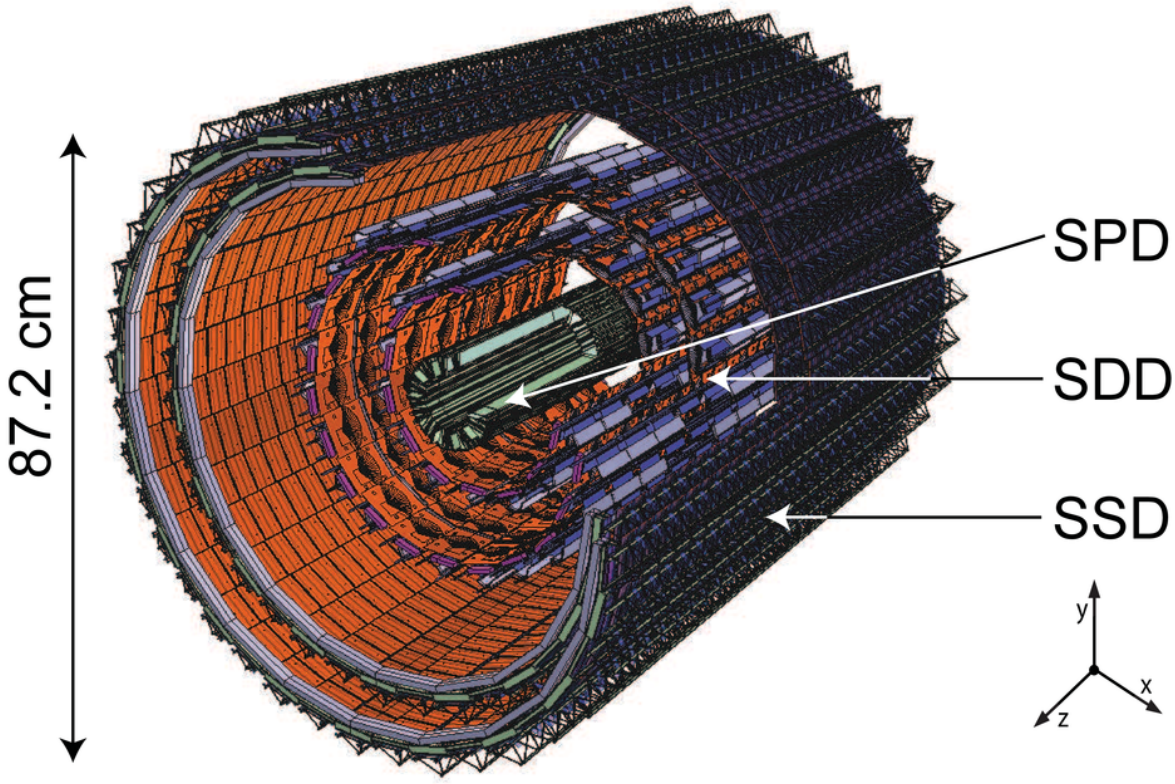

Fig. 3.7 The Inner Tracking System [84].

particles passing through dead regions of the TPC. It is made up of 2198 sensor modules. It consists of six cylindrical layers of silicon detectors, with radii between 3.9 cm and 43.0 cm and covers the pseudorapidity range $|\eta| < 0.9$. The innermost two layers of the ITS are the Silicon Pixel Detectors (SPD), followed by two layers of Silicon Drift Detectors (SDD) and the two outer layers are the Silicon Strip Detectors (SSD). The SPD is also a multiplicity estimator which is relevant for this analysis. Therefore we will give more details about the SPD than SDD and SSD, however, the multiplicity estimation with the SPD will be discussed in detail in Chapter 4.

- **Silicon Pixel Detectors (SPD)**

  As already mentioned, the SPD constitutes the two innermost layers of the ITS. Its primary task is to determine the position of the primary vertex and to measure the impact parameter of secondary tracks originating from weak decays of strange, charm and beauty particles. It is based on hybrid silicon pixels, consisting of a two dimensional matrix of reverse biased silicon detector diodes.

  The pseudorapidity range of the SPD extends to $|\eta| < 1.98$ as it was built to provide

a continuous charged-particle multiplicity coverage. The SPD also serves as a trigger detector and is used to identify events in which more than one collision takes place in the same bunch crossing i.e. the so called in-bunch pile-up events.

The SPD vertex is also necessary for the reconstruction of muon tracks (see Section 3.2.4) in the muon spectrometer. We will briefly discuss the algorithm for the determination of the SPD vertex as well as the SPD tracklets[2] which are used for the charged-particle multiplicity estimation in analysis.

There are two algorithms employed, namely, VertexerSPDz and VertexerSPD3D [85]. The latter reconstructs x, y and z positions of the primary vertex based on SPD tracklets. The tracklets are reconstructed by connecting points between the two layers of the SPD within a small azimuthal window from the expected interaction point and a chosen Distance of Closest Approach (DCA). Tracklet pairs whose crossing points lie within the fiducial interaction region are kept and their coordinates are computed. The coordinates of individual crossing points are then used to estimate the coordinates of the vertex. A second reconstruction is done and tracklets that are displaced from the vertex reconstructed in the first iteration are removed and the coordinates of the vertex are recomputed from the remaining tracklets. The former provides a measurement of the z-coordinate of the primary vertex assuming that the beam position in the transverse plane is known with an accuracy of 200 μm or better. The algorithm calculates the intersection point with the beam axis for each candidate tracklet. The candidate tracklets are reconstructed by correlating the SPD vertex with a cluster in the two layers. A straight line is drawn from the vertex to the cluster in the inner layer of the SPD and another one to the outer layer and differences in the azimuthal and polar angle are computed for different combinations of all the clusters in the outer layer. Candidates with a given $\Delta\phi$ and $\Delta\theta$ are accepted. Schematic diagrams of the reconstruction of the SPD vertex and tracklets is shown in Figure 3.8.

- **Silicon Drift Detector (SDD)**
  The SDD measures the spatial coordinates of the particles crossing it and can identify them. Each SDD is made from a 12.7 cm diameter and 0.3 mm thickness silicon wafer. The active area is 7.0 x 7.5 cm^2. When a particle crosses the thickness of the SDD electrons are released. They drift under the effect of an applied electric field towards an array of 256 anodes (channels). In this way the y-coordinate of the particle is given by the measurement of the drift time. The x-coordinate is obtained from the centroid of the electrons along the anodes. The SDD gives a high precision

[2] A tracklet is a segment of a track which is reconstructed in the SPD, the 2 innermost layers of the ITS

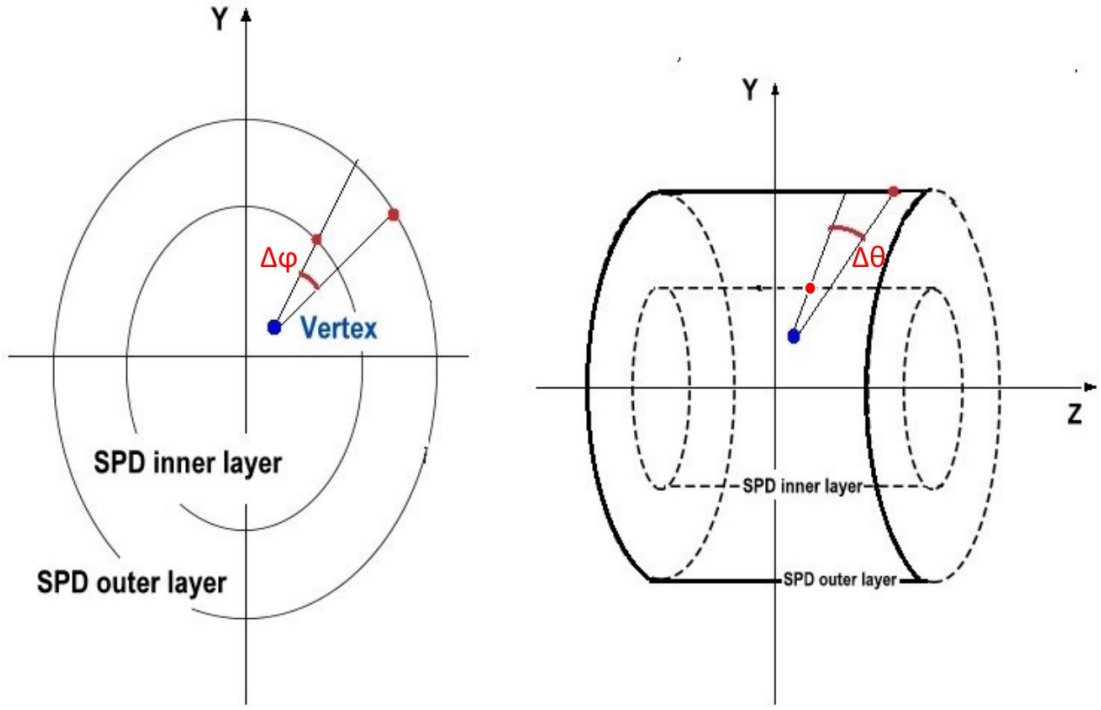

Fig. 3.8 Reconstruction of the SPD vertex and tracklets [85] .

position information and also provides energy loss ($\frac{dE}{dx}$) information which can be used for particle identification (PID).

- **Silicon Strip Detector (SSD)**
  The two outermost layers of the ITS are fundamental for the matching of tracks from the TPC to the ITS. They consist of double-sided SSDs mounted on carbon-fiber support structures. The SSD covers the pseudorapidity of $\eta < 0.97$. It is the outermost layer of the ITS. It has n and p type semiconductors, on the top and bottom of the detector. Holes and electrons are released as the particle goes through the detector, which are attracted towards the semiconductor readout. The SDD is used for position information and PID.

Table 3.1 summarises the characteristics of the ITS.

3.2.3 Global detectors

In this section we describe small detectors used for event characterisation and triggering. The VZERO, TZER0, Zero Degree Calometers and the Forward Multiplicity Detector constitute the global detectors. In this section we will briefly describe only those utilised in this analysis as well as their functions.

Layer	Type	r (cm)	Acceptance	Number of Modules
1	Pixel	3.9	$\|\eta\| < 2.0$	80
2	Pixel	7.6	$\|\eta\| < 1.4$	160
3	Drift	15.0	$\|\eta\| < 0.9$	84
4	Drift	23.9	$\|\eta\| < 0.9$	176
5	Strip	38.0	$\|\eta\| < 0.97$	748
6	Strip	43.0	$\|\eta\| < 0.97$	950

Table 3.1 Summary of the ITS characteristics [12].

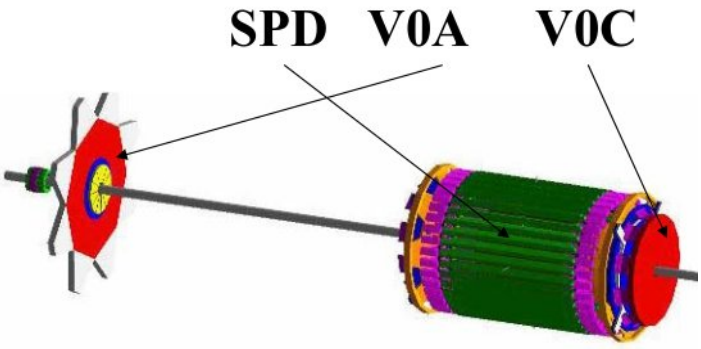

Fig. 3.9 V0A and V0C detectors with respect to the position of the SPD. [87] .

3.2.3.1 VZERO (V0)

The V0 [86] detector is made of two arrays of scintillator material, located 90 cm (C-side, V0C) and 340 cm (A-side, V0A) from the interaction point. The detectors are segmented into 72 elementary counters distributed in 5 rings, with a pseudo-rapidity coverage of -3.8 $< \eta <$ -1.7 and 2.8 $< \eta <$ 5.1. The measurement of the time-of-flight difference between the detectors allows to identify and reject the beam-gas events, thus providing a minimum bias trigger for the central barrel detectors and a validation signal for the muon trigger (see Section 3.2.4). The V0 is also used for measuring the charged particle multiplicity, where it is used for a centrality selection. It is also used for luminosity measurement.

3.2.3.2 TZERO (T0)

The T0 [86] detector consists of two arrays of Cherenkov counters, with a time resolution better than 50 ps, asymmetrically placed at 72.7 cm (C- side, T0C) and 375 cm (A-side, T0A) from the interaction vertex, with a pseudo-rapidity coverage of -3.28 $< \eta <$ -2.97 and 4.61 $< \eta <$ 4.92, respectively. It is designed to provide a start time, the so called T0 signal, for the TOF detector to measure the vertex position with a precision of $\pm$1.5

cm, thus providing an L0[3] trigger when the position is within the preset values and to measure the particle multiplicity and generate a centrality trigger. The T0 detector is also used for luminosity measurement.

3.2.3.3 Zero Degree Calorimeter (ZDC)

The ZDC [88] is dedicated to the measurement of the energy carried by spectactor nucleons (i.e. nucleons not involved in the interaction) at zero degrees with respect to the beam direction. Therefore, the ZDC allows one to deduce the number of participants and the centrality of the nucleus-nucleus collisions. It also provides triggering for Pb–Pb collisions. The ZDC detector is composed of two hadronic calorimeters, the neutron calorimeter (ZN, which measures the spectator neutrons) and the proton calorimeter (ZP, measuring protons). The two calorimeters are placed a distance of 112 m from the interaction point on the A and C side. The system is completed by two Electromagnetic calorimeters (ZEM, measuring the participating nucleons) located at 7 m from the interaction point on the C side. This allows one to solve ambiguities in the determination of the collision centrality. The ZDC also rejects electromagnetic background.

3.2.4 The Forward Muon Spectrometer

The forward Muon Spectrometer [89] measures dimuons from the decay of quarkonia (charm-anti-charm ($c\bar{c}$) e.g. J/Ψ and beauty-anti-beauty ($b\bar{b}$ e.g. Υ)), as well as low vector mesons (rho (ρ), omega (ω), ...) and muons from decays of heavy-flavours and electroweak bosons ($W^{\pm}$, Z^0), which are tools for studying QGP as well as the initial conditions of the collision.

The forward Muon Spectrometer is shown in Figure 3.10. The angular acceptance of the muon spectrometer is $2^o < \theta < 9^o$. In a right-handed coordinate system, (see Section 3.2.1), the angular acceptance translates to a polar angle of $171^o < \theta < 178^o$, with respect to the beam axis which corresponds to a pseudorapidity range of -4 $< \eta <$ -2.5. This allows the study of heavy quarks and quarkonia in a region complementary to the one explored by the ALICE central barrel and by other LHC experiments, namely, ATLAS, and CMS.

The spectrometer consists of a composite absorber with a thickness of ≈10 interaction lengths (λ_{int} - hadronic interaction length related to the energy loss of high energy parti-

[3]The fast part of the ALICE trigger is split into two levels: a Level 0 (L0) signal which reaches detectors at 1.2 μs, but which is too fast to receive all the trigger inputs and a Level 1 (L1) signal sent at 6.5 μs which picks up all remaining fast inputs.

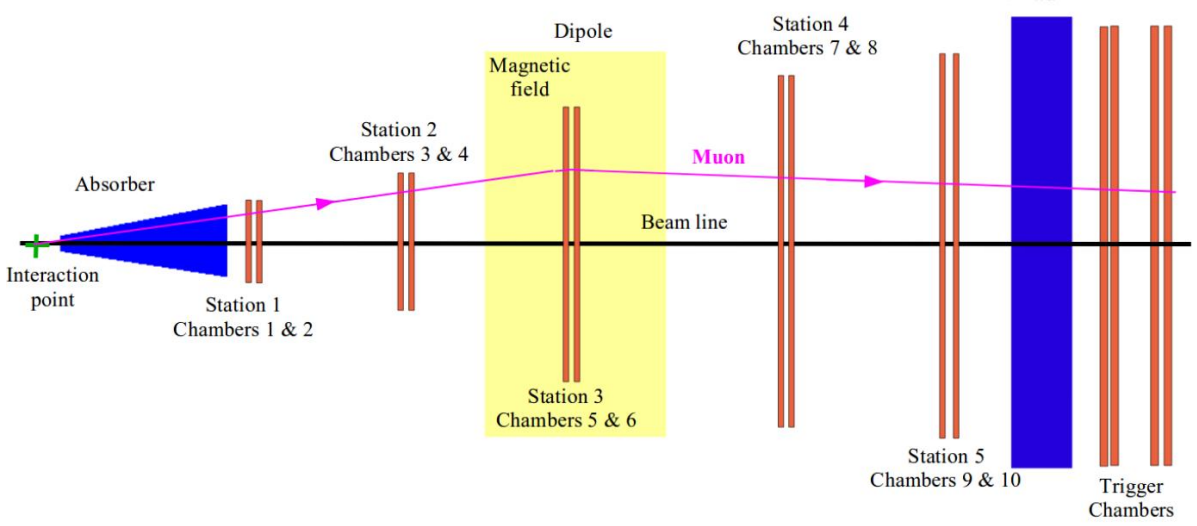

Fig. 3.10 Layout of the ALICE Muon Spectrometer[30].

cles) and a large dipole magnet that provides a 3 Tm field integral placed outside the L3 magnet. The spectrometer also has 5 tracking stations consisting of ten high granularity tracking chambers and 2 trigger stations with 4 planes of trigger chambers. Between the tracking and the trigger stations is a second absorber made of iron with a thickness of $\approx 7\lambda_{\text{int}}$ placed 16 m away from the nominal interaction point. The spectrometer is shielded throughout its length by a dense absorber tube with a diameter of 60 cm which surrounds the beam pipe

3.2.4.1 The front absorber, beam shield and muon filter

As already mentioned, the spectrometer has three absorber sections namely, the front absorber, the beam shield which surrounds the beam pipe and the muon filter between the tracking and trigger stations.

The front absorber has two important functions, the first is that of reducing the forward flux of charged particles by at least two orders of magnitude. This is achieved by minimizing the distance between the absorber and the vertex, taking into account the dimension of the ITS and the position of the multiplicity detectors. Consequently, the front absorber is placed at a minimal distance of 90 cm from the interaction point. The second function is to decrease the background of muons from the decay of pions and kaons by limiting their free path. The absorber design and composition is optimized to provide good shielding capabilities to limit multiple scattering which should not compromise the spectrometer mass resolution. To satisfy this requirement, low-Z material is used in layers of the absorber

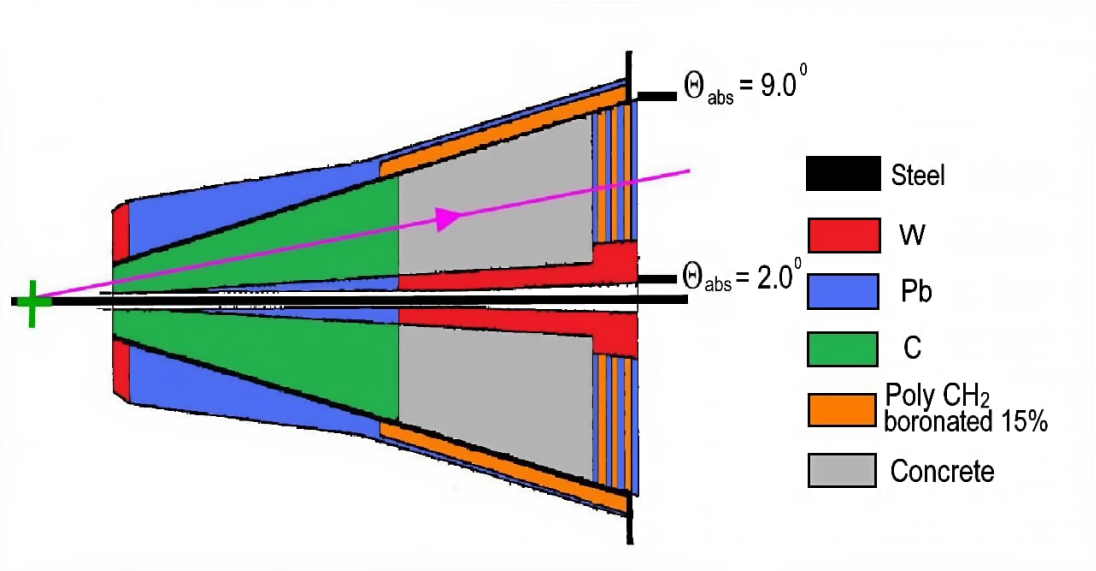

Fig. 3.11 A zoom into the front absorber[30].

close to the vertex and high-Z shielding materials at the rear end. A thickness of 20 cm of Lead interleaved with layers of boronated polyethylene, which can moderate neutrons by quasi-elastic scattering, was chosen for the front part while Lead and Tungsten were selected for the rear end, as shown in the schematic of the front absorber in Figure 3.11. Outside the muon arm acceptance, a tungsten cone located at an angle $\theta_{\rm abs} < 2^{\rm o}$ absorbs particles emanating from the beam pipe. At $\theta_{\rm abs} > 10^{\rm o}$ the absorber material is mainly lead, tungsten and boronated polyethlylene to reduce the particle load in the TPC. The absorber is completed by a combination of concrete and carbon.

The small-angle beam shield is made of dense materials, that is, pure tungsten in the regions nearest to the IP and a tungsten-lead mixture in regions further away from the IP, encased in a 4 cm thick stainless steel tube. Its outer envelop is pencil shaped, that is, follows the $2^{\rm o}$ acceptance line up to a maximum radius of 30 cm and then stays constant up to the end of the spectrometer. The small angle beam shield covers the beam pipe along the spectrometer extension. It protects the tracking detectors from particles produced at very small angles and from secondary particles generated in the beam-pipe due to the beam gas interaction. The small angle absorber ends with an iron plug of 1.1 m in diameter and 1 m thick, which protects the trigger detectors against background particles.

The muon filter is a 5.6 x 5.6 x 1.2 m^3 iron wall placed at 15 m from the interaction point, between the last tracking station and the first trigger station. It reduces the background on the trigger stations by absorbing pions and low momentum muons. The combined effect of the front absorber and the muon filter prevents muons with momentum less than 4 GeV/c from reaching the trigger station and enhances the trigger chamber performance.

Fig. 3.12 The dipole magnet[90].

3.2.4.2 The dipole magnet

The dipole magnet, as shown in Figure 3.12, is located at 7 m from the IP, outside the L3 magnet. It is 5 m long and weighs about 900 tons. It provides a magnetic field of up to 0.7 T in the horizontal direction. This translates to a field integral of 3 Tm between the IP and the muon filter, defined by the mass resolution of the spectrometer. The dipole magnet enables momentum measurement and charge determination of the muon tracks.

3.2.4.3 The tracking stations

The tracking system of the ALICE muon spectrometer covers a total area of $\approx$ 100 m^2, with the design driven by two main requirements [91, 92]: the spatial position resolution of $\approx$100 μm (which is necessary for an invariant mass resolution of 100 MeV/c^2 at the Υ mass) and the capability to operate in a high particle multiplicity environment. These requirements are fulfilled by employing Cathode Pad Chambers (CPC) arranged in five stations: two stations are placed before, one station inside and two stations after the dipole magnet. Each station is made of two chamber planes. Each chamber has two cathode planes which are both readout to provide two-dimensional hit information in bending and non-bending plane. These CPCs are based on a multi-wire proportional chamber principle and are gas detectors. They use a gas mixture of 80% Ar and 20% CO_2. In order to keep the occupancy at a 5% level, high granularity readout pads are needed. Since the hit density decreases with the distance from the beam, larger pads are used at larger transverse radii. The muon tracking system is equipped with a total of 10^6 electronics channels.

The first two stations are based on a quadrant structure with the readout electronics

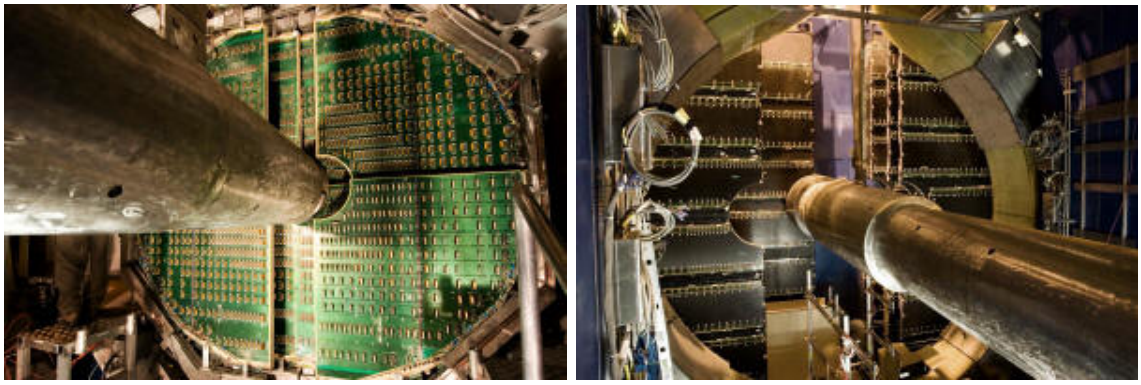

Fig. 3.13 An example of the tracking chambers in quadrant (left) and slat (right) architecture [93].

distributed on their surface while stations 3, 4 and 5 are based on a slat architecture. Figure 3.13 shows the two types of the tracking stations. The maximum size of a slat is 40×280 cm^2 and the electronics is mounted on the side of the slats. The position of the tracking stations is monitored by the so-called Geometry Monitoring System (GMS) to avoid misalignment during data taking which may compromise the tracking efficiency.

The front-end board (MANU, MAnas NUmerique, 64-channel) consists of 4 Multiplexed ANAlogic Signal processor chips (MANAS, 16-channel, acts a role of charge amplifier, filter and shaper chip), several ADCs and the controller chip (MARC, Muon Arm Readout Chip). The MARC is in charge of the zero suppression and the communication at the Data Signal Processor (DSP) level. Up to 26 MANUs are connected (via PATCH bus) to the translator board which allows the data transfer to the Concentrator Read-Out Cluster Unit System (CROCUS, for a total number of 20 CROCUS). The main tasks of the CROCUS are to concentrate data from the chambers, to transfer them to the DAQ, to perform the calibration of the front-end electronics and to dispatch the signals from the Central Trigger Processor (CTP).

In muon track reconstruction, the cluster-finder algorithm is used to associate clusters to the detector digits by taking the raw data as inputs. Then the charge signal (induced on the CPC pads from the passage of the muons) is fitted [94] and the cluster coordinates obtained from this fitting procedure are used as inputs for the subsequent muon track reconstruction. Two independent tracking algorithms have been developed. The first one is based on the traditional method i.e. fit the position of the track associated clusters to reconstruct the track, while the other is based on the Kalman filter [95]. The latter is the default option. Both algorithms have the following restrictions; the first estimation of track momenta should be $3 < p < 3000$ MeV/c. Secondly, the reconstructable track on stations 1, 2 and 3 should include 1 or 2 clusters while for stations 4 and 5, 3 or 4 clusters are required. Lastly, a cut on χ^2 is applied at both the cluster and track levels.

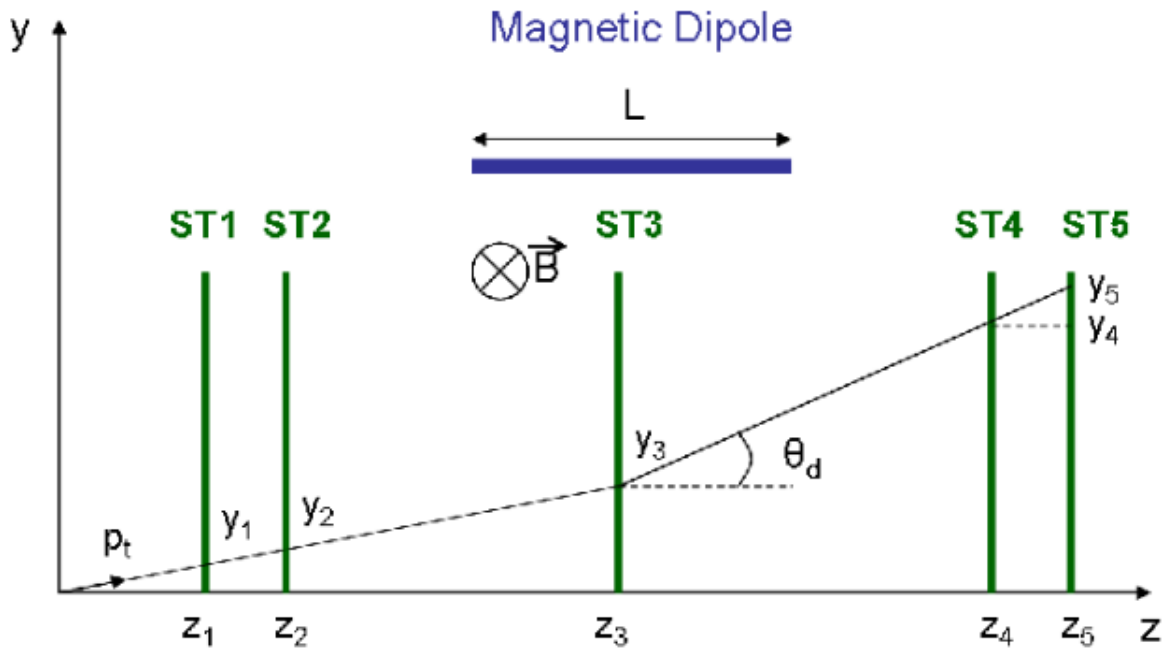

Fig. 3.14 Principle of track reconstruction[96]. The labels y_1, y_2, y_3, y_4, y_5 are the reconstructed positions of the muon on the respective tracking station, while z_1, z_2, z_3, z_4, z_5 are the corresponding z-vertex positions of the tracking stations. $\vec{B}$ is the magnetic field and θ_d is the deflection angle of the muon and Pt is the transverse momentum of the muon track (p_T).

The muon track reconstruction starts from stations 4 and 5 because they are less susceptible to background induced by the soft particles escaping the front absorber. At the beginning, the algorithm allows one to link cluster pairs on stations 4 and 5, independently, and to create segments by joining the two clusters position with a straight line. Then, the obtained segments are extrapolated through the magnetic field to the primary vertex (IP), in order to have a first estimation of the corresponding track parameters, such as the position, slope, inverse bending momentum and the related errors. Figure 3.14 shows the reconstruction of a muon track.

The momentum of the track (p) can be calculated using the Lorentz law as;

$$\vec{F} = \frac{d\vec{p}}{dt} = q(\vec{v} \times \vec{B}) \tag{3.5}$$

where q is the charge of the muon, $\vec{v}$ is the velocity, $\vec{B}$ is the magnetic field of the dipole magnet, respectively. The resulting curvature radius, R, is calculated from the momentum

obtained with Equation 3.5, as

$$\vec{p} = |\vec{B}| \times R = |\vec{B}| \times \frac{L}{\theta_d} \tag{3.6}$$

where, $|\vec{B}| = 0.3$ T, L is the length of the magnet and $\theta_{\rm d}$ is the deflection angle, with the geometry described in Figure 3.14. Consequently, with Equation 3.5, the first restriction for the two tracking algorithms is applied as $3 < {\rm p} < 3000$ MeV/c.

The second step of the tracking algorithms is to consider as departure the estimated track from station 5 (station 4) clusters and extrapolate it to the station 4 (station 5). The algorithm can search for at least one cluster on that station that could be associated to the track (i.e. the restriction of 3/4 clusters on stations 4 and 5). Another restriction, a cut on χ^2, is applied to associate clusters to track candidates. The Kalman based reconstruction algorithm considers all clusters that pass the criteria, while the traditional one usually considers the best associated cluster i.e. the one with the lowest χ^2. Once a cluster is associated, the track parameters have to be re-calculated. Note that the employed Kalman algorithm uses the Kalman filter procedure, while the traditional algorithm needs to fit again the associated clusters to evaluate the new parameters. The next step is the track extrapolation back to station 3. As before, a χ^2 cut is imposed as a cluster selection criteria as well as a χ^2 cut on the track. A minimum requirement of one cluster associated to the track candidates has to be considered, including at least 1 or 2 clusters on station 3. After that, the remaining tracks with the re-evaluated parameters are extrapolated down to station 2, and later to station 1. It is necessary to mention that the selection criteria is the same as the one implemented at station 3 i.e. the χ^2 cut on the clusters and the track and a minimum of 1 associated cluster.

3.2.4.4 The trigger stations

When the LHC is operating at its nominal run conditions, about 80% of low $p_{\rm T}$ muons from charged hadron ($\pi^{\pm}$ and $\rm K^{\pm}$) decays are anticipated to reach the trigger stations in central Pb–Pb collisions. Consequently, a $p_{\rm T}$ cut is applied at the trigger level that eliminates low $p_{\rm T}$ muons from charged hadrons that are not acompanied by the high $p_{\rm T}$ ones emitted in the decay of heavy quarkonia, as well as in the semi-muonic decay of heavy-flavour hadrons.

The trigger stations consist of 4 Resistive Plate Chamber (RPC) planes arranged in 2 stations placed 1 m apart behind the iron muon filter. The RPCs are gas chambers utilizing a gas mixture of $\rm C_2H_2F_4$ (89.7%), $\rm C_4H_{10}$ (10%) and $\rm SF_6$ (0.3%). The total active area is $\approx$140 $\rm m^2$. The RPC is made up of "low-resistivity" ($\rho \approx 2 \times 10^9$ Ω.cm) bakelite

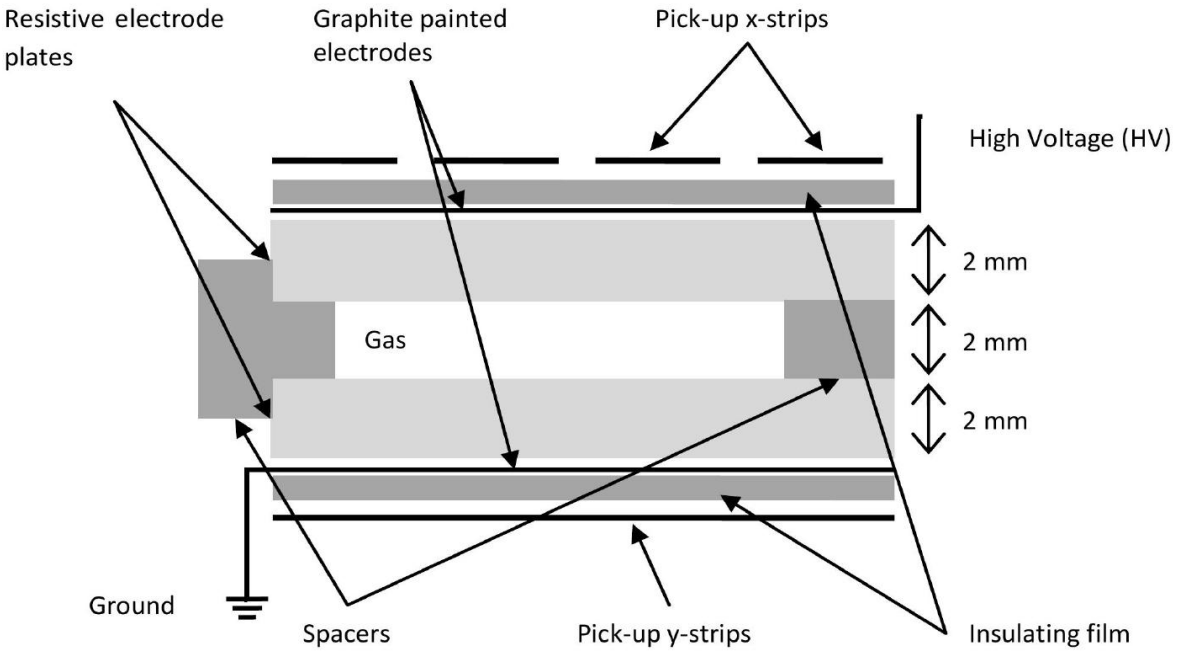

Fig. 3.15 Resistive Plate Chambers. Figure adapted from [92].

electrodes separated by a 2 mm wide gas gap as shown in Figure 3.15. The active area covered by the first station is 6.12 × 5.44 m^2 and the second is 6.50 × 5.78 m^2. The larger dimension of the detection planes is along the vertical direction (bending plane), where the acceptance of the system extends from 2^o to 10^o , while in the non-bending plane it is in the range 2^o to 9^o. To avoid the inactive zones, the RPCs are positioned on a mechanical structure in two parallel planes, to allow superposition of active and dead areas. RPCs are read on both sides with copper strips. The horizontal strips (X) measure the coordinate along y direction (bending plane), while the vertical strips (Y) measure the coordinate along x direction (non- bending plane). In order to ensure a flat occupancy throughout the detection plane, the pitch and length of the strips increases with distance from the beam pipe, in proportion to the hit-rate per unit area. The pitch of the strips is also governed by the space resolution of better than 1 cm required for the p_T cut.

The selection of candidate muon tracks, namely, trigger tracks, is implemented via an algorithm at the electronics level. The algorithm takes as input the measured position of the clusters on the first trigger station, (y_1 , z_1), shown in Figure 3.16. The two points and the primary vertex, form a trajectory. The dashed line in Figure 3.16, corresponds to the muon with infinite momentum p it can be extrapolated to the second trigger station at point (y_2^{inf} , z_2). However, the trajectory of an entering muon with finite momentum is deflected when going through the magnetic field, as showed by the solid line in Figure 3.16. It can reach the point (y_1 , z_1) at the station 1, then be extrapolated to point (y_2 , z_2) at station 2, then, one can measure the deviation of the track relative to a particle

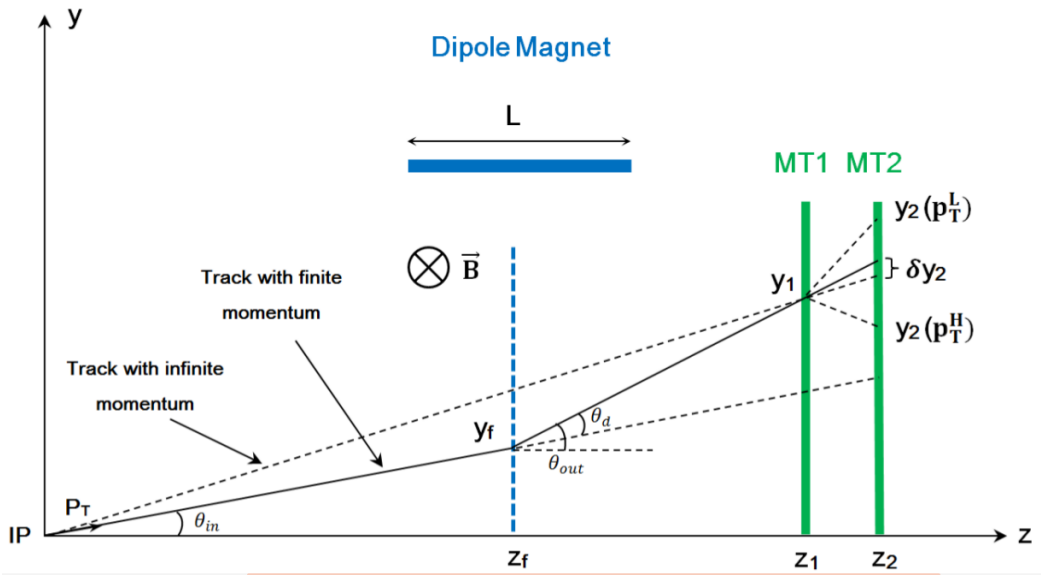

Fig. 3.16 Principle of p_T cut done by the muon trigger. MT1 and MT2 are the muon trigger stations 1 and 2 , respectively[92].

Signal description	Trigger name	Trigger class
At least one single muon above low p_T cut	Single muon low p_T	CMSL7-B-NOPF-MUFAST
At least one single muon above high p_T cut	Single muon high p_T	CMSH7-B-NOPF-MUFAST

Table 3.2 Trigger signal descriptions, names and classes they belong to according to the nomenclature chosen in ALICE. [97].

with infinite momentum on the station 2, labeled as σy_2 in Figure 3.16. The measured deviation should be smaller than a certain value, for instance, $\delta y_2 \leq \delta Y_2 = y_2(p_T{}^L)$- $p_T{}^H$), which corresponds to the desired p_T coverage $p_T{}^L < p_T < p_T{}^H$ [97].

The subsequent cuts on this deviation, performed by means of the LUT (Look-Up-Tables), allow the rejection of low p_T muons which have large deviation. The two sets of cuts, namely, low p_T and high p_T cuts, are loaded in the LUT in the local board. The so-called "all p_T cut " corresponds to the case for which no cut on the deviation is applied at the LUT level. Trigger signals are delivered to the ALICE Central Trigger Processor (CTP), less than 800 ns after the interaction, at a 40 MHz frequency. The trigger signals and their corresponding classes relevant in the data analysed in this thesis are as tabulated in 3.2.

These were the triggers used for Run 2. The types of trigger are changed depending on

the physics of interest, e.g Run 1 triggers were different from the ones discussed here for Run 2.

3.3 The Geometry Monitoring System

As already seen from the discussions above, the momentum and charge determination of muons relies heavily on the position of the particle in both the triggering and the tracking stations. Consequently, misalignment of detector elements will result in misassignment of the track momentum leading to a compromised efficiency of the muon spectrometer. The global position of the muon spectrometer therefore plays an important role in ensuring its efficiency. The Geometry Monitoring System (GMS) is therefore, employed to measure the displacement of the muon chambers from their initial positions measured when there is no magnetic field (i.e. when the magnets are switched off and the muon tracks pass straight, through the chambers without being deflected), to their positions when the magnetic field is turned on.

The GMS is shown in Figure 3.17. It consists of an array of 460 optical sensors placed at each corner of the tracking chambers. Images of optical lines are constantly recorded and compared to the initial positions (also known as references), during data taking. The image displacements give information on the effects of the magnetic field on the positions of the chambers, e.g. displacements and deformations caused by thermal expansions. The deviations can then be corrected.

3.4 ALICE online systems

The ALICE experiment includes five online systems namely, Central Trigger Processor (CTP), High-Level Trigger (HLT), Data Acquisition (DAQ), Experiment Control System (ECS) and Detector Control System (DCS). The task of the online system is outlined in the following sections.

3.4.1 The Central Trigger Processor

The Central Trigger Processor combines the information from all triggering detectors and, for every bunch-crossing of the LHC, makes a decision within microseconds whether the resulting data are worth being collected. The CTP processes the trigger signals from the detectors are collected and uses them to define the different **"trigger classes"**. A trigger

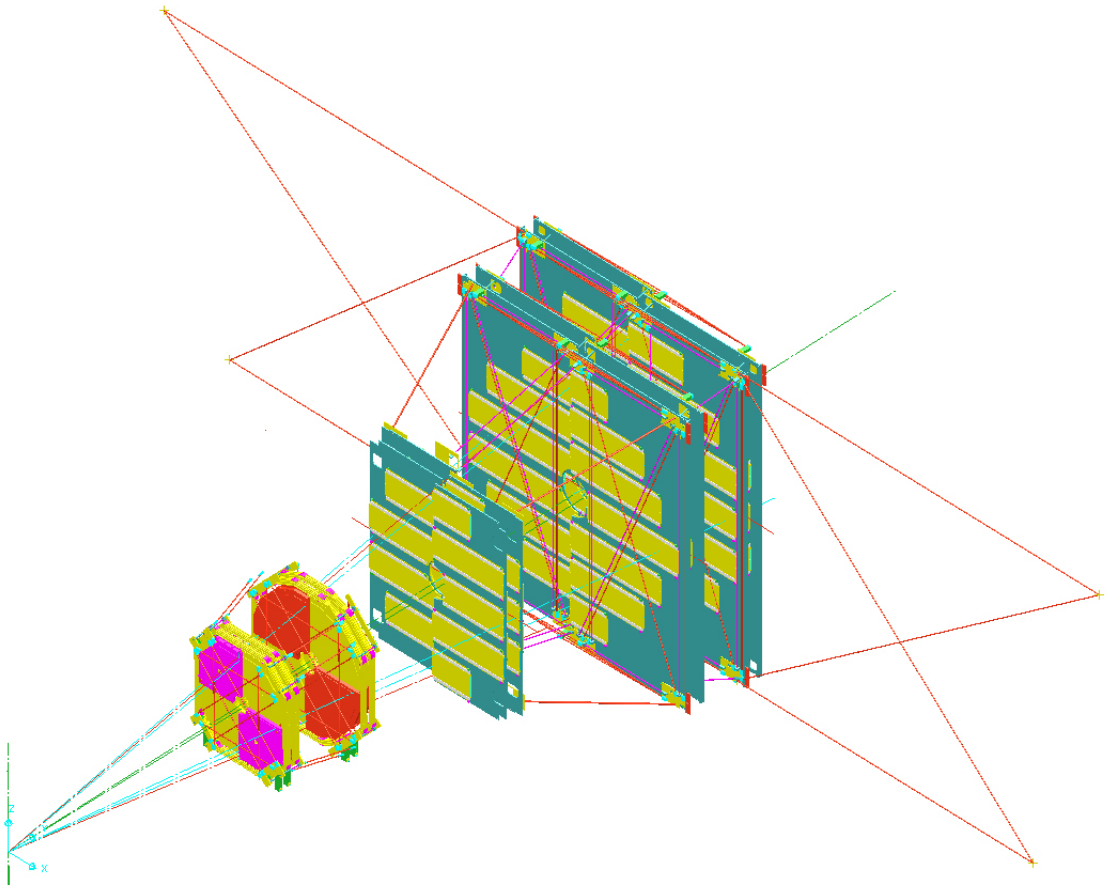

Fig. 3.17 General view of the GMS setup showing the optical lines used to produce the images [98]

class is defined by a combination of different trigger inputs via logical connectors (AND, OR). For example, the minimum bias trigger class, is defined as the logical "AND" of input signals from the two V0 arrays, V0-A and V0-C. The minimum bias trigger class is called **CINT7-B-NOPF-MUFAST** in the data analysed in this thesis. For each trigger class, the rate is defined as the number of events that fulfill the trigger condition in a unit of time. Therefore, the CTP selects physics events with different rates and performs a scaling down of these rates in order to fit the bandwidth requirements of the DAQ. It also has to cope with many different detectors which are busy at different periods following a valid trigger. The first trigger signal, called Level 0 (L0), arrives at about 1.2 μs after the collision. The L0 signals (24 L0 inputs) from the fastest detectors, such as the SPD, V0, T0, PHOS, EMCAL and the Muon Trigger system, are treated with a three states logic, i.e. asserted, not relevant and negated combined with logic AND and OR in order to select a certain class of events. The information of slower detectors is used to create a Level 1 trigger signal (L1) that is dispatched after 6.5 μs. The ALICE trigger system has been provided with a past-future protection circuit which looks for other events in a time window before and after the collision under investigation. This helps to reject pile-up

events and improves the readout of the detectors. The last level of trigger is the Level 2, which waits for the past-future protection and arrives after 88 μs. The CTP data are stored both in the raw data stream and in dedicated **trigger scalers**. In particular, there are scalers for all the inputs and for each trigger class that store the number of events passing each stage of the trigger (L0, L1, L2).

3.4.2 The High-Level Trigger (HLT)

The CTP is complemeted by the High-Level Trigger (HLT). The HLT further processes the data from the detector and rejects or accepts events based on an online analysis to allow the data to fit the available storage bandwidth while preserving the interesting physics events. The HLT has an online event display front-end that allows visualisation of events and monitoring during online data taking.

3.4.3 The Data Acquisition system (DAQ)

The core function of the DAQ system is to realize the data-flow from the detector up to the data storage. The DAQ system also includes software packages performing the monitoring of data quality and the system performance. The DAQ system is shown in Figure 3.18.

The DAQ system consists of four layers of computers. The first layer, are the Local Data Concentrators (LDCs) which read out event fragments from the optical Detector Data Links (DDLs). The DDLs are point to point links running at maximum 6 GB/s. Several LDCs collect the data from a single sub-detector at a typical data rate that can go above 13 GB/s and up to twelve DDLs can be connected to the same LDC. The second layer consists of the Global Data Collectors (GDCs) which perform the event building by receiving all the fragments of a given event and assembling them into a full event. The third layer of computers are the Transient Data storage (TDS) which store the data from the GDCs before migrating it to the fourth layer of computers called the Permanent Data Storage (PDS). The data is then published from the PDS via the Grid (See Section 3.7).

3.4.4 The Experimental Control system (ECS)

The ALICE experimental control system (ECS) is shown in Figure 3.19. The ECS provides an interface between the subdetectors and the online systems.

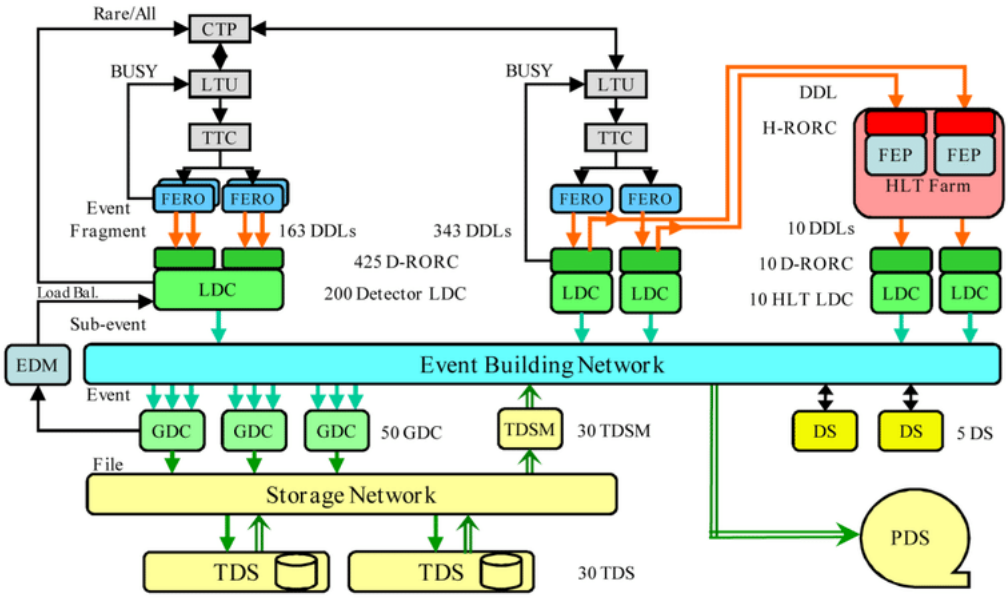

Fig. 3.18 The ALICE Data Acquisition System architecture [99]

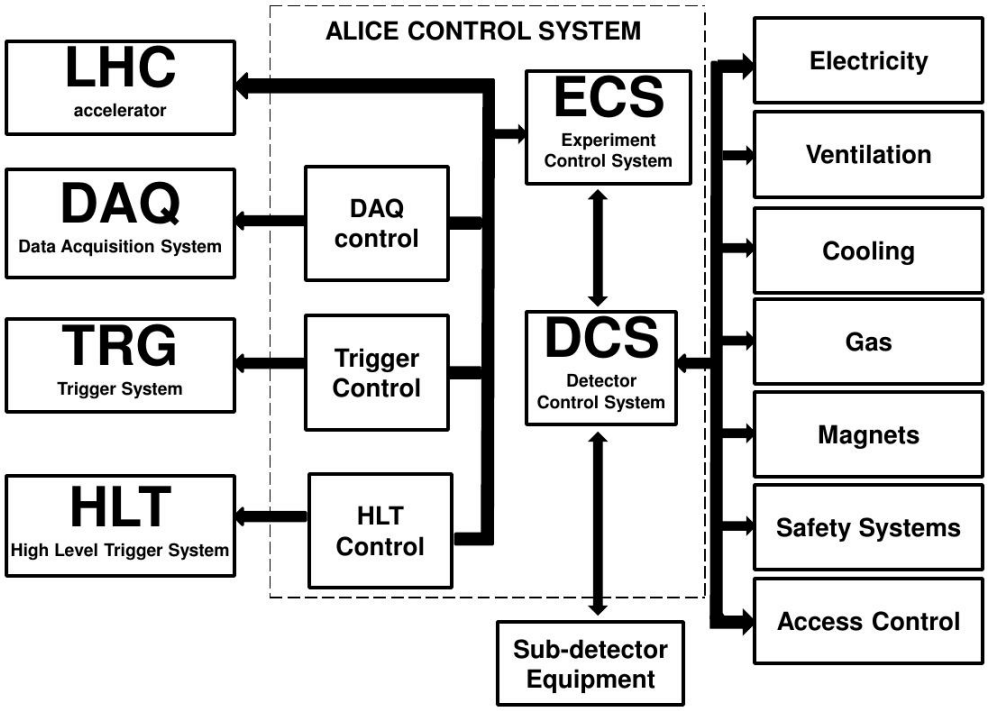

Fig. 3.19 The ALICE experiment Control System [100]

The subdetectors are placed in groups, called partitions, according to trigger requirements and capabilities. Each partition is controlled via a "Partition Control Agent" (PCA). The ECS controls the operations of individual subdetectors in each partition via a "Detector Control Agent" (DCA). Detectors participating during data taking are said to be "active" in the particular partition. Therefore, two types of operations can be performed in a partition namely, those involving all the active detectors, called global operations, and those involving only one active detector, called individual detector operations. Furthermore, detectors can be active in the partition or can be operating independently, i.e. in standalone mode.

The ECS handles both global and individual detector operations by monitoring the DCS status of all the active detectors. When a global operation starts, the ECS inhibits all the individual detector operations. The Run Control (RC) process sends commands to DAQ and the Trigger Partition Agent (TPA) and prepares them for data taking. The TPA links the partitions to the CTP. A similar operation takes place when an individual detector operation is done. However, in the standalone mode, there is an additional interface called the DCA Human Interface (DCAHI), which allows an operator to send commands to the subdetector. This interface is also available for operators even when the detector is active in a partition, however, the operator cannot send any commands but receives information via the PCA Human Interface (PCAHI).

During data taking the ECS is monitored and manipulated by an operator who is responsible for calibrating the detectors, starting, stopping and monitoring the global data taking and resetting the CTP when necessary.

3.4.5 The Detector Control System (DCS)

The DCS ensures safe and reliable operation of the ALICE detector by remotely controlling and monitoring all experimental equipment such that the detector can be operated via a unique set of panels from a single workstation, the ALICE Control Room (ACR) at the LHC point 2 (P2). The DCS configures, controls and monitors the ALICE detector subsystems' high and low-voltage power supplies as well as other services (gas, magnet, cooling, safety, magnetic field, etc), to ensure safety of the detectors while collecting quality data. The DCS also monitors the environmental safety to ensure that the areas accessible by personnel during data are safe from radiation. This is done using the RAdiation Monitoring System for the Environment and Safety (RAMSES). The DCS allows optimal operation of the ALICE detector to achieve high running efficiencies. Each detector has a dedicated FSM panel that allow experts to manipulate detector statuses during troubleshooting and calibration on standalone mode.

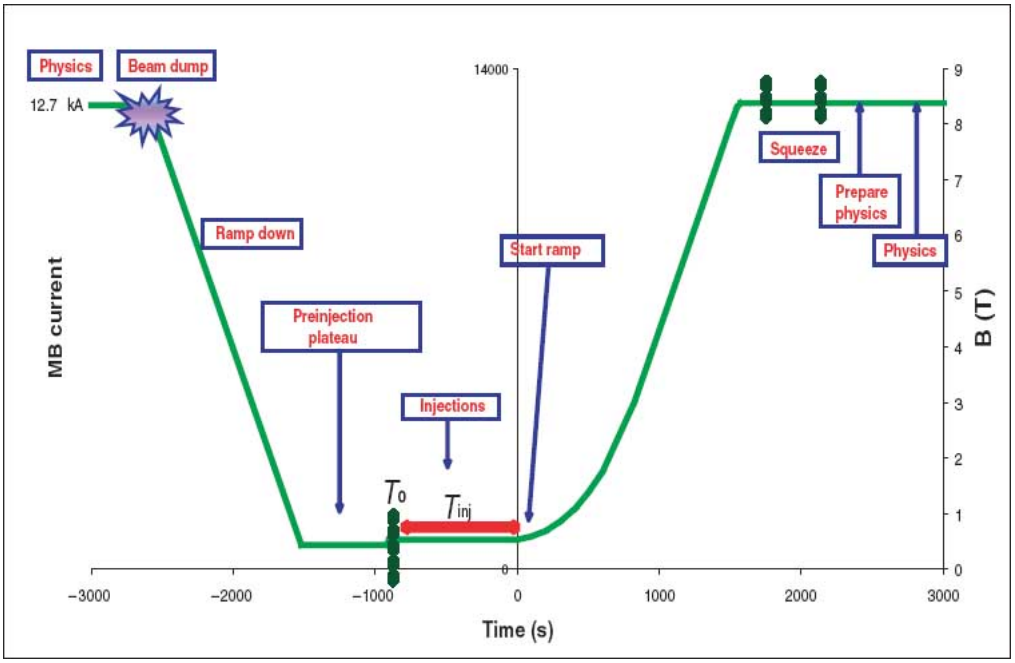

Fig. 3.20 LHC beam modes. MB current represents the current on the dipole magnet while B represents the magnetic field of the dipole magnet [102].

The DCS recieves communication from the LHC via "handshakes" and configures the detectors according to the LHC operation modes. The LHC operation modes give information on the acceleration cycle. The FSM allows individual detectors to assume different states depending on the LHC mode. During data taking all detectors participating should be well calibrated and properly conditioned to do so. The DCS also allow resetting of power supplies in case of trips during data taking.

3.5 LHC operations

The LHC operations are defined in terms of two modes, namely, the accelerator and the beam modes. The accelerator mode provides a summary of the LHC machine state while the beam modes provide a description of the accelerator cycle. The LHC follows a strict sequence of operations to enable transition to the next step. Figure 3.20, shows the LHC beam modes. A full description of the LHC modes can be found in [101, 102]. We will give a brief description of the activities at each beam mode.

SETUP
The beam is circulating in the transfer lines, about to be injected into the LHC

INJECTION PROBE BEAM
The beam is inserted into the LHC ring 1 or ring 2 to ensure a safe circulation path

before injecting higher intensities. This state is used to test all accelerator components for readiness for a physics beam. The aim of this stage is to establish a safe circulating beam with a given lifetime. Just before the start of injection, the LHC sends a handshake to inform experiments so that they can prepare by putting all detectors to a SAFE state. The SAFE state means that the detector is protected from beams that could be deemed to be potentially harmful to the detecor.

INJECTION SETUP BEAM
This beam is wholly representative of the physics beam, however with fewer particles, therefore it is used to make more precise measurements than the INJECTION PROBE BEAM and tests before filling the physics beam.

INJECTION PHYSICS
The machine had been optimised and can be able to have a circulating beam with the appropriate lifetime, therefore, it is ready to accept higher intensities needed for physics.

PREPARE RAMP and RAMP
Injection is complete, the machine prepares to ramp up the the energy.

FLAT TOP
When energy ramp is finished. Pre-squeeze checks are done. Calibration runs are performed in preparation for data taking. At this stage the ALICE CTP clock should be synchronized with the LHC clock. This ensures that the optimal energy reached can be maintained consistently for the required period of the collisions. For example, at this point the Muon tracking stations are calibrated by performing a pedestal run - noise calibrations for the FEE, which is done at a HV equal to or below 1200 V.

SQUEEZE and ADJUST
In the SQUEEZE mode, the beams are focused by minimising the beam size to maximise the luminosity. This increases the intensity of the beam. Shortly after the SQUEEZE mode, the beams are adjusted and focused in order to enable collisions, this is the ADJUST mode.

STABLE BEAMS
Stable conditions with collisions in the experiments, are declared when backgrounds and life time are under control. Small adjustment of beam parameters are permitted. Once the luminosity has been adjusted according to the requirements of the detector, data taking maybe started by the ECS operator. At this point all the detectors are brought to READY, e.g. the muon tracking chambers FEE HV equal to 1650 V.

During **STABLE BEAMS** ALICE takes data until a **BEAMDUMP** occurs. After this, the **RAMP DOWN** of magnets and cycling after a dump at the end of a Physics

fill happens. At this stage the calibration of the Muon Trigger Stations at a **READY** state (full operational HV $\approx$ 10 kV) is done.

3.5.1 Data taking conditions

The main objective of the LHC is to deliver collisions meeting the criteria presented by experiments for the physics of interest. The criteria is based on the luminosity and cross sections expected by experiments for the physics to be investigated with the collected data. In November 2016, the proton-lead collisions program was started. In this thesis we analysed data collected in two period during this program. The first period was with the proton beam going towards the muon spectrometer and the collision products were detected at what we define as positive (forward) rapidity. These collisions are referred to as p–Pb collisions. The period is referred to as LHC16r. The second one refers to when the Pb beam was going towards the Muon Spectrometer and the collision products were detected at negative (backward) rapidity. These collisions are referred to as Pb–p collisions. The period is referred to as LHC16s. The bunch spacing for the two periods were 100ns and 200 ns for proton and Pb bunches. The energies of the colliding beams were 6.5 TeV and 2.51 TeV for p and Pb per nucleon, respectively [103]. The obtained centre-of-mass energy, $\sqrt{s}_{NN}$ = 8.16 TeV, is calculated using Equation 3.7

$$\sqrt{s}_{NN} = 2\sqrt{s} \times \sqrt{\frac{Z_1 Z_2}{A_1 A_2}} \tag{3.7}$$

where, $\sqrt{s}$ is the energy of the proton beam, $A_1 = 1$ and $Z_1 = 1$ are the atomic number and the mass of the proton, respectively. $A_2 = 208$ and $Z_2 = 82$ are the atomic number and the mass of lead ion. The luminosity delivered to experiments by the LHC during these two periods is shown in Figure 3.21. The luminosity delivered to ALICE is shown in red.

As already mentioned above (See section 3.4.1 and section 3.2.4.4), different trigger classes are used to distinguish interactions and to select physics of interest for different analysis groups per experiment. The data samples analysed in this thesis were collected using the minimum bias trigger (MB, i.e. CINT7-B-NOPF-MUFAST) and the single muon triggers (CMSL7-B-NOPF-MUFAST, CMSH7-B-NOPF-MUFAST). The single muon data sample was collected by applying a trigger p_{T} cut of about 0.5 GeV/c and 4.2 GeV/c, they are referred to as muon single low (MSL) p_{T} and muon single high (MSH) p_{T} respectively. Typically, in heavy-flavour analysis, these two triggers are always considered in order to check whether it is necessary to combine CMSL and CMSH data samples to improve the statistics for precisions in the different p_{T} regions of interest. The triggers are identified

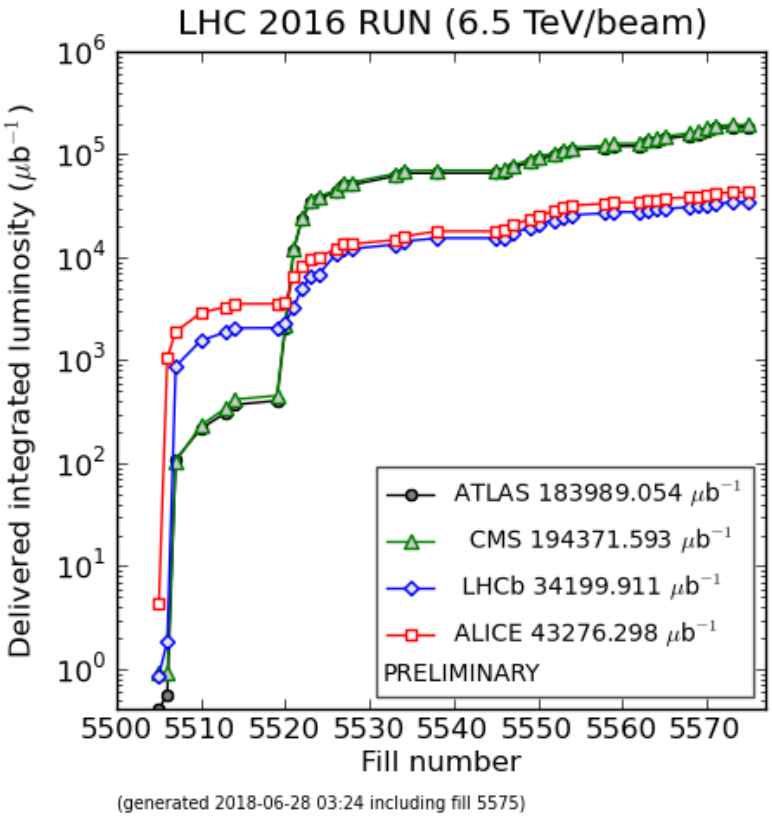

Fig. 3.21 Delivered integrated luminosity for p–Pb and Pb-p collisions at $\sqrt{s}_{NN} = 8.16$ TeV [104]

and distinguished using their names also known as a "trigger string" as well as the trigger input and the ID at hardware level. A summary of the triggers with trigger strings and appropriate inputs are shown in Table 3.3.

Triggers	p_{T} **cut (GeV/c)**	**Trigger string**	**Trigger Input (ID)**
MB	-	CINT7-B-NOPF-MUFAST	-
MSL	0.5	CMSL7-B-NOPF-MUFAST	0MSL (18)
MSH	4.2	CMSH7-B-NOPF-MUFAST	0MSH (19)

Table 3.3 Summary of triggers used in this analysis and their configuration

The statistics collected by the MB and muon triggers in p–Pb and Pb–p collisions are shown in Figure 3.22.

Since p–Pb collisions are asymmetric, the center-of-mass (CMS) frame does not coincide with the laboratory one. Hence, there is a rapidity shift effect of the CMS frame in the

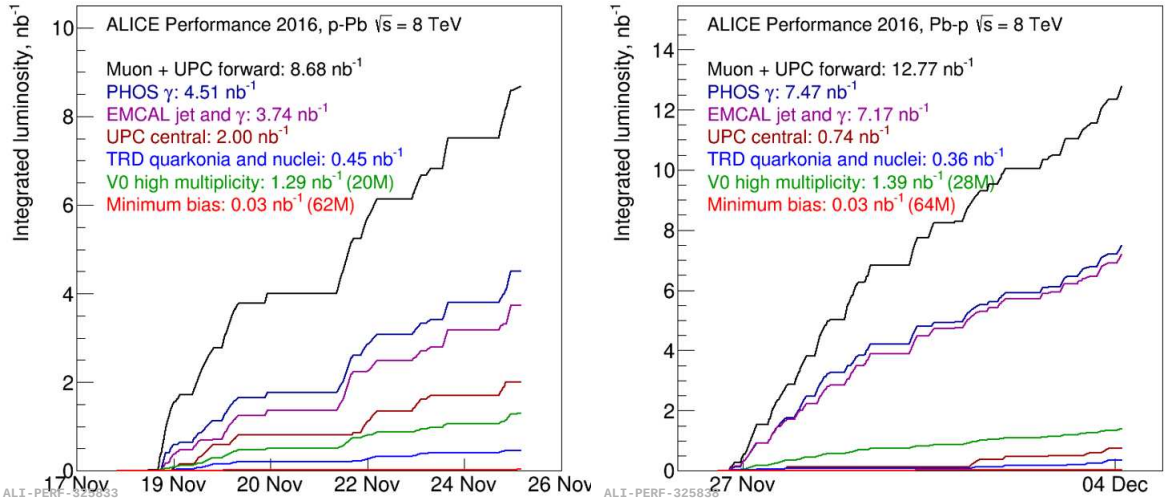

Fig. 3.22 Recorded number of events for the MB (red) and muon (black) triggers in p–Pb and Pb–p collisions (shown in blue) as a function of time [105, 106]

longitudinal direction Δy, given by,

$$\Delta y = \frac{1}{2} \ln \left(\frac{Z_p A_{Pb}}{Z_{Pb} A_p} \right) \tag{3.8}$$

$\approx$ 0.465 units in the proton direction.

Therefore, for the two beam configurations, namely p–Pb and Pb–p the corresponding measurement of muons in the positive direction which covers the forward rapidity interval is $2.03 < y_{CMS} < 3.53$ while the negative direction i.e. the backward rapidity covers the interval $-4.46 < y_{CMS} < -2.96$.

3.6 Data reconstruction and storage

As already mentioned in the above sections, the CTP and HLT select interesting physics data from the collisions. The accepted data undergoes reconstruction known as **passes**. The results from each reconstruction are stored in the Event Summary Data (ESD) files. The data usually stored in the ESD includes information from the different detectors that is later used by analysers for calibration, detector performance studies as well as analysis. Calibration and alignment data are produced during the first reconstruction and stored in the **Offline Calibration Database (OCDB)** together with the scalers and the information on the magnetic field. Quality Assurance analysis is done on the ESD data and they are filtered to produce the Analysis Object Data (AODs) files. The AODs contain information relevant for use in a specific analysis. Both ESDs and AODs

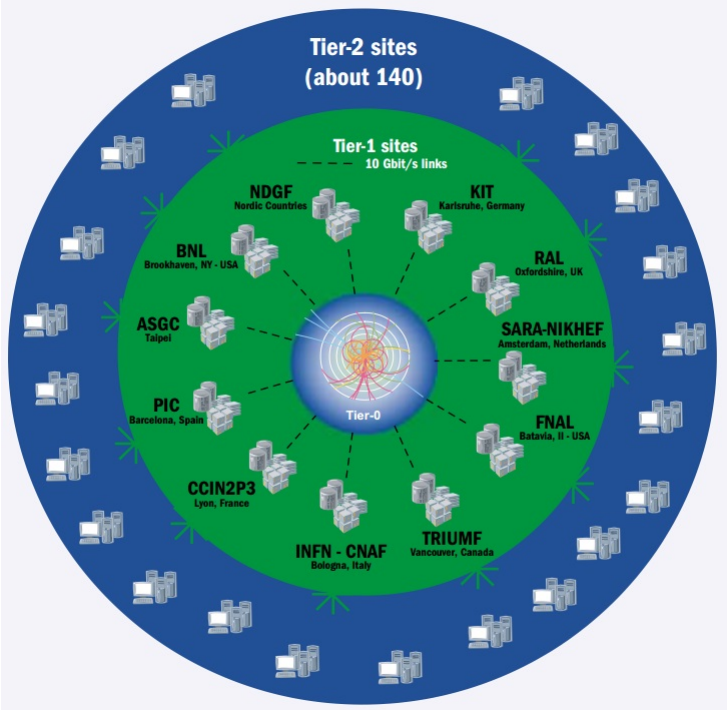

Fig. 3.23 The setup of the WLCG [107]

are stored on the ALICE Grid.

3.7 The ALICE Grid

The grid infrastructure that serves ALICE and other LHC experiments is managed by the Worldwide LHC Computing Grid (WLCG) [107], whose structure is shown in Figure 3.23. The WLCG provides resources to store, distribute and analyse the data collected by experiments, making it available to all authorised users regardless of their physical location. The computing resources are concentrated in computer centres called Tiers, where Tier-0 is the major computing centre located at CERN and it houses raw data from the experiments. This task is shared with Tier-1 sites which are located outside CERN, composed of highly safe storage mediums for a backup. These Tier-1 computing centres provide resources for processing raw data, reconstruction and data analysis during data taking. Tier-2 computing centres, also located outside CERN, e.g. Centre of High Performance Computing (CHPC), located in Cape Town, provide end user operations such as Monte Carlo simulation, data analysis and stores copies of the ESDs and AODs for data analysis. The ALICE data analysis software is also archived on the grid.

Access to the WLCG resources is through authorisation by Virtual Organisations (VO) of the LHC experiments who issues annual grid certificates. For ALICE the access is granted

via AliEN - the ALICE Environment. Users make job requests from one of the many entry points into the system. A job request can be storage, processing capacity, or download of analysis software. The ALICE grid is monitored by the Monitoring Agents using a Large Integrated Services Architecture (MonALISA) who publishes the progress of analysis and simulation tasks and their statuses. The Application Programming Interface is used to provide the interface between AliEN and ROOT based framework. A unique ALICE offline framework, the so-called AliROOT framework is used by end users for analysis of experimental and simulated data as well as simulation and data reconstruction.

3.8 The AliROOT framework

The AliROOT framework, shown in Figure 3.24, is a set of tools used by the ALICE Collaboration to process data. The framework is based on an Object Oriented programming language, C++. It uses the ROOT framework developed by CERN. The AliROOT framework [108, 109]:

1. Provides simulation of hadronic collisions and the ALICE detector response.
   The hadronic collisions are simulated using PYTHIA, HIJING, and PHOJET generators. The generators are interfaced to AliROOT. GEANT4 and FLUKA are available for users to choose as particle transport packages to simulate the detector responses.

2. Reconstructs the raw physics data from simulated and real events
   If a particle produces a hit[4] on the detector elements, objects are created that consist of the sum of the energy deposited by all the hits so that there is one digit. The energy on the digit is converted into a digital signal via an Analogue to Digital Converter (ADC). The digits are then used as input to the reconstruction chain. A local reconstruction of clusters is performed in each detector. Vertexes and tracks are reconstructed and particles types are identified. This step produces ESD. AODs are produced from various stages and filtering criteria of the reconstruction.

The data analysis using the AliROOT framework on the ALICE grid will be presented in Chapter 4.

[4]Energy deposited by a particle on interaction with a detector element

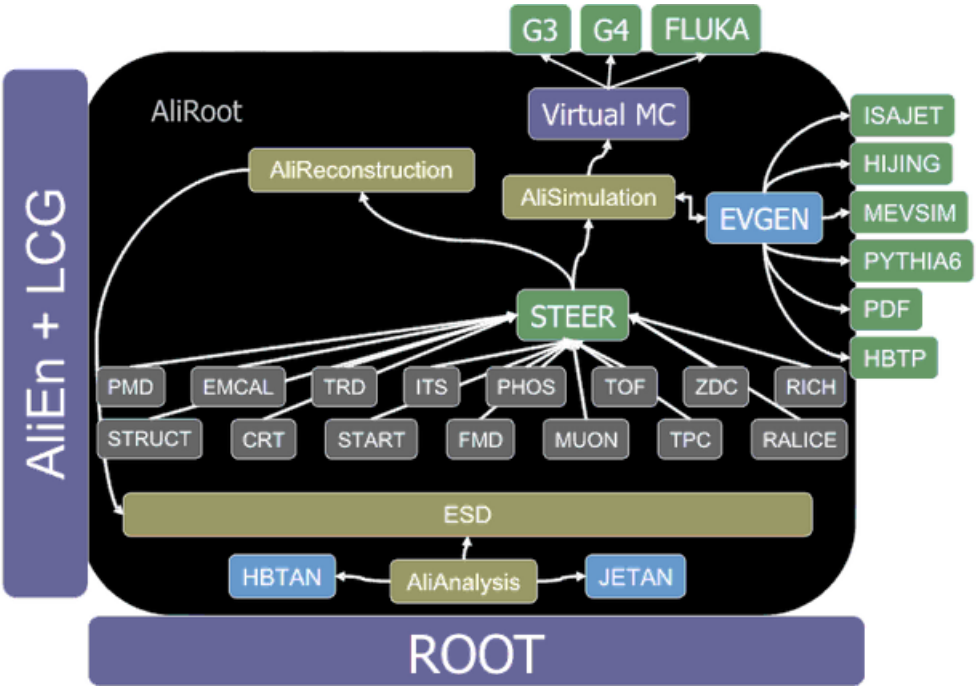

Fig. 3.24 The AliROOT framework [110].

CHAPTER 4

Analysis strategy

The chapter discusses the work done by the author on the measurement of heavy-flavour decay muon production as a function of charged-particle multiplicity in p–Pb collisions at $\sqrt{s_{\rm NN}} = 8.16$ TeV.

4.1 Brief overview

The heavy-flavour production is studied via the single muon decay channel,

$$c, b \rightarrow \mu + X \tag{4.1}$$

with a braching ratio (B.R) of 10.33 ± 0.2 % and 10.86 ± 0.2 % for the decay of charm and beauty, respectively[111]. The muons are reconstructed in the ALICE forward muon spectrometer. The aim is to study the self-normalised heavy-flavour decay muon yield, also known as the relative yield of heavy-flavour decay muons, as a function of self-normalised charged-particle multiplicity. The self-normalised charged-particle multiplicity, also known as the relative multiplicity, is defined as

$$\frac{dN_{ch}/d\eta_i}{\langle dN_{ch}/d\eta \rangle} = \frac{\langle N^{corr}_{trkl} \rangle_i . \alpha_i}{\Delta\eta . \langle dN_{ch}/d\eta \rangle} \tag{4.2}$$

where,

- ✓ $dN_{ch}/d\eta_i$ is the charged particle pseudorapidity density in multiplicity bin i
- ✓ $\langle dN_{ch}/d\eta \rangle$ is the mean

  charged-particle density
- ✓ α_i is the proportionality factor which is obtained from Monte Carlo (MC)
- ✓ $\langle N_{trkl}^{corr} \rangle_i$ is the mean number of tracklets in multiplicity bin i

This chapter discusses the analysis strategy in this order;

1. The first part will focus on the data sample and event selection.
2. The second part will be a discussion of the multiplicity measurement, i.e. the steps leading to obtaining the relative charged particle multiplicity. Here, an overview of the first method of multiplicity determination called the **data driven method** is given. This method was used in this study before the ALICE Collaboration introduced a new strategy, the so-called **Official framework**.
3. The third part will focus on the multiplicity measurement using the **Official framework**.
4. The last part will focus on the extraction of heavy-flavour decay muon yields in the defined multiplicity bins as well as a discussion of all other ingredients needed to obtain the yields of heavy-flavour decay muons.

4.2 Data samples, event and track selection

The following section is dedicated to the data samples and event selection criteria used to choose the runs and events used in this study.

4.2.1 Data samples

Only runs passing the ALICE Quality Assurance checks, shown in Table 4.1, are selected for physics analysis.

The total number of runs for the two periods (LHC16r and LHC16s) considered in this analysis is shown in Table 4.2. The list of the runs considered is shown in Appendix A.1.

Period	LHC16r and LHC 16s
Run type	Physics
Beam mode	Stable
Trigger detectors	At least Muon Trigger
Readout detectors	At least Muon Tracking, Muon Trigger and SPD
Run quality	Not bad for readout detectors
Run duration	$\geq$ 10 minutes

Table 4.1 Quality Assurance (QA) criteria for runs selected for physics analysis [112].

Period	Number of runs
LHC16r	57
LHC16s	75

Table 4.2 Summary of the number of runs per period.

4.2.2 Event selection

The event selection is applied to remove background events after the online event selection at hardware level. The following selection cuts are applied;

1. **Physics selection**
   The physics selection rejects background events contributed by beam-gas interactions. The physics selection is implemented by cutting on the time information from V0A and V0C as follows;

$$4 < (t_{V0A} + t_{V0C}) < 12 \text{ ns}$$
$$10 < (t_{V0A} - t_{V0C}) < 18 \text{ ns}$$

   Figure 4.1 shows a schematic representation of the implementation of V0 cuts. Furthermore, background events are identified via a correlation between the number of

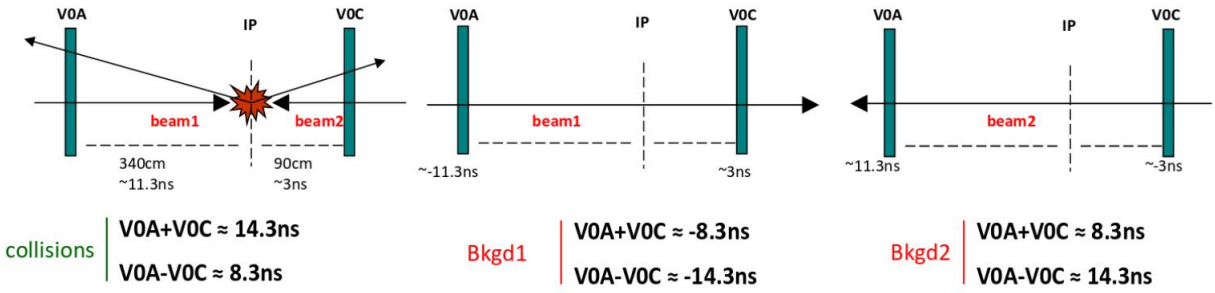

Fig. 4.1 Schematic of the V0 time cut used to reject beam-gas interactions [113].

tracklets (N_{trkl}) and the number of SPD clusters (N_{cl}), as shown in Figure 4.2 and Figure 4.3.

2. **Good vertex selection**
   Only events originating from the primary vertex and inside the SPD ($|z_v^{SPD}| < 10$) are considered for analysis, since at this geometrical region the efficiency of the detector is well defined for vertex determination. In addition to the geometrical region, it is required that all events should contain at least one charged particle. The number of vertex contributors is defined as the number of SPD tracklets that are used in the determination of the vertex position. It is known that the value of the contributors is negative when the vertex reconstruction fails: "-2" indicating the absence of reconstructed points in SPD and "-1" indicating that it is not possible to build suitable tracklets [114]. Events with at least 1 contributor are selected for this analysis. Furthermore, the resolution of the SPD should be better than 0.25 cm and the "vertexer tracks" as well as the "vertexter : Z" labels are used to tag events with more than one reconstructed tracklet. Applying these cuts further improves the measurement by rejecting events with zero contributors.

3. **Trigger selection**
   Data samples considered in this analysis consist of minimum bias (MB), single muon high p_T (CMSH) and single muon low p_T (CMSL) triggered events. The triggers have been discussed in Chapter 3.

Table 4.3, shows the effects of the good vertex cuts on number of events. The cut on the SPD vertex removes $\approx 7\%$ of the selected events. This is because the events are not distributed symetrically around the norminal IP due to the fact that the primary vertex does not always coincide with the nominal IP [115]. The vertex distributions for p–Pb (LHC16r) and Pb–p (LHC16s) collisions are shown in Figure 4.4. It can be seen that the distributions are slightly shifted to the right, i.e. the maximum point of each distribution is not at the nominal IP.

4.3 Multiplicity measurement : Data driven method

Charged-particle multiplicity is defined as the number of charged particles produced per event. It is estimated using the mean number of tracklets in the SPD. The number of tracklets is proportional to the number of charged particles produced. During the data taking, the SPD acceptance varies due to dead regions in the detector. The dead channels will affect the tracklet information in the given part of the SPD. Therefore, to accurately

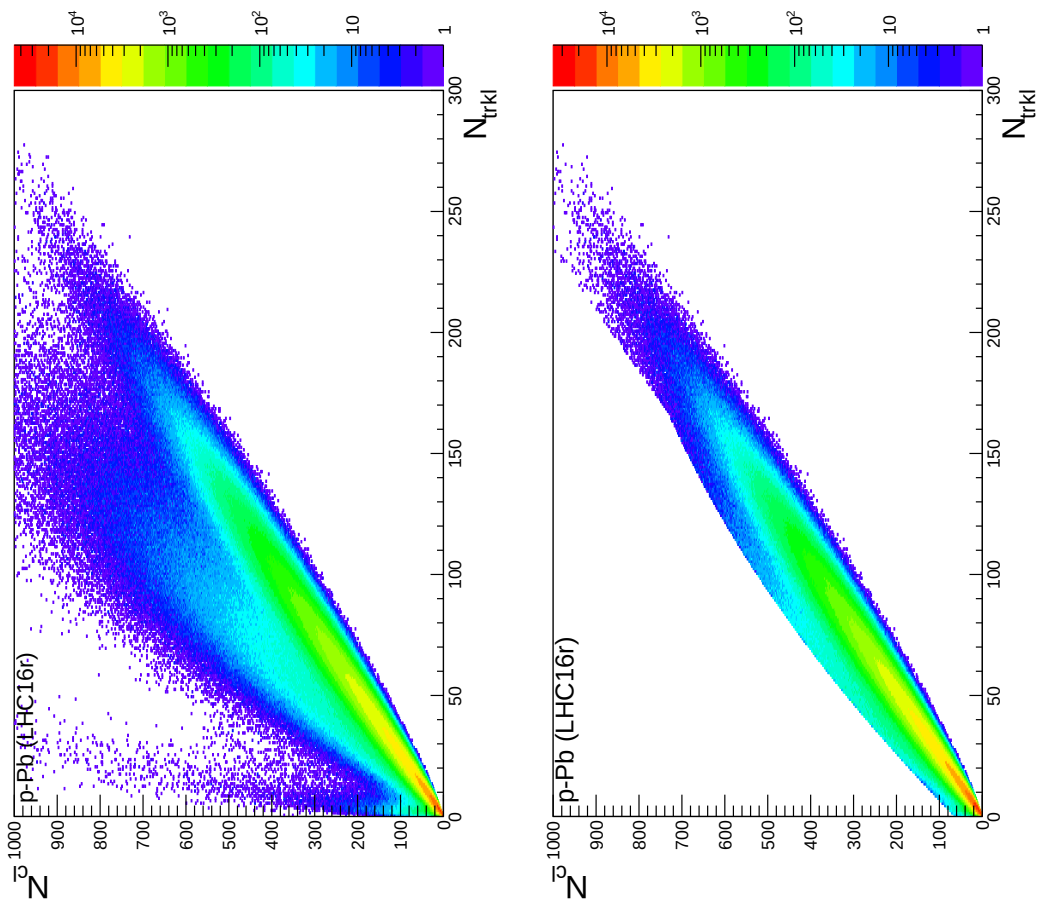

Fig. 4.2 Correlation of the number of SPD clusters (N_{cl}) vs the number of tracklets (N_{trkl}). The top and bottom plots show the correlation before and after the tracklet vs cluster cut for LHC16r (p–Pb collisions).

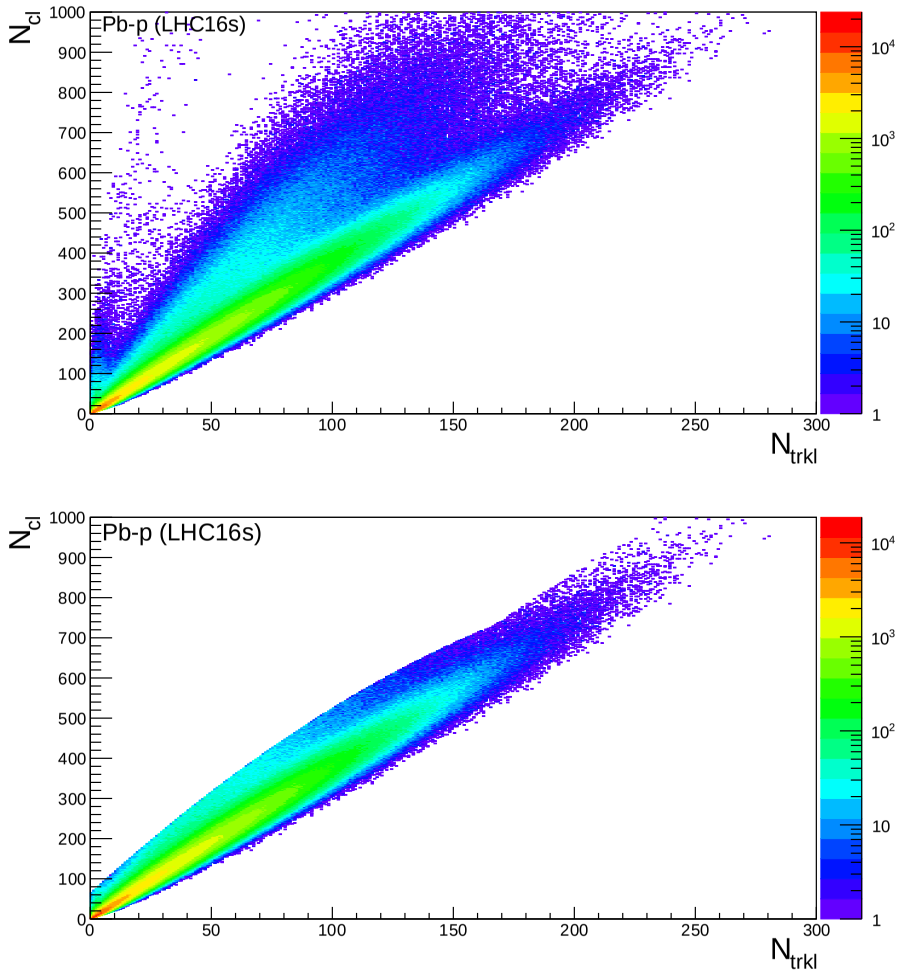

Fig. 4.3 Correlation of the number of SPD clusters (N_{cl}) vs the number of tracklets (N_{trkl}). The top and bottom plots show the correlation before and after the tracklet vs cluster cut for LHC16s (Pb–p collisions).

p-Pb (LHC16r)	MB		CMSL (CMSH7)	
	Events passed	**Events passed (%)**	**Events passed**	**Events passed (%)**
Physics Selection	6 592 311	90.1	23 587 812 (19 573 896)	89.7 (89.7)
Reconstructed Vertex	6 592 311	90.1	23 587 812 (19 573 896)	89.7 (89.7)
$N_{contributors} > 0$	6 541 040	89.4	23 561 515 (19 573 896)	88.6 (88.7)
$\sigma_v^{SPD} < 0.25$ cm	6 519 091	89.1	23 561 515 (19 573 896)	88.6 (88.7)
$\mid z_v^{SPD} \mid < 10$ cm	6 064 926	82.9	21 352 623 (17 980 925)	81.2 (82.4)
Pb-p (LHC16s)	**MB**		**CMSL (CMSH7)**	
	Events passed	**Events passed (%)**	**Events passed**	**Events passed (%)**
Physics Selection	3 119 696	89.7	34 632 816 (29 778 866)	89.9 (89.8)
Reconstructed Vertex	3 119 696	89.7	34 555 768 (29 778 866)	89.7 (89.8)
$N_{contributors} > 0$	3 081 439	88.6	34 555 768 (29 778 866)	89.7 (89.8)
$\sigma_v^{SPD} < 0.25$ cm	3 071 006	88.3	34 517 245 (29 778 866)	89.6 (89.8)
$\mid z_v^{SPD} \mid < 10$ cm	2 831 029	81.4	31 242 729 (27 623 386)	81.1 (83.3)

Table 4.3 Number of events after applying good vertex selection cuts for p–Pb and Pb-p collisions.

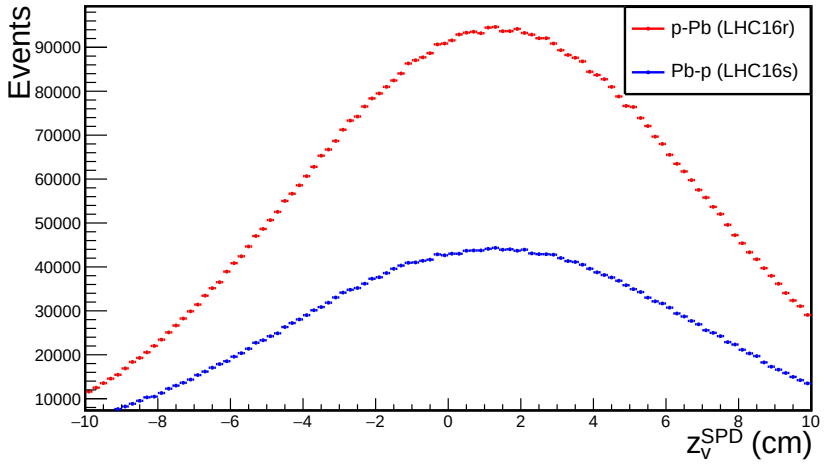

Fig. 4.4 The z vertex co-ordinate of the SPD vertex in p–Pb and Pb–p collisions. The maximum of the distributions in both cases is shifted towards the right with respect to the norminal interaction point.

evaluate the multiplicity of the event, one needs to correct for the missing acceptance thus taking into account the SPD efficiency. Only then is it possible to convert the number of tracklets N_{trkl} into the corresponding number of charged particles (N_{ch}). The number of active SPD channels during data taking is studied as a function of the run. Figure 4.5 shows the variation of the active SPD modules with the run number.

As can be seen in Fig 4.5, the number of modules in the inner and outer layers of the SPD varies with the run as well as the period of data taking. This is taken into account when correcting the measured number of SPD tracklets. The number of measured tracklets i.e. raw number of tracklets (N_{trkl}^{raw}) is shown in Fig 4.6.

The number of raw tracklets N_{trkl}^{raw} is plotted as a function of the z_v^{SPD}. The physical properties of an event are expected to be the same regardless of where the event took place on the z_v^{SPD}, hence the 2-Dimensional plot of the N_{trkl}^{raw} as a function of the z_v^{SPD} is expected to be homogenous, however, this is not the case as can be seen in Figure 4.7.

To further elaborate on this point, the mean number of raw tracklets $\langle N_{trkl}^{raw} \rangle$ is plotted as a function of the z_v^{SPD} to obtain tracklet profiles. In this case, it is expected to obtain a flat tracklet profile, i.e. the $\langle N_{trkl}^{raw} \rangle$ is the same in all z_v^{SPD} positions. If this is true it means that the efficiency of the SPD is homogenous. However, due to the presence of dead SPD channels, a z_v^{SPD} dependence of the mean number of reconstructed tracklets is observed, as shown in Fig 4.8. If the efficiency of the SPD was uniform the result would have been a flat distribution along the z_v^{SPD}.

The method used to correct for the z_v^{SPD} dependence by equalizing the $\langle N_{trkl}^{raw} \rangle$ distribution

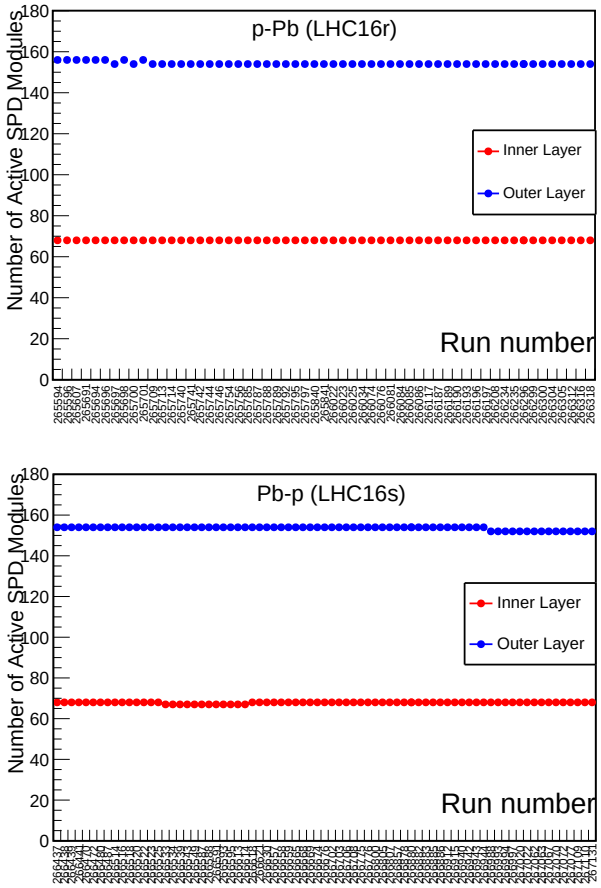

Fig. 4.5 SPD active modules as a function of the run number for p-Pb (top) and Pb-p (bottom) collisions.

along the z_v^{SPD} will be described in the following sections. The so-called "data-driven" correction has been widely used by the ALICE Collaboration in multiplicity studies. More details about the method may be found [116, 117, 118].

4.3.1 Data driven correction method

The aim of the data-driven correction method is to equalise the $\langle N_{trkl} \rangle$ along the z-vertex direction hence equalising the SPD efficiency. Event multiplicities are therefore corrected by the efficiency loss of the detector with respect to a reference region in an event by event basis. The method assumes that the number of missing or excessive tracklets follows a Poissonian distribution. Therefore, we compute the number of missing or excessive tracklets ΔN per event, with respect to a chosen reference $\langle N_{ref} \rangle$ as follows;

$$\Delta N = N_{trkl}^{raw} \frac{\langle N_{ref} \rangle - \langle N_{trkl}^{raw}(z) \rangle}{\langle N_{trkl}^{raw}(z) \rangle} \tag{4.3}$$

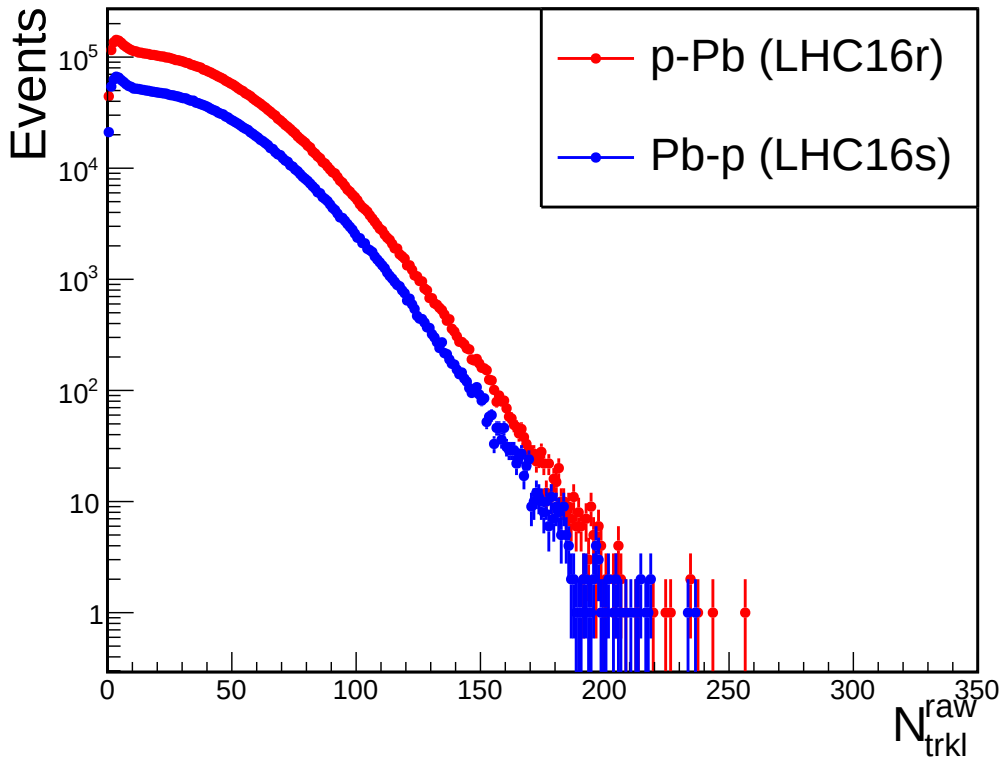

Fig. 4.6 Raw tracklet distribution for p-Pb (red) and Pb-p (blue) collisions.

- N^{raw}_{trkl} is the raw number of tracklets
- $\langle \mathrm{N}_{\mathrm{ref}} \rangle$ is the mean number of tracklets at reference position
- $\langle N^{raw}_{trkl}(\mathrm{z}) \rangle$ is the mean number of tracklets at a specific vertex position

To obtain the corrected number of tracklets $N^{corr}_{trkl}(\mathrm{z})$ we randomise $N^{raw}_{trkl}(\mathrm{z})$ by Poisson smearing the excess ΔN as follows

$$N^{corr}_{trkl} = N^{raw}_{trkl} + gRandom \rightarrow Poisson(\Delta N) \tag{4.4}$$

N^{corr}_{trkl} is not the true multiplicity since the SPD efficiency at the reference value is not 100%. The efficiency correction will be discussed in Section 4.3.3.

As already noted, the data-driven method requires a reference value of mean number of tracklets $\langle \mathrm{N}_{\mathrm{ref}} \rangle$ within a selected z-vertex position and η. $\langle \mathrm{N}_{\mathrm{ref}} \rangle$ can be the maximum or minimum value obtained from the raw tracklet profiles in Figure 4.8.

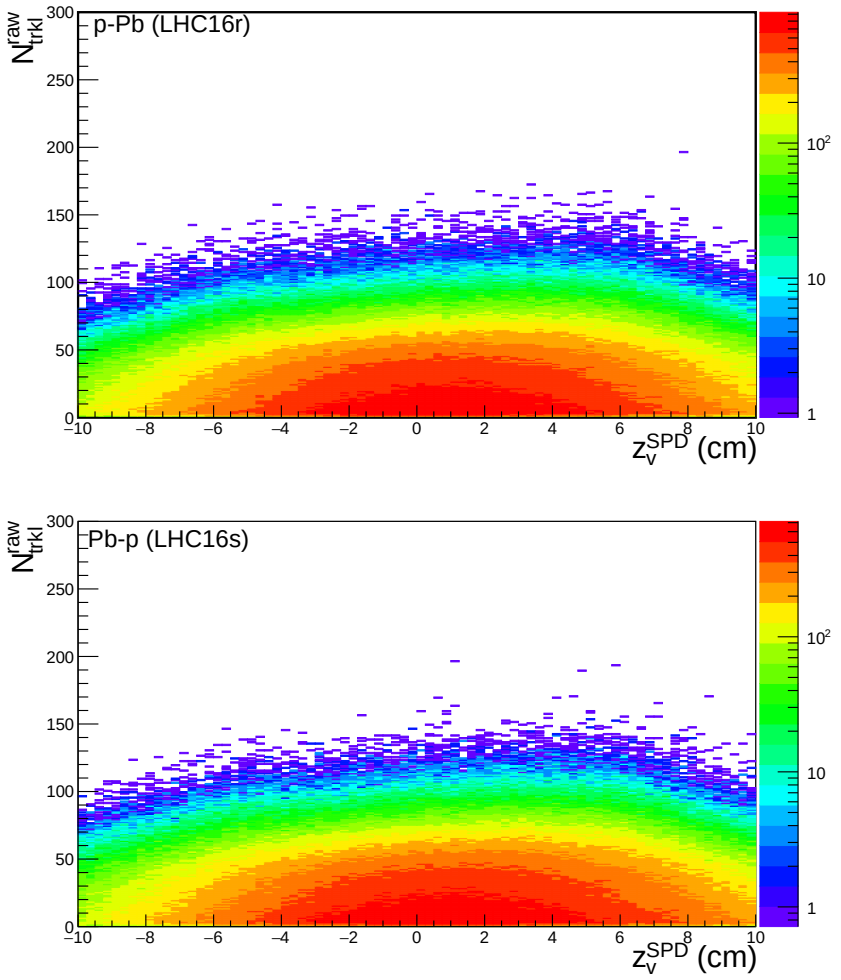

Fig. 4.7 Raw number of tracklets as a function of the SPD vertex for p-Pb (top) and Pb-p (bottom) collisions.

	min	**max**
pPb (LHC16r)	23.61	34.52
Pbp (LHC16s)	23.19	34.76

Table 4.4 Maximum and minimum $\langle N_{trkl}^{raw} \rangle$ for p–Pb and Pb–p collisions.

4.3.2 Choice of reference value

In previous multiplicity studies [116], three possible cases were considered for $\langle N_{\mathbf{ref}} \rangle$ used for the correction, namely, the minimum, mean and maximum of the $\langle N_{trkl}^{raw} \rangle$ as a function of z_v^{SPD} distribution. The following factors were considered in order to choose the most appropriate reference;

1. the resolution of the correlation of N_{trkl}^{raw} with N_{trkl}^{corr}

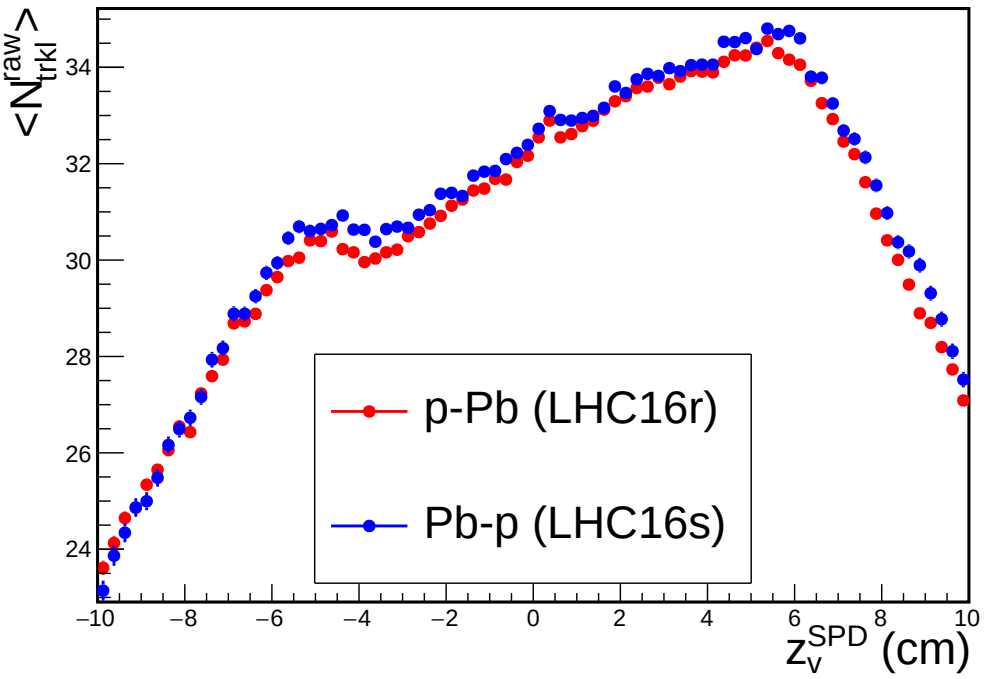

Fig. 4.8 Average raw number of tracklets as a function of the SPD vertex for p-Pb (red) and Pb-p (blue) collisions.

2. the effects the correction has on low multiplicity

3. optimisation of the multiplicity slicing and extraction of the heavy-flavour decay muon signal in all bins while high enough multiplicities

It was found in previous studies [116] that correcting with respect to the minimum of the $\langle N_{trkl}^{raw} \rangle$ results in the best resolution of the N_{ch} compared to the other cases. Despite the fact that the resolution is good, correcting low multiplicity events with respect to the minimum may result in the creation of corrected events with negative multiplicity since $\Delta N < 0$. Correcting the distribution with the maximum value widens the N_{trkl}^{corr} distribution though compromising the resolution. It was agreed to use the maximum as a reference so as to get a wider multiplicity distribution and make the multiplicity slicing easier. It has been shown in [116] that the choice of the reference does not affect the effectiveness of the method. Table 4.4 shows the maximum and minimum values of the $\langle N_{trkl}^{raw} \rangle$ obtained from Figure 4.8 for the two data sets. The corrected (N_{trkl}^{corr}) distributions are shown (in red) together with the raw distribution (in blue) on Figure 4.9. It can be seen that the effect of the correction is a wider distribution as already mentioned above. Figure 4.10 shows the corrected tracklet profiles ($\langle N_{trkl}^{corr} \rangle$) as function of the z_v^{SPD}. The distributions have a flat trend around the chosen $N_{\mathbf{ref}}$ value.

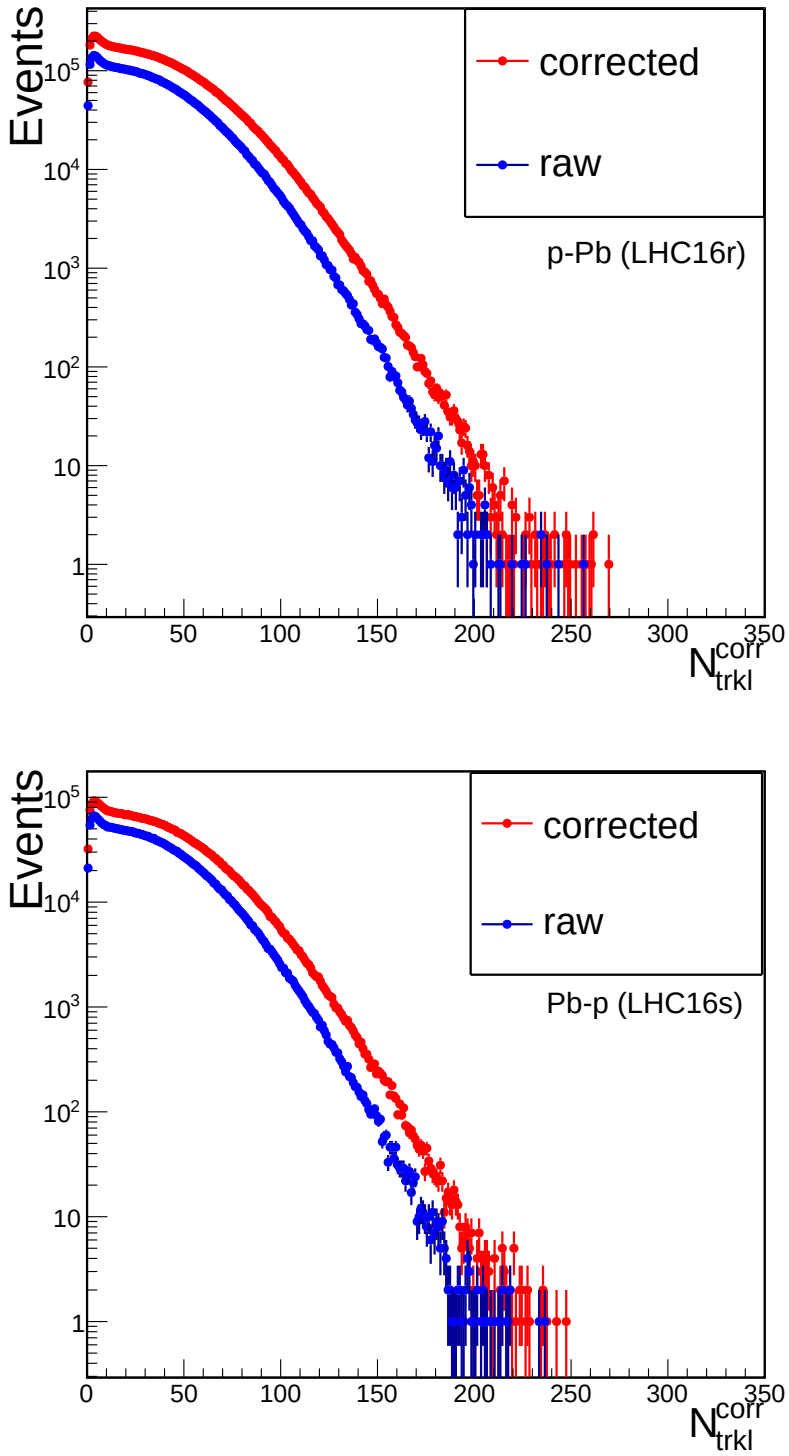

Fig. 4.9 Corrected N_{trkl} distributions for p-Pb and Pb-p collisions are shown in red while the raw distributions are shown in blue.

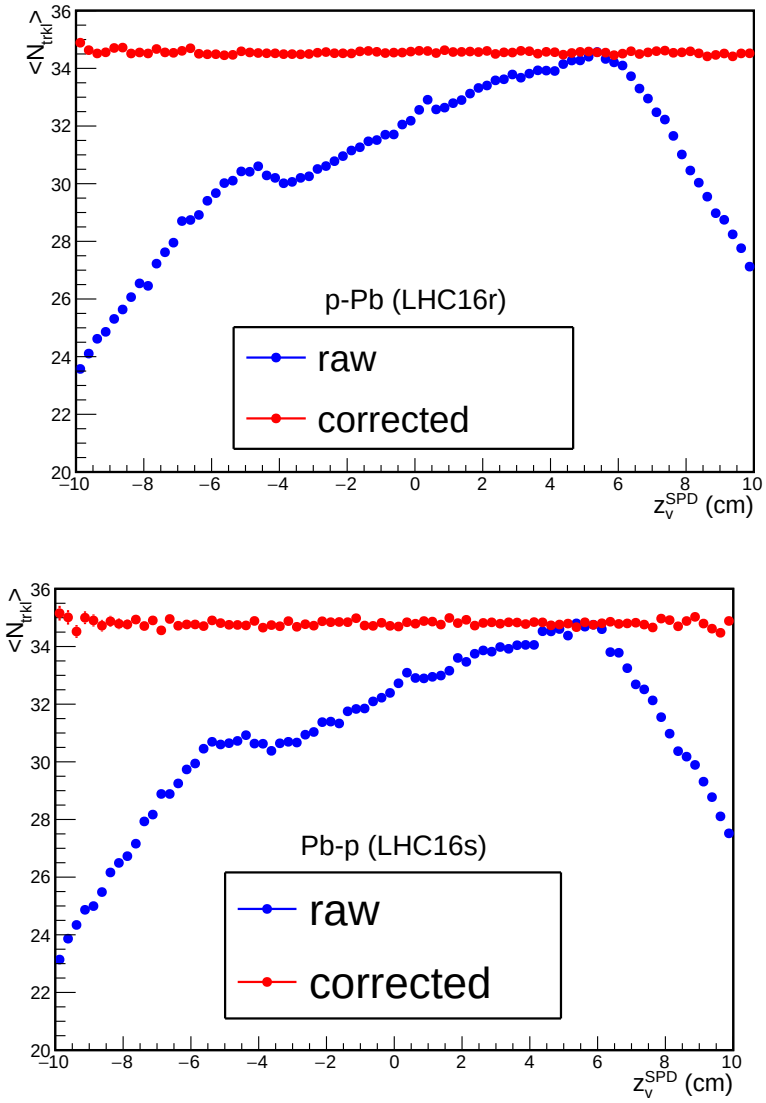

Fig. 4.10 $\langle N_{trkl}^{corr} \rangle$ distributions for p-Pb and Pb-p collisions.

4.3.3 Multiplicity efficiency correction

As a reminder, the number of tracklets measured in the SPD is approximated to be proportional to the actual number of charged particle.

$$N_{ch} = \alpha N_{trkl} \tag{4.5}$$

Therefore, the α factor represents the efficiency of the SPD. To determine this efficiency we use Monte Carlo (MC) simulations. The MC simulations generate events and count the number of charged-particles produced N_{trkl}^{gen} thus considering an ideal detector where the efficiency is 100%, then pass the same events into the SPD (realistic simulation) and count

the number of charged particles as seen by the SPD. The realistic simulations take into account the conditions of the SPD during the data taking period under considerations.

The two sets of MC productions used for the efficiency evaluation in this study are based on EPOS [73, 74] and DPMJET [119] generators. Both productions were available on the ALICE Grid [120]. The details of the 4 sets of MC productions are shown in Table 4.5.

	EPOS Number of events (runs)	**DPMJET Number of events (runs)**
pPb (LHC16r)	4 388 067 (57)	4 673 716 (75)
Pbp (LHC16s)	4 388 067 (57)	5 610 381 (75)

Table 4.5 Number of events and runs for the DPMJET and EPOS MC productions.

4.3.4 Comparison of MC productions and data

Firstly, the MC is compared to data distributions to check for compatibility before using them to estimate the efficiency of the SPD. To do this, the MC production is analysed using the same procedure used in data and extract the raw tracklets (N_{trkl}^{raw}) distributions.The raw tracklet distributions in this case are the reconstructed tracklets obtained from a realistic simulation by taking into account the conditions of the SPD. Figure 4.11 shows the N_{trkl}^{raw} distribution from data (black) plotted with the distributions obtained from the MC productions in DPMJET and EPOS (in red).

In both periods, neither of the generators describes the data precisely. At high multiplicity there are significant difference between the data and the MC. The MC distributions do not reach as high N_{trkl}^{raw} as the data and they also show a steeper decrease than the data. DPMJET distributions show a similar trend with the data at low multiplicity while the EPOS distributions do not reproduce data as well as DPMJET. Therefore, DPMJET distributions describe data better than the EPOS ones. For these reasons, the DPMJET productions are used instead of the EPOS.

The differences between data and MC distributions were corrected using the procedure described in [118] by applying a set of weights run-by-run. The following is a brief descritption of each of the applied weights.

1. **Run weight (W_{run})**
   A run-by-run weight was applied to correct for the different number of events between data and MC. This weight is defined as a ratio of events from data to the MC per run.

2. **Z-vertex weight ($W_{Zvertex}$)**
   A z-vertex weight was applied to correct for the difference and the systematic shift

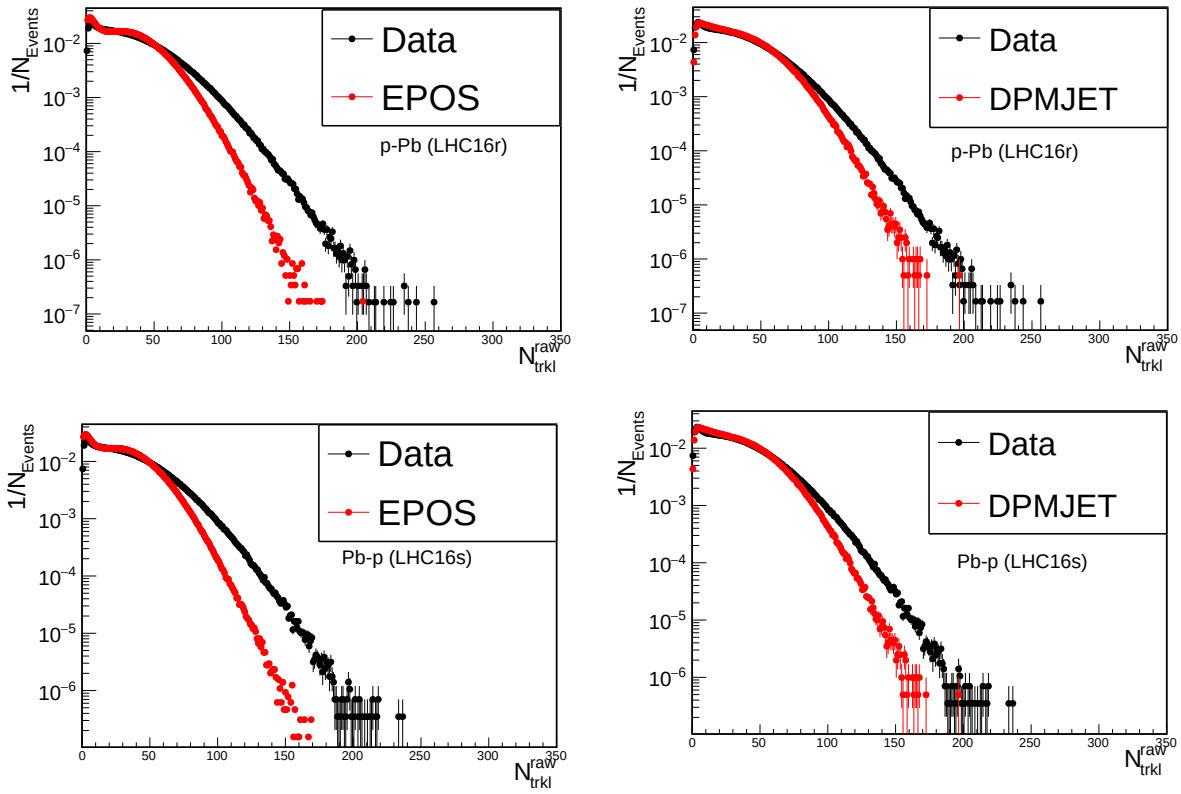

Fig. 4.11 Raw tracklet distributions from MC productions, DPMJET and EPOS compared to data for p–Pb (top) and Pb-p collisions (bottom).

in z_v^{SPD}. The weight is defined as a polynomial fit to the ratio of the distribution in data/MC.

3. **N_{trkl}^{raw} weight (W_{Nraw})**
   A N_{trkl}^{raw} weight, to correct for the different shape of N_{trkl}^{raw} , and by extension N_{trkl}^{corr} distribution. The weight was defined as the ratio of data/MC distributions.

The product of the three weights (shown in Equation 4.6) was applied to the raw tracklet distributions, to correct the differences between MC and data. Figure 4.12 shows the effects of the weights on raw tracklets distributions from DPMJET for p-Pb and Pb-p productions.

$$W_{run} \times W_{Nraw} \times W_{Zvertex} \tag{4.6}$$

The ratio of the "weighted" distributions to the "no weights" distributions is also shown in Figure 4.13. It can be seen that the effect of each weights is more pronounced towards high multiplicity. The distributions are widened thus increasing their multiplicity reach.

A comparison of the weighted raw tracklet distributions with data is shown in Figure

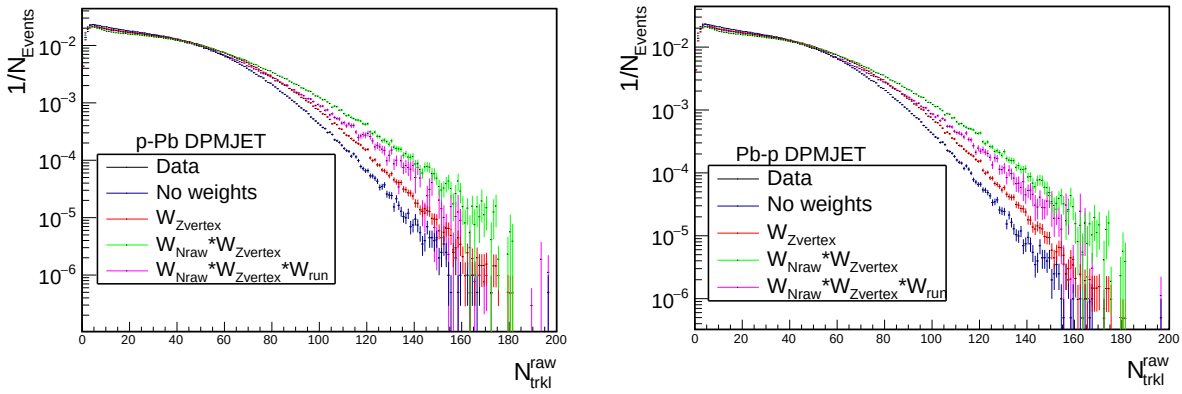

Fig. 4.12 Effect of the applied weights on the tracklets distributions for DPMJET p-Pb and Pb-p MC productions.

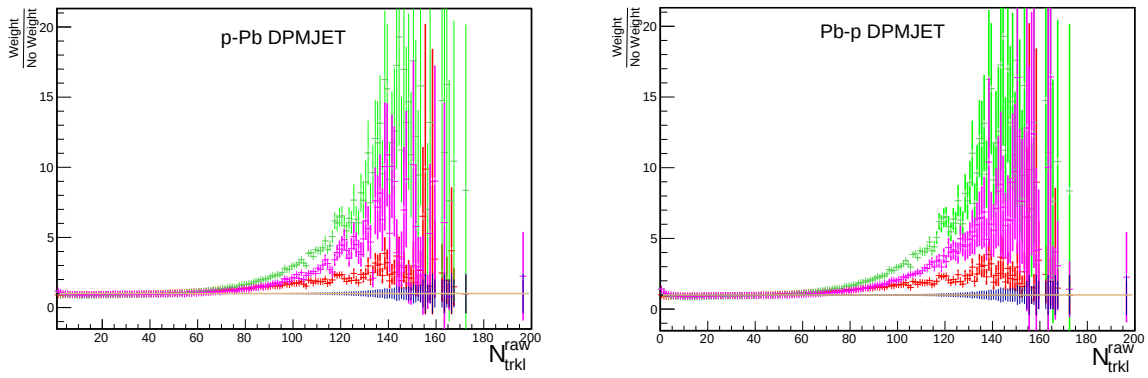

Fig. 4.13 Ratio of the weighted distributions to the ones without the weights.

4.14.

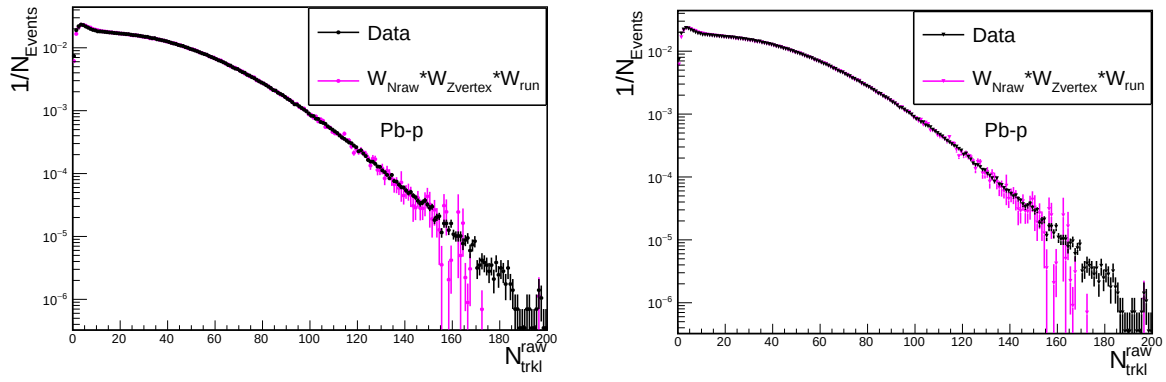

Fig. 4.14 Data plotted with weighted DPMJET distributions.

Furthermore, the tracklet profiles, $\langle \mathrm{N}_{\mathrm{trkl}}^{raw} \rangle$ and $\langle \mathrm{N}_{\mathrm{trkl}}^{corr} \rangle$ obtained from the MC production were plotted and compared to data. This was done in order to confirm that the MC distributions describe the data well as this would affect the efficiency correction. The

corrected tracklets profiles are obtained using the same procedure discussed in Section 4.3.1. Figure 4.15 shows the tracklet profiles.

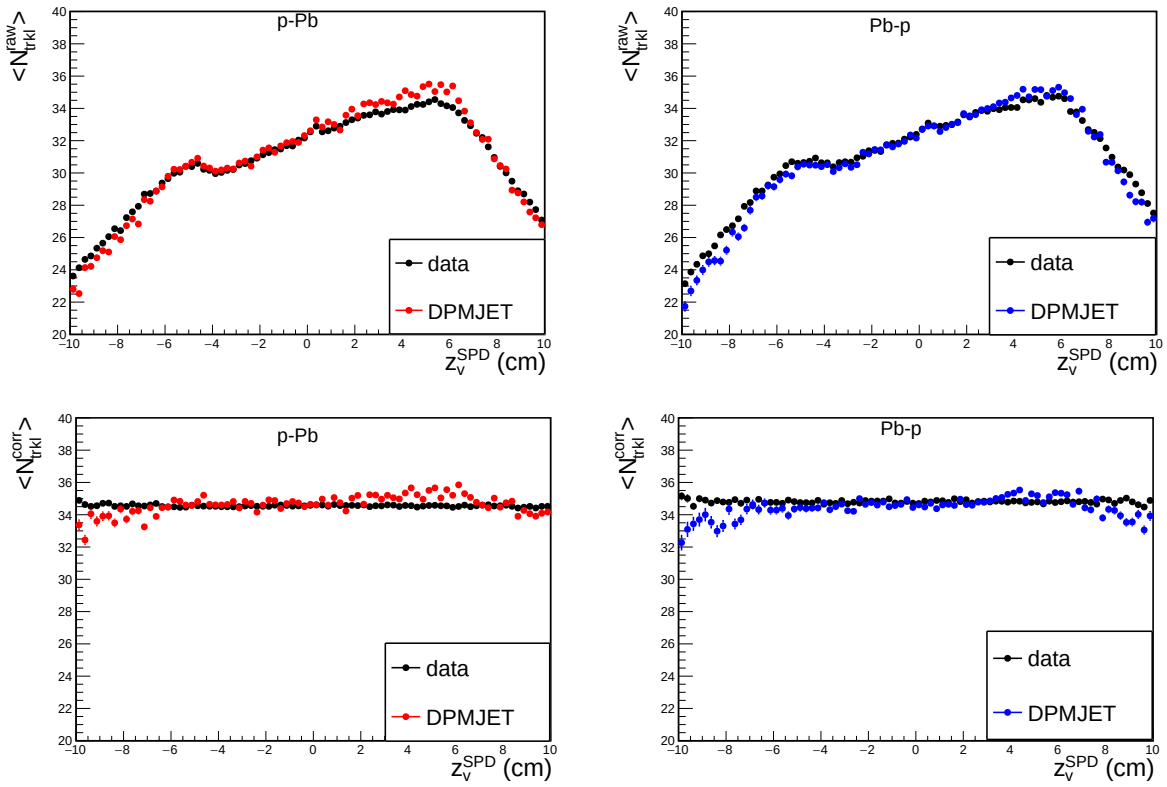

Fig. 4.15 Comparison of raw and and corrected tracklet profiles from DPMJET to data.

As can be seen from Figure 4.15, there is a better agreement between data and DPMJET hence is it safe to use the obtained tracklet distributions to evaluate the efficiency correction α factor.

4.3.5 Evaluation of the efficiency correction factor α

In the absence of detector effects, the number of corrected tracklets (N_{trkl}^{corr}) is expected to be the same as the number of generated charged particles (N_{trkl}^{gen}). Since the number of tracklets corresponds to the number of charged particles, then N_{ch}–N_{trkl}^{corr} correlation should be perfectly linear. Therefore, to evaluate the α correction factor, the correlation of N_{gen}–N_{trkl}^{corr} is plotted. Figure 4.16, shows the N_{gen}–N_{trkl}^{corr} correlation.

The distributions were fitted with a linear function. Two methods were used to obtain the α factor, namely;

- The α factor were evaluated from the linear fit of the entire distribution. This was

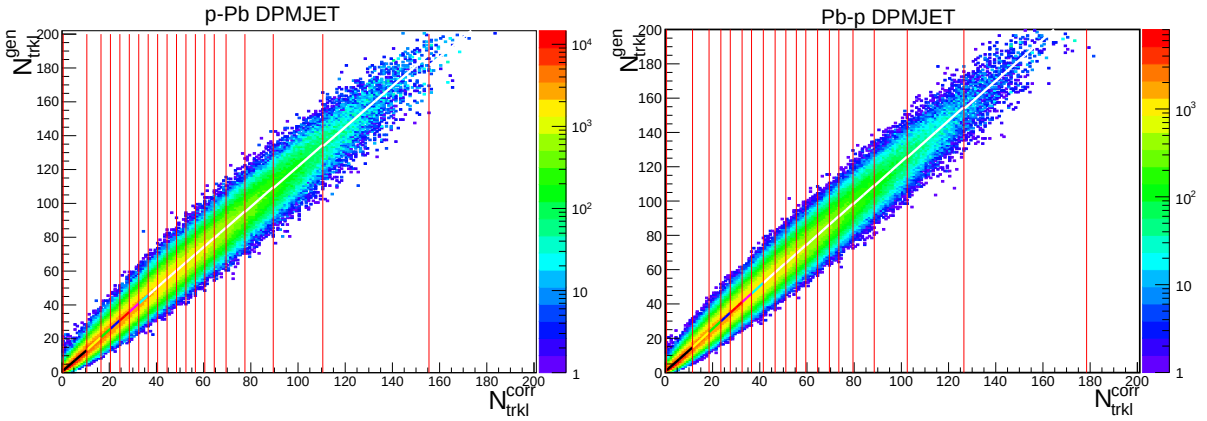

Fig. 4.16 Generated charged particle multipicity as a function of the corrected charged particle multiplicity. The line with different colours represent a linear fit used to extract the α values in different multiplicity bins. Note that a similar function is used to extract α_{global} factors.

termed, global alpha (α_{global}), computed as;

$$\alpha_{global} = \frac{\langle N_{ch} \rangle}{\langle N_{corr} \rangle} \tag{4.7}$$

where $\langle$ $N_{ch}\rangle$ is the mean number of generated charged particles and is the mean number of corrected tracklets $\langle$ $N_{corr}\rangle$ over the entire distribution.

- N_{gen}–N_{trkl}^{corr} was fitted with a linear function in different multiplicity bins and α factors were evaluated in multiplicity bins. This was termed α_i, computed as

$$\alpha_i = \frac{\langle N_{ch} \rangle_i}{\langle N_{corr} \rangle_i} \tag{4.8}$$

where $\langle$ $N_{ch}\rangle_i$ is the mean number of generated charged particles in the ith bin and $\langle N_{corr}\rangle_i$ is the mean number of corrected tracklets.

In order to test the effectiveness of the α two methods, the following ratios were plotted

1. $\frac{\langle N_{ch} \rangle_i}{\alpha_{global} \times \langle N_{corr} \rangle_i}$
2. $\frac{\langle N_{ch} \rangle_i}{\alpha_i \times \langle N_{corr} \rangle_i}$

If the method is good enough, the ratio is expected to be consistent with unity otherwise it deviates. Figure 4.17 shows the two ratios obtained using the MC results from p-Pb DPMJET.

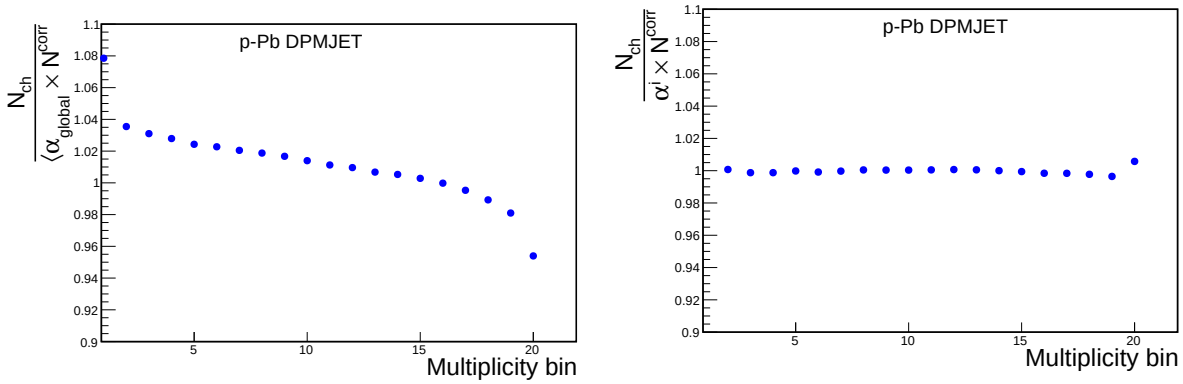

Fig. 4.17 Ratio of the number of generated charged particles and the corrected number of tracklets further corrected with by the α factor

In Figure 4.17 (left) one can see that the α factors are multiplicity dependent. Using α_{global} to correct for the efficiency of the SPD may results in a bias. The deviations from linearity with the α_{global} are up to $\approx 9\%$ while they are a few % with α_i. Therefore, it is better to obtain the α correction factors in different multiplicity bins.

4.3.6 The multiplicity axis ($\langle \frac{dN_{ch}}{d\eta} \rangle_i$)

The goal is to obtain the event meand charged-particle multiplicity in different multiplicity bins, computed as follows;

$$< \frac{dN_{ch}}{d\eta} >_i = \frac{< N_{trkl}^{corr} >_i . < \alpha >_i}{\Delta\eta} \tag{4.9}$$

where $\Delta\eta$ is equal to 2, since the multiplicity is measured at $|\eta| < 1$

The event meand charged-particle multiplicty forms the numerator of the multiplicity result shown in Equation 4.2. The denominator, $<\frac{dN_{ch}}{d\eta}>$ is taken from an independent analysis [121]. The values obtained for $|\eta| < 1$ are shown in Table 4.6.

Collision system	$\langle \frac{dN_{ch}}{d\eta} \rangle$
p–Pb	20.33 ± 0.83
Pb–p	20.32 ± 0.83

Table 4.6 $<\frac{dN_{ch}}{d\eta}>$ values at $\mid \eta \mid < 1$.

Table 4.7, shows a summary per multiplicity bin of the N_{trkl}^{corr}, α values and the obtained $\frac{dN_{ch}/d\eta}{\langle dN_{ch}/d\eta \rangle}$.

Multiplicity bins (p–Pb)	N_{trkl}^{corr}	α	$\frac{dN_{ch}/d\eta_i}{<dN_{ch}/d\eta>}$	Multiplicity bins (Pb–p)	N_{trkl}^{corr}	α	$\frac{dN_{ch}/d\eta_i}{<dN_{ch}/d\eta>}$
1-10	5.40	1.300	0.17	1-11	5.66	1.300	0.18
11-16	13.22	1.27	0.41	12-18	14.23	1.275	0.45
17-20	18.34	1.266	0.57	19-23	21.03	1.272	0.65
21-24	22.31	1.260	0.69	24-27	24.64	1.271	0.77
25-28	26.29	1.258	0.81	28-32	30.66	1.266	0.95
29-32	30.12	1.256	0.93	33-36	33.67	1.264	1.05
33-36	34.28	1.254	1.05	37-41	37.42	1.262	1.16
37-40	38.34	1.251	1.18	42-46	42.36	1.258	1.31
41-44	42.24	1.249	1.29	47-50	47.69	1.256	1.47
45-48	46.56	1.246	1.43	51-55	51.72	1.254	1.60
49-52	49.55	1.244	1.51	56-59	56.34	1.251	1.73
53-56	55.26	1.241	1.69	60-64	60.59	1.249	1.86
57-60	57.68	1.238	1.75	65-69	65.47	1.247	2.01
61-64	61.97	1.235	1.88	70-73	70.71	1.245	2.17
65-69	66.75	1.231	2.02	74-79	75.92	1.243	2.32
70-77	72.68	1.228	2.19	80-88	83.20	1.240	2.53
78-89	82.73	1.225	2.49	89-102	93.62	1.237	2.84
90-110	98.46	1.220	2.95	103-126	109.97	1.233	3.32
111-155	122.59	1.215	3.66	127-178	135.64	1.229	4.09
156-299	169.23	1.201	5.01	179-299	189.66	1.211	5.65

Table 4.7 Summary per multiplicity bin of the N_{trkl}^{corr}, α values and the obtained $\frac{dN_{ch}/d\eta}{\langle dN_{ch}/d\eta \rangle}$, utilizing the data driven method described in Section 4.3.1.

4.3.7 Systematic uncertainties

4.3.7.1 Residual pile-up

Physics selection cuts discussed in Section 4.2.2 employ various pile-up cuts to deal with events occuring simultaneously. These cuts removes $\approx 10\%$ of the accepted events. However, there can be residual pile-up even after applying the Physics Selection cuts. The uncertainty is evaluated from the residual pile-up by varrying the SPD pile-up cut;

AliESDEvent::IsPileupFromSPD();

The $\langle\ N_{trkl}^{corr}\ \rangle$ is extracted in each multiplicty bin. The differences were less than 1%, hence the uncertainty considered in the final uncertainty.

4.3.7.2 N_{gen}–N_{trkl}^{corr} and α evaluation

The correlation of the generated charged-particle multiplicity to the corrected ones was used to evaluate the value of α. Two methods were used to evaluate α namely, α_i and

α_{global}. Two methods were used to obtain the generated number of tracklets and take the ratio of the obtained generated charged particle multiplicity. The ratio is used to evaluate the systematic uncertainty in each multiplicity bin. The uncertainties range from 0.08% up to $\approx$ 5.5%.

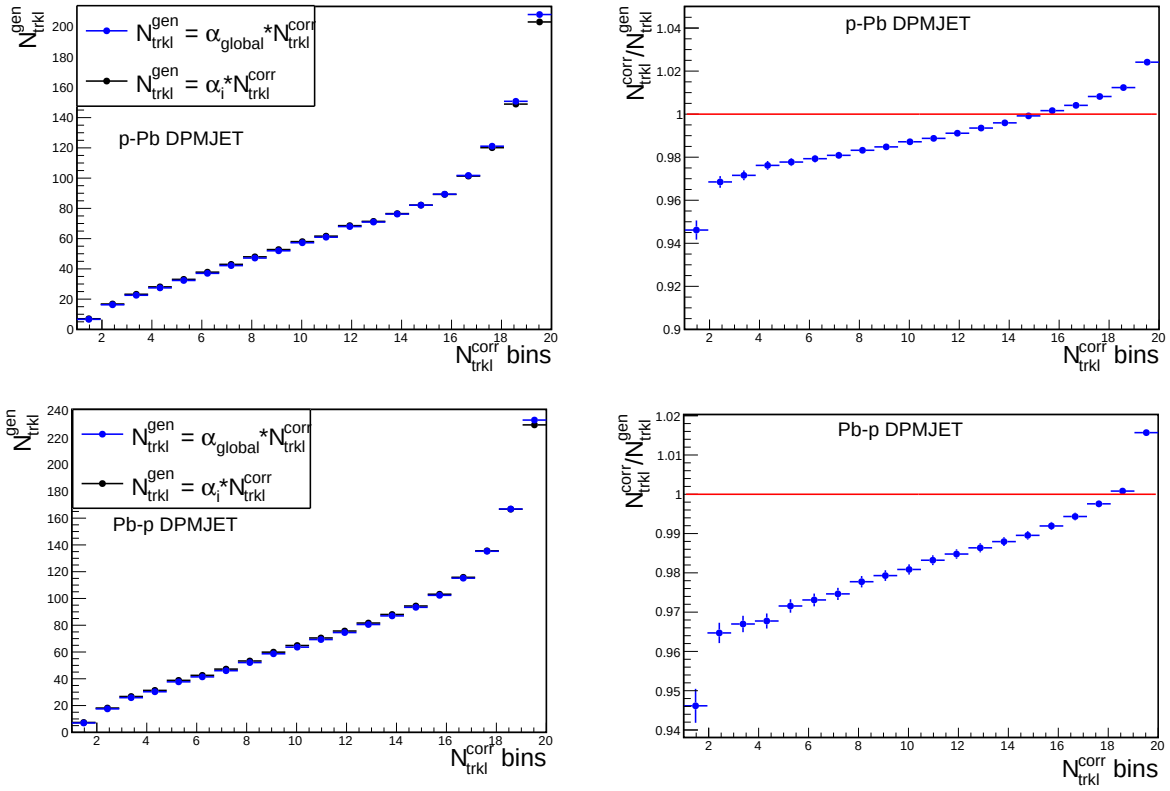

Fig. 4.18 The right plot is $\langle N^{gen}_{trkl} \rangle$ computed for each multiplicity bin from α_{global} and α_{global} values. The left plot shows the ratio of the two methods.

Table 4.8, shows the uncertainties per multiplicity obtained from Figure 4.18.

4.3.7.3 MC inputs

In this study only DPMJET productions were used to evaluate the efficiency correction of the SPD. Therefore for the uncertainty on inputs, the ones obtained in [118] are quoted, where both DPMJET and EPOS "$N_{gen} = \alpha N^{corr}_{trkl}$" were studied with both α_i and α_{global} with different configurations of N_{gen}–N^{corr}_{trkl} correlations. The systematic uncertainty was defined as the "spread between values within the same multiplicity bin". The systematic uncertainty was estimated to be 2%

Multiplicity bin p-Pb	uncertainty %	Multiplicity bin p-Pb	uncertainty %
1-10	5.38	1-11	5.38
11-16	3.53	12-18	3.15
17-20	3.30	19-23	2.84
21-24	3.23	24-27	2.38
25-28	2.84	28-32	2.23
29-32	2.69	33-36	2.07
33-36	2.54	37-41	1.91
37-40	2.23	42-46	1.68
41-44	2.07	47-50	1.52
45-48	1.91	51-55	1.28
49-52	1.68	56-59	1.13
53-56	1.52	60-64	0.89
57-60	1.36	65-69	0.65
61-64	1.20	70-73	0.40
65-69	1.05	74-79	0.08
70-77	0.81	80-88	0.16
78-89	0.57	89-102	0.49
90-110	0.24	103-126	0.82
111-155	0.08	127-178	1.23
156-299	1.57	179-299	2.41

Table 4.8 Uncertainties per multiplicity bin calculated from the differences between the two methods used to evaluate the α correction factors.

4.3.7.4 z_v^{SPD} dependence residual

The residual z_v^{SPD} is studied using the α values obtained by fitting the N_{gen}–N_{trkl}^{corr} correlations extracted in bins of z_v^{SPD} as shown in the Appendix, Figure A.4 and Figure A.5 for p-Pb and Pb-p collisions, respectively. α_{global} is obtained for each distribution and the values are plottted as a function of z_v^{SPD}.

The residual z_v^{SPD} dependence is therefore estimated as the maximal spread of the computed α_{global} values per z_v^{SPD} bin shown in Figure 4.19. The maximal spread of the obtained α_{global} values for p-Pb and Pb-p collisions is $\approx 2.5\%$

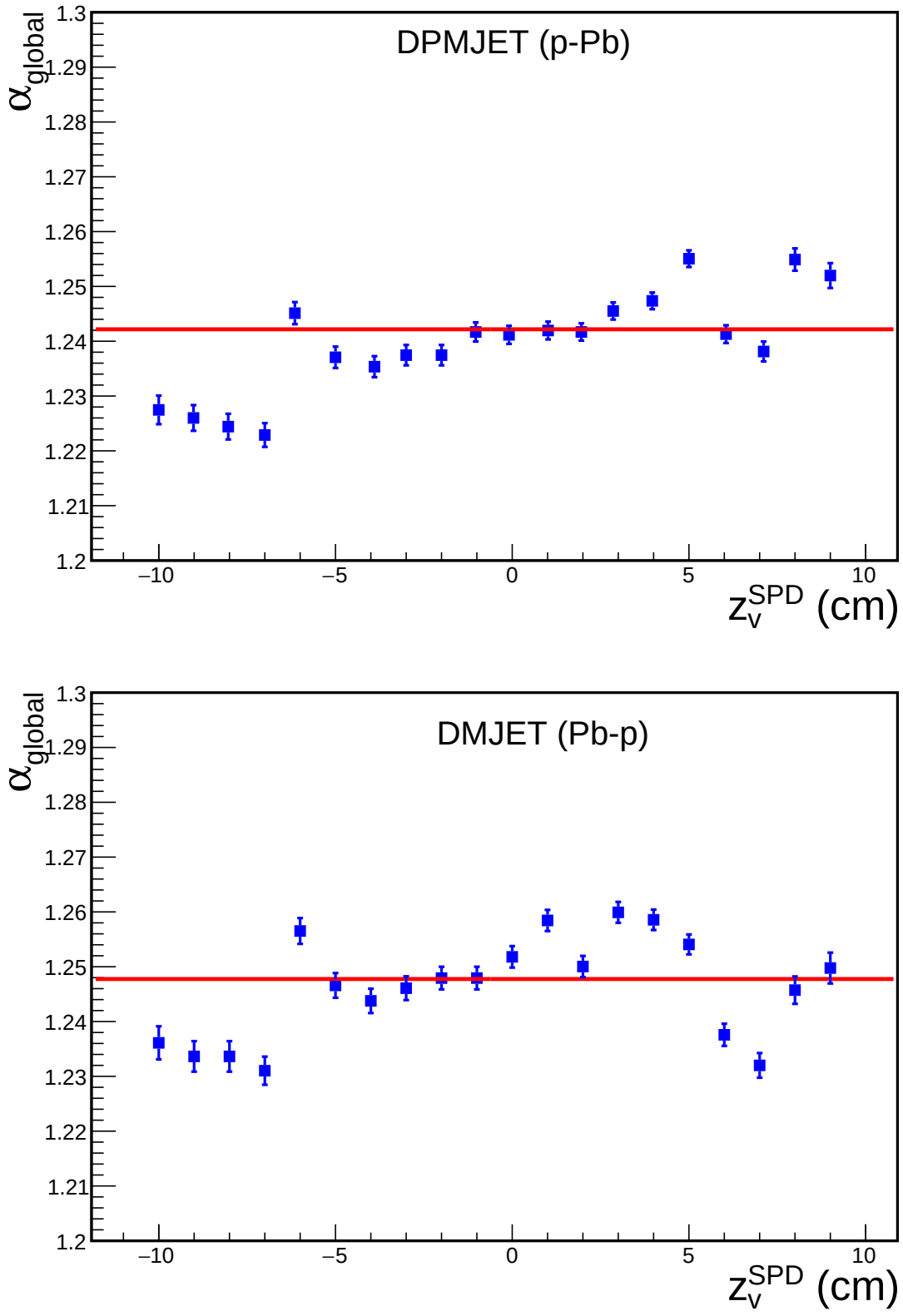

Fig. 4.19 N_{gen}–N_{trkl}^{corr} correlations in z_v^{SPD} bins for DPMJET in Pb-p collisions. The red line is the fit used to obtain the α_{global} in each distribution.

As already mentioned in Section 4.1, this method has disadvantages since it requires a correction for the efficiency, which presented challenges with the slicing of the multiplicity bins. As a result, a centralised method, the so-called "official framework" was adopted to evaluate the multiplicity and can be used the same way across all collision systems. In the next section the new method so-called "Official frameowrk" is discussed.

4.4 Multiplicity measurement : Official framework

A detailed overview of the official framework can be found in [122]. The multiplicity measurement starts from the selection of the runs that satisfy the following criteria [123, 121]

1. The runs should be flagged as "good" after applying the criteria in Table 4.1.
2. The polarity of the magnetic field for the L3 solenoid and the dipole should be the same, e.g. ++
3. The readout detectors are as specified in [122].

The next step is the event selection, where the first requirement is that the events pass the event selection criteria already discussed in Section 4.2.2. Furthermore, the events must be tagged as pileup by a function found in AliROOT called;

AliESDEvent::IsPileupFromSPD()

where default parameters of this function are used. The function is used to remove pile-up events.

4.4.1 Multiplicity estimation

The multiplicity estimation in the "official framework" is based on different estimators, namely SPDtracklets, V0, ZDC estimators, CLO (first layer of the SPD) and CL1 (second layer of the SPD). In this analysis we chose the SPDtracklets estimator which is a midrapidity estimator based on tracklets to determine the event multiplicity. Absolute yields ($dN_{ch}/d\eta$), of the multipicity were studied in the "Official framework". The events are classified into centrality classes using either the number of clusters in the outer layer of the SPD (CL1 estimator) with acceptance $\eta < 1.4$, or the amplitude measured by the V0, A-side, for pPb (V0A estimator) or in the C-side for Pbp (V0C estimator) collisions. Centrality classes were defined as percentiles of the visible cross-section. The central-

Centrality class	$dN_{ch}/d\eta_i$	Systematic uncertainty
0-1	75.49	± 2.01
1-5	57.26	± 1.49
5-10	46.82	± 1.22
10-15	40.57	± 1.05
15-20	35.98	± 0.94
20-30	30.70	± 0.80
30-40	25.03	± 0.66
40-50	20.22	± 0.53
50-60	15.92	± 0.41
60-70	11.78	± 0.31
70-100	4.77	± 0.15

Table 4.9 Summary of approved values of the centrality bins, absolute yields and the associated systematic errors [121].

ity percentiles increase from central (0-10%) to peripheral collisions (70-100%). Central collisions have more participants and thus produce a high volume of charged particles while peripheral collisions have less participants hence produce a low volume of charged particles. Table 4.9, shows the approved values of the centrality bins, absolute yields and the associated systematic errors. These values are stored in [121] and are accessible to all analysers.

The absolute yields ($dN_{ch}/d\eta$) were produced by the "Official frame work", from which we had to calculate the self normalised multiplicity yields ($\frac{dN_{ch}/d\eta}{\langle dN_{ch}/d\eta \rangle}$). This required combining the centrality bins accordingly. This was done by calculating the weighted mean of the absolute yields of the centrality bins e.g. for the centrality percentile 0-10% bin, the weighted mean of the absolute yield is calculated as follows;

$$dN_{ch}/d\eta_{0-10\%} = \frac{1(75.49) + 4(57.26) + 5(46.82)}{1+4+5}$$

The same was done to obtain the systematic uncertainties, therefore the associated systematic uncertainty for the centrality percentile 0-10% was computed as follows;

$$\Delta dN_{ch}/d\eta_{0-10\%} = \frac{1(2.01) + 4(1.49) + 5(1.22)}{1+4+5}$$

The relative multiplicity yield are then computed and the associated errors are propagated

using Equation 4.10

$$\Delta\frac{dN_{ch}/d\eta}{\langle dN_{ch}/d\eta\rangle} = \frac{(\frac{dN_{ch}}{d\eta}\times\Delta\langle\frac{dN_{ch}}{d\eta}\rangle)+(\langle\frac{dN_{ch}}{d\eta}\rangle\times\Delta\frac{dN_{ch}}{d\eta})}{\langle dN_{ch}/d\eta\rangle^2+\Delta\langle dN_{ch}/d\eta\rangle^2} \tag{4.10}$$

Table 4.10 shows the combined centrality bins, the absolute yields of multiplicity (weighted meand), the relative multiplicity yields and their the associated systematic uncertainties.

Discussions on other associated errors are still going on, however, at the time of the writting of this thesis it was agreed to use the errors shown in Table 4.10.

Events triggered by the CINT7-B-NOPF-MUFAST were used for multiplicity estimation to study the correlation of the heavy-flavour decay muon yields as a function of the relative charged-particle multiplicity. To extract the yields of heavy-flavour decay muon a multi-dimensional array containing the multiplicity information are used, as well as the muon counts as triggered by the CMSH7-B-NOPF-MUFAST and CMSL-B-NOPF-MUFAST for high and low-p_{T} single muons, respectively, in the same centrality bins as those in 4.10. In the sections that follow the measurement of the heavy-flavour decay muon yields are discussed.

4.5 Heavy-flavour decay muon signal extraction

In the sections that follow we will give details on the steps leading to signal extraction. The signal is extracted from events that pass the selection criteria already discussed in Section 4.2.2. Here the details of the muon analysis from the selection of muon tracks after selecting interesting events to the extraction of the signal are discussed.

4.5.1 Track selection

Muon tracks are reconstructed in the Forward Muon Spectrometer. The muon track selection is applied offline in the analysis. The single muons considered in this study are selected using the muon trigger classes, namely **CMSL7-B-NOPF-MUFAST** for low p_{T} and **CMSL7-B-NOPF-MUFAST** for high p_{T} muons. The following cuts are applied;

- $\mathbf{-4.0 < \eta < -2.5}$
  The cut takes into account the geometrical acceptance of the Forward Muon Spectrometer. It removes tracks at the edge of the spectrometer

Centrality class	$dN_{ch}/d\eta$	systematic uncertainty ($\Delta dN_{ch}/d\eta$)	$\frac{dN_{ch}/d\eta}{<dN_{ch}/d\eta>}$	systematic uncertainty ($\Delta\frac{dN_{ch}/d\eta}{<dN_{ch}/d\eta>}$)
0-10	53.86	± 1.40	3.10	± 0.177
10-20	38.28	± 1.00	2.02	± 0.126
20-30	30.7	± 0.80	1.62	± 0.101
30-40	25.03	± 0.66	1.32	± 0.083
40-50	20.22	± 0.53	1.07	± 0.067
50-60	15.92	± 0.41	0.84	± 0.052
60-70	11.78	± 0.31	0.62	± 0.039
70-100	4.77	± 0.15	0.25	± 0.017

Table 4.10 Summary of approved values of the centrality bins, absolute yields and the computed relative yields and associated systematic uncertainties from the "Official framework".

- **ThetaAbs cut** (θ_{abs})
  The cut takes into account the polar angle at the end of the absorber, 171°$< \theta_{\text{abs}} <$ 178°. It rejects muons crossing the high-density region of the front absorber, where multiple scattering plays an important role.

- **Momentum (p) x distance of closest approach** (pxDCA)
  The pDCA cut removes beam-induced background and particles. The DCA of particles produced at the IP follows a Gaussian distribution due to the multiple scatterings in the absorber, whereas the particles coming from elsewhere do not. The tracks with pDCA greater than $6\sigma_{pDCA}$ are rejected.

- **Trigger-tracking matching**
  Lastly, the muons are identified by matching the tracks reconstructed in the muon tracking chambers to the ones reaching the trigger chambers.

Figure 4.20 shows the raw inclusive single muon p_{T} distributions after each cut for the CMSH triggered events in p–Pb and Pb–p collisions.

The goal is to obtain the self-normalised yield of heavy-flavour decay muons given by;

$$\frac{dN^{\mu\leftarrow HF}/d\eta_i}{\langle dN^{\mu\leftarrow HF}/d\eta\rangle} = \frac{N^{\mu}_{tot}(1-f^{bkg})}{F_{norm}\times N_{CMSL(H)}\times\epsilon}\times\langle\frac{F_{norm}\times N_{CMSL(H)}\times\epsilon}{N^{\mu}_{tot}(1-f^{Bkg})}\rangle \tag{4.11}$$

where N^{μ}_{tot} is the number of muons and $N_{CMSL(H)}$ is the number of CMSL(H) triggers, f^{bkg} is the background fraction i.e. the fraction of muon contributions from other sources other than c and b quarks, F_{norm} is the trigger normalisation factor and ϵ is the product of acceptance and efficiency of the trigger and tracking. All quantities inside $\langle\ \rangle$ are integrated over the multiplicity, the rest are calculated per multiplicity bin. In the following sections the procedure to obtain the quantities in the Equation 4.11 is detailed.

4.5.2 Event Normalisation

For rare processes in high luminosity environment provided by the LHC, a criterion to select interesting events (trigger) was used in order to meet data storage capacities and rates. The low and high muon p_{T} triggers ensured that the yields of muons were extracted from events consisting of at least a single muon. These events consist of only a fraction of the minimum bias statistics. In the following section the "event normalisation", i.e. the method used to obtain the minimum bias equivalent sample of muon triggered events is presented. The value obtained from this method will be referred to as the normalisation factor "F_{norm}".

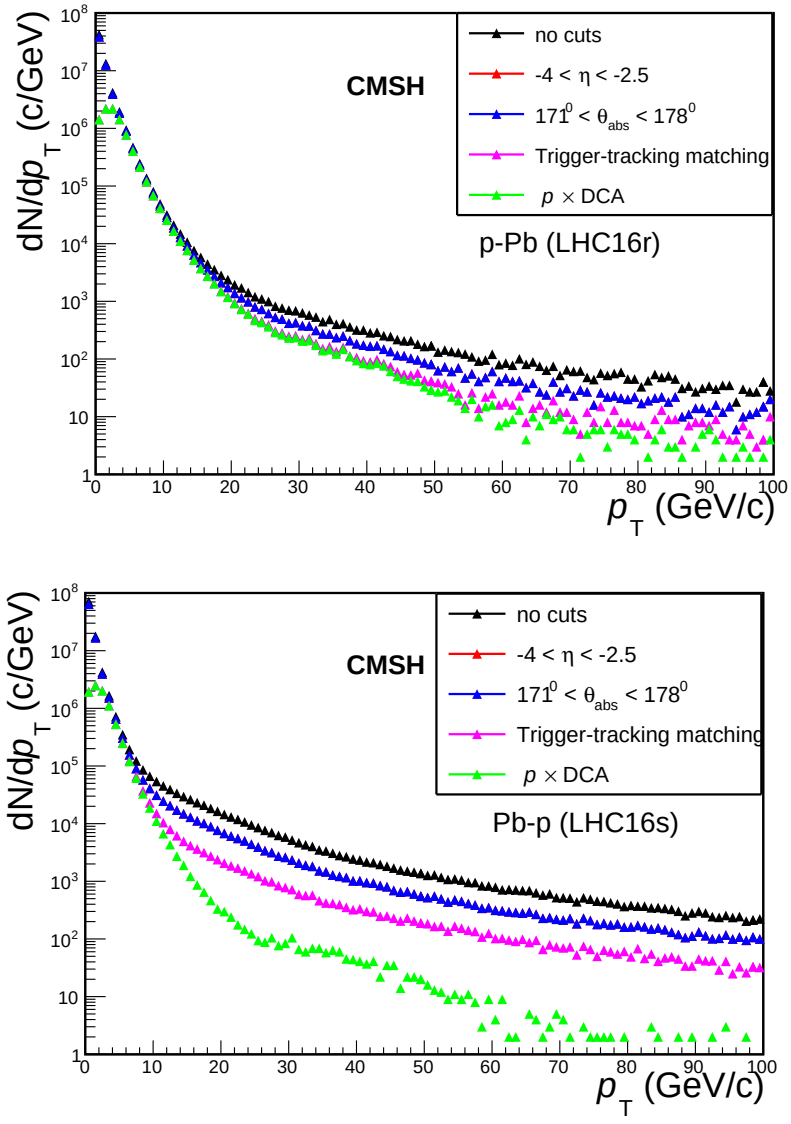

Fig. 4.20 Raw inclusive single muon distributions before cuts and after each stage of implementation of the cuts for CMSH triggered events. Note that the -4 $< \eta <$ -2.5 cut is not visible because it cuts the same events as $171^0 < \theta_{abs} < 178^0$.

Two methods are used in the muon analysis to calculate F_{norm}, namely, the "online" and the "offline" method. The former uses L0b (level zero before any selection") counters before the CTP decision while the latter uses CTP inputs and trigger outputs. The corresponding normalisation factors are computed as follows;

1. **With the offline method**

   The normalisation factors are considered seperately for the single muon low and high p_T triggers. The normalisation factor for the low p_T trigger, F_{norm}^{MSL} is computed as

follows

$$F_{norm}^{MSL} = \frac{N_{MB} \times F_{pile-up}}{N_{(MB\&0MSL)}} \tag{4.12}$$

while the normalisation factor for the high p_{T} trigger, F_{norm}^{MSH} is computed as follows;

$$F_{norm}^{MSH} = \frac{N_{MB} \times F_{pile-up}}{N_{(MB\&0MSL)}} \times \frac{N_{MSL}}{N(_{MSL\&0MSH})} \tag{4.13}$$

where N_{MB}, N_{MSL} and N_{MSH} are the number of MB, MSL and MSH triggers, while $0MSL$ and $0MSH$ are the L0 trigger inputs for the muon single low and high p_{T} triggers, respectively. $F_{pile-up}$ takes into account several collisions occuring in the event. $F_{pile-up}$ can be calculates as follows;

$$F_{pile-up} = \frac{\mu^i}{1 - e^{-\mu^i}} \tag{4.14}$$

where i represent the run and μ is the interaction rate computed as

$$\mu = -\ln(1 - \frac{PURITY_{MB}^i \times L0b_{MB}^i}{N_{bunches}^i \times f_{LHC}}) \tag{4.15}$$

where $L0b_{MB}$ is the scaler value recorded for minimum bias and $PURITY_{MB}$ is computed as the fraction of MB events passing the Physics Selection, $N_{bunches}^i$ is the number of colliding bunches per run, f_{LHC} is the frequency of the LHC and the i shows that the quantities are computed per run. The obtained $PURITY_{MB}$ is shown in 4.21.

As can be seen in Equation 4.13, the normalisation factor for the CMSH trigger is from the normalisation factor obtained for CMSL triggered events. This is because the number of CMSH triggered events (CMSH7-B-NOPF-MUFAST) in the minimum bias trigger (CINT7-B-NOPF-MUFAST) is too small to be used for the dertemination of the normalisation factor.

2. **With the scaler (online) method**
   For online scalers the purity factor (F_{purity}) $\mathrm{PURITY}_{\mathrm{MSL/MSH}}$, is computed as the fraction of MSL/MSH events passing the Physics Selection,

$$F_{purity} = \frac{N^{Physel}}{N^{All}} \tag{4.16}$$

	p-Pb		Pb-p	
	Online	**Offline**	**Online**	**Offline**
CMSL	22.7 ± 0.04	23.03 ± 0.04	16.7 ± 0.02	16.9 ± 0.04
CMSH	765.70 ± 0.51	774.98 ± 1.94	603.00 ± 0.22	613.31 ± 1.57

Table 4.11 Summary of weighted mean F_{norm} values computed with the online and offline methods for CMSL and CMSH triggers and the assoiated statistical errors .

from the offline counters and used to correct for the ratio of physics selected events in the sample. Figure 4.21, shows the PURITY factors for MB, MSH and MSL triggers. The purity factor is greater than 97% for the three triggers and both data taking periods. The obtained pile-up fractions for the two periods of data taking are shown in Appendix A.1.

F_{norm} for the online method, is therefore, calculated as follows;

$$F_{norm}^{MSH} = \frac{L0b_{MB} \times F_{pile-up} \times PURITY_{MB}}{L0b_{MSH} \times PURITY_{MSH}} \tag{4.17}$$

where $L0b_{MB}$ and $L0b_{MSH}$ are the scaler values recorded for minimum bias and muon single high triggers, respectively.

Table 4.11, shows a summary of the weighted mean of the normalisation factors obtained with both methods while Figure 4.22 and Figure 4.23 show the F_{norm} as a function of the run number for CMSL and CMSH triggers at forward and backward rapidity.

As can be seen from Figure 4.22 and Figure 4.23, the online method produces a more stable normalisation factor per run than the offline method. This is because the online scalers contain larger statistics than the offline counters.

4.6 Multiplicity dependence of F_{norm}

The multiplicity dependence of the normalisation factor was studied by scaling the integrated factor (F_{norm}) calculated with the offline method as;

$$F_{norm}^{i} = F_{norm}^{int} \times \frac{N_{CINT}^{i}}{N_{CINT}} \times \frac{N_{CMSL(H)}}{N_{CMSL(H)}^{i}} \tag{4.18}$$

where i represents the multiplicity bin under consideration, F_{norm}^{int} is the normalisation factor integrated over all multiplicity bins as calculated in Equation 4.12 and Equation

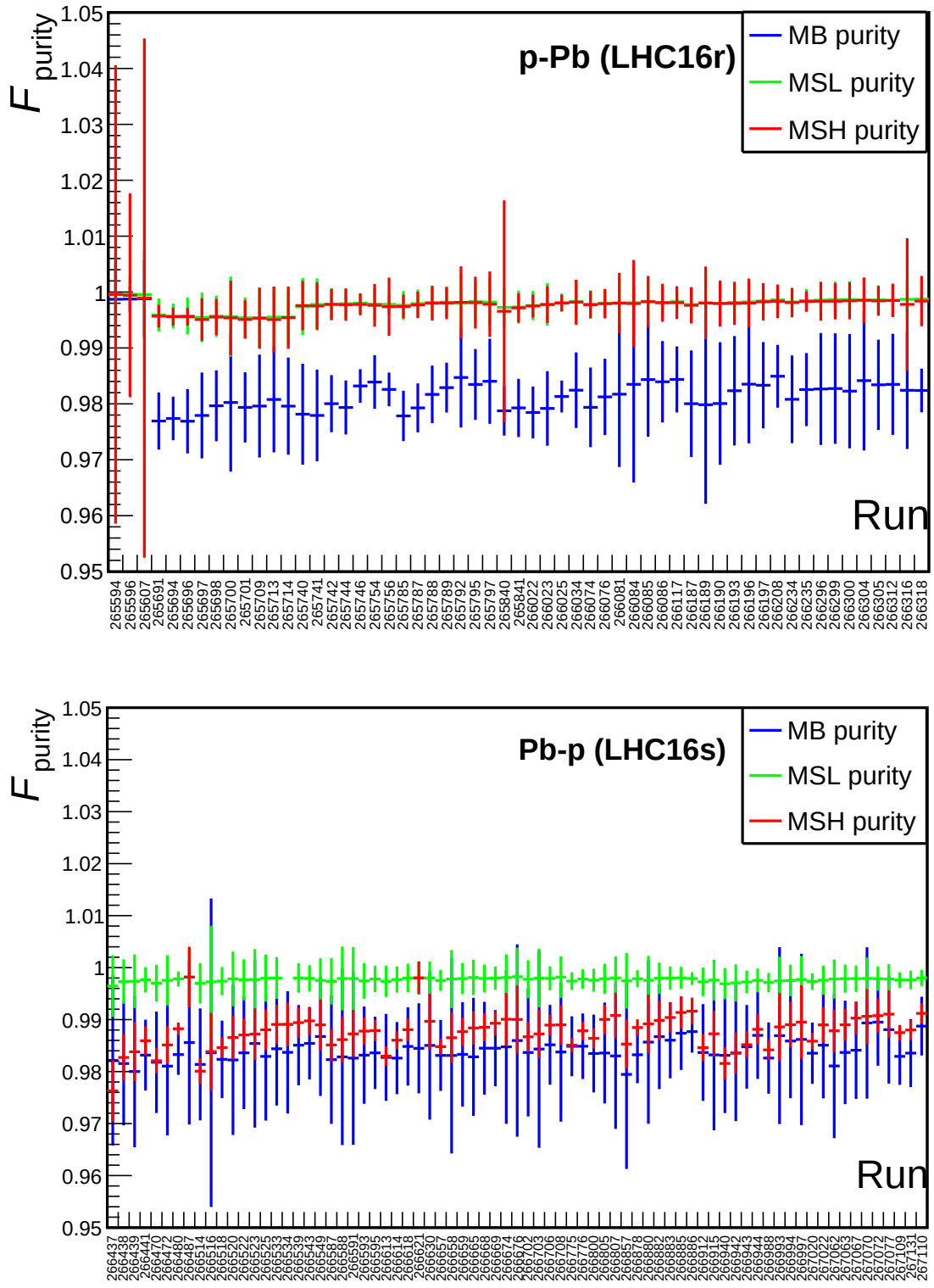

Fig. 4.21 Purity factors obtained for MB, CMSL and CMSH triggers. The vertical bars are the statistical uncertainties.

Multiplicity bin	F_{norm} (p-Pb)	Multiplicity bin	F_{norm} (Pb-p)
1-10	152.22	1-11	111.70
11-16	61.95	12-18	45.46
17-20	43.96	19-23	32.26
21-24	43.98	24-27	32.27
25-28	29.82	28-32	21.88
29-32	25.58	33-36	18.77
33-36	22.45	37-41	16.48
37-40	19.96	42-46	14.65
41-44	18.14	47-50	13.31
45-48	16.53	51-55	12.13
49-52	15.22	56-59	11.17
53-56	14.07	60-64	10.33
57-60	13.12	65-69	9.63
61-64	12.28	70-73	9.01
65-69	11.55	74-79	8.47
70-77	10.55	80-88	7.74
78-89	9.32	89-102	6.84
90-110	7.99	103-126	5.86
111-155	6.51	127-178	4.77
156-300	5.15	179-299	3.78

Table 4.12 Normalisation factors in multiplicity bins for CMSL triggered events in p-Pb and Pb-p collisions

4.13 as discussed in [124]. Table 4.12 and Table 4.13 shows the obtained values of F_{norm} in multiplicity bins for CMSL and CMSH triggered events, respectively.

4.7 Acceptance x Efficiency (A $\times$ ϵ)

To study the A x ϵ, a suitable kinematic distribution of heavy-flavour decay muons needs to be determined. The following decay channels contribute to the signal of heavy flavour muons considered here;

$$\begin{aligned} \mathrm{b} &\rightarrow \mu + \mathrm{X} \qquad (\text{B.R } 10.86\%) \\ \mathrm{b} &\rightarrow \mathrm{D} \rightarrow \mu + \mathrm{X} \qquad (\text{B.R } 9.66\%) \\ \mathrm{c} &\rightarrow \mu + \mathrm{X} \qquad (\text{B.R } 10.33\%) \end{aligned}$$

Multiplicity bin	F_{norm} (p-Pb)	Multiplicity bin	F_{norm} (Pb-p)
1-10	4122.62	1-11	4053.97
11-16	2084.69	12-18	1649.80
17-20	1479.44	19-23	1170.80
21-24	1480.25	24-27	1171.45
25-28	1003.59	28-32	794.23
29-32	861.00	33-36	681.38
33-36	755.76	37-41	598.09
37-40	671.90	42-46	531.73
41-44	610.68	47-50	483.28
45-48	556.28	51-55	440.23
49-52	512.26	56-59	405.39
53-56	473.74	60-64	374.91
57-60	441.81	65-69	349.64
61-64	413.52	70-73	327.26
65-69	388.80	74-79	307.69
70-77	355.32	80-88	281.20
78-89	313.78	89-102	248.32
90-110	268.91	103-126	212.81
111-155	219.08	127-178	173.38
156-300	173.36	179-299	137.19

Table 4.13 Normalisation factors in multiplicity bins for CMSH triggered events in p-Pb and Pb-p collisions

Similarly to other analysis, FONLL predictions [125] were used. The colliding system was proton-proton (pp) at $\sqrt{s} = 8$ TeV to obtain the cross section distributions of the heavy flavour decay muons in $2 < p_{\mathrm{T}} < 40$ GeV/c. CTEQ6.6 [126] PDFs were used to obtain the differential cross sections of the three decay contributions and their sum as a function of p_{T} and η. The cross sections and their sum are shown in Figure 4.24, including systematic uncertainties for PDFs.

The sum of the distributions is fitted with the following function;

for p_{T};

$$p_0(10^{x(p_1\times(1-10^{(xp_2)}+p_3)} \times \frac{1}{x^{p_4}} \times (p_5 + xp_6 + x^2p_7)) \tag{4.19}$$

for η;

$$p_0 + xp_1 + x^2p_2 + x^4p_3 + x^6p_4 + x^8p_5 \tag{4.20}$$

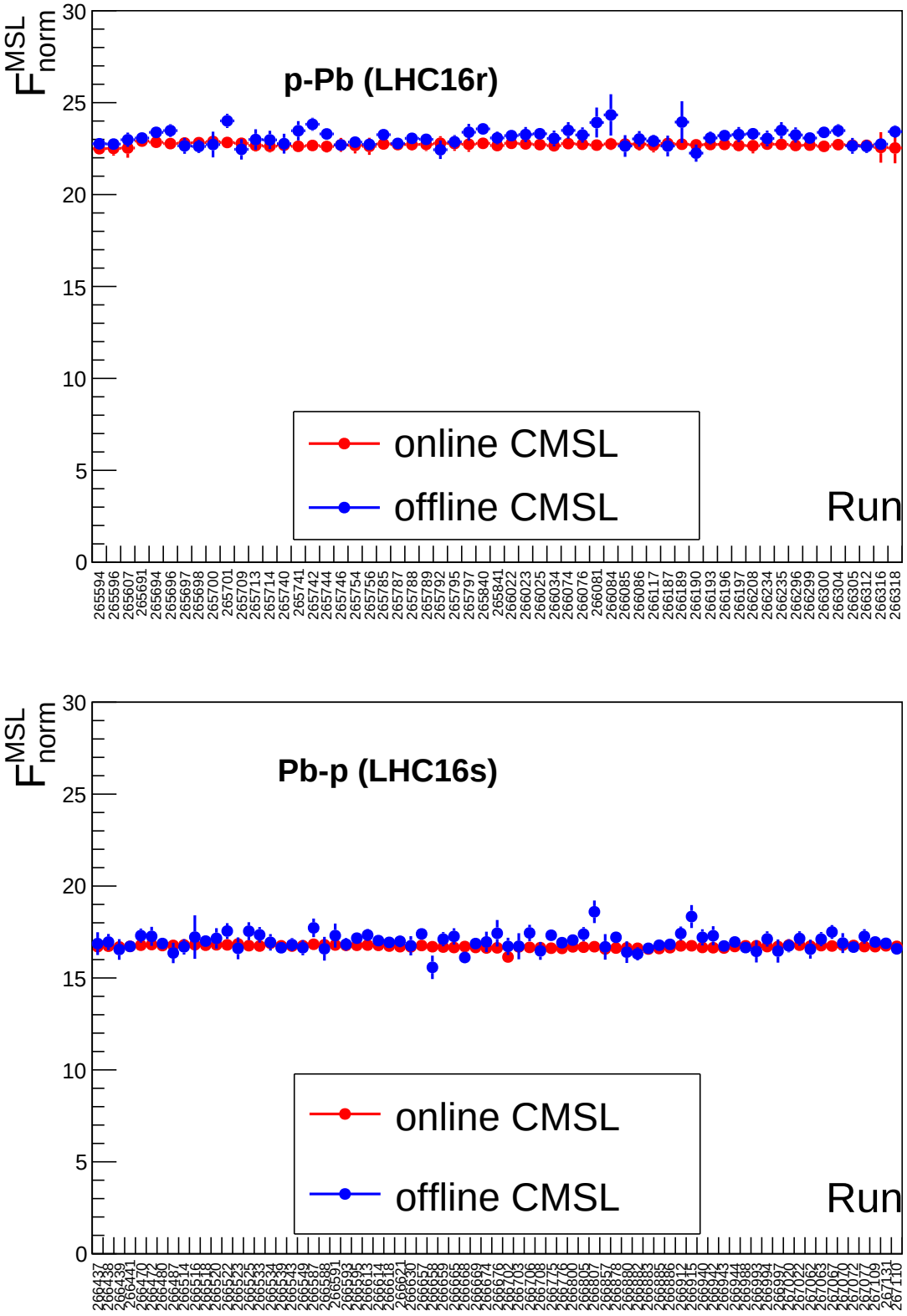

Fig. 4.22 Normalisation factors obtained from online and offline methods for forward and backward rapidity for the CMSL trigger. The vertical bars are the statistical uncertainties

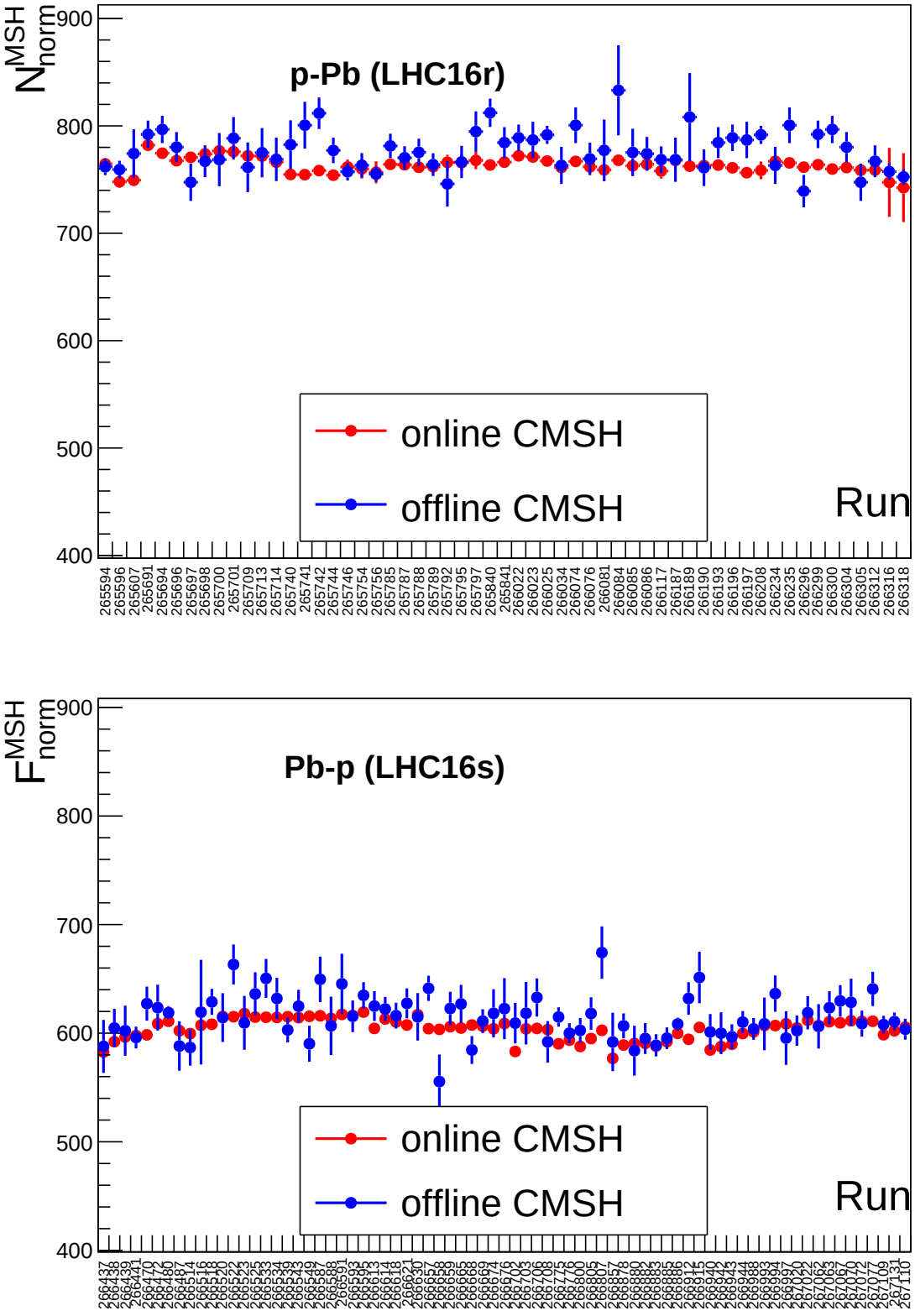

Fig. 4.23 Normalisation factors obtained from online and offline methods for forward and backward rapidity for the CMSH trigger. The vertical bars are the statistical uncertainties.

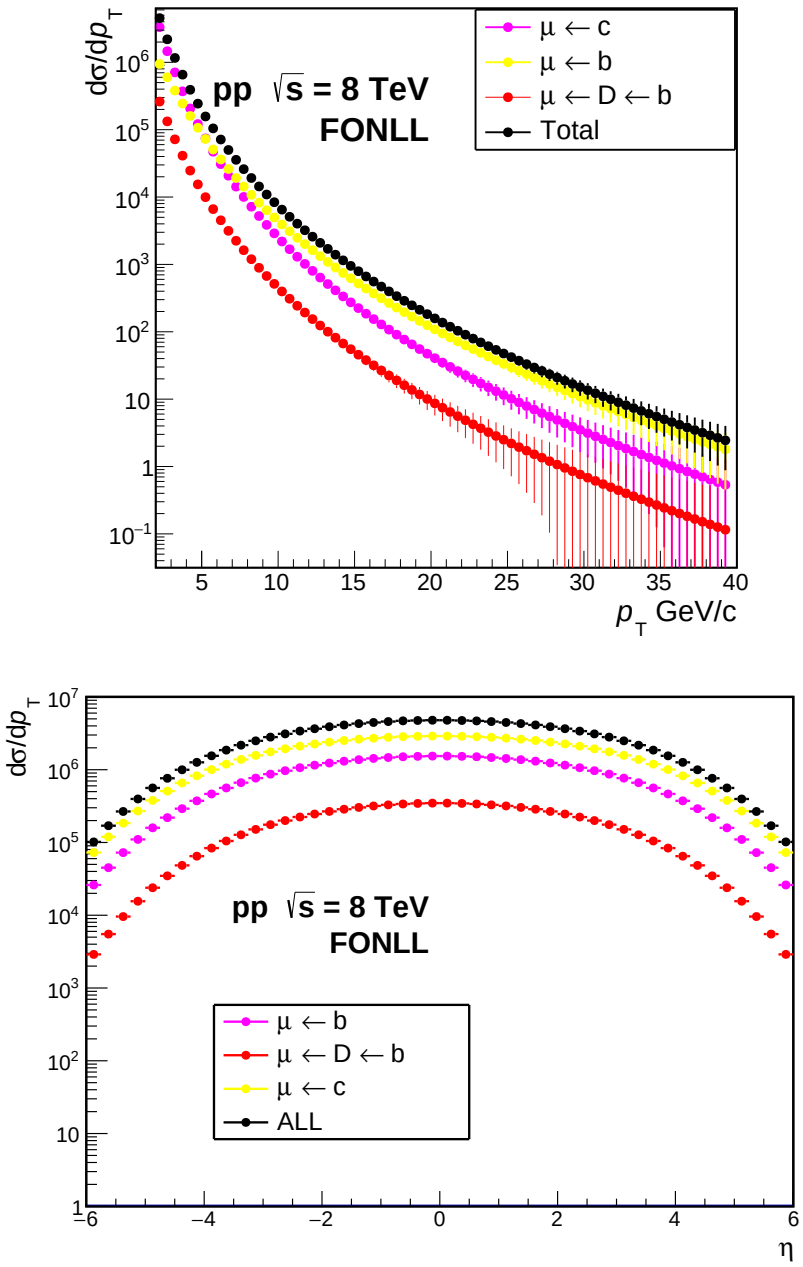

Fig. 4.24 Differential cross sections of heavy-flavour decay muons as a function of p_{T} and η obtained from FONLL [125]. The systematic uncertainties are shown as bars. They include uncertainties associated to PDF.

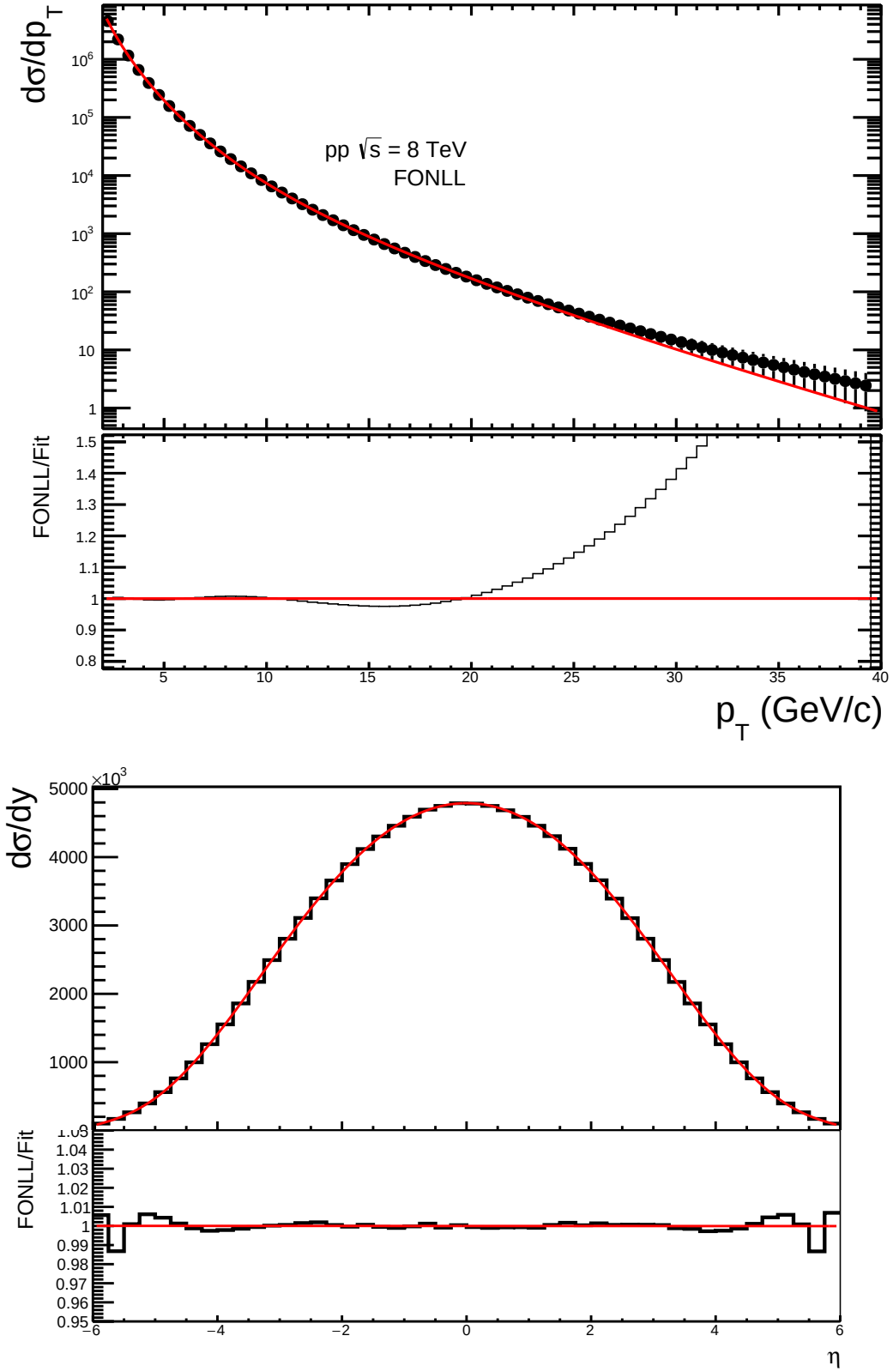

Fig. 4.25 Sum of the differential cross sections of heavy-flavour decay muons as a function of p_{T} and η fitted with functions in Equation 4.19 and Equation 4.20, respectively.

The fits to the sum of the differential cross sections in η and p_{T} are shown in Figure 4.25. The fits are then used as input to generate muons with kinematics based on FONLL run by run. The simulation takes into account the tracking and trigger efficiences of the Forward Muon Spectrometer during data taking by accessing the Offline Calibration Data Base (OCDB). The resulting generated (ideal detector scenario) and reconstructed (realistic detector scenario) distributions are shown in Figure 4.26.

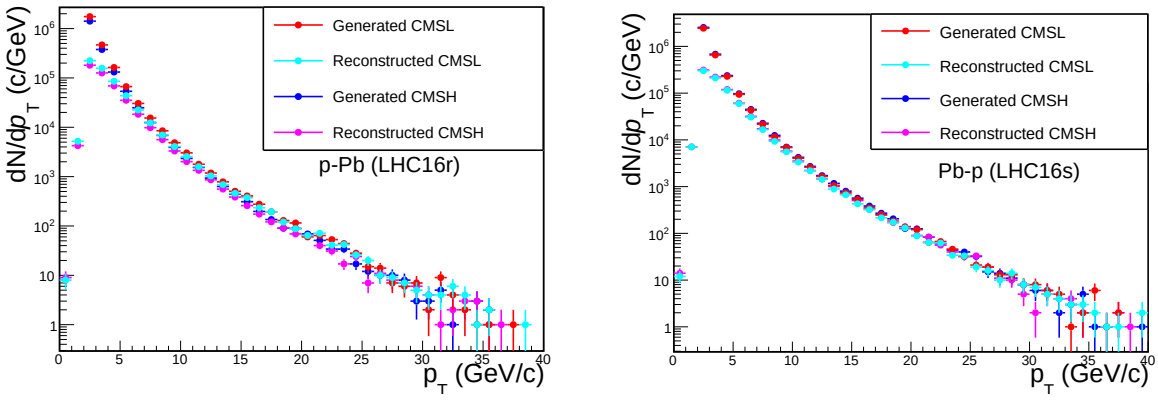

Fig. 4.26 Generated and reconstructed distributions obtained from FONLL for CMSL and CMSH triggered events at forward and backward rapidity.

The ratio of the reconstructed distributions to the generated distributions give an estimate of the A $\times$ ϵ. Figure 4.27, shows the obtained A $\times$ ϵ at forward and backward rapidity, with both CMSL and CMSH triggers.

The results are used to correct the measured number of single muons $\mathrm{N}^{\mu}_{measured}$ to obtained the actual produced number of muons ($\mathrm{N}^{\mu}_{produced}$), as shown in Equation 4.21.

$$N^{\mu}_{produced} = \frac{N^{\mu}_{measured}}{A \times \epsilon} \tag{4.21}$$

This will be discussed further in Chapter 5. However, it was found in previous multiplicity studies, [117] that the A $\times$ ϵ of heavy-flavour decay muons does not depend on the charged particle multiplicity. Hence, the A $\times$ ϵ is not computed in multiplicity bins.

4.8 Background subtraction strategy

The heavy-flavour decay muon signal is obtained from the total single muon p_{T} distributions, shown in Figure 4.20.

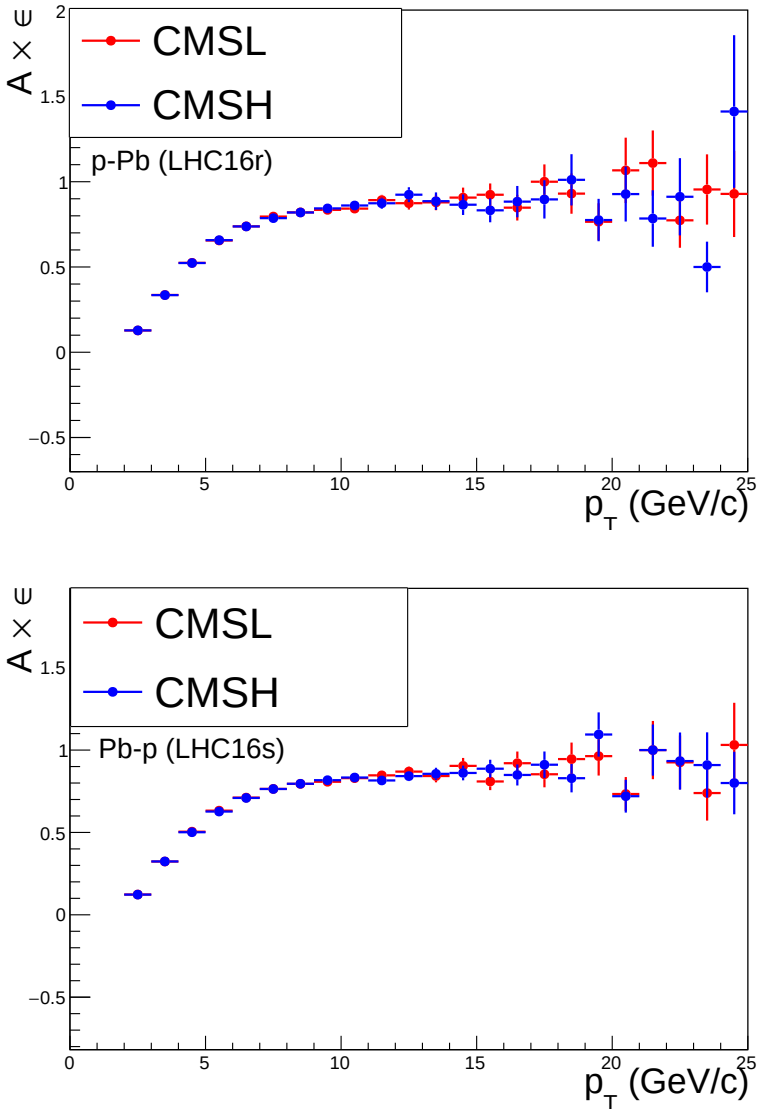

Fig. 4.27 A $\times$ ϵ as a function of p_{T} for CMSL and CMSH triggers at forward and backward rapidity. The vertical bars are the statistical uncertainties.

As already discussed, the raw inclusive single muon distributions were obtained from data after applying both the event and track selection cuts discussed in Section 4.2.2 and Section 4.5.1 . The raw inclusive single muon p_{T} distributions are composed of muons from light (π, K), heavy-flavour (c, b) as well as W and Z boson decays as shown in the two figures in Figure 4.28 [127, 128]. Muons from primary light hadrons, mainly pions and kaons, dominate in the low p_{T} region ($p_{\mathrm{T}} < 1$ GeV/c) and secondary muons (muons produced from interactions of hadrons in the absorber) can be neglected for $p_{\mathrm{T}} > 2$ GeV/c. The yields of hadrons and fake tracks are strongly reduced and considered to be negligible after all analysis cuts are applied. The contribution of Z and W bosons starts to rise close to 20 GeV/c, outside the region of interest in this study, hence negligible in this study.

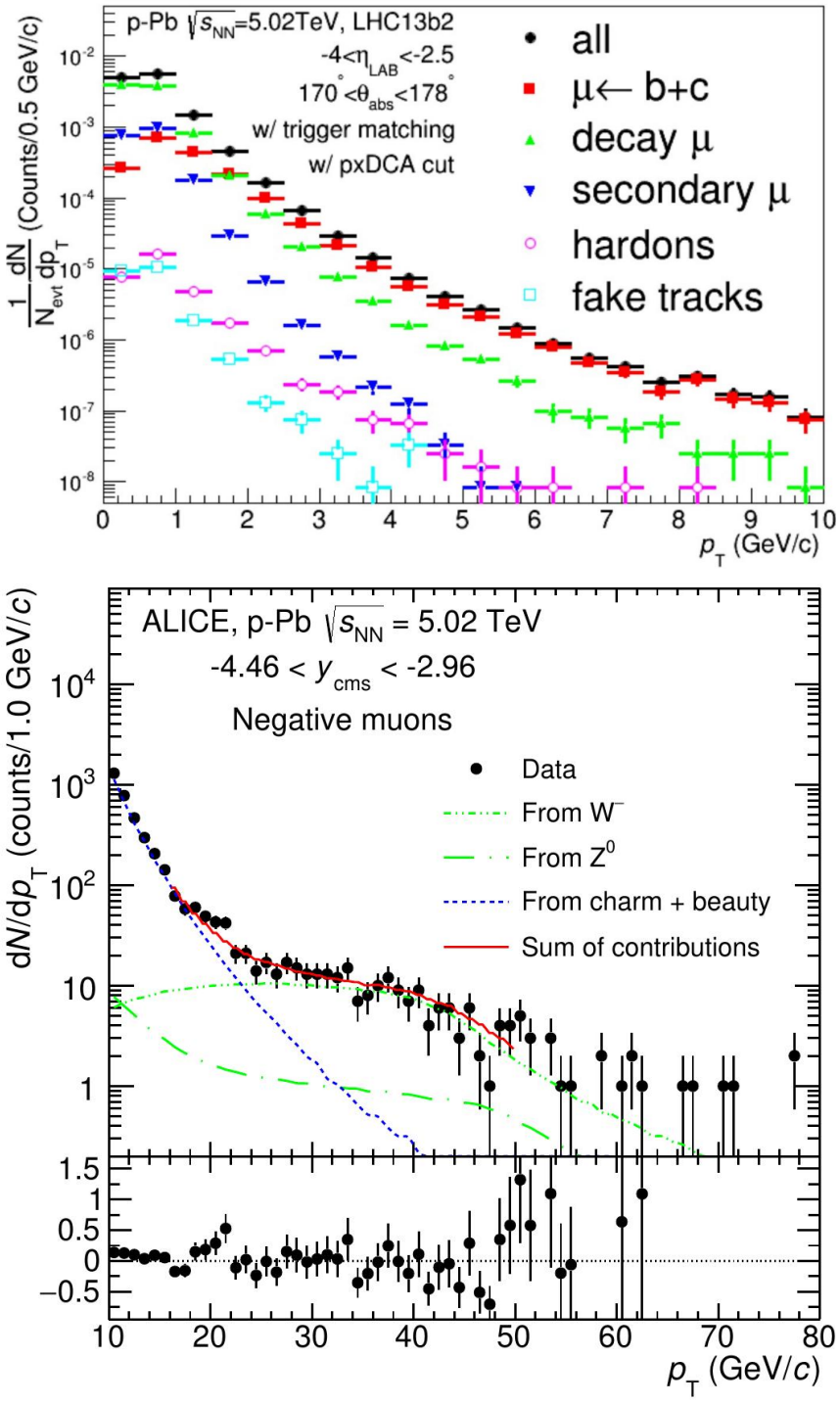

Fig. 4.28 Sources of muon contributions to the single muon p_T distributions extracted from PYTHIA simulation [127, 128].

Therefore, the extraction of the signal of heavy-flavour decay muon was done in the region $2 < p_T < 20$ GeV/c. Only the subtraction of background from pions and kaons at low p_T was done. The background procedure is discussed in the following sections.

4.8.1 Background subtraction of muons from pion and kaons

In the single muon analysis, the background subtraction strategy is based on :

1. Extrapolation of the p_{T} spectra of pions and kaons measured at mid-rapidity to high p_{T}
2. Extrapolation of the rapidity distribution of pions and kaons from mid to forward rapidity
3. Use the extrapolated distributions as input to generate and reconstruct muons from pions and kaons at forward rapidity.

This was not possible to do in this analysis because the p_{T} distributions available for p-Pb and Pb-p collisions at midrapidity were up to very low p_{T} i.e. 3.4 GeV/c [129]. Consequently, a hybrid method was suggested where the estimated background contribution of muons from pions and kaons at forward and backward rapidity obtained from the steps mentioned above for a study in p–Pb and Pb–p collisions at $\sqrt{s_{NN}}$ = 5.02 TeV [127] are used. The distributions are shown in Figure 4.29. The distributions are presented in centrality percentiles that were considered in [127].

The background distributions from $\sqrt{s_{NN}}$ = 5.02 TeV were rescaled to $\sqrt{s_{NN}}$ = 8.16 TeV in order to estimate the muon background contribution of pions and kaons for this study. The correction factors were obtained from PYTHIA simulations [22]. The next sections will be the discussion of this procedure.

4.8.1.1 PYTHIA simulations

PYTHIA simulations were perfomed using PYTHIA 8.230 [22] with nuclear modified PDFs, EPS09 NLO (Next to Leading Order) [130] to take care of the non-negligible Cold Nuclear Matter Effects at low p_{T}. The p_{T} distributions of muons from pions and kaons at forward ($2.03 < \mathrm{y_{cms}} < 3.53$) and backward rapidity ($-4.46 < \mathrm{y_{cms}} < -2.96$) at $\sqrt{s_{NN}}$= 5.02 TeV and 8.16 TeV were extracted. The p_{T} distributions obtained with EPS09, NLO PDFs are shown in Figure 4.30. The distributions show a smooth trend at low p_{T} however towards high p_{T} there is a significant presence of fluctuations due to lack of statistics. Similar distributions were extracted with EPS09, LO (Leading Order) as a cross check of the procedure. The obtained distributions of muons from pions and kaons obtained with EPS09, LO PDFs are shown in Figure A.2.

The correction factors used to rescale $\sqrt{s_{NN}}$= 5.02 TeV distributions to $\sqrt{s_{NN}}$= 8.16 TeV were computed as the ratio of $\sqrt{s_{NN}}$ = 8.16 TeV distributions to $\sqrt{s_{NN}}$ = 5.02

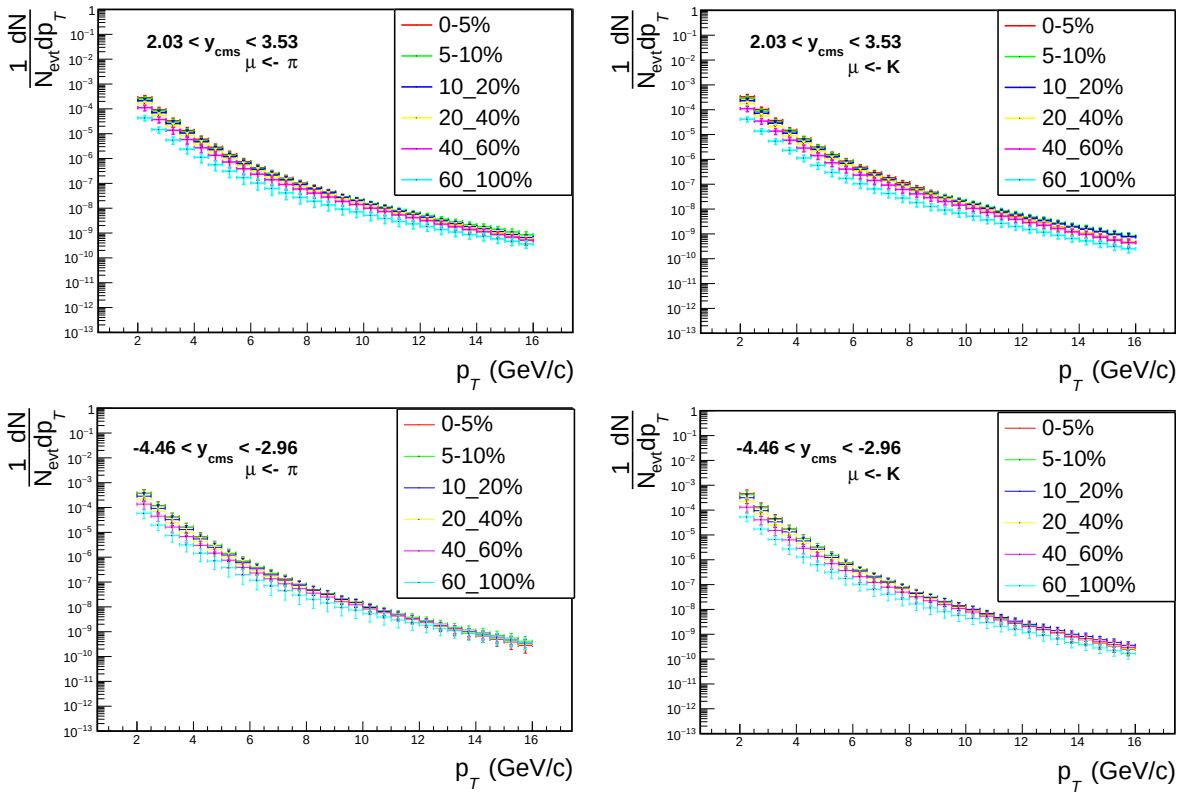

Fig. 4.29 Forward and backward rapidity background distributions of muons from π and kaons from [127].

TeV. Figure 4.31 and Figure A.3 show the correction factors obtained with EPS09, NLO and EPS09, LO at forward and backward rapidity, respectively. Due to the fluctuations observed with the EPS09, LO distributions, the scaling, was therefore, performed using the correction factors obtained with EPS09, NLO. The EPS09, LO distributions are used to obtain the systematic uncertainty associated with the extraction of the correction factors from PYTHIA.

Figure 4.32 a comparison of two PDFs, the resulting associated systematic uncertainties are shown in Table 4.14.

Decay	Collision system	systematic uncertainty(%)
$\mu \leftarrow \pi$	p–Pb (forward rapidity)	$\pm$1.38
$\mu \leftarrow$ K	p–Pb (forward rapidity)	$\pm$ 1.38
$\mu \leftarrow \pi$	Pb–p (backward rapidity)	$\pm$ 1.33
$\mu \leftarrow$ K	Pb–p (backward rapidity)	$\pm$ 1.32

Table 4.14 Summary of the associated systematic uncertainty for the extraction of the correction factors from PYTHIA simulations.

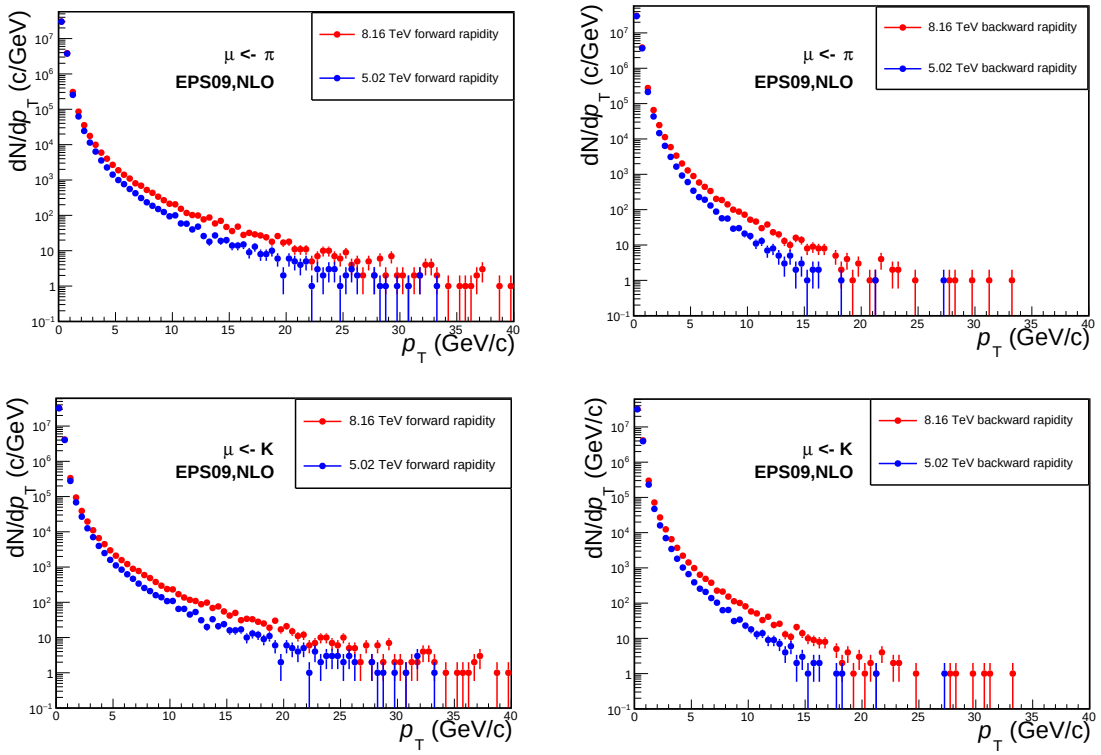

Fig. 4.30 Transverse momentum distributions for muons from pions and kaons at forward and backward rapidity obtained from PYTHIA simulations with EPS09, NLO. The vertical bars are statistical errors.

The rescaled distributions for forward and backward rapidity are shown in Figure 4.33 and Figure 4.34, respectively.

As expected, the distributions exhibit similar features as the correction factors used to perfom the rescaling. At low p_{T} the distributions show a smooth trend while toward 16 GeV/c this is not the case.

4.8.1.2 Extrapolation of rescaled distributions to high p_{T}

As already mentioned, the signal of heavy-flavour decay muons is expected at $2 < p_{\mathrm{T}} < 20$ GeV/c, therefore, the rescaled distributions were restrictive on the p_{T} reach, since they only covered $2 < p_{\mathrm{T}} < 16$ GeV/c. It was resolved to perform fits to extrapolate the rescaled distributions to higher p_{T} and use the fits to evaluate the contribution of muons from pions and kaons on the single muon p_{T} distributions obtained at $\sqrt{s_{NN}}$ =8.16 TeV.

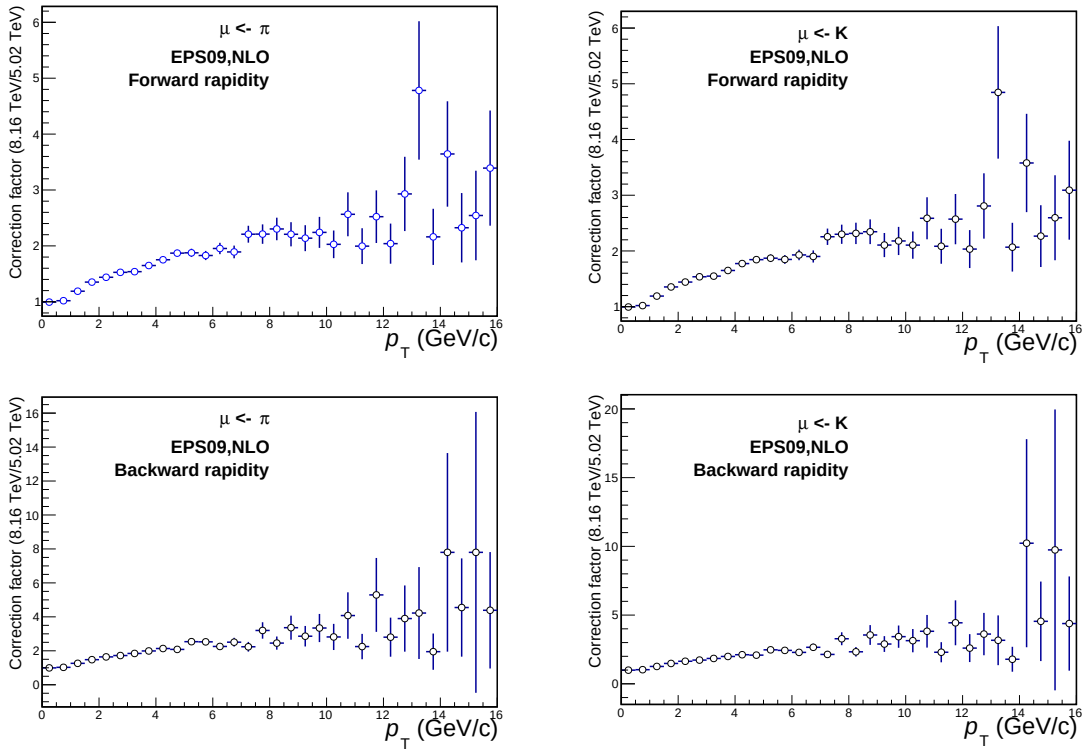

Fig. 4.31 Rescaling factors obtained from the ratio of 8.16 TeV and 5.02 TeV transverse momentum distributions of muons from pions and kaon obtained from PYTHIA simulations with EPS09, NLO at forward and backward rapidity. The vertical bars represent the statistical errors.

The rescaled distributions were fitted with a power law function shown in Equation 4.22,

$$\frac{p_0}{(p_1^2 + x^2)^{p_3}} \tag{4.22}$$

The extrapolation results are shown in Figure 4.35 and Figure 4.36. It can be seen that the transition from low p_{T} ($2 < p_{\mathrm{T}} < 10$ GeV/c) of the fit of the rescaled data points to the extrapolated high p_{T} points is smoother. Fitting and extrapolating the distributions eliminates fluctuations introduced by the correction factors on the background distributions. Consequently, the fit and the extrapolated points were then used to compute the background fraction in each centrality bin. The background fractions were computed as a ratio of the background distributions (in this case, the fit and extrapolation points in Figure 4.35 and Figure 4.36) to the total single muon distribution (background + signal) in each centrality percentile.

$$Background\ fraction = \frac{\mathrm{background_i}}{(\mathrm{background} + \mathrm{signal})_\mathrm{i}} \tag{4.23}$$

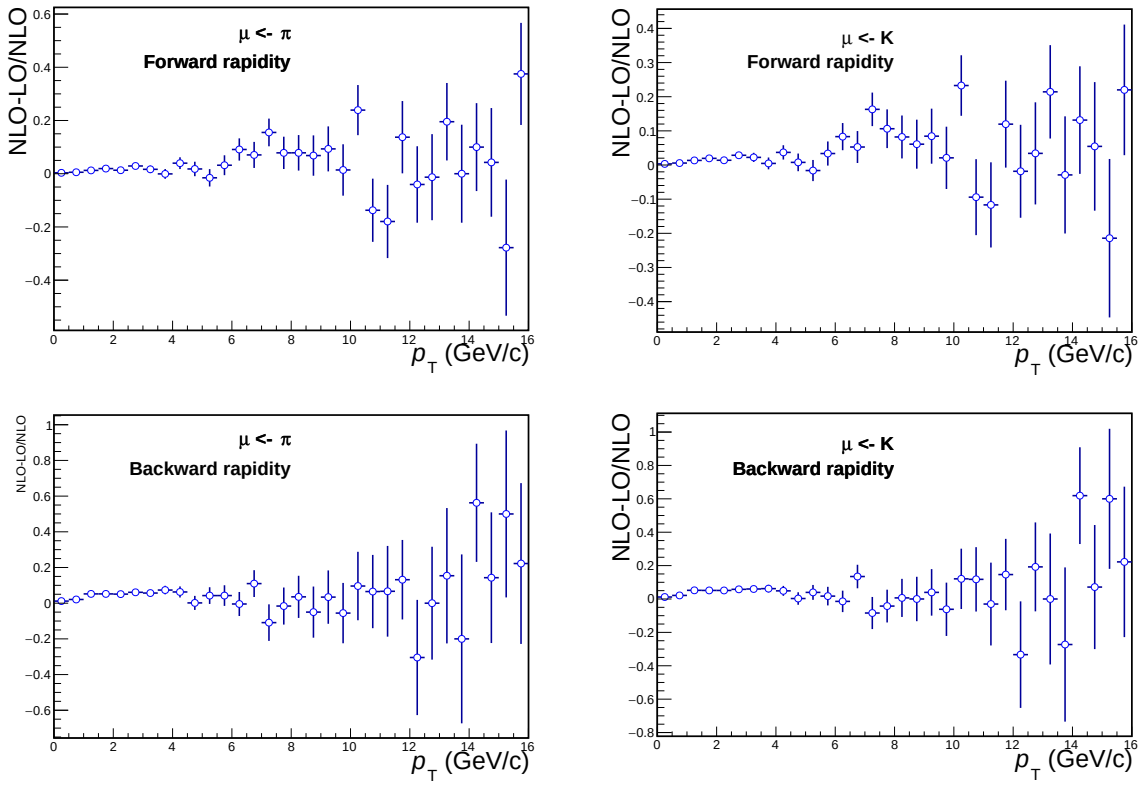

Fig. 4.32 Comparison of EPS09, LO and EPS09, NLO for pions and kaons at backward rapidity. The vertical bars are the associated statistical errors. The extracted systematic uncertainty is shown in Table 4.14.

where i denotes the centrality percentile.

The background fractions obtained with Equation 4.23 are shown in Figure 4.37 for both forward and backward rapidity.

As expected, the background fraction decreases with p_{T} since the contribution of pions and kaons is more pronounced at the low p_{T} region of the single muon p_{T} distribution.

The signal is then obtained using Equation 4.24,

$$\text{signal} = (1 - \text{background fraction}) \times \text{raw inclusive muon } \mathrm{p_T} \tag{4.24}$$

Since the signal is extracted in multiplicity bins, the raw inclusive single muon p_{T} distributions are divided into percentile classes. Figure 4.38. shows the raw inclusive single muon p_{T} distributions in multiplicity percentiles.

The results will be discussed in the chapter 5.

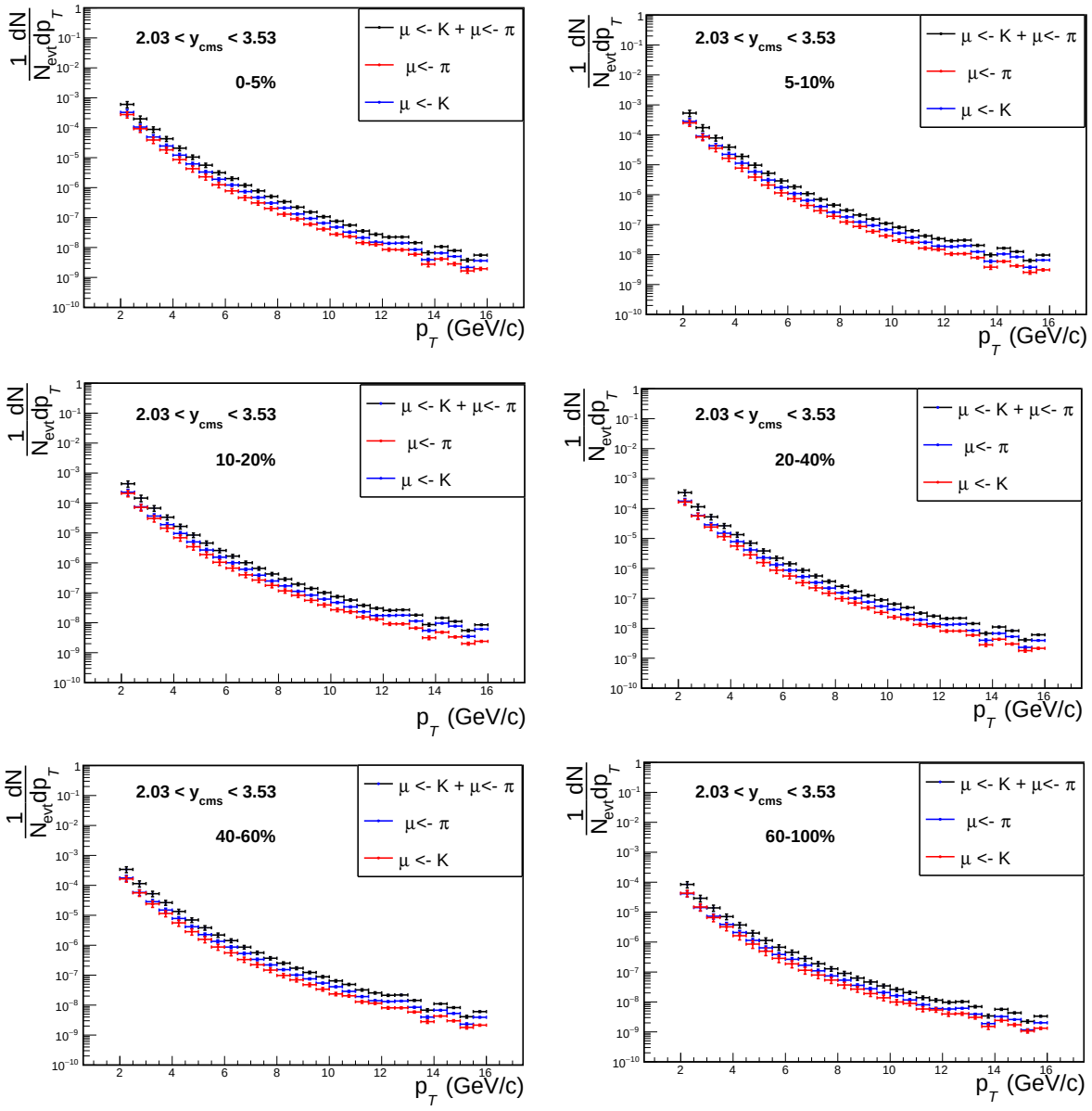

Fig. 4.33 Forward rapidity distributions of muons from pions and kaons obtained in p–Pb collisions at 5.02 TeV.

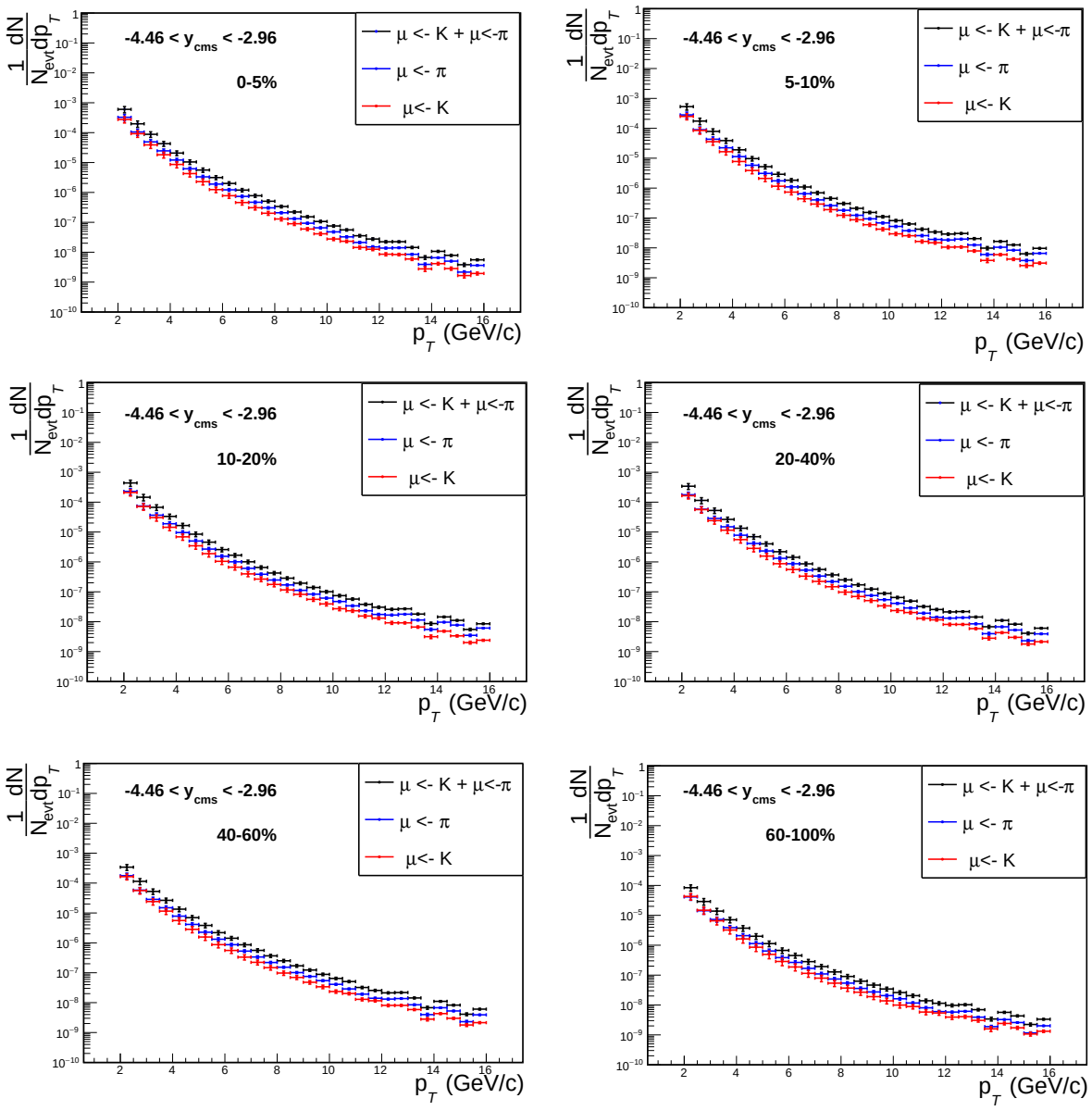

Fig. 4.34 Backward rapidity distributions of muons from pions and kaons obtained in p–Pb collisions at 5.02 TeV.

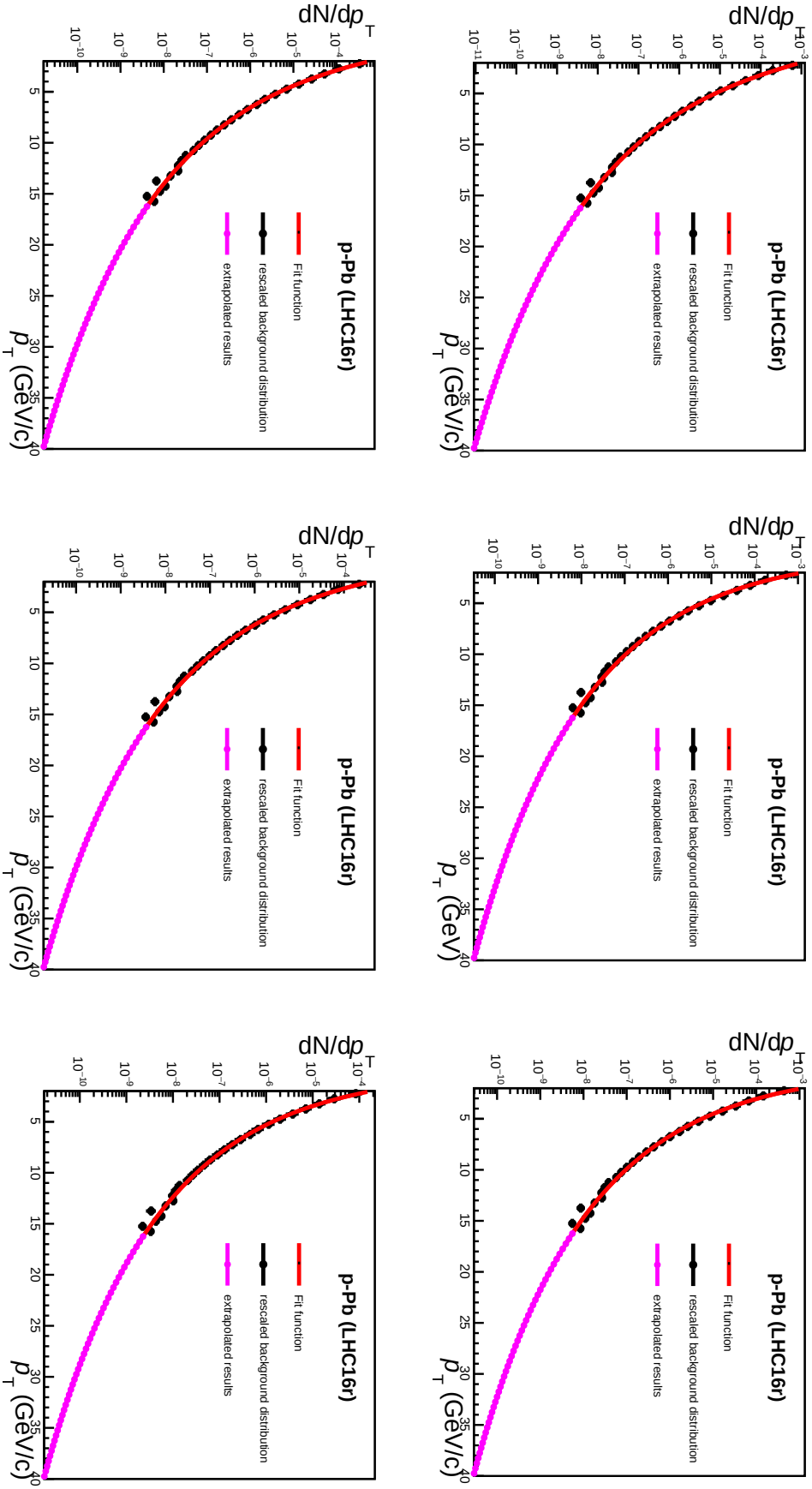

Fig. 4.35 Extrapolated rescaled transverse momentum distributions for muons from pions and kaons at forward.

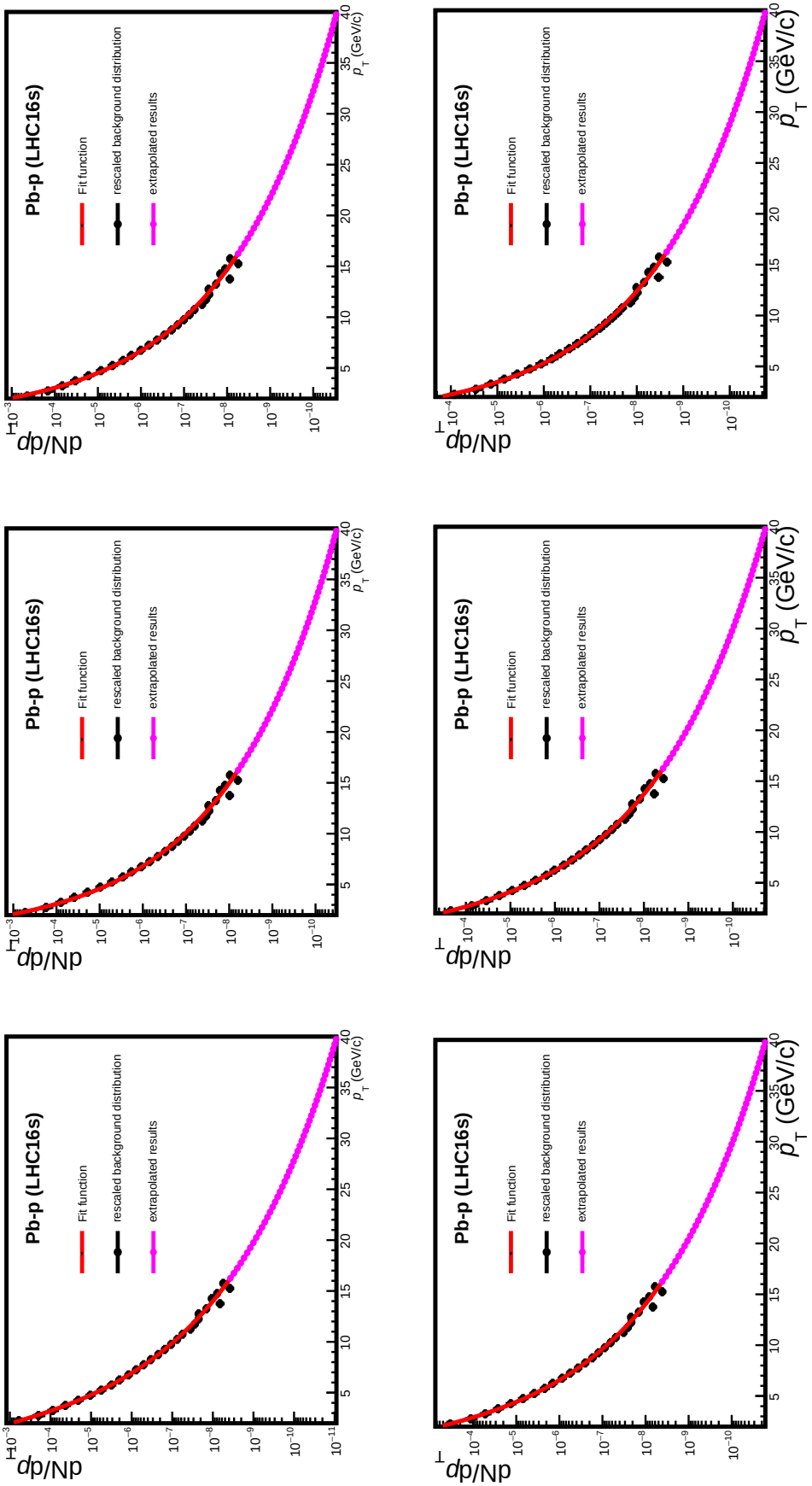

Fig. 4.36 Extrapolated rescaled transverse momentum distributions for muons from pions and kaons at backward rapidity.

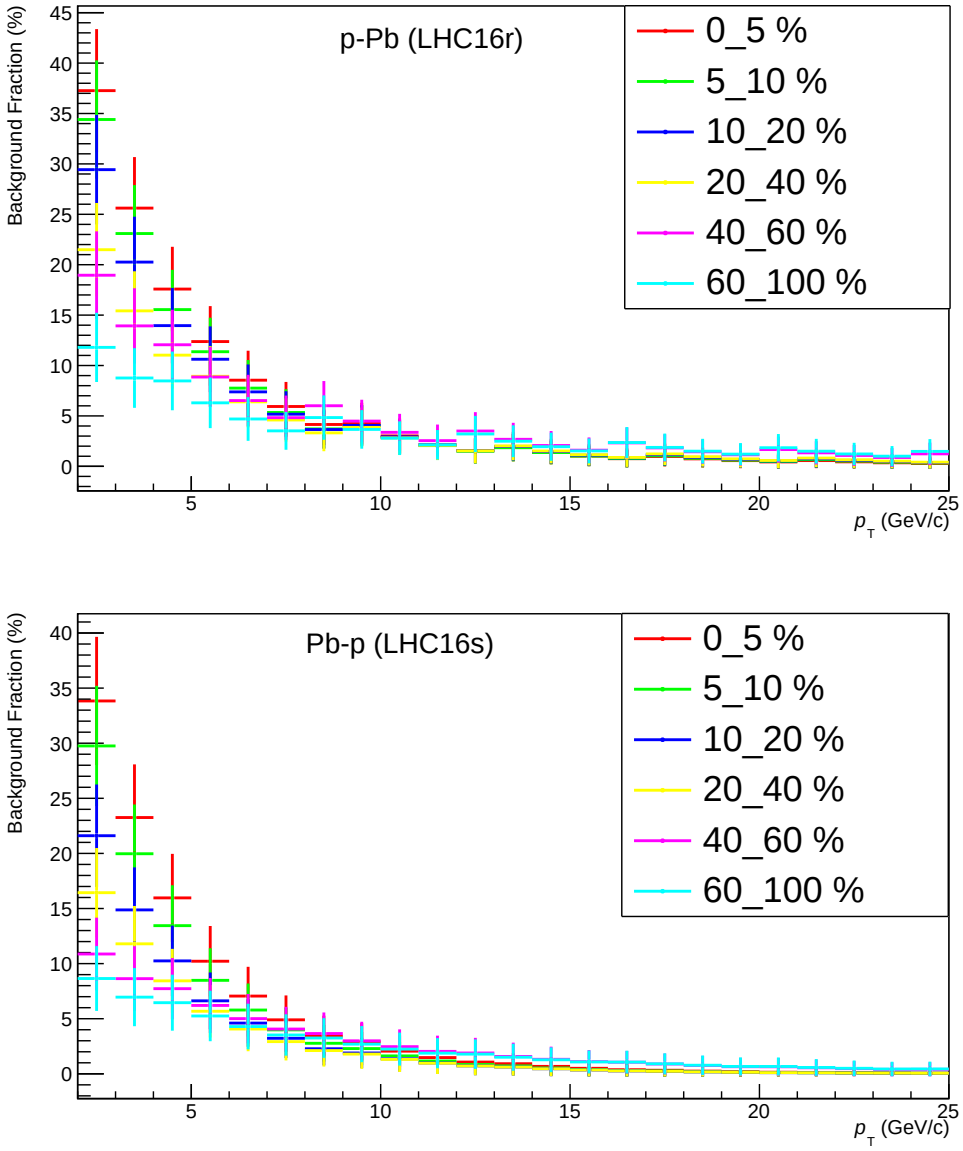

Fig. 4.37 Percentage background contribution of muons from pions and kaons per centrality percentile. The vertical error bars represent the associated statistical uncertainties.

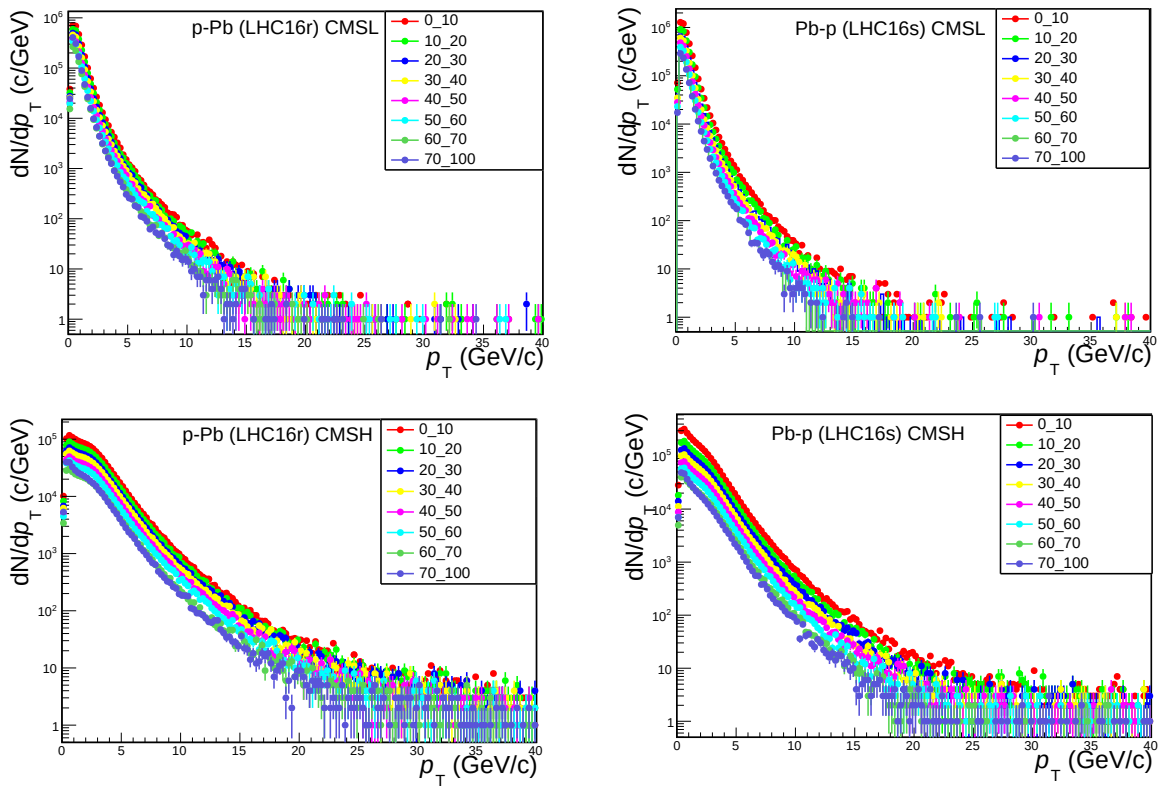

Fig. 4.38 Raw inclusive single muon p_{T} distributions for p–Pb and Pb–p collisions for CMSL and CMSH triggered events in different centrality percentiles. The vertical bars represent the statistical uncertainties.

4.8.2 Background fractions in multiplicity and centrality bins

The background fractions obtained in Section 4.8.1.2 are integrated and plotted as a function of the centrality percentile (top plots) as shown in Figure 4.39 and also as a function of the charged-particle multiplicity (bottom plots). Note that the centrality percentiles are from high multiplicity (0-10%) to low multiplicity (70-100%). The integrated background fractions are fitted with Equation 4.22 and the fit is evaluated to compute the background fraction for the desired centrality percentiles as well as multiplicity bins.

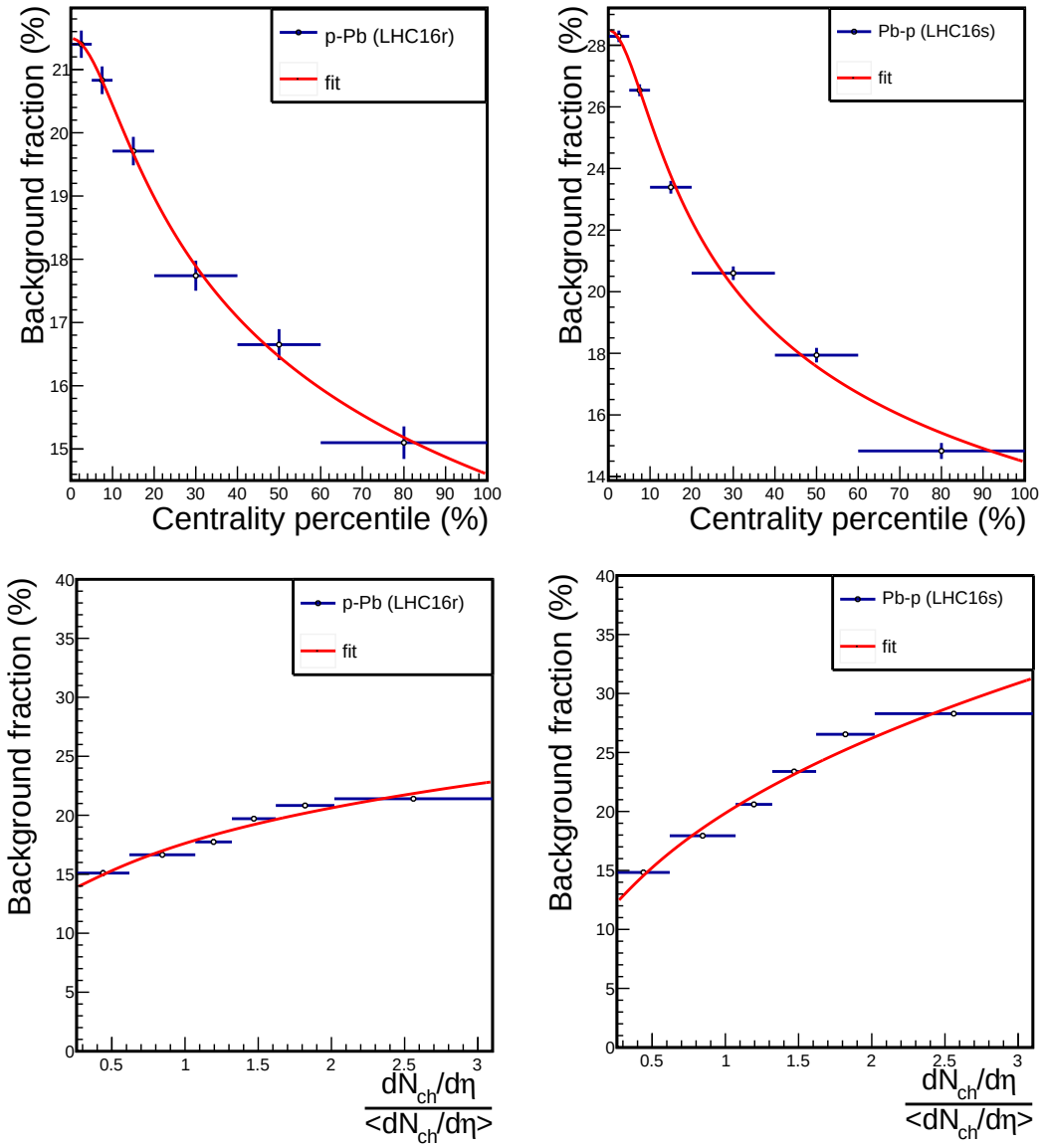

Fig. 4.39 Integated background contribution of muons from pions and kaons per centrality percentile is shown with blue points. The red line is a fit.

4.9 Systematic uncertainties

The following is a summary of the systematic uncertainties associated with the determination of the heavy-flavour decay muon signal. At the writing of this thesis, the uncertainties associated with multiplicity measurement using the "Official framework" were still under discussion. Therefore, this thesis provides preliminary methods used so far following uncertainties found in [121].

Various sources of systematic uncertainties for the heavy-flavour decay muon yield analysis procedures are discussed, as well as the error propagation in order to obtain the final results of heavy flavour decay muon as a function of the charged-particle multiplicty.

4.9.1 Event normalisation procedure

The uncertainty associated with the normalisation procedure is estimated as the difference between the online and offline method. It is 1.2% for p–Pb and 1.7% for Pb–p collisions.

4.9.2 Detector response

4.9.2.1 Tracking efficiency

The systematic uncertainty on the muon tracking efficiency is defined as the difference between the muon tracking efficiency obtained from MC and that from a data-driven approach based on the redundancy of the tracking stations. The tracking efficiency has been studied in the measurement of J/Ψ versus multiplicity in p–Pb collisions at 8.16 TeV [118]. The uncertainty on the tracking efficiency at the di-muon level was found to be 1%, therefore for single muon it will be half the value, implying that it is 0.5%.

4.9.2.2 Trigger efficiency

The uncertainty on the trigger efficiency is estimated by means of the trigger response function. The trigger response function is defined as the ratio of the inclusive muon distribution matching with the low p_{T} trigger condition to the one matching with all p_{T} trigger[1] condition and the comparison of the efficiency corrected p_{T} distributions asking

[1] All p_{T} trigger condition refers to the case when all muons are selected without requiring tracking-trigger matching

the matching with MSL and MSH triggered events. The trigger efficiency amounts to 1% (4%) for MSL (MSH) and does not depend on the data taking periods.

4.9.2.3 Tracker-trigger matching

The tracker-trigger matching depends on the choice of the χ^2 cut in matching the tracks reconstructed in the tracker to those detected in the trigger. The uncertainty at dimuon level amounted to 1%, therefore at single muon level it is 0.5%.

4.9.2.4 Misalignment

The misalignment is estimated by taking the deviation of efficiency based on different misalignment scenarios with respect to the (default) one based on realistic detector response. It is estimated to 0.5% p_{T} in (GeV/c).

4.9.3 Background subtraction

The background subtraction procedure for muons from pions and kaons contains the following components

- 5.02 TeV inputs
  The background distributions used to obtain the rescaled 8.16 TeV ones show a contribution of 5–20% at forward, while it is about 10–30% at backward rapidity [127].
- Pythia scaling factors
  The systematic on the scaling is calculated as the difference between the p_{T} distributions obtained with EPS09, LO and EPS09, NLO. The differences are shown in Fig 4.32. The systematic uncertainties are shown in Table 4.14.

4.9.4 Summary of systematic uncertainties

Systematic uncertainty	**p-Pb**	**Pb-p**
Normalization procedure	1.2%	1.7%
Tracking efficiency	0.5%	
Trigger efficiency	1% (CMSL) 4% (CMSH)	
Tracker-trigger matching	0.5%	
Misalignment	0.5%	
Background subtraction	1.38%	1.32%

Table 4.15 Summary of systematic uncertainties associated with heavy-flavour decay muon signal extraction

It is imperative to note that the results are quoted as self-normalised yields which means that all uncertainities that are not multiplicity dependent cancel in the calculation of the self-normalised yield. Also as already mentioned, background concerning the contribution of muons from the decay of electroweak bosons was also not considered in this study because, as shown in Figure 4.28, W and Z contribution becomes relevant in $p_{\mathrm{T}} > 20$ GeV/c, which is outside the region of interest ($2 < p_{\mathrm{T}} < 20$ GeV/c) in this study. However, the signal extraction may be improved by considering other simulation generator (EPOS, DPMJET) to estimate the background subtraction for pion and kaons at this energy, provided a wider p_{T} range can be accessible.

The next chapter, discusses the results.

CHAPTER 5

Discussion of results

This chapter presents the results obtained by the author following the strategy discussed in Chapter 4. The results are compared to other multiplicity studies at the same center-of-mass energy.

5.1 Overview

The aim of this study was to obtain the self-normalised yield of heavy-flavour decay muons given by Equation 5.1.

$$\frac{dN^{\mu\leftarrow HF}/d\eta_i}{\langle dN^{\mu\leftarrow HF}/d\eta\rangle} = \frac{N^{\mu}_{tot}(1-f^{bkg})}{F_{norm}\times N_{CMSL(H)}} \times \langle \frac{F_{norm}\times N_{CMSL(H)}}{N^{\mu}_{tot}(1-f^{bkg})}\rangle \tag{5.1}$$

where f^{bkg} is the background fraction and all quantities inside $\langle\ \rangle$ are integrated over the multiplicity. As already mentioned, the A $\times$ ϵ for heavy-flavour decay muons is independent of the charged-particle multiplicity therefore all quantities that do not vary with the multiplicity cancel out in the calculation of the self-normalised yields. For this reason, the A $\times$ ϵ is not shown in Equation 5.1.

The self normalised yield of heavy-flavour decay muons as a function of the charged-particle multiplicity measured using the two methods described in Chapter 4, namely, the

data driven method and the **Official framework** are presented.

Multiplicity bin (p–Pb)	$\frac{dN^{HF\leftarrow\mu}/d\eta}{\langle dN^{HF\leftarrow\mu}/d\eta\rangle}$	**Multiplicity bin (Pb–p)**	$\frac{dN^{HF\leftarrow\mu}/d\eta}{\langle dN^{HF\leftarrow\mu}/d\eta\rangle}$
1-10	0.19 ± 0.036	1-11	0.15 ± 0.030
11-16	0.46 ± 0.023	12-18	0.39 ± 0.027
17-20	0.66 ± 0.023	19-23	0.57 ± 0.027
21-24	0.77 ± 0.021	24-27	0.69 ± 0.025
25-28	0.95 ± 0.020	28-32	0.82 ± 0.023
29-32	1.06 ± 0.019	33-36	0.94 ± 0.022
33-36	1.16 ± 0.019	37-41	1.06 ± 0.022
37-40	1.32 ± 0.018	42-46	1.20 ± 0.021
41-44	1.48 ± 0.018	47-50	1.49 ± 0.020
45-48	1.60 ± 0.017	51-55	1.61 ± 0.020
49-52	1.80 ± 0.016	56-59	1.72 ± 0.019
53-56	1.86 ± 0.016	60-64	1.90 ± 0.019
57-60	1.96 ± 0.015	65-69	2.03 ± 0.019
61-64	2.02 ± 0.015	70-73	2.24 ± 0.019
65-69	2.12 ± 0.015	74-79	2.41 ± 0.018
70-77	2.27 ± 0.015	80-88	2.55 ± 0.018
78-89	2.57 ± 0.016	89-102	2.96 ± 0.020
90-110	2.88 ± 0.018	103-126	3.37 ± 0.022
111-155	3.23 ± 0.020	127-178	4.17 ± 0.024
156-300	3.96 ± 0.022	179-299	5.98 ± 0.028

Table 5.1 Summary table of results showing the relative multiplicty and the self normalised yield of heavy-flavour muons and the systematic associated uncertainty in multiplicity bins.

5.2 Results

5.2.1 Based on the data driven method

The self-normalised yields obtained in multiplicity bins using the data driven method are shown in Table 5.1. The results of self normalised yield of heavy-flavour muons plotted as a function of charged-particle multiplicity are shown in Figure 5.1. The backward and forward rapidity results are shown. The vertical bars represent the statistical uncertainties while the rectangles represent the systematic uncertainties. An increasing trend of the

heavy-flavour decay muon yields as a function of multiplicity is observed in both forward and backward rapidity. The increase is similar at low multiplicity within uncertainties, however, at high multiplicity, we see two different trends. At forward rapidity the yields show a slower increase with an almost gradual flattening. At backward rapidity the heavy-flavour decay muon yields continue to rise in faster than linear fashion.

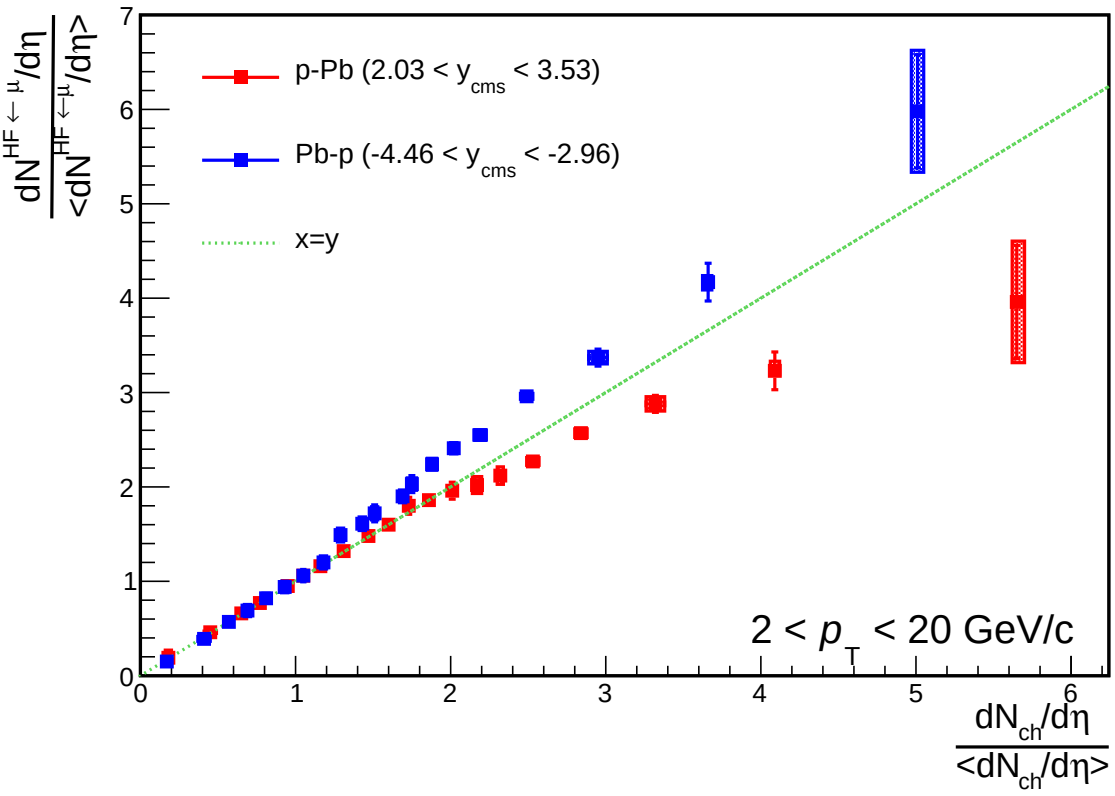

Fig. 5.1 Results of the self-normalised heavy flavour decay muon yields as a function of the self-normalised charged-particle multiplicity obtained using the data driven method. The boxes represent the systematic uncertainty while the vertical bars represent the statistical uncertainties. The green dashed line is x=y.

The difference between the two results at high multiplicity could be attributed to the expected CNM scenario at forward rapidity [131] where, heavy-flavour muon yields are suppressed at forward rapidity while no suppression is observed at backward rapidity.

5.2.2 Based on the "Official framework"

The self normalised yields obtained using the **Official framework** are shown in Table 5.2. Table 5.2 shows the centrality percentiles, the self normalised yields of the charged-particle multiplicity and the heavy flavour decay muons. Figure 5.2 shows the results

for p–Pb and Pb–p collisions i.e. the yield of heavy-flavour decay muons as a function of the charged-particle multiplicity. Similarly, an increasing trend is observed at both backward and forward rapidity. Also a slowly flattening trend is observed towards higher multiplicity at forward rapidity. This is not the case at backward rapidity.

Centrality percentile	$\frac{dN_{ch}/d\eta}{\langle dN_{ch}/d\eta \rangle}$	$\frac{dN^{HF\leftarrow\mu}/d\eta}{\langle dN^{HF\leftarrow\mu}/d\eta \rangle}$ **(p–Pb)**	$\frac{dN^{HF\leftarrow\mu}/d\eta}{\langle dN^{HF\leftarrow\mu}/d\eta \rangle}$ **(Pb–p)**
0-10	3.1 ± 0.14	2.65 ± 0.144	3.60 ± 0.182
10-20	2.02 ± 0.1	2.23 ± 0.124	2.39 ± 0.129
20-30	1.62 ± 0.08	1.82 ± 0.105	1.80 ± 0.103
30-40	1.32 ± 0.06	1.60 ± 0.095	1.41 ± 0.084
40-50	1.07 ± 0.05	1.25 ± 0.078	1.05 ± 0.067
50-60	0.84 ± 0.04	1.03 ± 0.067	0.78 ±00.053
60-70	0.62 ± 0.03	0.71 ± 0.050	0.51 ± 0.039
70-100	0.26 ± 0.01	0.65 ± 0.049	0.45 ± 0.036

Table 5.2 Summary table of results showing the relative multiplicty and the self normalised yield of heavy-flavour muons and the associated systematic uncertainty in centrality percentiles.

5.3 Comparison of the "Official framework" and the data driven method

The results from the two methods were plotted together in Figure 5.3. The backward rapidity data shows a good agreement between the two methods for common multiplicities. In forward rapidity, the result show incompatibility, especially in the lower and high multiplicity bins. The backward rapidity data also shows a similar disagreement in the first and last multiplicity bin. This difference could be attributed to the fact that merged multiplicity bins in the first bin were used, while the last bin of the official framework is also merged from several other multiplicity bins. Therefore the relative yield at the first and at last bin is a combination of all yields at low and high multiplicity, respectively. This also explains the fact the multiplicity reach of the official framework is lower than that of the data driven method.

The differences between results obtained at forward and backward rapidities particularly at high multiplicity are related to the dependence of heavy-flavour production on the collision geometry. Indeed, it is expected that the multiplicity of produced particles depends on the number of nucleons overlapping in the collision region, and therefore

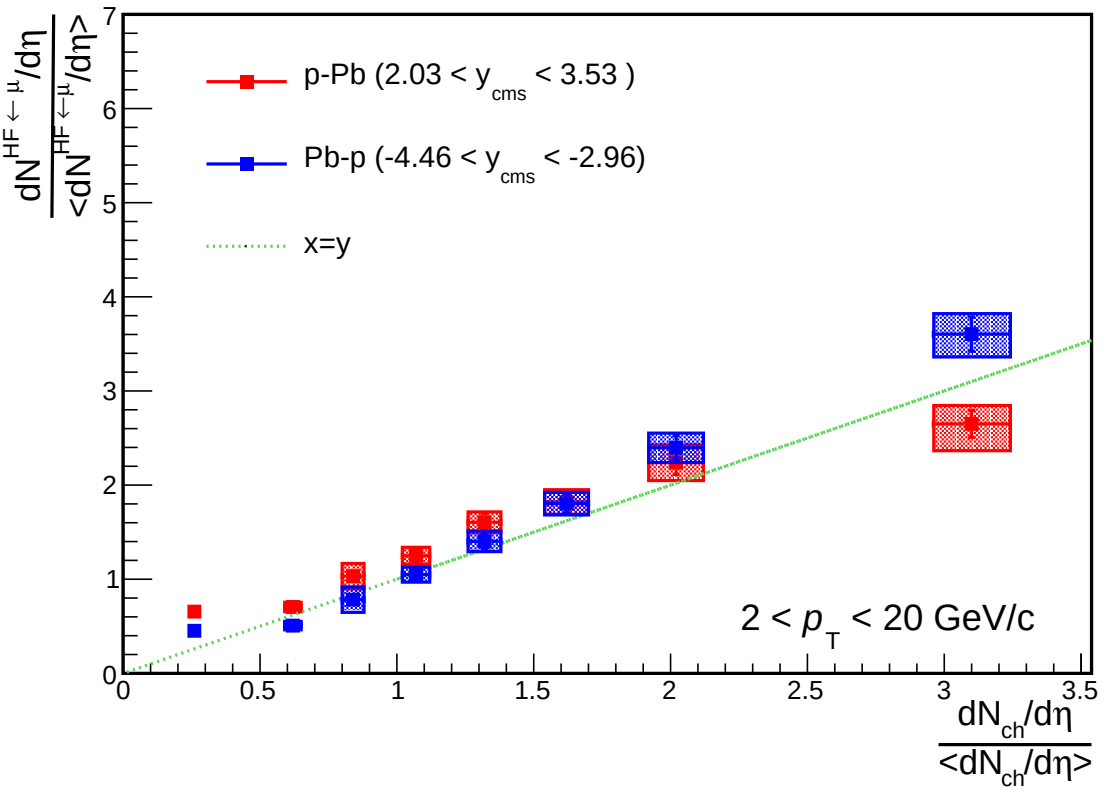

Fig. 5.2 Superimposed results of the self-normalised yield of heavy flavour muons as a function of multiplicity at forward and backward rapidity obtained using the "official framework". The boxes represent the systematic uncertainty while the vertical bars represent the statistical uncertainties. The green dashed line is x=y.

.

on the geometry of the collision. CNM effects are expected to be more pronounced in central collisions, i.e. high multiplicity events [68]. Moreover the forward rapidity is a low Bjorken-x probe region where nuclear shadowing plays a role hence the slow increase of heavy-flavour decay muons yield.

5.4 Comparison with other measurements

5.4.1 Heavy-flavour decay electron yields vs charged-particle multiplicity

The yield of heavy-flavour decay electrons was measured as a function of charged-particle multiplicity at $\sqrt{s_{NN}} = 8.16$ TeV [75], following the data driven method using the SPD as the multiplicity estimator. The heavy-flavour decay electrons as well as the charged-

particle multiplicity were measured at mid-rapidity, $|\eta| < 1$ in two p_{T} intervals, namely, $3 < p_{\mathrm{T}} < 6$ GeV/c and $6 < p_{\mathrm{T}} < 9$ GeV/c. Figure 5.4 shows the results obtained in this study plotted together with those obtained from the heavy-flavour decay electron study in the p_{T} intervals mentioned above.

Although the yields of heavy-flavour decay electron and muons are both increasing, the trends are mostly compatible at backward rapidity, within uncertainties, where a similar increase, that is faster than linear is observed towards higher multiplicities. At forward rapidity, the yields of heavy-flavour decay electrons continue to scale with the multiplicity at faster than linear rate while those of heavy-flavour muons scale at a slower rate. This could be because nuclear shadowing is expected at forward rapidity rather than at mid-rapidity. Therefore, the absence of the nuclear shadowing at mid-rapidity could be the reason for the similar increasing trend observed with the heavy-flavour decay muons at backward rapidity while the trend differs with that of heavy-flavour decay muons at forward rapidity.

5.4.2 J/ψ yields vs charged-particle multiplicity

J/ψ yields as a function of charged particle multiplicity are measured at forward rapidity using the muonic decay channel [118]. The charged particle multiplicity was obtained using the data driven method at $|\eta| < 1$ with the SPD as the multiplicity estimator. The results of the J/ψ yields as a function of charged particle multiplicity at forward and backward rapidity are plotted with the results obtained in this current study. The comparison is shown in Figure 5.5.

At both forward and backward rapidity the behaviour of the heavy-flavour decay muon yields and those of the J/ψ are similar within uncertainties. At forward rapidity both measurements show an increasing trend which is slower than linear at higher multiplicities while at backward rapidity the increase of the yields is faster than linear. Again, this could be an indication of collective effects in p–Pb collisions an attribute of Pb–Pb collisions where the QGP is expected.

At the writing of this thesis the theroretical calculations for these studies were not yet available. Therefore the comparison with theoretical calculations is not shown.

The next chapter presents the summary, conclusion as well as the outlook of the study.

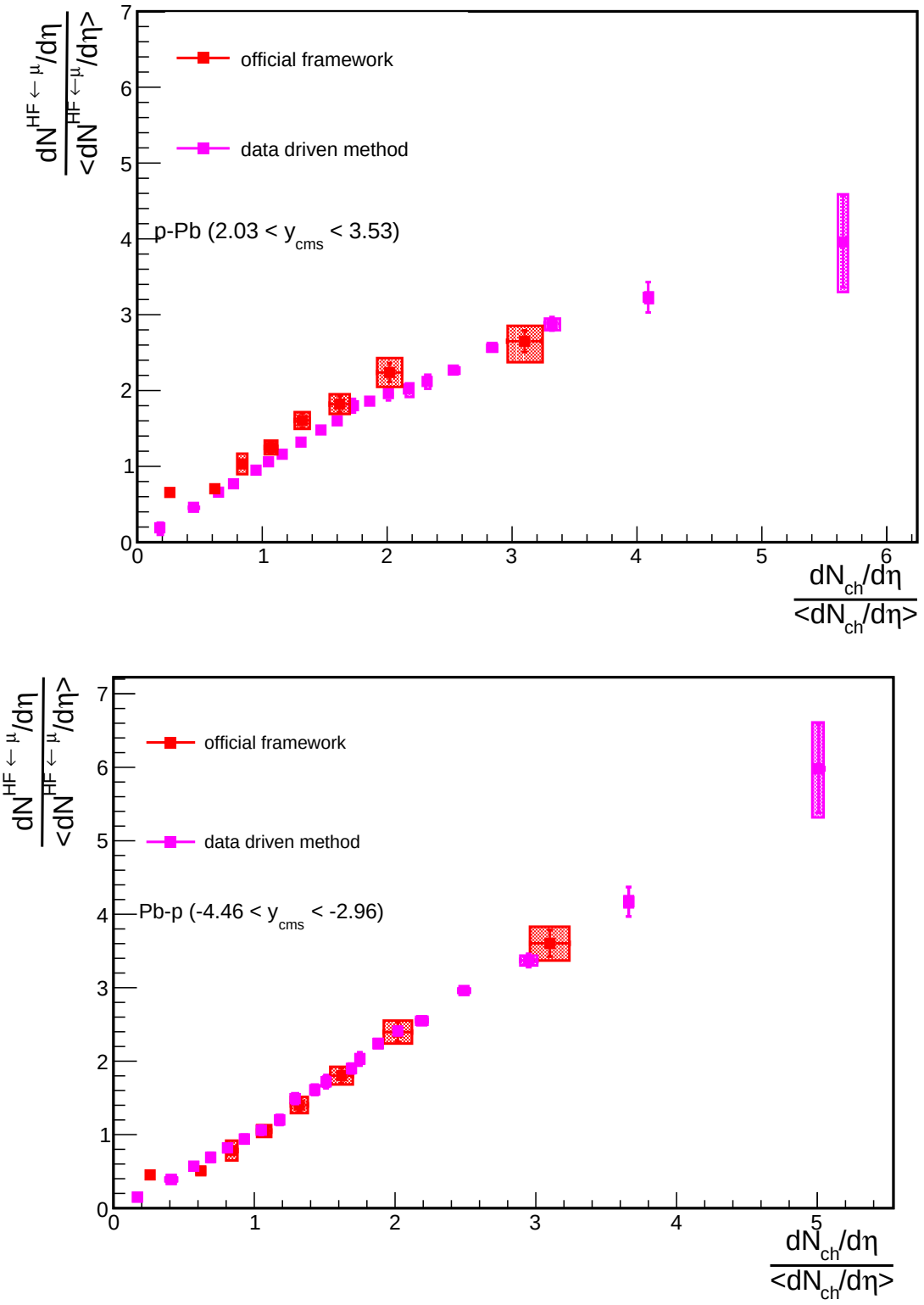

Fig. 5.3 Comparison of the "official framework" and data driven method. The boxes represent the systematic uncertainty while the vertical bars represent the statistical uncertainties.

.

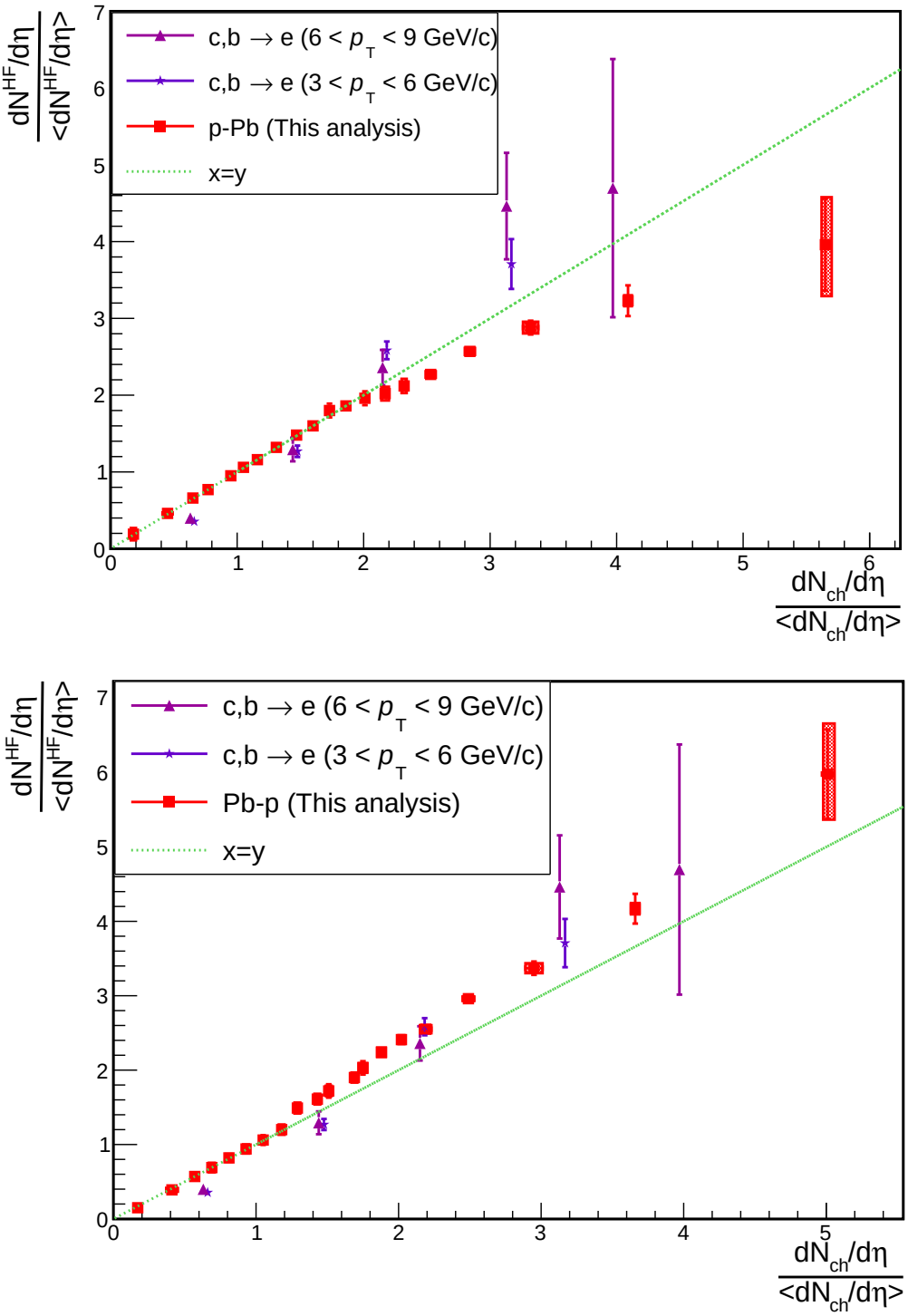

Fig. 5.4 Comparison of the heavy-flavour decay muon measurement (this from thesis forward rapidity (top) and backward rapidity (bottom)) with heavy-flavour decay electron measurements obtained using the data driven method. The boxes represent the systematic uncertainty while the vertical bars represent the statistical uncertainties. The green line is the graph x=y. .

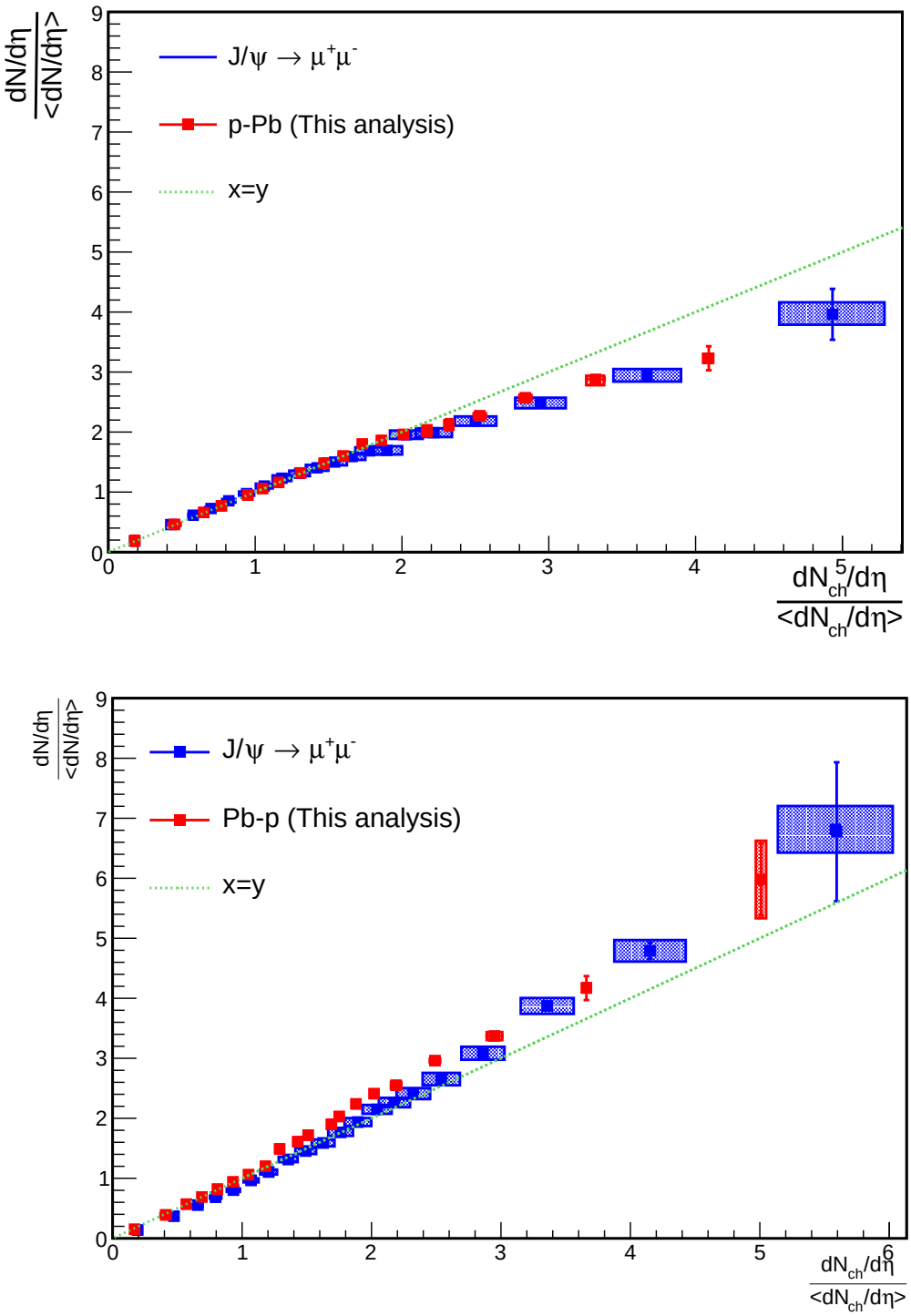

Fig. 5.5 Comparison of the J/ψ yields as a function of charged particle multiplicity [118] with the results obtained in this study in p-Pb (top) and Pb-p (bottom) collisions. The boxes represent the systematic uncertainty while the vertical bars represent the statistical uncertainties. The green dashed line is x=y.

.

CHAPTER 6

Summary, conclusion and outlook

6.1 Summary

In this thesis the production of heavy-flavour decay muons as a function of the charged-particle multiplicity was studied. The results are essential for understanding the role of MPIs as well as Multiple binary nucleon-nucleon collisions in particle production at LHC energies. Furthermore, p–Pb collisions give important information on CNM effects thus can be used to disentangle these effects from the effects of the QGP on particle yields. The production of heavy-flavour decay muons at forward (p–Pb) and backward (Pb-p) rapidities probes different Bjorken-x regions in order to understand CNM effects on the yields of heavy-flavour decay muons. One of the important aspects of the measurements was that the charged-particle multiplicity is measured at mid-rapidity, a different region from where the heavy-flavour muon decay yields are measured thus eliminating possible biases that could be caused by measuring both signals in the same pseudorapidity region.

The first chapter gave a brief introduction to heavy-ion collisions and the advent of state-of-the-art detectors developed in order to study the different sophisticated phenomena thought to be exhibited by these collisions. The objectives and motivation of this study were detailed. Chapter 2, gave a lengthy discussion on heavy-ion collisions, the formation of the QGP and the probes used to study its properties. In particular, the role of heavy-flavour hadrons with a focus on the inclusive decay into muons. Their production yields

are affected by the formation of the QGP in heavy-ion collisions and they are also subject to CNM effects which modify their yields even in the absence of the QGP. These effects are studies in p–Pb collisions. As well known, their production at LHC energies is via gluon-gluon fusion, therefore,their measurements at forward rapidity are interesting because of "shadowing" in this region of small Bjorken-x.

Chapter 3 presents the apparatus, i.e. the ALICE detector, with special attention given to the detectors used in this thesis to extract the required signals. The description of the data taking conditions and the software tools were also detailed.

Chapter 4 presented the analysis strategy and in Chapter 5, a discusssion of the results obtained from the current study was given. The results were presented for the two methods: data driven as well as "official framework". The multiplicity reach of the **data driven method** is higher ($\frac{dN_{ch}/d\eta}{\langle dN_{ch}/d\eta\rangle} \approx 5$) than that of the **official framework** ($\frac{dN_{ch}/d\eta}{\langle dN_{ch}/d\eta\rangle} \approx 3$), this difference is due to the way the multiplicity bins were defined in the two methods.

The results in both methods show an increase of the self normalised yield of heavy-flavour decay muons as a function of charged-particle multiplicity. The increase is different for backward and forward rapidity measurements. At forward rapidity, an increase that slows down at high multiplicity is observed compared to the increase observed at backward rapidity which is sharper at high multiplicity. The results were compared with the ones obtained in similar studies, i.e. heavy-flavour decay electrons as a function of multiplicity and J/ψ as a function of charged-particle multiplicity at $\sqrt{s_{NN}} = 8.16$ TeV. These measurements were done using the data driven method, therefore they were compared with results from this study obtained from the data driven method as well. For heavy-flavour decay-electron, the multiplicity bins are different from the ones in our study, however, a similar increasing trend at backward rapidity is observed for both heavy-flavour muons and heavy-flavour decay electrons. However, the comparison at forward rapidity shows that the heavy-flavour electron yields continue to scale with the multiplicity while the heavy-flavour decay muon yields slowly flatten out. The comparison with J/ψ yields show a similar trend for both forward and backward rapidity. These observations suggest collective behaviour in p–Pb collisions where the QGP is not expected. Furthermore, the slowly flattening increase at forward rapidity is attributed to the presence of *shadowing effects* which reduce the yields of heavy-decay muons and J/ψ at forward rapidity. Theoretical model calculations were not yet available for all the results discussed in this section at the writting of this thesis.

6.2 Conclusions

Qualitatively, a similar strong increase, i.e. faster than linear (particularly, at backward rapidity) is observed at high multiplicity, for heavy-flavour decay muons as a function of charged-particle multiplicity as that observed in the J/ψ study at both forward and backward rapidity. This observation raises a question whether CNM effects are also involved in production of heavy-flavour decay muons vs multiplicity case. On the other other hand, the results from this study show a similar strong linear increases at higher multiplicity specifically at backward rapidity as that observed in the study of heavy-flavour decay electrons and D-meson at $\sqrt{s_{NN}} = 5.02$ TeV at mid-rapidity. The similarity between the D mesons and the heavy-flavour decay muons is expected. The D mesons and the heavy-flavour decay muon are both cases of open heavy flavours however, the measurements differ in that the D meson is measured exclusively via a hadronic decay channel with a branching ratio of 55% while heavy-flavour decay muons are measured inclusively (summed charm and beauty mesons with braching ratio of $\approx 10\%$), due to the mass resolution limitation of the Muon Spectrometer. An interesting observation is the similarity between the heavy-flavour decay muons and D mesons to the J/ψ, where J/ψ is the case of a hidden charm meson. This similarity could be a strong indication that the enhanced yield of heavy flavour production is not influenced by hadronic activity but rather by charm and beauty quark production processes. Furthermore, this could be a hint for the presence of collective effects in p-Pb collisions. Comparison with theoretical calculations are vital and are needed in order to clarify.

6.3 Outlook

Since there were no inputs available to generate the background distributions directly for p–Pb collisions at $\sqrt{s_{NN}} = 8.16$ TeV at forward and backward rapidity, the background subtraction strategy may be improved by comparing the scaling factors obtained from PYTHIA with other generators. This was not possible in this thesis due to time constraints. This could also contribute in the improvement of the background estimation and systematic uncertainties on the background subtraction.

It would be interesting to perform the same study at $\sqrt{s_{NN}} = 5.02$ TeV for comparison with the current results to see if there is an energy dependency. Another interesting comparison would be with results from pp collisions at the same energy. Comparison with theoretical model calculations is anticipated in the near future.

The study may be further extended by considering a reference pp data at the same centre-

of-mass energy and studying the nuclear modification factor in order to give information on CNM effects as well as infer the extent to which they contribute to the production of heavy-flavours in Pb-Pb collisions where the QGP is expected to be formed. Furthermore, the study may be used to answer the question as to whether collective effects are also exhibited by proton-nucleus collisions at LHC energies.

In Run 1 and 2, only inclusive measurements of heavy-flavour decays could be performed in the ALICE Muon Spectrometer due to limitations in the mass resolution as well as the lack of detectors close to the interaction vertex. This impacted tracks reconstructed in that it was impossible to separate muons coming from charm and beauty hadron decays. After the installation of the Muon Forward Tracker, which will be placed in between the ITS and the Front Absorber of the Muon Spectrometer during the upgrade phase (long shutdown 2) it is envisaged that in Run 3 we will be able to measure heavy-flavour hadron decays exclusively at forward rapidity. These improvements will allow separation of charm and beauty hadron decays, thereby facilitating a better understanding of heavy-flavour hadron production at forward rapidity. Results from these measurements would complement those performed in the central barrel where exclusive open heavy-flavour measurements in the semi-electronic decay channel are already possible.

Appendices

APPENDIX A

A.1 Runlists

A.1.1 LHC16r p–Pb collisions

265594 265596 265607 265691 265694 265696 265697 265698 265700 265701 265709 265713 265714 265740 265741 265742 265744 265746 265754 265756 265785 265787 265788 265789 265792 265795 265797 265840 265841 266022 266023 266025 266034 266074 266076 266081 266084 266085 266086 266117 266187 266189 266190 266193 266196 266197 266208 266234 266235 266296 266299 266300 266304 266305 266312 266316 266318

A.1.2 LHC16s Pb–p collisions

266437 266438 266439 266441 266470 266472 266480 266487 266514 266516 266518 266520 266522 266523 266525 266533 266534 266539 266543 266549 266587 266588 266591 266593 266595 266613 266614 266618 266621 266630 266657 266658 266659 266665 266668 266669 266674 266676 266702 266703 266706 266708 266775 266776 266800 266805 266807 266857 266878 266880 266882 266883 266885 266886 266912 266915 266940 266942 266943 266944 266988 266993 266994 266997 267020 267022 267062 267063 267067 267070 267072 267077 267109 267131 267110

A.2 Pile-up fractions

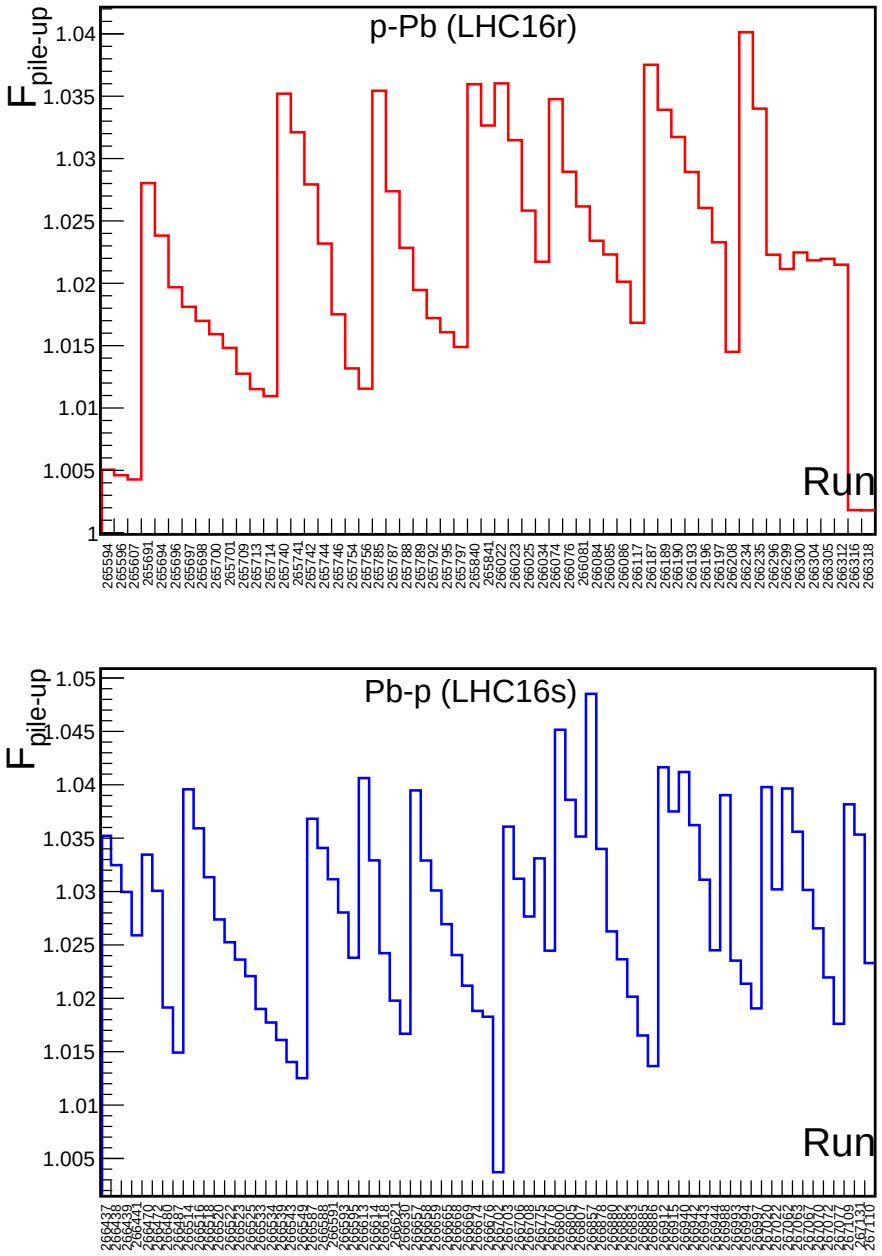

Fig. A.1 Pile-up fractions for p-Pb and Pb-p collisions

A.3 Pythia simulations

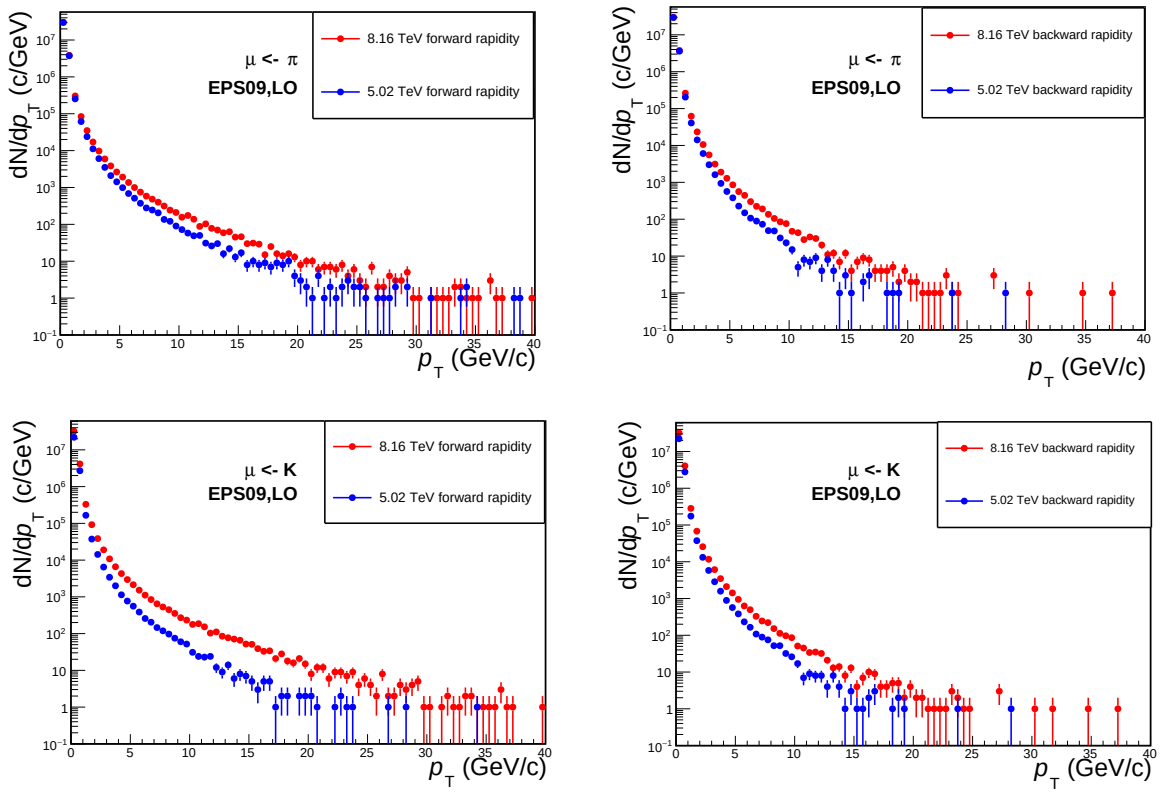

Fig. A.2 Transverse momentum distributions for muons from kaons at forward and backward rapidity obtained from PYTHIA simulations with EPS09, LO.

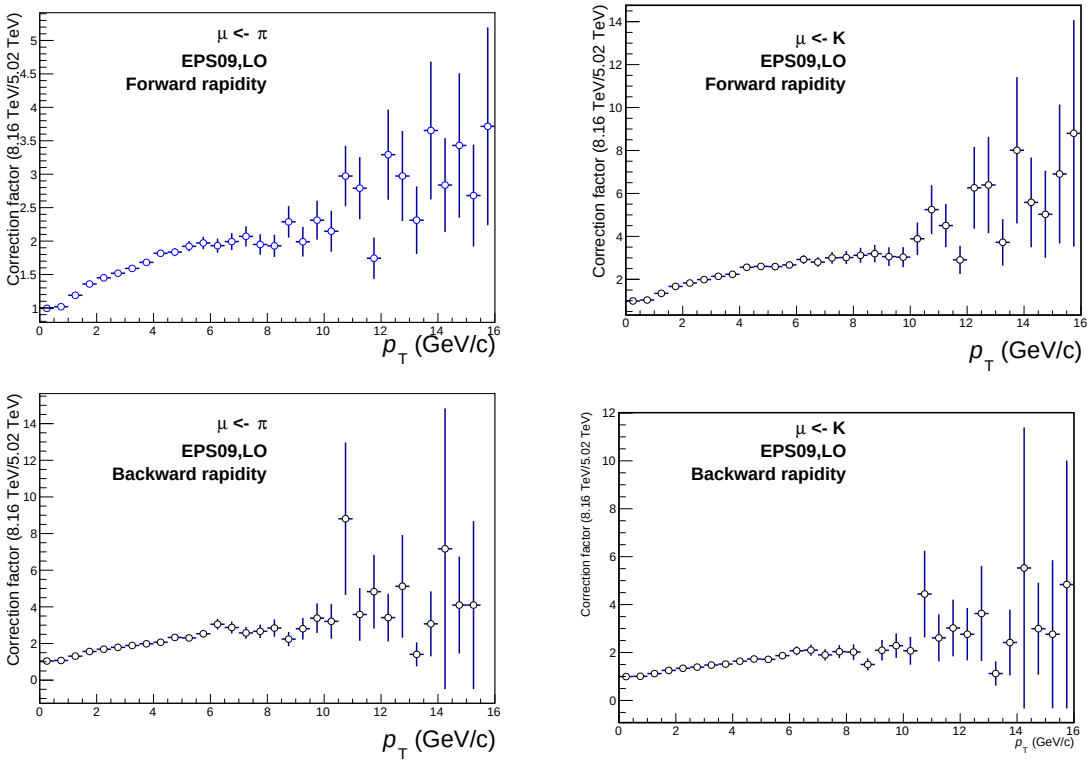

Fig. A.3 Rescaling factors obtained from the ratio of 8.16 TeV and 5.02 TeV transverse momentum distributions of muons from pions and kaon obtained from PYTHIA simulations with EPS09, LO at backward

A.4 Residual z_v^{SPD} plots

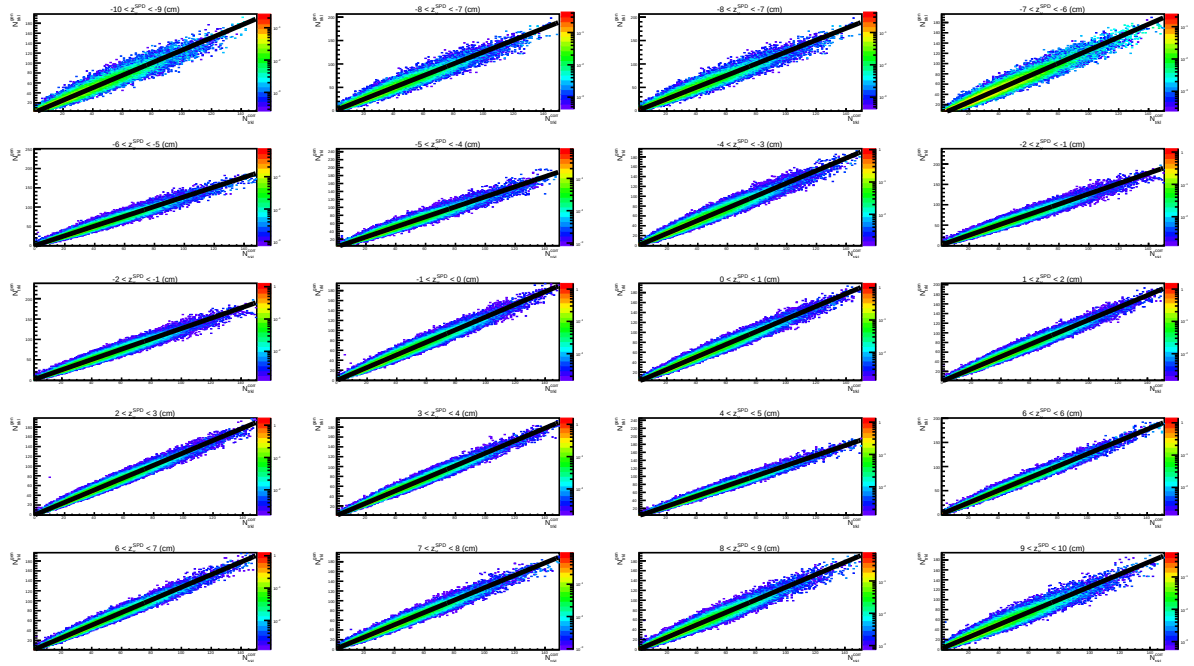

Fig. A.4 N_{gen}–N_{trkl}^{corr} correlations in z_v^{SPD} bins for DPMJET in p-Pb collisions. The black line is the fit used to obtain the α_{global} in each distribution.

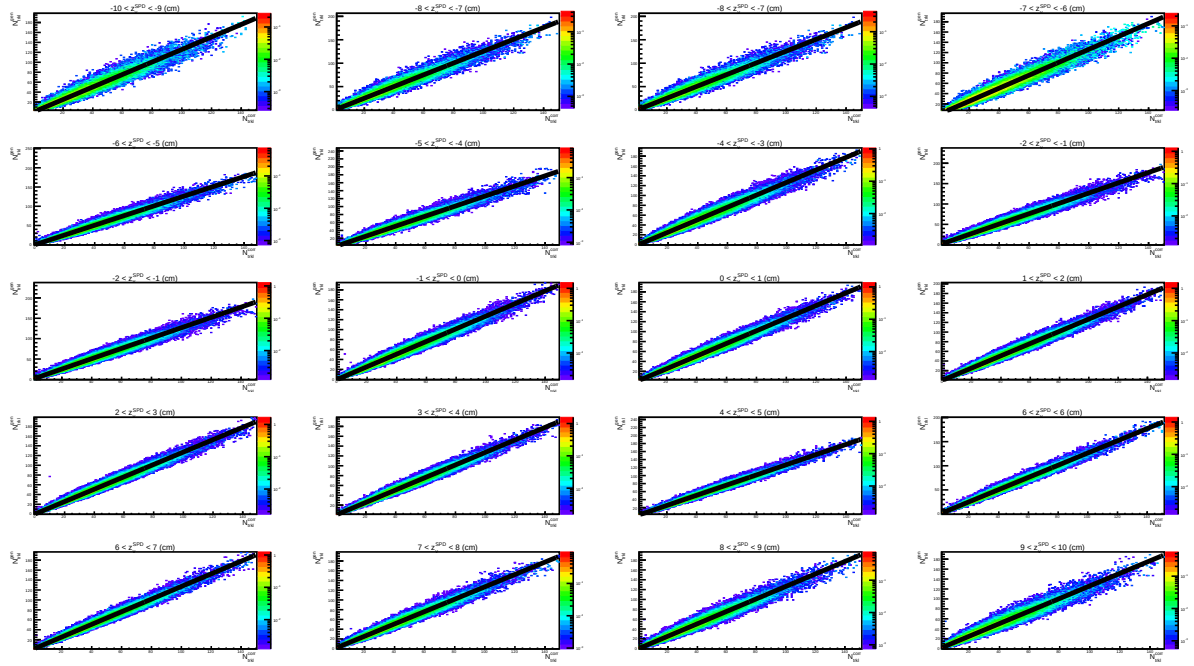

Fig. A.5 N_{gen}–N_{trkl}^{corr} correlations in z_v^{SPD} bins for DPMJET in Pb-p collisions. The black line is the fit used to obtain the α_{global} in each distribution.

Bibliography

[1] I. Bars, "Standard model of particles and forces in the framework of two-time physics," *Physical Review D*, vol. 74, no. 8, p. 085019, 2006.

[2] J. Birrell and J. Rafelski, "Quark–Gluon Plasma as the possible source of cosmological dark radiation," *Physics Letters B*, vol. 741, pp. 77–81, 2015.

[3] G. P. Engel, L. Giusti, S. Lottini, and R. Sommer, "Chiral symmetry breaking in QCD with two light flavors," *Physical review letters*, vol. 114, no. 11, p. 112001, 2015.

[4] X. Luo, "Spontaneous chiral-symmetry breaking of lattice QCD with massless dynamical quarks," *Science in China Series G: Physics, Mechanics and Astronomy*, vol. 50, no. 1, pp. 6–14, 2007.

[5] "The Large Hadron Collider." https://home.cern/science/accelerators/large-hadron-collider. [Online; accessed 14-May-2020].

[6] M. Harrison, T. Ludlam, and S. Ozaki, "RHIC project overview," *Nuclear Instruments and Methods in Physics Research Section A: Accelerators, Spectrometers, Detectors and Associated Equipment*, vol. 499, no. 2-3, pp. 235–244, 2003.

[7] I. Arsene, I. Bearden, D. Beavis, C. Besliu, B. Budick, H. Bøggild, C. Chasman, C. Christensen, P. Christiansen, J. Cibor, *et al.*, "Quark–Gluon Plasma and color glass condensate at RHIC? the perspective from the brahms experiment," *Nuclear Physics A*, vol. 757, no. 1-2, pp. 1–27, 2005.

[8] G. Martinez, "Advances in Quark–Gluon Plasma," *arXiv preprint arXiv:1304.1452*, 2013.

[9] N. Evans, J. Hormuzdiar, S. D. Hsu, and M. Schwetz, "On the QCD ground state at high density," *Nuclear Physics B*, vol. 581, no. 1-2, pp. 391–408, 2000.

[10] U. Heinz and M. Jacob, "Evidence for a new state of matter: An assessment of the results from the cern lead beam programme," *arXiv preprint nucl-th/0002042*, 2000.

[11] J. Schukraft, "Heavy ion physics at the large hadron collider: what is new? what is next?," *Physica Scripta*, vol. 2013, no. T158, p. 014003, 2013.

[12] T. A. Collaboration, "The ALICE experiment at the cern LHC," *Journal of Instrumentation*, vol. 3, no. 08, p. S08002, 2008.

[13] A. Collaboration, "Measurement of electrons from beauty hadron decays in pp collisions at $\sqrt{s}$= 7 TeV," *Physics Letters B*, vol. Volume 721, no. issues 1-3, 10 April 2013, pp. 13–23, 20 June 2016.

[14] A. Collaboration, O. Busch, T. Chujo, and Y. Miake, "D-meson production in p–Pb collisions at $\sqrt{s_{NN}}$= 5.02 TeV and in pp collisions at $\sqrt{s}$= 7 TeV," *PHYSICAL REVIEW C Phys Rev C*, vol. 94, p. 054908, 2016.

[15] C. Zampolli *et al.*, "Heavy flavour measurements in pp and Pb–Pb collisions with the ALICE experiment at LHC," *arXiv preprint arXiv:1209.5636*, 2012.

[16] A. Bredenstein, A. Denner, S. Dittmaier, and S. Pozzorini, "NLO QCD corrections to production at the LHC: 1. quark-antiquark annihilation," *Journal of High Energy Physics*, vol. 2008, no. 08, p. 108, 2008.

[17] M. L. Mangano, "Two lectures on heavy quark production in hadronic collisions," *arXiv preprint hep-ph/9711337*, 1997.

[18] B. Abelev, J. Adam, D. Adamová, A. Adare, M. Aggarwal, G. A. Rinella, M. Agnello, A. Agocs, A. Agostinelli, Z. Ahammed, *et al.*, "Pseudorapidity density of charged particles in p+ Pb collisions at $\sqrt{s_{NN}}$ = 5.02 TeV," *Physical Review Letters*, vol. 110, no. 3, p. 032301, 2013.

[19] B. Abelev, J. Adam, D. Adamova, A. Adare, M. Aggarwal, G. A. Rinella, M. Agnello, A. Agocs, A. Agostinelli, Z. Ahammed, *et al.*, "Transverse momentum distribution and nuclear modification factor of charged particles in p+ Pb collisions at $\sqrt{s_{NN}}$ = 5.02 TeV," *Physical review letters*, vol. 110, no. 8, p. 082302, 2013.

[20] , "The Super Proton Synchrotron." https://home.cern/tags/super-proton-synchrotron, Cern Accelerating Science. [Online; accessed 22 February 2020].

[21] J. Adam, D. Adamová, M. M. Aggarwal, G. A. Rinella, M. Agnello, N. Agrawal, Z. Ahammed, S. Ahmad, S. U. Ahn, S. Aiola, *et al.*, "Centrality dependence of the charged-particle multiplicity density at midrapidity in Pb–Pb collisions at $\sqrt{s_{NN}} =$ 5.02 TeV," *Physical review letters*, vol. 116, no. 22, p. 222302, 2016.

[22] T. Sjöstrand, S. Ask, J. R. Christiansen, R. Corke, N. Desai, P. Ilten, S. Mrenna, S. Prestel, C. O. Rasmussen, and P. Z. Skands, "An introduction to pythia 8.2," *Computer physics communications*, vol. 191, pp. 159–177, 2015.

[23] S. Porteboeuf, T. Pierog, and K. Werner, "Producing hard processes regarding the complete event: the epos event generator," *arXiv preprint arXiv:1006.2967*, 2010.

[24] B. Abelev, J. Adam, D. Adamová, A. Adare, M. Aggarwal, G. A. Rinella, M. Agnello, A. Agocs, A. Agostinelli, Z. Ahammed, *et al.*, "Multiplicity dependence of the average transverse momentum in pp, p–Pb, and Pb–Pb collisions at the LHC," *Physics Letters B*, vol. 727, no. 4-5, pp. 371–380, 2013.

[25] C. collaboration *et al.*, "Observation of long-range near-side angular correlations in proton-lead collisions at the LHC," *arXiv preprint arXiv:1210.5482*, 2012.

[26] E. Shuryak and I. Zahed, "High-multiplicity p p and p a collisions: Hydrodynamics at its edge," *Physical Review C*, vol. 88, no. 4, p. 044915, 2013.

[27] A. Bzdak, B. Schenke, P. Tribedy, and R. Venugopalan, "Initial-state geometry and the role of hydrodynamics in proton-proton, proton-nucleus, and deuteron-nucleus collisions," *Physical Review C*, vol. 87, no. 6, p. 064906, 2013.

[28] A. Collaboration *et al.*, "J/ψ production as a function of charged particle multiplicity in pp collisions at $\sqrt{s}$= 7 TeV," 2012.

[29] A. Grigoryan, H. Gulkanyan, V. Papikyan, M. H. Bello, M. I. Cortés, T. A. Fernández, M. Martínez, C. M. Rodríguez, M. G. Tejeda, A. Vargas, *et al.*, "Centrality dependence of particle production in p–Pb collisions at $\sqrt{s_{NN}} = 5.02$ TeV," *Physical Review C-Nuclear Physics*, vol. 91, no. 6, pp. 064905–064905, 2015.

[30] "Single muon and J/ψ yield in forward rapidity as a function of particle multiplicity at mid-rapidity in the ALICE experiment." https://indico.cern.ch/event/114069/contributions/1321669/attachments/45279/65157/Vienne2011-Lenhardt_v3.pdf. Accessed: 2019-07-25.

[31] "Read more on the ALICE Upgrade plans." http://alice.web.cern.ch/detectors/read-more-alice-upgrade-plans. [Online; accessed 14-May-2020].

[32] S. L. Glashow, "Partial-symmetries of weak interactions," *Nuclear Physics*, vol. 22, no. 4, pp. 579–588, 1961.

[33] The ATLAS Collaboration, "ATLAS muon drift tube electronics," *Journal of Instrumentation*, vol. 3, no. 09, p. P09001, 2008.

[34] T. C. Collaboration, "Sensitivity and environmental response of the CMS RPC gas gain monitoring system," *Journal of Instrumentation*, vol. 4, no. 08, p. P08006, 2009.

[35] Wikipedia contributors, "Kalman filter — Wikipedia, the free encyclopedia." https://en.wikipedia.org/w/index.php?title=Kalman_filter&oldid=906108519", 2019. [Online; accessed 24-July-2019].

[36] LHCb Collaboration *et al.*, "Observation of J/ψp resonances consistent with pentaquark states in Λb0 $\rightarrow$ J/ψk–p decays," *Physical review letters*, vol. 115, no. 7, p. 072001, 2015.

[37] S. Bethke, "Experimental tests of asymptotic freedom," *Progress in Particle and Nuclear Physics*, vol. 58, no. 2, pp. 351–386, 2007.

[38] Garth Huber., "QCD phase diagram." "http://dnp.phys.uregina.ca/content/photo/qcd-phase-diagram", 2014. [Online; accessed 21-Jan-2020].

[39] S. Sarkar, H. Staz, and B. Sinha, "The physics of the Quark–Gluon Plasma. introductory lectures," 1999.

[40] J. Adam, D. Adamová, M. M. Aggarwal, G. A. Rinella, M. Agnello, N. Agrawal, Z. Ahammed, S. U. Ahn, S. Aiola, A. Akindinov, *et al.*, "Direct photon production in Pb–Pb collisions at $\sqrt{s_{NN}}$= 2.76 TeV," *Physics Letters B*, vol. 754, pp. 235–248, 2016.

[41] M. L. Miller, K. Reygers, S. J. Sanders, and P. Steinberg, "Glauber modeling in high-energy nuclear collisions," *Annu. Rev. Nucl. Part. Sci.*, vol. 57, pp. 205–243, 2007.

[42] A. Dubla, "Measurements of heavy-flavour production and azimuthal anisotropy in Pb–Pb collisions with the ALICE detector," 2014.

[43] M. Djordjevic, "Jet suppression at LHC: theory vs. experiment," in *Journal of Physics: Conference Series*, vol. 509, p. 012094, IOP Publishing, 2014.

[44] D. David and B. Betz, "High-pt hadron suppression and jet quenching," in *The Physics of the Quark-Gluon Plasma*.

[45] R. Thews, "Formation time scales for quarkonia in a deconfining medium," *arXiv preprint hep-ph/9409209*, 1994.

[46] R. Baier, Y. L. Dokshitzer, A. H. Mueller, S. Peigne, and D. Schiff, "Radiative energy loss of high energy quarks and gluons in a finite-volume Quark-Gluon Plasma," *Nuclear Physics B*, vol. 483, no. 1-2, pp. 291–320, 1997.

[47] B.-W. Zhang, E. Wang, and X.-N. Wang, "Heavy quark energy loss in a nuclear medium," *Phys. Rev. Lett.*, vol. 93, p. 072301, Aug 2004.

[48] Y. L. Dokshitzer and D. E. Kharzeev, "Heavy-quark colorimetry of QCD matter," *Physics Letters B*, vol. 519, no. 3-4, pp. 199–206, 2001.

[49] C. M. Ko and W. Liu, "Suppression of heavy quarks in heavy-ion collisions," *Nuclear Physics A*, vol. 783, no. 1-4, pp. 233–240, 2007.

[50] A. Collaboration *et al.*, "Measurement of electrons from semileptonic heavy-flavour hadron decays at midrapidity in pp and Pb-Pb collisions at $\sqrt{s_{NN}}$= 5.02 TeV," *arXiv preprint arXiv:1910.09110*, 2019.

[51] A. Barbano, A. Collaboration, *et al.*, "D-meson nuclear modification factor and elliptic flow measurements in Pb–Pb collisions at $\sqrt{s_{NN}}$ = 5.02 TeV with ALICE at the LHC," *Nuclear Physics A*, vol. 967, pp. 612–615, 2017.

[52] Z. Zhang, A. Collaboration, *et al.*, "Production of muons from heavy-flavour hadron decays at forward rapidity in Pb–Pb collisions at $\sqrt{s_{NN}}$ = 5.02 TeV," *Nuclear and Particle Physics Proceedings*, vol. 289, pp. 405–408, 2017.

[53] R. Sharma, I. Vitev, and B.-W. Zhang, "Light-cone wave function approach to open heavy flavor dynamics in qcd matter," *Physical Review C*, vol. 80, no. 5, p. 054902, 2009.

[54] M. He, R. J. Fries, and R. Rapp, "Heavy flavor at the large hadron collider in a strong coupling approach," *Physics Letters B*, vol. 735, pp. 445–450, 2014.

[55] K. J. Eskola, H. Paukkunen, and C. A. Salgado, "An improved global analysis of nuclear parton distribution functions including rhic data," *Journal of High Energy Physics*, vol. 2008, no. 07, p. 102, 2008.

[56] A. D. Martin, W. J. Stirling, R. S. Thorne, and G. Watt, "Parton distributions for the LHC," *The European Physical Journal C*, vol. 63, no. 2, pp. 189–285, 2009.

[57] J.-J. Aubert, G. Bassompierre, K. Becks, C. Best, E. Böhm, X. de Bouard, F. Brasse, C. Broll, S. Brown, J. Carr, *et al.*, "The ratio of the nucleon structure functions F2n for iron and deuterium," *Physics Letters B*, vol. 123, no. 3-4, pp. 275–278, 1983.

[58] J. Arrington *et al.*, "New measurements of the emc effect in few-body nuclei," in *Journal of Physics: Conference Series*, vol. 69, p. 012024, IOP Publishing, 2007.

[59] A. Bodek and J. L. Ritchie, "Fermi-motion effects in deep-inelastic lepton scattering from nuclear targets," *Physical Review D*, vol. 23, no. 5, p. 1070, 1981.

[60] A. Bodek and J. L. Ritchie, "Further studies of fermi-motion effects in lepton scattering from nuclear targets," *Physical Review D*, vol. 24, no. 5, p. 1400, 1981.

[61] A. Collaboration *et al.*, "Measurement of electrons from heavy-flavour hadron decays as a function of multiplicity in p–Pb collisions at $\sqrt{s_{NN}} = 5.02$ TeV," *arXiv preprint arXiv:1910.14399*, 2019.

[62] S. Acharya, F. T. Acosta, D. Adamová, J. Adolfsson, M. M. Aggarwal, G. A. Rinella, M. Agnello, N. Agrawal, Z. Ahammed, S. U. Ahn, *et al.*, "Λc+ production in pp collisions at $\sqrt{s} = 7$ TeV and in p–Pb collisions at $\sqrt{s_{NN}} = 5.02$ TeV," *Journal of High Energy Physics*, vol. 2018, no. 4, p. 108, 2018.

[63] A. Karasu Uysal and C. ALICE, "Production of muons from heavy-flavour hadron decays in p–Pb collisions at $\sqrt{s_{NN}} = 5.02$ TeV," *Physics Letters B*, vol. 770, pp. 459–472, 2017.

[64] J. M. Campbell, J. Huston, and W. Stirling, "Hard interactions of quarks and gluons: a primer for lhc physics," *Reports on Progress in Physics*, vol. 70, no. 1, p. 89, 2006.

[65] K. Jakobs, "Physics at the lhc–from standard model measurements to searches for new physics," *arXiv preprint arXiv:1206.7024*, 2012.

[66] J. Pumplin, D. R. Stump, J. Huston, H.-L. Lai, P. Nadolsky, and W.-K. Tung, "New generation of parton distributions with uncertainties from global qcd analysis," *Journal of High Energy Physics*, vol. 2002, no. 07, p. 012, 2002.

[67] P. Bartalini, E. Berger, B. Blok, G. Calucci, R. Corke, M. Diehl, Y. Dokshitzer, L. Fano, L. Frankfurt, J. Gaunt, *et al.*, "Multi-parton interactions at the lhc," *arXiv preprint arXiv:1111.0469*, 2011.

[68] A. collaboration *et al.*, "Measurement of D-meson production versus multiplicity in p–Pb collisions at$\sqrt{s_{NN}} = 5.02$ TeV," *Journal of High Energy Physics*, vol. 2016, no. 8, 2016.

[69] R. Bernhard, R. Field, R. Chierici, M. Cacciari, A. Moraes, M. Strikman, D. Treleani, T. Rogers, A. Stasto, A. Achilli, *et al.*, "Proceedings of the first international workshop on multiple partonic interactions at the LHC (mpi08)," *arXiv preprint arXiv:1003.4220*, 2010.

[70] T. Sjöstrand and M. van Zijl, "A multiple-interaction model for the event structure in hadron collisions," *Physical Review D*, vol. 36, no. 7, p. 2019, 1987.

[71] S. Porteboeuf and R. G. de Cassagnac, "J/ψ yield vs. multiplicity in proton-proton collisions at the LHC," *arXiv preprint arXiv:1012.0719*, 2010.

[72] E. Ferreiro and C. Pajares, "Open charm production in high multiplicity proton-proton events at the LHC," *arXiv preprint arXiv:1501.03381*, 2015.

[73] H. J. Drescher, M. Hladik, S. Ostapchenko, T. Pierog, and K. Werner, "Parton-based gribov–regge theory," *Physics Reports*, vol. 350, no. 2-4, pp. 93–289, 2001.

[74] K. Werner, B. Guiot, I. Karpenko, and T. Pierog, "Analyzing radial flow features in p–Pb and pp collisions at several TeV by studying identified-particle production with the event generator EPOS3," *Physical Review C*, vol. 89, no. 6, p. 064903, 2014.

[75] P. Dhankher, "Multiplicity dependence of heavy-flavour hadron decay electron production in p–Pb collisions at $\sqrt{s_{NN}}$= 8.16 TeV measured with ALICE at the LHC," vol. 10, no. 1, p. 28, 2019.

[76] D. Adamová, M. M. Aggarwal, G. A. Rinella, M. Agnello, N. Agrawal, Z. Ahammed, N. Ahmad, S. U. Ahn, S. Aiola, A. Akindinov, *et al.*, "J/ψ production as a function of charged-particle pseudorapidity density in p–Pb collisions at $\sqrt{s_{NN}}$= 5.02 TeV," *Physics Letters B*, vol. 776, pp. 91–104, 2018.

[77] B. Abelev, J. Adam, D. Adamová, A. Adare, M. Aggarwal, G. A. Rinella, M. Agnello, A. Agocs, A. Agostinelli, Z. Ahammed, *et al.*, "J/ψ production and nuclear effects in p–Pb collisions at $\sqrt{s_{NN}}$ = 5.02 TeV," *Journal of High Energy Physics*, vol. 2014, no. 2, p. 73, 2014.

[78] "Cern accelerator complex." https://stfc.ukri.org/research/particle-physics-and-particle-astrophysics/large-hadron-collider/cern-accelerator-complex/. Accessed: 2019-07-25.

[79] O. source, "Acceleration sequence of pb ions," accessed 11 November 2019.

[80] K. Wille, *The physics of particle accelerators: an introduction*. Clarendon Press, 2000.

[81] J.-P. Revol, "First measurements at lhc: early hadronic physics (soft+ qcd) with alice, atlas, cms, totem and lhcb," *Nuclear Physics B-Proceedings Supplements*, vol. 177, pp. 60–68, 2008.

[82] C. Lippmann and D. Vrani, "Alice tpc numbering conventions," 2007.

[83] B. Abelev, J. Adam, D. Adamová, M. Aggarwal, G. A. Rinella, M. Agnello, A. Agostinelli, N. Agrawal, Z. Ahammed, N. Ahmad, *et al.*, "Technical design report for the upgrade of the ALICE inner tracking system," Tech. Rep. 8, 2014.

[84] A. collaboration *et al.*, "Alignment of the ALICE Inner Tracking System with cosmic-ray tracks," *Journal of Instrumentation*, vol. 5, no. 03, p. P03003, 2010.

[85] E. Bruna, A. Dainese, M. Masera, and F. Prino, "Vertex reconstruction for proton-proton collisions in ALICE," Nov 2009.

[86] A. Collaboration, I. Bearden, H. Bøggild, C. Christensen, J. Gaardhøje, J. Grossiord, T. Malkeiwicz, B. Nielsen, G. Paic, T. Wladyslaw, *et al.*, "ALICE technical design report on forward detectors: FMD, T0 and V0, CERN, 2004," tech. rep., CERN-LHCC-2004-025.

[87] P. Cortese, V. Chambert, R. Simon, J. Contreras, P. Van de Vyvre, A. Di Bartolomeo, V. Petrov, A. De Haas, F. Navach, A. Kolojvari, *et al.*, "ALICE forward detectors: FMD, TO and VO: Technical design report," tech. rep., ALICE-TDR-011, 2004.

[88] C. ALICE, "Technical design report of the Zero Degree Calorimeter (ZDC). CERN Report, vol," tech. rep., CERN/LHCC/99-005, 1999.

[89] A. Morsch, "The ALICE forward muon spectrometer at the LHC," *Nuclear Physics A*, vol. 638, no. 1-2, pp. 571c–574c, 1998.

[90] "ALICE at full power." https://cds.cern.ch/journal/CERNBulletin/2005/04/News%20Articles/816158?ln=en. Accessed: 2019-07-25.

[91] P. Dupieux, "The ALICE Muon Spectrometer and related physics," 2007.

[92] D. Stocco, "Development of the ALICE Muon Spectrometer: preparation for data taking and heavy flavor measurement," 2008.

[93] "The ALICE dimuon spectrometer." http://aliceinfo.cern.ch/Public/en/Chapter2/Chap2_dim_spec.html. Accessed: 2019-07-25.

[94] A. Zinchenko *et al.*, "A new approach to cluster finding and hit reconstruction in

muon chambers of ALICE. ALICE internal note, 2003,"

[95] Wikipedia contributors, "Kalman filter — Wikipedia, the free encyclopedia." https://en.wikipedia.org/w/index.php?title=Kalman_filter&oldid=906108519", 2019. [Online; accessed 24-July-2019].

[96] X. Zhang, *Study of Heavy Flavours from Muons Measured with the ALICE Detector in Proton-Proton and Heavy-Ion Collisions at the CERN-LHC*. PhD thesis, 2012.

[97] F. Guerin *et al.*, "ALICE internal note (march, 2006)," tech. rep., ALICE-INT-2006-0002.

[98] "tude du pqg par mesures de paires de muons :l'exprience ALICE." https://www.ip2i.in2p3.fr/alice/alice_activites.shtml. Accessed: 2019-07-25.

[99] T. Anticic, F. Carena, W. Carena, S. Chapeland, O. Cobanoglu, E. Denes, R. Divia, U. Fuchs, T. Kiss, J. Marin, I. Makhlyueva, F. Ozok, K. Schossmaier, C. Soos, P. Vande Vyvre, A. Vascotto, and S. Vergara, "The ALICE data-acquisition system," vol. 741, pp. 227 – 229, 11 2005.

[100] T. Anticic, F. Carena, W. Carena, S. Chapeland, O. Cobanoglu, E. Dénes, R. Divià, U. Fuchs, T. Kiss, J. Marin, *et al.*, "The ALICE data-acquisition system," in *IEEE Nuclear Science Symposium Conference Record, 2005*, vol. 1, pp. 227–229, IEEE, 2005.

[101] R. Alemany, M. Lamont, S. Page, *et al.*, "Functional specification: LHC modes," *ref. doc LHC-OP-ES-0005-10-00*, 2007.

[102] R. Schmidt, R. Assmann, E. Carlier, B. Dehning, R. Denz, B. Goddard, E. Holzer, V. Kain, B. Puccio, B. Todd, *et al.*, "Protection of the CERN Large Hadron Collider," *New Journal of Physics*, vol. 8, no. 11, p. 290, 2006.

[103] ALICE Collaboration, "ALICE electronic logbook." https://alice-logbook.cern.ch/logbook/date_online.php?p_cont=rund&p_run=266318&p_tab=gi&p_subtab=rc, 2016. [Online; accessed 26-Jan-2020].

[104] Grazia Luparello for the ALICE run Coordination, "Luminosity plots." http://lpc-afs.web.cern.ch/lpc-afs/LHC/2016/PbPb_luminosity_integrated_fills_2016_log.png, 2016. [Online; accessed 26-Jan-2020].

[105] ALICE Collaboration.

[106] ALICE Collaboration.

[107] "WLCG, world wide LHC computing grid." http://wlcg-public.web.cern.ch/tier-centres. Accessed: 2019-07-25.

[108] A. Gheata, "ALICE analysis framework," *PoS*, p. 028, 2008.

[109] A. Morsch, "ALICE simulation framework," tech. rep., 1999.

[110] "ALICE Offline." http://alice-offline.web.cern.ch/AliRoot/Manual.html. Accessed: 2019-07-25.

[111] K. A. Olive; Particle Data Group, "Sipd14091900000067," *Chinese Physics C*, no. 9, 2014.

[112] D. Stocco. https://twiki.cern.ch/twiki/bin/view/ALICE/MuonpPbQA2016. Accessed: 2019-07-25.

[113] E. Kryshen, "Event selection and characterization," Online source accessed 22-07-2019.

[114] E. Bruna, A. Dainese, F. Prino, and M. Masera, "Vertex reconstruction for proton-proton collisions in ALICE," tech. rep., 2009.

[115] D. Colella. Private Communication.

[116] D. Adamov *et al.*, "J/ψ production as a function of charged-particle pseudorapidity density in p–Pb collisions at $\sqrt{s_{NN}} = 5.02$ TeV," *Physics Letters B*, vol. 776, pp. 91 – 104, 2018.

[117] M. Marchisone, "Muon production from open heavy flavours in pp collisions at 8 TeV: cross section and multiplicity dependence." https://alice-notes.web.cern.ch/node/642.

[118] J. Crkovska, "Forward J/ψ production as a function of the charged particle multiplicity at midrapidity in p–Pb and Pb–p collisions at $\sqrt{s_{NN}} = 8.16$ TeV." https://alice-notes.web.cern.ch/node/648.

[119] S. Roesler, R. Engel, and J. Ranft, "The monte carlo event generator dpmjet-iii," in *Advanced Monte Carlo for radiation physics, particle transport simulation and applications*, pp. 1033–1038, Springer, 2001.

[120] "MonALISA repository for ALICE," 2017. https://alimonitor.cern.ch/catalogue/#/alice/sim/2017/LHC17e3a1/266318/001.

[121] P. P. V. Z. Beomkyu Kim, Yongwook Baek, "Reference Multiplicity." "https://twiki.cern.ch/twiki/bin/viewauth/ALICE/ReferenceMult#

Centrality_dependent_p_Pb_at_AN5".

[122] D. D. Chinellato, "Tools and Common Parameters for Multiplicity dependence Studies performed on proton-proton collision data." https://alice-notes.web.cern.ch/node/362.

[123] V. Zaccolo, "Relative Multiplicity : A homgenous way of doing it." "https://indico.cern.ch/event/691799/contributions/2978432/attachments/1637117/2612714/PAG-Mult_20Apr18-Valentina.pdf".

[124] J. Martin Blanco, "Study of J/ψ production dependence with the charged particle multiplicity in p-pb collisions at $\sqrt{s_{NN}}$ = 5.02 TeV and pp collisions at $\sqrt{s}$ = TeV = 8 TeV with the ALICE experiment at the LHC," tech. rep., 2016.

[125] M. Cacciari, S. Frixione, N. Houdeau, M. Mangano, P. Nason, and G. Ridolfi, "FONLL heavy quark production," 2016.

[126] R. Placakyte, "Parton distribution functions," *arXiv preprint arXiv:1111.5452*, 2011.

[127] S. Li, "Event activity dependence of muons from heavy-flavour hadron decays in p–Pb collisions at $\sqrt{s_{NN}}$ = 5.02 TeV." https://alice-notes.web.cern.ch/node/417.

[128] A. collaboration *et al.*, "W and Z boson production in p–Pb collisions at $\sqrt{s_{NN}}$ = 5.02 TeV," *Journal of High Energy Physics*, vol. 2017, no. 2, p. 77, 2017.

[129] S. Pisano, "Production of pions, kaons and protons in p–Pb collisions at 8.16 TeV." https://alice-notes.web.cern.ch/node/769.

[130] K. Eskola, H. Paukkunen, and C. Salgado, "EPS09 a new generation of NLO and LO nuclear parton distribution functions," *Journal of High Energy Physics*, vol. 2009, p. 065065, Apr 2009.

[131] S. Acharya, D. Adamová, M. M. Aggarwal, G. A. Rinella, M. Agnello, N. Agrawal, Z. Ahammed, N. Ahmad, S. U. Ahn, S. Aiola, *et al.*, "Production of muons from heavy-flavour hadron decays in p–Pb collisions at $\sqrt{s_{NN}}$ = 5.02 TeV," *Physics Letters B*, vol. 770, pp. 459–472, 2017.